UNIVERSIDAD POLITÉCNICA DE MADRID
Escuela Técnica Superior de Ingenieros de Telecomunicación

Design and Development of Two-Photon Polymerization System for Photonics Micro/Nanostructure Fabrication

DOCTORAL THESIS

Submitted for the degree of Doctor by:

Byron Oswaldo Ganazhapa Jiménez
MSc. Electronic Engineering

Madrid, 2024

UNIVERSIDAD POLITÉCNICA DE MADRID
Escuela Técnica Superior de Ingenieros de Telecomunicación

Doctoral Degree in Electronic Systems Engineering

Design and Development of Two-Photon Polymerization System for Photonics Micro/Nanostructure Fabrication

DOCTORAL THESIS

Submitted for the degree of Doctor by:

Byron Oswaldo Ganazhapa Jiménez
MSc. Electronic Engineering

Under the supervision of:
Dr. Patxi Xabier Quintana Arregui
Dr. Manuel Caño García

Madrid, 2024

Title: Design and Development of Two-Photon Polymerization System for Photonics Micro/Nanostructure Fabrication

Author: Byron Oswaldo Ganazhapa Jiménez

Doctoral Programme: Electronic Systems Engineering

Thesis Supervision:

Dr. Patxi Xabier Quintana Arregui, Full-profesor at Escuela Técnica Superior de Ingenieros de Telecomunicación – UPM (Supervisor)

Dr. Manuel Caño García, researcher at Departamento de Electrónica y Tecnología de Computadores – Universidad de Granada (Supervisor)

External Reviewers:

Thesis Defense Committee:

Thesis Defense Date:

This thesis has been supported by the "Ayudas para la realización de Doctorados Industriales de la Comunidad de Madrid" (IND2020/TIC-17424).

To my family…

Acknowledgement

Muchas gracias a todos quienes han formado parte en este proyecto de investigación; amigos, colegas y familiares.

Agradezco a todos catedráticos e investigadores del GFA, principalmente a mis directores de tesis, Xabier y Manuel (Lolo) por guiarme en la formación académica y ayudarme en la realización de este proyecto con sus ideas brillantes y experiencia. Agradezco a mis colegas, Javier y Ricardo, por acompañarme en la investigación, intercambiar ideas y comentarios constructivos, y por colaborar en la medición y presentación de resultados. También agradezco a Morten y José Manuel por su contribución en la presentación de resultados científicos y en la realización de esta tesis. ¡Gracias a todos de todo corazón!

Agradezco a todos los colegas de la empresa Lasing S.A., especialmente a Gonzalo, Alberto y Pablo por la formación profesional brindada hacia mi persona para la realización de este doctorado industrial. ¡Gracias sinceras por dejarme ser parte de la familia Lasing S.A.!

Ringrazio la mia compagna Barbara. Sei stata al mio fianco ogni secondo della mia vita, incoraggiandomi ad andare avanti in ogni scelta difficile e ostacolo, per cui sono felice e pieno di vita. Ringrazio tantissimo Dio per la tua esistenza, sei la mia anima e gioia che riempie il mio cuore. Dedico questa tesi specialmente a te. Ti amo tantissimo!

Ringrazio anche Antonio e Loredana per il loro sostegno e i loro consigli; siete la mia famiglia che nessun altro potrà mai avere in questo mondo, e siete i miei genitori accoglienti.

Agradezco a mi familia, Wilma, Segundo, Marta, Karla y Mónica por estar siempre a mi lado. Se que me han visto un ejemplo para seguir, pero la verdad es que son ustedes quienes han sido mi motor desde mis inicios. Dedico esta tesis también a ustedes. ¡Los quiero muchísimo!

Muchas gracias a todos.

Abstract

This Thesis is focused on the design, manufacturing, test, calibration, and optimization of a two-photon polymerization (2PP) system for micro-fabrication of polymeric structures. The work has been carried out as a collaboration between the company Lasing S.A. and the Grupo de Fotónica Aplicada (GFA) of the Centro de Materiales y Dispositivos Avanzados para Tecnologías de la Información y Comunicaciones (CEMDATIC) at the Technical University of Madrid (UPM). It has been funded by the Comunidad de Madrid under an industrial PhD program.

In the initial phase, the system was designed and assembled at the company Lasing S.A., and subsequently installed in the cleanroom of the GFA, resulting in a fully operational system for the polymerization of two- and three-dimensional (2D, 3D) microstructures based on commercial photoresists.

Subsequently, the 2PP system was optimized to characterize the voxel in commercially available negative-tone and positive-tone photoresists. This work –a crucial aspect for achieving maximum resolution during direct laser writing (DLW) processes– was performed in the GFA cleanroom. The work provides a DLW analysis that correlates printing parameters (scanning speed and laser beam power control) with the lateral and axial voxel sizes.

Once the system was optimized, 2D polymeric microstructures were fabricated. This involved controlling the voxel and the focus on ultrathin polymer surfaces to obtain repeatable patterns consisting of periodic microgrooves or microlines with 0.5 µm spacing for liquid crystal (LC) alignment. These arbitrary patterns enabled the generation of polarizers with high-quality alignment in SU-8 and S1805 photoresists.

Finally, 3D polymeric microstructures were fabricated. In this case, the hatching technique was applied with an optimized voxel to fill the printed microstructures using both layer-by-layer and true 3D printing methods. Additionally, complex micro-scaffolds with resolution of about 0.5 µm were fabricated in mr-DWL photoresist.

The fully functional 2PP system has enabled the micro-fabrication of photonic structures for a wide range of future commercial and research applications, resulting in an industrial equipment that the company Lasing S.A. can commercialize.

Resumen

Esta tesis se centra en el diseño, fabricación, prueba, calibración y optimización de un sistema de polimerización de dos fotones (2PP) para la micro-fabricación de estructuras poliméricas. El trabajo se ha realizado en colaboración entre la empresa Lasing S.A. y el Grupo de Fotónica Aplicada (GFA) del Centro de Materiales y Dispositivos Avanzados para Tecnologías de la Información y Comunicaciones (CEMDATIC) en la Universidad Politécnica de Madrid (UPM). Este proyecto ha sido financiado por la Comunidad de Madrid bajo un programa de doctorado industrial.

En la fase inicial, el sistema fue diseñado y ensamblado en le empresa Lasing S.A., y posteriormente instalado en la cámara limpia del GFA, resultando en un sistema completamente operativo para la polimerización de microestructuras bidimensionales y tridimensionales (2D, 3D) basado en fotoresinas comerciales.

Posteriormente, el sistema 2PP fue optimizado para caracterizar el vóxel en fotoresinas comerciales de tono negativo y positivo. Este trabajo, un aspecto crucial para alcanzar la máxima resolución durante los procesos de escritura directa por láser (DLW), se llevó a cabo en la sala limpia del GFA. El trabajo proporciona un análisis de DLW que correlaciona los parámetros de impresión (velocidad de escaneo y control de la potencia del haz láser) con los tamaños lateral y axial del vóxel.

Una vez optimizado el sistema, se fabricaron microestructuras poliméricas 2D. Esto implicó controlar el vóxel y el enfoque en superficies poliméricas ultradelgadas para obtener patrones repetibles consistentes en micro-surcos o micro-líneas periódicas con un espaciado de 0.5 µm para la alineación de cristales líquidos (LC). Estos patrones arbitrarios permitieron la generación de polarizadores con alineación de alta calidad en los fotoresinas SU-8 y S1805.

Finalmente, se fabricaron microestructuras poliméricas 3D. En este caso, se aplicó la técnica de hatching con un vóxel optimizado para el relleno de las microestructuras impresas mediante los métodos de impresión capa por capa y 3D real. Además, se fabricaron micro-andamios complejos con una resolución de alrededor de 0.5 µm en la fotoresina mr-DWL.

El sistema 2PP completamente funcional ha permitido la micro-fabricación de estructuras fotónicas para una vasta variedad de aplicaciones comerciales y de investigación futuras, culminando en un equipo industrial que la empresa Lasing S.A. puede comercializar.

Table of Contents

List of Figures

List of Tables

Abbreviations and Acronyms

1PA	One-photon absorption
1PP	One-photon polymerization
1PP-DLW	One-photon polymerization direct laser writing
2D	Two-dimensional
2PA	Two-photon absorption
2PP	Two-photon polymerization
2PP-DLW	Two-photon polymerization direct laser writing
3D	Three-dimensional
3PA	Three-photon absorption
A	Linewidth
AFM	Atomic force microscope
AM	Additive manufacturing
AOM	Acousto-optic modulator
BS	Beam-splitter
C_5H_8O	Cyclopentanone
CR	Contrast ratio
CW	Continuous-wave
DLW	Direct laser writing
DM	Dichroic mirror
ESA	Excited-state absorption
F_2	Filter setup (attenuator disk + fixed filter 1 + fixed filter 2)
Femto, fs	Femtosecond
FOV	Field of view
Galvos	Galvanometer-based optical scanners
H	Shannon entropy
HWP	Half-wave plate
IC	Internal conversion
ISC	Intersystem crossing
ITO	Indium-tin oxide
LC	Liquid crystal
LPS	Lasing processing software

MEMS	Microelectromechanical systems
MPA	Multi-photon absorption
NA	Numerical aperture
N-IR	Near-infrared
OD	Optical density
OL	Objective lens
$P_{\parallel}$	Parallel polarization
$P_{\perp}$	Crossed polarization
PBS	Polarizing beam-splitter
Piezo	Piezoelectric transducer
Pt	Pitch
RD	Rubbing direction
SE	Stimulated emission
SEM	Scanning electron microscope
STED	Stimulated emission depletion
UV	Ultra-violet
WD	Working distance
φ	Alignment angle or Molecular orientation

CHAPTER 1

1. Introduction

1.1. Motivation

Optical lithography is a widely used printing process in the manufacturing of photonic and semiconductor devices. This process can be:

- **conventional**, using masks to transfer patterns onto a photosensitive material, or
- **maskless**, employing direct laser writing (DLW) techniques with ultra-violet lasers.

However, these techniques have limitations in terms of resolution and in the creation of three-dimensional (3D) structures. Conventional techniques are generally limited to two-dimensional (2D) structures in a single fabrication process on one layer of material. The creation of 3D structures requires multiple fabrication steps across several layers, which poses a significant challenge.

Two-photon polymerization (2PP) is an advanced maskless technique capable of manufacturing 3D micro and nanostructures with dimensional precision and complex geometries, achieving resolutions down to just a few nanometers.

In 2PP, the excitation of molecules, commonly photo-initiators within photoresists, is induced by two-photon absorption (2PA). This is a nonlinear and highly improbable phenomenon, meaning that the probability of simultaneous absorption of two or more photons is proportional to the square of the incident light intensity and therefore it is typically confined to a region around the focal point. As a result, 2PP only occurs in the volume where the photon density exceeds an intensity threshold, enabling the creation of 3D polymeric structures with arbitrary geometries and sub-diffraction features. This allows for the fabrication of free-form micro-devices by moving the focal point of an ultrafast pulsed laser within the photoresists.

Currently, there are various innovative 2PP systems, both custom-built and commercial, for manufacturing. Some of these systems aim to overcome the diffraction limit (based on optical microscopy principles) [1], others to optimize fabrication methods (such as layer-by-layer or true 3D) [2], [3], and others to increase production throughput [4]. However, all 2PP manufacturing methods are fully functional for the creation of micro-devices. Moreover, a wide variety of photoresists can be used in 2PP systems to fabricate microstructures for

multidisciplinary applications, including photonic engineering, electronics, medicine, and biology.

This PhD thesis focuses on the development of a 2PP system for creating polymeric structures using commercial photoresists. This fully functional 2PP system, designed as a commercial prototype for the company Lasing S.A., will have the capability to manufacture photonic devices of interest for research and development areas of CEMDATIC at UPM and the local market.

Intellectual Property and Commercialization

In the first phase of development, the prototype is not subject to intellectual property protection (IPR) by the research directors or the executives of Lasing S.A., as it follows the open hardware philosophy. However, for the second phase, Lasing S.A. will discuss the implementation of legal protection measures for the commercial product.

1.2. Objective of this thesis

The main objective of this PhD thesis is to design and fabricate a customized system for the manufacturing of 2D and 3D micro- and nanostructures using the 2PP technique. This 2PP system is configured to integrate components that include a femtosecond laser, optical elements, precision mechanical positioning mechanisms, and electronic hardware control components, which enable the system's setup, calibration, and programming. This programming facilitates both basic and complex micro-fabrication and optimization processes.

The fully functional 2PP system is designed to polymerize commercial photoresists, and it aims to optimize the DLW parameters for micro-fabrication. Additionally, the system is characterized by having fully customizable hardware, which allows for extending the functionalities of optical lithography.

Finally, the manufacturing of 2D and 3D devices is proposed, achieving the high resolution, such as patterns on polymer surfaces for liquid crystal (LC) alignment and micro-scaffolds with complex fabrication features. Therefore, this proposed 2PP system is an accessible fabrication prototype that only requires optimal conditions in clean room, free of contaminants or particles and controlled illumination that could interfere with the DLW process on the photoresists.

1.3. Structure of this thesis

This PhD thesis is structured in several parts.

In Chapter 2, a brief introduction to the lithography technologies used in micro-fabrication is presented, along with a comparison to state-of-the-art 2PP lithography. Additionally, basic concepts and some photon absorption mechanisms are explained, followed by the processes

involved in photopolymerization. Finally, several photoresists commonly used in 2PP are presented, and a broad range of applications developed through 2PP is listed.

In Chapter 3, a comprehensive overview of the principles of DLW in polymerization is provided, with a focus on advanced 2PP-DLW techniques designed to enhance resolution. It also includes a brief discussion of various focusing configurations employed in DLW.

In Chapter 4, the design and fabrication of the 2PP system are described, based on the proposal of an appropriate setup for micro-fabrication, considering hardware and optical design criteria. The chapter also includes details on the final assembly of the custom system. In addition, a setup for one-photon polymerization (1PP) is added for the optimization process.

In Chapter 5, the commissioning of the 2PP system is described, followed by its optimization for both 1PP-DLW and 2PP-DLW. Additionally, the chapter covers the characterization of voxels (lateral and axial sizes) in commercial negative-tone and positive-tone photoresists.

In Chapter 6, the results of micrometric 2D fabrication for functional devices are presented, specifically focusing on the surface alignment of polymers to create complex patterns in LC polarizers.

In Chapter 7, the results of micrometric 3D fabrication are presented. The chapter showcases microstructures created in 2.5D (layer-by-layer printing) and true 3D. Additionally, the successful fabrication of complex micro-scaffolds with the typical resolution achieved is discussed.

Finally, conclusions and potential future work are presented in Chapter 8.

CHAPTER 2

2. Two-photon polymerization

Two-photon polymerization (2PP) is an advanced micro/nanofabrication technique known for its capacity to produce highly intricate two-dimensional (2D) and three-dimensional (3D) structures with exceptional spatial resolution. This method has garnered significant attention across various fields due to its ability to create complex architectures that are challenging to achieve with conventional techniques, which often offer limited control over microstructural design.

To fabricate precisely tailored 3D micro/nanostructures using 2PP, it is essential to comprehensively understand photon absorption mechanisms, photopolymerization processes, and involved materials. Additionally, 2PP addresses critical limitations and challenges related to material selection and manufacturing processes. Recent advancements have provided valuable insights into future 2PP applications, incorporating a wide range of compatible material composites. Overall, this state-of-the-art review aims to provide a foundational understanding of the 2PP technique as a lithography technology, highlighting its role in producing high-precision functional micro/nanostructures for a broad range of applications.

This chapter begins with a brief overview of the state of the art in available technologies for microstructure manufacturing, followed by an exploration of the fundamental photon absorption mechanisms involved in photopolymerization. It then introduces the photosensitive materials used in 2PP. Additionally, the chapter examines a range of applications, including photonic devices, micromachining, surface patterning, microfluidics, and medical and biological uses.

2.1. State of the art

Nowadays, polymerization by commercial laser rapid prototyping machines is an indispensable part of industrial processing for high-resolution structures [5]. Ultrafast pulsed laser for fabrication is a widely used technology to induce the 2PP technique [6], [7]. Photosensitive materials (e.g. positive-tone and negative-tone photoresists) are commonly curable by ultra-violet (UV) lasers for any 2D microstructures [8]. However, with 2PP the materials are not polymerized by UV radiation, but by absorption of photons at longer wavelengths, usually in the near-infrared (N-IR) spectrum, generating submicrometer 3D structures [9], [10].

The 2PP technique effectively processes photosensitive materials with high resolution [11] and offers significant advantages over conventional fabrication techniques, such as template-guided electrodeposition [12] or mask-mediated photolithography for nanostructures [13]. For example, the laser power penetrates deeply into the processed materials, inducing polymerization in a region confined to the focal spot. Additionally, the nonlinear dependence of the polymerization rate on light intensity enables true 3D spatial resolution [5], [14]. These capabilities allow for the successful production of various photonic and micromechanical devices [9], [15], [16] and extend the technique's applications to biological and biomedical fields [17], [18], [19].

2.1.1. Additive manufacturing technologies

Currently, 2PP lithography, also known as 2PP direct laser writing (2PP-DLW), is a versatile prototyping technique for fabricating 2D and 3D micro/nanostructures. Unlike traditional layer-by-layer lithography or 2.5D techniques, which build structures in a layered or partially three-dimensional manner, 2PP enables the creation of complex 3D features with high precision. The capability to accurately control and maneuver the laser focal spot in any direction within the material is a key advantage, surpassing the limitations of other additive manufacturing (AM) technologies [20], [21]. Although AM technologies —encompassing various materials such as ceramics, acrylates, hydrogels, and metals— are widely used, they often present constraints in producing highly intricate micro/nanostructures. Therefore, a comparison of AM technologies with 2PP, as summarized in Table 2.1, underscores the distinct advantages and sophistication of the 2PP technique [22].

Table 2.1: Summary of relevant additive manufacturing (AM) technologies.

AM Technology	Manufacturing process	Printing Resolution	Typical materials	Advantage	Disadvantage	Ref.
2PP-DLW	2.5D, 3D	25–100 nm	Acrylates, epoxides, ceramics, hydrogels	Very high resolution	Low build speed, limited materials	[23], [24]
Micro stereolithography (M-SLA)	2.5D	1–10 µm	Acrylates, epoxides	High resolution	Low build speed, limited mechanical properties	[25]
Digital Light Processing (DLP)	2.5D	10−50 µm	Acrylates, epoxides	Low oxygen effect	Low vertical resolution, Limited mechanical properties	[21], [25]
Continuous Liquid Interface Production (CLIP)	2.5D	75 µm	Acrylates	High build speed	Low-viscosity material required	[21]
Selective laser sintering (SLS)	2.5D	80 µm	Polyamide powder, Polymers	Very high build speed, better mechanical properties	Limited materials, rough surfaces, powdery surface	[21], [26]
Inkjet and Aerosol Jet printing	2.5D	10 µm, 100 µm	Conductive inks and dielectrics	High resolution, very high build speed	low viscosity ink required	[25]
Laminated object manufacturing (LOM)	2.5D	200−300 µm	Polymers, paper	Good Chemical resistance and strength	Limited materials, low resolution	[21]
Direct ink writing (DIW)	2.5D	200 µm	Polymers, metals, ceramics, hydrogels	Broad range of materials, high build speed	Speed and temperature affect process	[20]
Direct laser deposition (DLD)	2.5D, 3D	25−500 µm	Metals, polymers, ceramics	Material waste reduced	Very high laser power, low build speed, rough surfaces	[27]

2.1.2. 2PP micro-fabrication systems available

2PP experimental systems implemented in the research labs consist of a number of custom-made setups built for specific needs. Each setup gathers specific features such as the laser source, optical components, motion control system, printing mode, and custom photosensitive materials, all operating under cleanroom conditions [2], [28], [29], [30], [31]. In contrast, commercial systems are designed to meet fundamental requirements for nano-, micro-, and mesoscale fabrication. These commercial systems offer a more generalized set of features and capabilities intended for a broad range of applications, focusing on reliability and ease of use.

Powerful micro-fabrication systems are flexible, precise, versatile, fast, and user-friendly. Many of them implement sophisticated techniques to enhance printing capabilities required for both scientific and industrial (R&D) applications [32], [33], [34]. Nevertheless, the state-of-the-art commercial systems listed in Table 2.2 represent the most relevant systems for micro-fabrication using the 2PP technique.

Table 2.2: Comparison of commercial systems for micro-fabrication based on 2PP.

2PP system (manufacturer)	**Resolution [nm]**	**Build volume [mm³]**	**Max. scan speed [m/s]**	**Manufacturing process**	**Roughness [nm]**	**Ref.**
Photonic Professional GT2 (*Nanoscribe GmbH*)	160	100×100×8	0.1–0.625	Layer-by-layer	≤ 20	[32]
MPO 100 (*Heidelberg Instruments*)	100	100×100×10	1–10	Layer-by-layer	≤ 10	[33]
NanoOne (*UpNano GmbH*)	100	100×120×49*	Up to 1.2	Layer-by-layer	≤ 10	[34]
MicroFAB-3D (*Microlight3D*)	< 200	100×75×20	10^{-4}–10^{-3}	Layer-by-layer	≥ 20	[35]
PROME-Uni (*Moji-nano Technology*)	70	300×300×70*	Up to 80	3D*	≤ 10	[36]
Laser Nanofactory (*Femtika*)	150	160×160×60*	Up to 0.03	3D	≤ 20	[37]

* The accessible printing volume is determined by the XYZ travel specified in the system's datasheet or manufacturer's reports.

The combination of ultrafast pulsed lasers and XYZ motion systems leads to increased process efficiency, higher quality, and more effective machining of very small features compared to conventional laser processing or other AM technologies [4].

The vast majority of AM technologies employ multiple-axis linear translational stages to perform object geometry on the photoresist material. Galvanometer-based optical scanners

(galvos) are frequently used for fast scan up to 10 m/s [33], or 80 m/s [36]. Galvos are electro-mechanical systems composed of mirrors installed on motors without mechanical inertia in an orthogonal configuration. This can be quickly rotated around their axes, allowing the beam to be scanned in two dimensions.

Galvos offers high precision and short latency times in the order of a few hundred microseconds, enabling fast mirror scanning in the kHz frequency domain with excellent angular resolution. However, they are limited by the field of view (FOV) of the objective lens. While this limitation can be addressed by stitching to create larger structures, it introduces potential alignment errors during the process of joining substructures created in smaller areas. Stitching requires the use of a linear translating stage to move the sample on the XY-plane [33], as well as along the Z-axis.

Linear translating stages have the advantage of not being constrained by the objective's FOV, as they enable movement of the sample along all three axes, with a travel range that can exceed tens of millimeters on each direction. However, they are limited in scanning speed, typically up to 1 mm/s [35], which impacts overall scanning time. Additionally, these stages tend to be bulkier and heavier, with limited acceleration capabilities.

The commercial systems presented in Table 2.2 employ both galvos and linear translational stages. The first set consists of fast stages with a large travel range for quicker coarse positioning of the sample, while the second set employs slower and more precise stages [32], [33], [34], [35]. Additionally, the scanning times and printing resolution (adjustable voxel) can be controlled by speed and laser exposure time to create 3D microstructures [4], [37]. These factors, along with the resulting surface roughness (typically less than 20 nm), should be carefully considered for systems intended for research labs and industrial applications [2].

2.2. Photon absorption mechanisms

The mechanisms of light-matter interaction can vary depending on the applied light intensity, the exposure time, the incident light wavelength, the light polarization, and the properties of the material. For instance, these interactions can lead to effects such as heating, melting, vaporization, gas formation (e.g., within metals), and, notably, induce polymerization (e.g., within polymers) [38].

Polymerization is a phenomenon driven by photoexcitation that leads to the cross-linking of monomers or oligomers in the excited state of the material [39], i.e., through the absorption of photons. The number of photons absorbed by the photosensitive molecules in the material can vary, ranging from single to multiple photons. The extent of photon absorption influences the manifestation of various linear and nonlinear optical phenomena [40], [41], [42]. These

phenomena are classified based on the material's response to the external electric field, which characterizes its linear or nonlinear optical polarization [38], [43].

In the following subsections, various photon absorption mechanisms that may be used to induce the polymerization of photosensitive materials are described. These mechanisms are presented in simplified terms, excluding detailed processes involving singlet or triplet states, to facilitate a better understanding of the fundamental concepts and terminology.

2.2.1. One-photon absorption

One-photon absorption (1PA), also called single photon absorption (SPA) is the common mechanism of light-matter interaction and is a linear quantum mechanical process, where an electron of an atom or molecule modifies its energy level upon absorption of one photon.

In conventional optical absorption, an electron absorbs the energy of an incident photon. The atom or molecule is driven from the ground state $|S_0\rangle$ to a higher electronic level, defined as excited state $|S_1\rangle$ [44], as depicted in Figure 2.1. The energy of the absorbed photon must be equal to or greater than the energy gap between $|S_1\rangle$ and $|S_0\rangle$ to induce an absorption event, as defined in Equation (2.1). After reaching the excited state, the system eventually returns to the ground state (the minimum energy configuration) by emitting either phonons (non-radiative decay) or photons (luminescence).

$$E_{S_0 \rightarrow S_1} \geq E_{S_1} - E_{S_0} = h\nu_{ph} \tag{2.1}$$

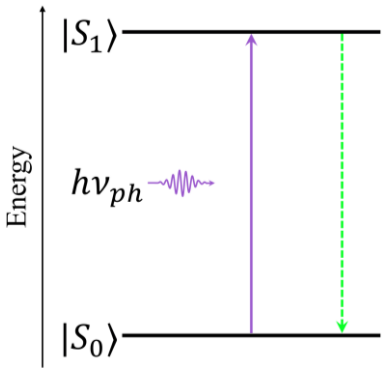

Figure 2.1: Schematic illustration of one-photon absorption (1PA). The violet upward arrow indicates the excitation process due to photon absorption, while the green downward arrow represents the return to the ground state $|S_0\rangle$ via radiative or non-radiative pathways.

The incremental decrease of the intensity light propagation through an absorptive medium (e.g. in the z direction), is proportional to the intensity itself:

$$\frac{dI(z)}{dz} = -\alpha I(z) \tag{2.2}$$

where I is the light intensity, z is the propagation distance, and α is the absorption coefficient of the material independent of the light intensity [40], [41], [45] when the saturation intensity is not reached. That means that 1PA is a linear optical process. From Equation (2.2), the intensity attenuation can be expressed by Lambert–Beer's law [40], [45]:

$$I\,(z) = I(0)e^{-\alpha z} \tag{2.3}$$

The probability of absorption is proportional to the initial light intensity $I(0)$, being higher near the surface of the material and decreasing as the light penetrates deeper. Consequently, the light intensity exponentially decreases along the propagation through the material as defined in Equation (2.3).

$$T = \frac{I(z = l)}{I(0)} = e^{-\alpha l} \tag{2.4}$$

The transmission defined in the Equation (2.4) depends on the absorption properties of the material but is not directly proportional to the initial intensity $I(0)$. The absorption probability in the material is influenced by the incident light intensity, but the relationship is more complex and not simply direct and proportional [40].

2.2.2. Multi-photon absorption

Multi-photon absorption (MPA) is a non-linear quantum mechanical process where the transition is driven by a few photons acting collectively [46]. MPA proceeds through one or more virtual states, allowing electron transitions to states that cannot be reached by 1PA [47].

To induce MPA, all photons must be present at the same time and place. The probability of the absorption event scales with the light intensity raised to the power of the number of photons needed (n-photon absorption $\propto n^{th}$ power of the photon flux density), typically two, known as two-photon absorption (2PA), but in some cases three-photon absorption (3PA) or more.

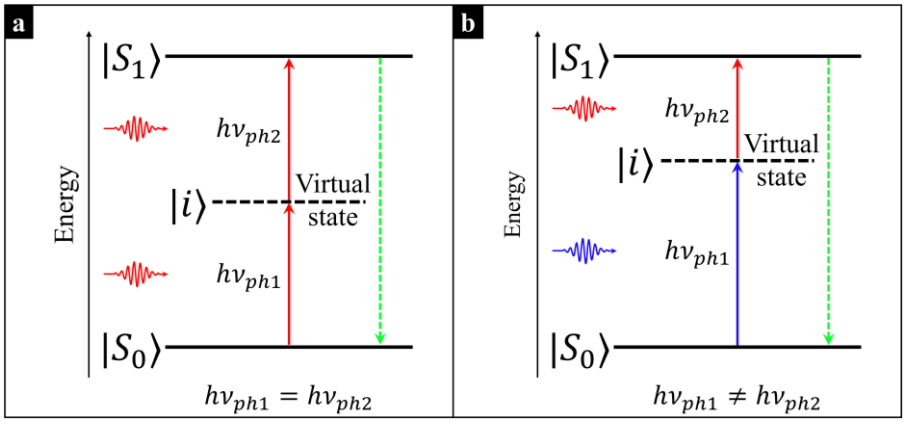

Figure 2.2: Schematic illustration of two-photon absorption (2PA) with a virtual energy state. a) degenerate, and b) non-degenerate 2PA. The red upward arrows indicate the excitation absorption, while green downward arrow indicates the relaxation back to the ground state $|S_0\rangle$ through radiative (fluorescence) or non-radiative pathways.

2PA is a well-known mechanism and was first theorized by Maria Goeppert Mayer in 1931 [48], experimentally observed by Kaiser and Garrett in 1961 [49], and subsequently implemented by Pao in 1965 [50].

2PA is a simultaneous absorption process with quantum mechanical three-states process, where an electron of an atom or molecule absorbs two photons simultaneously to transcend the energy gap in one excitation event [5]. The electronic transition from ground state to excited state $\left(|S_0\rangle \xrightarrow{\Delta h\nu} |S_1\rangle\right)$, the material is transparent to photons wavelength (i.e., the optical frequency ν of the photons is out of resonance of electrons in the material). When the first photon is absorbed, a non-stationary virtual state $|i\rangle$ is created, that has an extremely short lifetime, persisting for only several femtoseconds [24], in accordance with Heisenberg's uncertainty principle. 2PA occurs only if a second photon is absorbed within the lifetime of the virtual state before it decays. Afterwards, the system returns to the ground state either by relaxation (non-radiative decay) or by emitting fluorescence. Therefore, the energy gap is given by Equation (2.1), but the energy gap is twice the energy of either of the photons absorbed (degenerate case in Figure 2.2-a), or the sum of each different energy photon absorbed (non-degenerate case in Figure 2.2-b) [51].

$$\begin{aligned} &\textit{Degenerate 2PA:} && E_{S_0 \to S_1} = 2\, h\nu_{ph1,2} \\ &\textit{Non-degenerate 2PA:} && E_{S_0 \to S_1} = h\nu_{ph1} + h\nu_{ph2} \end{aligned} \tag{2.5}$$

The light intensity passing through a UV-absorptive optical medium does not follow the linear behavior described by Equation (2.2) or Equation (2.3) if the intensity of the incident light is high enough. The attenuation coefficient α is not constant and varies depending on the incident light due to an absorption saturation effect [41]. Therefore, the attenuation of intense light tightly focused on the material is higher, and Equation (2.2) must be redefined as:

$$\frac{dI(z)}{dz} = -\alpha I\,(z) - \beta I^2(z) \tag{2.6}$$

where β is the 2PA coefficient. In some cases, where 3PA or more processes are considered, Equation (2.6) should be generalized to be the following form:

$$\frac{dI(z)}{dz} = -\alpha I(z) - \beta I^2(z) - \gamma I^3(z) - \cdots \tag{2.7}$$

where γ is 3PA coefficient, and so on.

From Equation (2.6), the intensity attenuation can be expressed by the following expression [52], [53]:

$$I\,(z) = I(0)\frac{(1-R)^2 e^{-\alpha z}}{1 + \frac{\beta}{\alpha} I(0)\cdot(1-R)(1-e^{-\alpha z})} \tag{2.8}$$

where R is the reflectivity of the material.

The probability of exciting atoms or molecules is much higher at the focal spot of the light compared to any other region of the light beam. In other words, out-of-focus regions have a minimal effect on the attenuation of the light beam [6], because of high transmittance along of the material. This is due to the squared intensity of the incident light beam within the material, which is inversely proportional to the square of the focused area, $A^2(z)$, of any transverse section, and directly proportional to the number of molecules within the focused volume pixel, represented as $A^2(z) \times dz$, which is referred as a voxel in 2PP.

Thus, the coherent interaction of intense light with matter, as described by Equations (2.6) or (2.7), induces nonlinear phenomena that can be explained using advanced methods of nonlinear optics. MPA can reveal information about transitions that are not accessible through 1PA process. Initially, MPA was applied as a spectroscopic tool to identify energy states that are not connected to the ground state through 1PA [19], [24], [47].

2.2.3. Excited-state absorption

Excited-state absorption (ESA) is another nonlinear quantum mechanical process that is considered a type of MPA mechanism. ESA involves a stepwise process of MPA characterized by the presence of a real intermediate energy state with relatively long lifetime [54]. Stepwise 2PA with three-states systems is introduced to explain ESA as depicted in Figure 2.3.

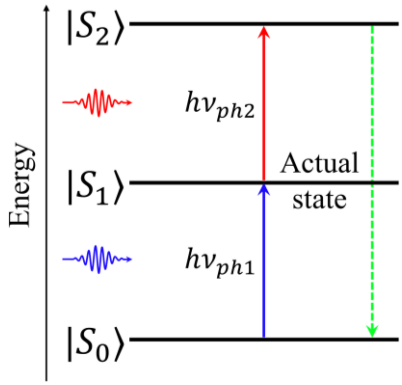

Figure 2.3: Schematic illustration of excited-state absorption (ESA) with an actual energy state. The diagram describes the case of degenerate 2PA to illustrate ESA. The red and blue upward arrows indicate the excitation absorption, while green downward arrow indicates the relaxation back to the ground state $|S_0\rangle$ through radiative (fluorescence) or non-radiative pathways.

ESA involves the sequential absorption of photons by an atom or molecule, where the excited state $|S_1\rangle$ is further pumped to a higher energy state $|S_2\rangle$ by absorbing another photon with the same energy $h\nu_{ph1} = h\nu_{ph2}$. For example, if the lifetime of the excited state $|S_1\rangle$ is relatively long compared to the duration of the incident light (i.e., very short excitation exposure time), a

second photon can be directly absorbed ($|S_1\rangle \longrightarrow |S_2\rangle$). Afterwards, the atom or molecule returns to the ground state $|S_0\rangle$ by non-radiative decay or luminescence. [55]:

$$E_{S_0 \to S_2} = E_{S_0 \to S_1} + E_{S_1 \to S_2} \tag{2.9}$$

The difference between ESA and simultaneous 2PA lies in the coherence of the incident light. ESA typically involves two light sources, which may have the same or different wavelengths, with pulse durations on the order of picoseconds to nanoseconds. ESA can satisfy MPA when the system has already absorbed one or more photons and, from that excited state $|S_1\rangle$, continues to absorb additional photons to reach even higher energy states [41], [47]. This phenomenon is fundamental in certain nonlinear optical processes, such as laser light generation and advanced spectroscopy.

ESA may be considered as two sequential 1PAs and can be combined with simultaneous 2PA to improve the optical power limitation behavior of photosensitive materials with joint optimization of the efficiency and spectral overlap of the two processes [51], [56].

2.2.4. Cooperative absorption and luminescence

Cooperative absorption (CA) and cooperative luminescence (CL) in photon absorption are nonlinear optical effects that arise from the interaction between species in a material. In these processes, which are depicted in Figure 2.4, the interaction involves two types of species, A and B. These effects are strongly dependent on the concentration of the species and the relative distance between them, often requiring high concentrations to observe significant interactions [43].

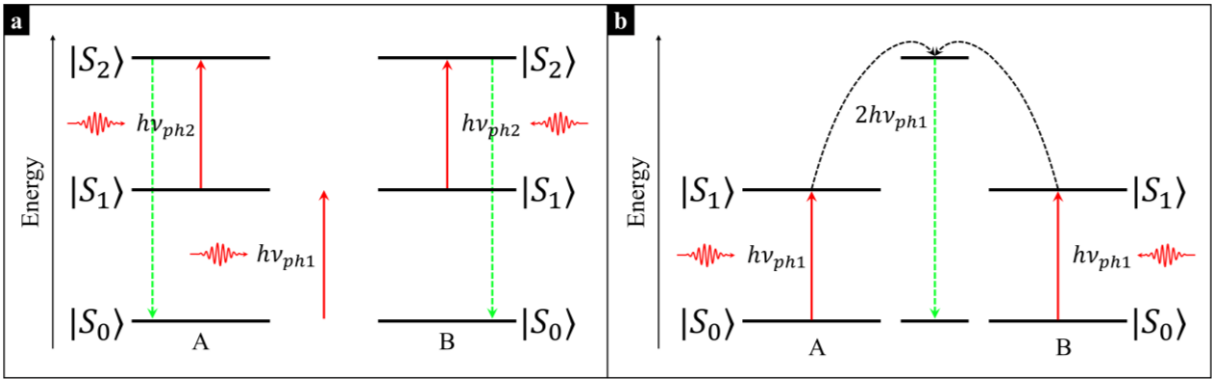

Figure 2.4: Cooperative mechanisms of MPA, cooperative absorption (CA) in (a) and cooperative luminescence (CL) in (b). The red upward arrows indicate the excitation absorption, while green downward arrows indicate the radiative pathways.

In CA of Figure 2.4-a, the absorption process of species A and B ($|S_0\rangle \longrightarrow |S_1\rangle$) occurs when there is cooperative absorption of one photon or simultaneous absorption by two relatively separated atoms or molecules within the species. Subsequently, a photon of the same energy is

observed by species A and B separately, leading to a higher excitation state ($|S_1\rangle \longrightarrow |S_2\rangle$). After completing the absorption of the second photon, each species emits photons with higher energy than the absorbed photons [57], [58].

In CL of Figure 2.4-b, the absorption process of species A and B ($|S_0\rangle \longrightarrow |S_1\rangle$) occurs when photons are absorbed separately. Cooperation occurs during the emission process, where the energy of the emitted photons is approximately double that of the excitation photons, resulting in luminescence. Moreover, cooperative emission can also occur when the absorbed photons produce luminescence in real non-excited states that coincide with the transition to the ground state [59].

2.3. Polymerization induced by 2PA

The 2PP process is a versatile technique based on 2PA that uses laser radiation to convert unsaturated molecules in the liquid state to solid macromolecules through light-induced polymerization reactions in the UV, visible, and N-IR spectral ranges [5], [60].

Most of the available photosensitive materials, commonly known as photoresists, are designed to be polymerized using UV light sources. These materials have a higher absorption probability, typically in the 315-400 nm, and are transparent in the N-IR.

The non-linear effect of the intensity concentration from an ultrafast pulsed N-IR laser (approximately $\lambda = 800$ nm and $\tau = 100$ fs) on liquid photoresists can initiate polymerization within the voxel, where the photon flux density is sufficiently high [24], [61]. 2PA effectively halves the wavelength of the incident light ($h\nu_{ph} = E_{S_0 \rightarrow S_1}/2$), as described in Equation (2.5). This results in polymerization occurring within the focal region of the laser in the UV spectral range of the photoresist [62], [63].

The key components of the photoresist used for 2PP are monomers mixed with photo-initiators or photosensitizers that are normally sensitive to the UV light and produce a free radical once excited by 2PA [6]. The concentration of the monomers and photo-initiators varies according to the manufacturers or researchers to develop an effective photoresist that performs 2PP efficiently [51], [64], [65], [66], [67].

The polymerization process consists of three steps:

(i) photo-initiation (Equations (2.10), (2.11), and (2.12)),

(ii) chain propagation (Equation (2.13)), and

(iii) termination (Equation (2.14)).

In polymeric materials, photo-initiation is the most important step, as it involves the production of active species that attack the monomers. In this step, the photo-initiators absorb two photons,

creating a pair of free photo-produced radicals, with a highly chemically reactive unpaired valence electron:

$$PI + 2h\nu_{ph} \rightarrow PI^* \rightarrow 2R_I^{\bullet} \tag{2.10}$$

where PI is photo-initiator, $R_I^{\bullet}$ is photo-produced radical with unpaired electron (free radical) and PI^* is an intermediate state of the photo-initiator after absorbing photons energy. In the case of the photosensitizers, one molecule absorbs two photons and then transfers the energy to an active photo-initiator [5], [68]. The photo-initiation process is expressed as:

$$S + 2h\nu_{ph} \rightarrow S^* \ldots PI \rightarrow PI^* \rightarrow 2R_I^{\bullet} \tag{2.11}$$

where S is the photosensitizer.

When using additive substances, such as co-initiators, they can work in combination with photo-initiators to enhance the formation of free radicals (or ionic polymerization). A co-initiator by itself does not absorb light, but is involved in the production of radicals species generated by photo-initiators [5]. Co-initiators can improve the polymerization rate or the efficiency of the photo-initiator by assisting in the generation of radicals necessary for polymerization [69].

The second reaction of initiation is the addition of the photo-produced radical to the first monomer producing the chain-initiating radical:

$$R_I^{\bullet} + M \rightarrow RM^{\bullet} \tag{2.12}$$

where M is monomer and $RM^{\bullet}$ is monomer-radical with unpair electron.

In the second step, chain propagation consists of the successive additions of monomer-radical to new monomer producing the reaction that propagates through the photoresist:

$$\begin{gathered} RM^{\bullet} + M \rightarrow RM_2^{\bullet} \ldots \\ RM_n^{\bullet} + M \rightarrow RM_{n+1}^{\bullet} \end{gathered} \tag{2.13}$$

In the third step, termination occurs when two photo-produced radicals bond to each other, cross-linking the monomers to form a long polymer chain ($RM_{n,m}$), with n and m monomers, or due to monomer depletion caused by the action of inhibitors [4], [6]:

$$\begin{gathered} RM_n^{\bullet} + RM_m^{\bullet} \rightarrow RM_{n+m}R \\ \text{or} \\ RM_n^{\bullet} + RM_m^{\bullet} \rightarrow RM_n + RM_m \end{gathered} \tag{2.14}$$

To improve the quantum yield of polymerization photo-initiation, one or more low-weight molecules that are more sensitive to light irradiation are added. These molecules form radical or cationic initiator species upon absorbing photons [5].

2.4. Materials for 2PP processing

Photoresists are widely used in photopolymerization processes with conventional technologies, generally being photosensitive to UV light. These technologies include M-SLA, DLP, CLIP, and specifically 2PP-DLW. A summary of these techniques is provided in Table 2.1.

Several photoresists require a specific energy dose to expose the targeted area for polymerization [63], depending on the efficiency of the chemical compounds involved in the photo-initiation, propagation, and termination reactions. Adjusting the energy dosage can therefore achieve effective polymerization. Additionally, UV or visible light absorbers, which do not necessarily participate in photo-initiation, but can improve resolution [70]. Another important criterion is the layer thickness before exposure. The limits of deposition techniques, such as spin-coating, depend on both the method used and the properties of the photoresist. In this context, the viscosity and wetting behavior of the photoresist on the solidified part are critically important. Consequently, both negative-tone and positive-tone photoresist materials with varying characteristics are widely developed and used, including solvent-free options, to optimize the efficiency of polymerization processing. These developments advance the state of the art in 2PP applications using the most suitable photoresist, with its features summarized in Table 2.3.

2.4.1. Negative-tone vs positive-tone photoresists

Negative-tone and positive-tone photoresists refer to the performance of the material during the photopolymerization process: in negative-tone photoresists, the areas exposed to light undergo cross-linking the monomers that then form polymer chains, making the cross-linked regions less soluble to the developer/solvents and remaining a cured micro/nanostructure on a substrate after development. In contrast, in positive-tone photoresists, the material is first solidified by heat and then exposed to light. The exposed areas experience bond breaking in the polymer chains due to molecular degradation, generating shorter units that become more soluble. These regions are removed during development, resulting in an inverse pattern of the exposed areas.

- SU-8 is an epoxy-based negative-tone photoresist, initially developed by IBM and currently commercialized by Kayaku Advanced Materials [71]. This is the most used photoresist for the fabrication of photonic devices and metamaterials with high resolution using optical lithography in the blue–UV spectral region [72]. SU-8 is thermally stable, transparent in the visible spectral region, and leaves behind a well-defined 3D microstructure once it is exposed to the light with high resistance to developing solutions while the unexposed portion is easily removed by solvents [73]. SU-8 is presented in various formulations to improve mechanical properties, resolution, aspect-ratio, adhesion to subtracts, curing speed, microstructures quality and viscosity (SU-8 100, 2000, 3000, 4000 and 6000 series). It is

also modified by researches & developers for specific developed applications [70], [74], [75], [76], [77].

- SCR-500 is an acrylate-based negative-tone photoresist developed by JSR Corporation [78], and is widely used in 2PP processes. This photoresist is sensitive to the UV spectral range and is employed to enhance resolution in nanostructure manufacturing for photonics and microelectronics applications [23], [79].
- EpoCore & EpoClad are epoxy-based, negative-tone photoresists from the chemically amplified series developed by Micro Resist Technology [80]. These photoresists are highly transparent in the visible spectral range, sensitive in the UV range, and exhibit high thermal stability. They are designed for pattern transfer processes in lithography, offering excellent mechanical stability. Currently, they are available in different viscosity for microelectronic applications, such as waveguides used in spectroscopy [81], [82], [83].
- ma-N is a novolak-based negative-tone photoresists developed by Micro Resist Technology [80]. This photoresist is sensitive to the UV spectrum and is used to enhance resolution and adhesion during nanostructure manufacturing, while also offering thermal stability [84]. Currently, it is available in ma-N 400, 1400 and 2400.
- mr-DWL is a chemically amplified, epoxy-based negative-tone photoresist developed by Micro Resist Technology [80]. This photoresist is highly transparent in the visible spectral range, thermally stable, sensitive to the UV range (especially around 400 nm), and offers high resistance and suitability for 2PP-DLW in optical and microelectronic applications [83], [85]. Currently, it is available in mr-DWL 5, 40, and 100.
- AZ-Photoresists are chemically amplified, acrylate-based photoresists, available in both positive-tone and negative-tone formulations (the latter using cross-linkers), developed by MicroChemicals GmbH [86]. These photoresists offer improved uniformity, mechanical stability, and thermal stability, with high resolution and aspect ratio suitable for lithography and optical and microelectronic applications [87], [88].
- S1800 G2 series are novolak-based positive-tone photoresist commercialized by Kayaku Advanced Materials [71]. This series is designed for photolithography applications, providing high resolution, thermal stability, and uniform coating. This photoresist is suitable for optoelectronic and microelectronic applications, offering excellent pattern transfer performance [89].

2.4.2. Solvent-free photoresists

- IP-Photoresists are acrylic and methacrylic-based negative-tone photoresists, developed by Nanoscribe specially for 2PP [32]. These photoresists are designed for use in immersion

printing technologies, such as dip-in laser lithography and oil immersion techniques [90]. They are optimized for high-resolution micro-fabrication across various applications [91], especially bio-applications [18]. IP-Photoresists exhibit high resolution and strong mechanical stability for 3D micro/nanostructures. They come in various formulations, including IP-S, IP-L, IP-Q, IP-G, and IP-dip, tailored to different applications and microstructure manufacturing needs. Advantages of IP-Photoresists include low shrinkage, high aspect ratios, and smooth surface finishes with excellent shape accuracy. Additionally, new variants like IP-Visio offer low fluorescence and non-cytotoxicity, making them suitable for bio-applications [92]. For integrated photonic applications, the IP-n162 variant features a high refractive index [93].

- OrmoComp is an inorganic-organic hybrid negative-tone photoresist developed by Micro Resist Technology [80]. This is especially compatible to 2PP-DWL processes for (nano)-imprint sensible to UV spectral range with high exposure dosage. OrmoComp is thermally stable, high resolution and non-oxygen sensibility. Finally, it is designed for micro-optics, microfluidics, coupling connection applications, and bio-applications [94], [95].
- Other solvent-free photoresists, such as organically modified ceramics (ORMOCER), include OrmoClear, OrmoStamp, OrmoCore, and OrmoClad. These materials can be used in 2PP-DLW [39], [96]. However, they require high exposure energy in the UV spectral range and are highly transparent to near-UV and visible light. As a result, they may need higher photon flux to effectively induce 2PA.

2.4.3. Other photosensitive polymers

- Polymers that can be used for 2PP are those that require prior preparation to be exposed to light to induce 2PA, such as pentaerythritol triacrylate (PETA), polyethylene glycol (PEG), and polyethylene glycol diacrylate (PEGDA) precursor solutions [11], [97]. Their characteristics are summarized in Table 2.3.
- Other photoresists that may be used are thiol-acrylic-based, which have favorable properties for inducing 2PA [98]. Monomers like trimethylolpropane triacrylate (TMPTA), polyethylene glycol (PEG), and bisphenol a epoxy acrylate (BAEA) are also effectively polymerized by combining appropriate photo-initiators to develop high-performance photoresists for 3D microstructure fabrication [66], [97], [99]. Additionally, incorporating solvents into the photoresist formulation can further enhance the efficiency of 2PP [100].

Table 2.3: Photoresists available for 2PP.

Photoresist	Tone	Photo-initiator	Monomer	Solvent	Developer
SU-8	Negative	Triaryl sulfonium hexafluoroantimonate	Eight epoxy functional groups	Gamma-butyrolactone (GBL) or cyclopentanone	Propylene glycol methyl ether acetate (PGMEA) and mr-Dev 600
IP-Photoresist	Negative	Triaryl sulfonium hexafluoroantimonate mixed with Rhodamine B for TPA.	2-(hydroxymethyl)-2-[[(1-oxoallyl)oxy]methyl]-1,3-propanediyl diacrylate (for IPDip)	Solvent-free	PGMEA and mr-Dev 600
SCR-500	Negative	2,7-dibromo-9,9-diethylhexyl-9H-fluorene, diphenyl(4-vinylphenyl) amine photosensitizer	Urethane acrylate-based oligomer	Chloroform	Ethanol
ma-N	Negative	Aromatic bisazide	Novolak-based	Safe solvents	aqueous-alkaline development
EpoCore & EpoClad	Negative	Camphorquinone	Epoxy-based oligomers	Cyclopentanone	mr-Dev 600
mr-DWL	Negative	bis(p-tolyl)iodonium hexafluorophosphate	Epoxy-based	GBL, propylene carbonate	mr-Dev 600

Photoresist	Tone	Photo-initiator	Monomer	Solvent	Developer
AZ-Photoresist	Positive and Negative	diazo-naphthoquinone (DNQ) for positive-tone. Melamine cross-linker for negative-tone	Acrylic-based monomers	Acetone, Isopropoanol, or Ethanol	Metal Ion Free (MIF) and Inorganic developers
S1800 Series	Positive	Diazo photoactive compound	mixed cresol novolak-based	Ethylene glycol derived ether. Methoxy-1-propanol acetate	MIF, Metal-Ion-Bearing (MIB), Microposit developer
OrmoComp	Negative	Diphenyl (2,4,6-trimethyl-benzoyl) phosphine oxide; ,3,5-trisIJ2-(9-ethylcabazyl-3) ethylene) benzene	Inorganic-organic hybrid polymer	Solvent-free	OrmoDev
PETA	Negative	Irgacure 369 or 819 (Silane crosslinker)	Pentaerythritol triacrylate	Acetone, Isopropanol, or Ethanol	Methyl isobutyl keton
PEG	Negative	2-Hydroxy-2-methyl-1-phenyl-propan-1-one	Polyethylene glycol (PEG 258) and PEG diacrylate (PEG 700)	TE buffer	Ethanol solution containing 0.05% Tween 20
PEGDA	Negative	2-hydroxy-40-(2-hydroxyethoxy)-2-methylpriophenone and Irgacure photo-initiators	Polyethylene glycol diacrylate precursor solution	Methanol	mr-Dev 600

2.5. 2PP applications

Applications are being developed using various tailored photoresists with optical, electrical, mechanical and chemical properties to create 2D and 3D micro/nanostructures for functional devices. For instance, materials optimized for mechanical and optical properties are used for signal conduction in optoelectronics and surface patterning for liquid crystal (LC) alignment in displays [101]. Some applications of 2PP are outlined below.

2.5.1. Photonics devices

2PP enables the creation of intricate micro/nanostructures beyond the diffraction limit, supporting rapid prototyping. Its high resolution, material versatility, and true 3D capabilities offer disruptive solutions for miniaturized photonic devices, advancing optical designs beyond traditional methods [102].

Micro-lenses are manufactured using 2PP with various strategies to achieve specific optical properties while ensuring mechanical stability and shape reproducibility [103], [104]. 2PP allows the creation of intricate submicrometric structures beyond the diffraction limit, enabling rapid prototyping and alignment-free 3D designs. Its high resolution, material versatility, and true 3D capabilities offer disruptive solutions for miniaturized photonic devices with advanced optical designs [105], [106]. These include axicon lenses [107], convergent lenses [9], meta-lenses [108], among others [102].

Periodic structures, such as woodpiles or micro-pillar arrays, are valuable for optically active microstructures, including photonic crystals, waveguides, micro-resonators and metamaterials [15], [109], [110], [111]. Additionally, 2PP has enabled innovative strategies for fabricating micro-optical elements in vortex beam generators [112], [113], as well as for the compact optical integration of dynamic and geometric phase elements [114].

2PP has been explored for fabricating optical fibers for holograms. This includes creating multifocal diffractive optical components on fiber end facets [115], and ring-shaped phase masks on fiber tips for improved projection and beam shaping [116].

Integrated optics has other potential applications [117]. For example, the fabrication of single-channel photonic links using 3D waveguides [118] and the hybrid integration of light sources with photonic circuits [119], [120] (see Figure 2.5).

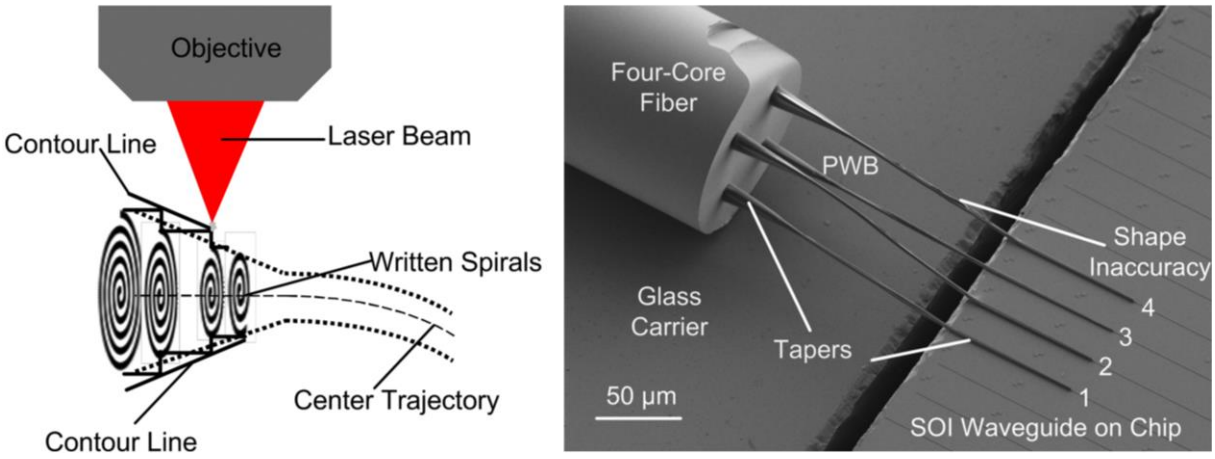

Figure 2.5: Fiber-to-chip interface using photonic wire bonds (PWB) to connect the individual cores of a multi-core fiber to different on-chip silicon-on-insulator (SOI) waveguides [121]. Line trace strategies in 2PP processes (left) and PWB in negative-tone photoresists (right).

Attractive photonic devices for controlling and manipulating the propagation of light were created using 2PP [122]. For instance, crystals with 3D dielectric structure that generate a photonic bandgap which blocks certain frequencies of electromagnetic waves [123], [124]. 2PP has been used to develop advanced 3D photonic devices, including chiral photonic crystals that exhibit properties such as circular dichroism and differential transmittance [125].

2.5.2. Micromachines and microelectromechanical systems

Micro- and nanomachines consist of 3D, movable micro-components produced by 2PP, which float freely in a photoresist due to its high viscosity [63].

To manipulate a micromachine, photoresists are typically doped with magnetic particles to magnetically driven micro-turbine or micro-springs [126], [127] (see Figure 2.6-a).

The interaction between laser light and optical micromachines allows for precise adjustments of their movements and behaviors at the micrometer scale. Laser beams influence both the rotational symmetry of the micromachines and the torque they exert [128].

A useful application of optically driven micromachines is the creation of lobular rotors within a microchannel. These rotors can function as micropumps to control the flow rate of fluids in microfluidic devices [129] (see Figure 2.6-b).

Advances in sensors, actuators, and communication systems at the micrometric scale are crucial for microelectromechanical systems (MEMS) [130]. Electrode patterns enhance MEMS functionality and enable complex applications [131]. Moreover, electrodes and microchannels are essential in microfluidic applications within MEMS, including fluid analysis and precise fluid handling for lab-on-a-chip systems [132].

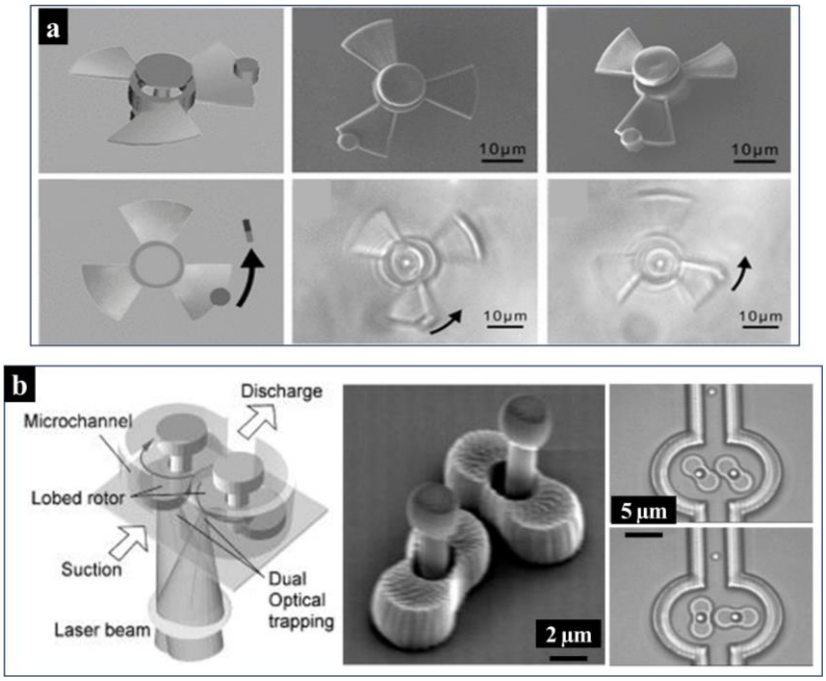

Figure 2.6: Micromachine models developed in 2PP. a) Model of a micro-turbine with circumgyration cycle in remote control [127]. b) Model of a lobed micropump with optically driven movements [129].

2.5.3. Surface patterning, alignment, and grating

Recent investigations have applied 2PP to surface patterning for the fabrication of devices that manipulate light in novel ways. For instance, aligning polymeric surfaces to control LC molecules is a common application [133]. Several strategies have been explored, including single polymerized layers [93], multiple layers [134] (see Figure 2.7), and rewriting LC patterns [135]. Chapter 6 is dedicated to surface patterning and alignment techniques for generating arbitrarily patterned polarizers in two polymeric photoresists.

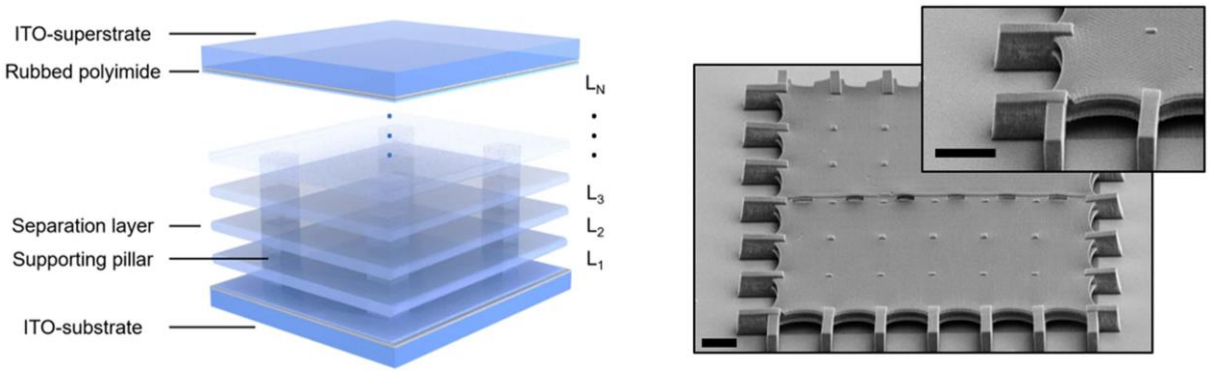

Figure 2.7: Multi-layer structure in liquid crystal (LC) alignment using 2PP [134]. Design with N number of LC layers (left) and a three-layer LC cell (right). A multi-layer LC spatial light modulator enables significant phase changes while maintaining fast response times.

Grating structures, in combination with 2PP, significantly accelerate the reproduction of microstructures. For instance, holographic diffraction gratings are used to generate interference

patterns that precisely control the polymerization process in photoresists [62]. Additionally, spatial light modulators can divide the laser beam to enable simultaneous fabrication of multiple microstructures [136]. The use of diffractive optical elements further enhances the efficiency in manufacturing complex structures through parallel processing [137].

2.5.4. Micro-fluidics

Microfluidic systems are widely used in chemistry, biology, medicine, environmental science, and materials science. These systems, part of MEMS, can integrate functional 3D microstructures made with negative-tone photoresists and 3D microfluidic structures from positive-tone photoresists.

Sensors based on negative-tone photoresists, integrated into microchannels to measure liquid flow rates, were developed via 2PP for optoelectronic systems [138]. Methods for controlling flow rates were developed, including microstructures designed to manage liquid transport in microchannels [139], and filtering systems for particle separation using micro-sieves fabricated in existing micro-devices [140] (see Figure 2.8).

Before mentioning the bio-applications, functional micro-components embedded in microfluidic devices can be fabricated using 2PP, employing a mixture of proteins and photo-initiators [141].

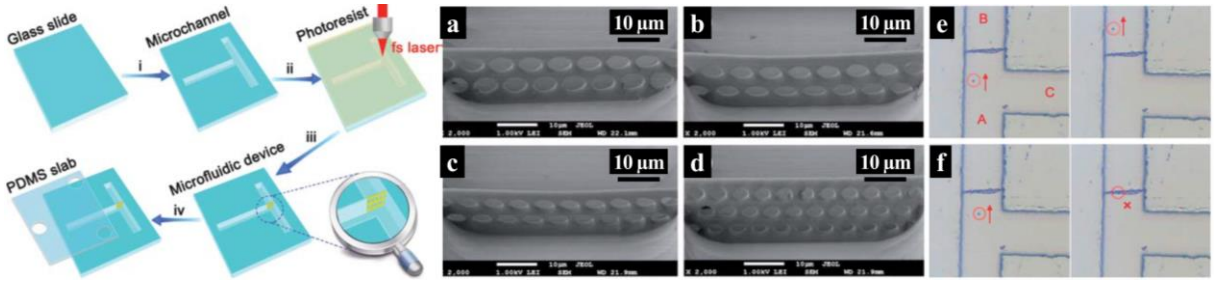

Figure 2.8: Embellishment of a microfluidic system by 2PP [140]. Schematic illustration for fabrication in SU-8, covering the device with a PDMS slab (left). Microsieve pores of different sizes to sort particles (center). Control of the microfluidics (right). If the particle size is smaller than the pores, it will pass through the sieve; otherwise, it will be blocked.

2.5.5. Medical and biological applications

Medical and biological applications on 2PP are also extensively developed with biocompatible photoresists from tissue engineering, cell engineering and biological MEMS [18], [142], [143].

One of the microdevices developed through 2PP related to microfluidics are microneedles designed for the transdermal delivery of protein and nucleic acid-based pharmacological agents [144]. Microdevices aimed at treating neurodegenerative diseases, focusing on cell survival and integration, have also been developed [145] (see Figure 2.9). Additionally, micro-actuators inspired by human flexible joints are created with multiple deformation modalities for

applications in soft robots, wearable devices, and similar technologies [146]. Functional microdevices featuring microvalves implanted into the human body are presented to prevent the reversal of blood flow in veins [147].

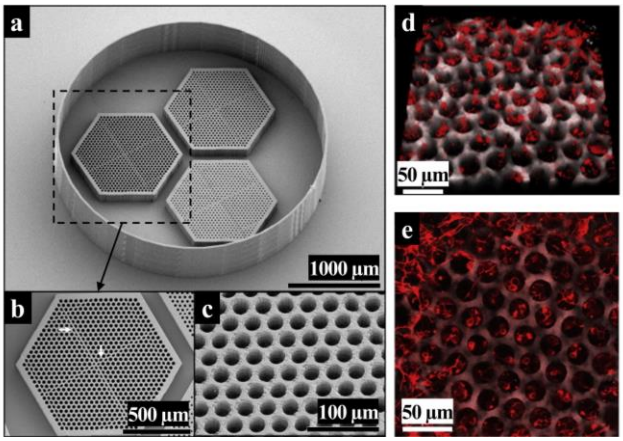

Figure 2.9: Induced pluripotent stem cell-derived retinal progenitor cells in juxtaposed micro-scaffolds [145]. a) Microstructure for cell loading. b)-c) Ordered and consistently sized vertical pores. d) Micro-scaffolds loaded with human retinal progenitor cells. e) Cell movement and survival in micro-scaffold pores.

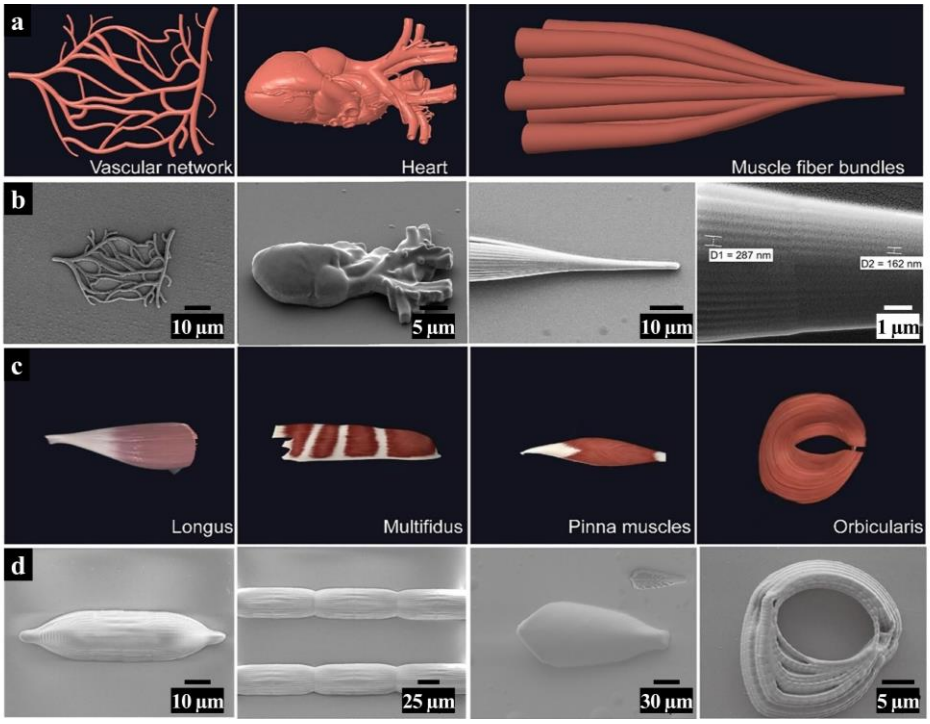

Figure 2.10: Models of human tissues using 2PP [143]. Vascular network, heart, and muscle fiber bundles in (a), and their printed models in (b). Orbicularis, longus, multifidus, and pinna muscles in (c), and their printed models in (d). The functional tissues are stimulated by applying electrical signals.

2PP opens new strategies in biomedical applications for creating artificial organ and tissue substrates [148]. For instance, it enables the printing of both the internal and external shapes of

functional muscle tissues, which can be activated through electrical stimulation using hydrogels [143] (see Figure 2.10).

Finally, micro-scaffolding using 2PP has been extensively applied in various biological and medical sectors. Micro-scaffolds are artificial structures designed for studying cell migration, tissue growth and development [15], [149], [150], [151], [152] (see Figure 2.9). Successful micro-scaffolds, as detailed in Chapter 7, involve optimization of microstructures and have the potential of enhancing the analysis of bio-applications.

CHAPTER 3

3. Direct laser writing

The two-photon polymerization (2PP) technique has found applications in micro-optics, microelectronics, microelectromechanical systems (MEMS), microfluidics, biology, and medicine due to its resolution capabilities beyond the diffraction limit. However, achieving high precision in fabrication processes, such as micro-optics and photonic crystals, requires dealing with dimensional accuracy, shape, and surface finish in micro/nanostructures to eliminate inaccuracies that can significantly impact device performance or even render them unusable.

To produce precise two- and three-dimensional (2D, 3D) micro/nanostructures, it is essential to systematically and comprehensively assess the factors affecting the accuracy of the direct laser writing (DLW) process. This chapter reviews the principles of DWL in polymerization, covering advanced 2PP-DLW methods for enhancing resolution. Additionally, the chapter briefly discusses focusing configurations.

3.1. DLW method in photopolymerization, 1PP vs 2PP

DLW is an optical lithography technique widely used in the fabrication of polymer structures. DLW is typically based on one-photon absorption (1PA) to trigger a photochemical reaction in a UV-sensitive photoresist [8], [13], [153], a process known as one-photon polymerization (1PP), sometimes referenced as OPP [154]. In a maskless process, 1PP-DLW utilizes a focused laser spot moving across the photoresist surface, typically to create 2D microstructures. This method is commonly implemented using continuous-wave (CW) lasers at blue-UV wavelengths focused through high numerical aperture (NA) objective lenses (OL) [154], [155]. However, a significant limitation of 1PP is that light absorption occurs primarily near the surface of the photoresist, restricting the fabrication of true 3D microstructures throughout the entire layer thickness [45]. As the light penetrates deeper into the material, the absorption probability decreases, especially in photoresists with a high concentration of photo-initiators (high optical density), leading to reduced polymerization efficiency in deeper layers [1]. For photoresists with a lower concentration of photo-initiators, 3D microstructures might be achieved (low optical density); however, this can result in lower resolution due to the formation of a conical exposure region where polymerization occurs both above and below the focal plane, leading to overexposure and reduced precision.

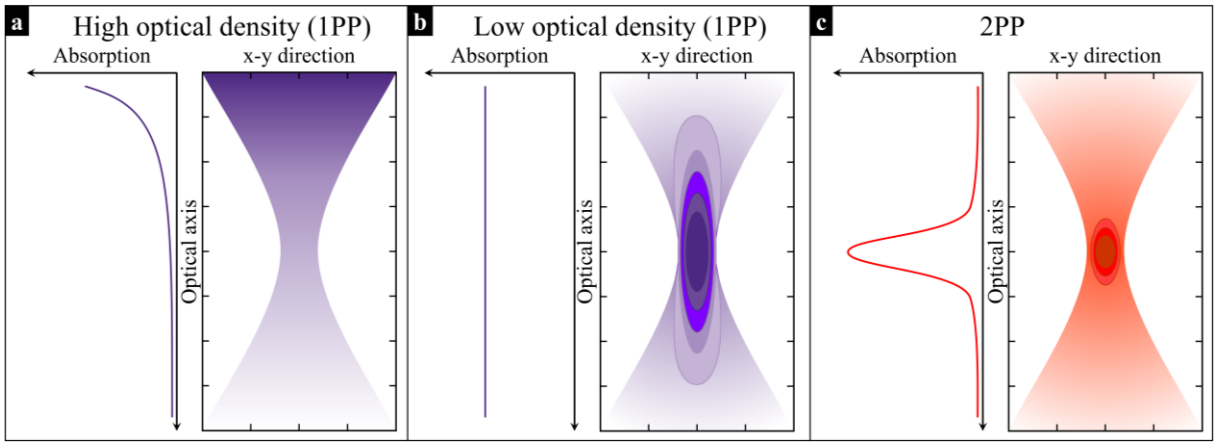

Figure 3.1: Illustration of absorption probability behavior for 1PA and 2PA when focusing a Gaussian beam from above into a photoresist volume. (a) Strongly absorbing photoresist attenuating the incoming beam through 1PA. (b) Weakly absorbing photoresist allows the beam to penetrate the photoresist and be absorbed at all z-positions via 1PA. (c) Highly absorbing photoresist in the laser spot where absorption occurs through 2PA.

In contrast, 2PP-DLW is a non-linear process that enables the fabrication of high-resolution 3D microstructures within a photoresist volume [156]. In 2PP-based direct laser writing (2PP-DLW), the nonlinear mechanism of two-photon absorption (2PA) predominates [157], allowing polymerization to occur exclusively within a confined volume pixel, known as a voxel. This voxel is generated by tightly focusing an ultrafast pulsed laser—typically a femtosecond (femto) laser—operating in the near-infrared (NIR) range [99], [158]. The key advantage of 2PP is that the probability of absorption is proportional to the square of the light intensity, which localizes the polymerization strictly within the focal region [53]. In this process, the N-IR wavelength used is typically longer (approximately double) than the wavelength used in a 1PP-DLW process (i.e., $\lambda_{N\text{-}IR} \approx 2\lambda_{UV}$), enabling 2PA by the photo-initiator molecules. This non-linearity prevents undesired exposure and polymerization outside the voxel, enabling precise control over the fabrication of complex 3D structures. Moreover, the N-IR wavelengths used in 2PP are out of resonance with the vibrational modes of the material, making the photoresist transparent and allowing deeper light penetration without significant loss of energy [19]. Figure 3.1 shows and comparison of the absorption probability of 1PP vs 2PP.

In 2PP, the ultrafast pulsed laser delivers a high concentration of photons within an extremely short time window [159], significantly increasing the probability that two photons will be absorbed simultaneously by a photo-initiator molecule. This requirement for both temporal and spatial overlap makes 2PP inherently more selective than 1PP, enabling high-resolution micro-fabrication with minimal exposure beyond the focal point. Thus, the polymerized region of 2PP is smaller than that of 1PP [2]. Figure 3.2 shows the intensity distribution of 1PP vs 2PP. Moreover, the polymerization threshold in 2PP can be precisely tuned by adjusting parameters such as laser power, pulse duration, repetition rate, and exposure time, offering extensive control over the properties of the resulting microstructure.

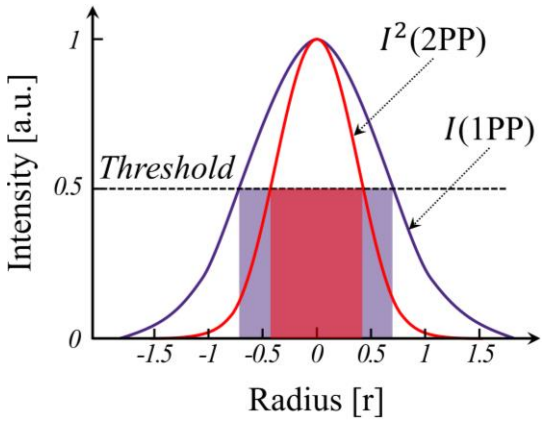

Figure 3.2: Light intensity distribution in the laser focus of a Gaussian beam for 1PP and 2PP processes. Polymerization occurs in regions where the intensity exceeds the threshold.

Table 3.1: Comparison of properties for 1PP-DLW versus 2PP-DLW method.

Properties	**1PP-DLW**	**2PP-DLW**	**Ref.**
Photon absorption mechanism	1PA	2PA	[41], [44]
Light propagation	$\frac{dI(z)}{dz} = -\alpha I(z)$	$\frac{dI(z)}{dz} = -\alpha I(z) - \beta I^2(z)$	[41]
Transmitted light intensity	$I(z) = I(0)e^{-\alpha z}$	$I(z) = I(0)\frac{(1-R)^2 e^{-\alpha z}}{1+\frac{\beta}{\alpha}I(0)\cdot(1-R)(1-e^{-\alpha z})}$	[41]
Transmittance of the photoresist (T), with thickness l	$\frac{I(z=l)}{I(0)} = e^{-\alpha l}$	$\frac{I(z=l)}{I(0)} = \frac{(1-R)^2 e^{-\alpha l}}{1+\frac{\beta}{\alpha}I(0)\cdot(1-R)(1-e^{-\alpha l})}$	[45], [157]
Absorption probability (p)	$p \propto I$	$p \propto I^2$	[1], [157]
Polymerization Threshold (D)	$D = I \cdot t$	$D = I^2 \cdot t$	[1]
Polymerization Efficiency	Decreases with depth, particularly in photoresists with high optical density.	Efficient polymerization strictly within the voxel.	[1]

To successfully obtain microstructures in both 1PP-DLW and 2PP-DLW, sufficient cross-linking of monomers is necessary to form stable polymer chains. However, achieving effective polymerization in 2PP is more complex than in 1PP due to the intricate interaction between laser parameters and material properties [38]. In 1PP, polymerization occurs when the exposure dose surpasses a certain threshold, leading to widespread polymerization in exposed areas. In contrast, 2PP requires higher light intensity to achieve the necessary photon flux density for effective 2PA. Despite the added complexity, the 2PP-DLW process is generally preferred for applications requiring precise 3D microstructures, as it offers superior resolution and accuracy compared to 1PP-DLW processes [1].

Finally, while 1PP-DLW is effective for fabricating 2D structures or basic 3D designs with limited depth control [160], 2PP-DLW excels in creating intricate 3D microstructures with high

spatial resolution due to its nonlinear optical effects. The choice between 1PP and 2PP depends on application requirements, the desired structural complexity, resolution and the specific properties of the photoresist material [161]. Table 3.1 provides a comparative overview of the key characteristics of 1PP-DLW and 2PP-DLW methods.

3.2. Advanced 2PP-DLW methods for improving resolution

Resolution is the most important parameter in 2PP-DLW for micro/nanostructures, surpassing Abbe's diffraction limit [162] of the material [163], [164], as expressed in Equation (3.1). Several methods and techniques are developed to reduce polymeric nanostructure sizes, i.e., lateral and axial of the voxel, from prepolymer preparation (such as adding effective photo-initiators [165] and radical quenchers [166]), to depletion mechanisms [2], [158], [167].

$$d = \frac{\lambda}{2NA} \tag{3.1}$$

In standard 2PP-DLW, a laser excites the photo-initiators via 2PA. Then, they undergo relaxation, i.e., vibronic relaxation, and internal conversion (IC), while remaining in the lower excited singlet state $|S_1\rangle$ [168]. Afterward, a significant number of these photo-initiators undergo intersystem crossing (ISC) from the lower singlet state $|S_1\rangle$ to a reactive pathway and long-lived triplet state $|T_1\rangle$. Triplet relaxation also occurs without IC coupling [168]. From the lowest $|T_1\rangle$ state, free radicals are generated via cleavage or charge transfer to other molecules, which then propagate polymerization by adding monomers until the chains are terminated or the monomer is depleted. Once the polymer is sufficiently cross-linked, it becomes irreversible and insoluble. This process is explained in Chapter 2. Therefore, processes that reduce this chain propagation can contribute to improved resolution.

Next, the main depletion microscopy to be applied to lithography is presented.

3.2.1. STED-DLW

The development of stimulated emission depletion (STED) microscopy is one of the most widely used technologies for reducing feature size in combination with 2PP-DLW to break the diffraction limit [169], as defined in Equation (3.1), achieving resolutions higher than 10 nm [170].

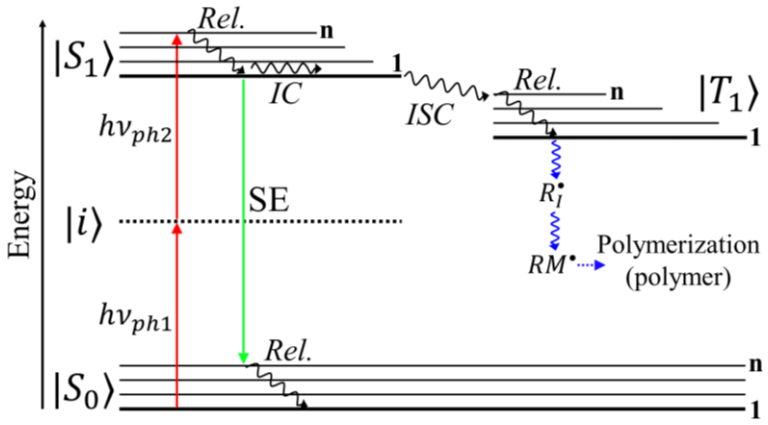

Figure 3.3: Schematic illustration of the molecular electronic states and transitions in STED-DLW [1]. After the photo-initiators (PI) undergo intersystem crossing (ISC) from $|S_1\rangle$ to $|T_1\rangle$ and relaxation (Rel.), polymerization is initiated by the generation of radicals ($R_I^\bullet$) from the lower $|T_1\rangle$ of the PI. These generated radicals then react with monomers to form monomer-radicals ($RM^\bullet$), which are crucial for the formation of long polymer chains.

In STED-DLW, a femto laser is used to excite the photo-initiators to a higher singlet state $|S_1\rangle$ via 2PA (population of the photo-initiators by the excitation pulse). Subsequently, a second laser (depletion laser) induces stimulated emission (SE) of the excited photo-initiators before they can transition to the reactive triplet state $|T_1\rangle$ via ISC, partially inhibiting polymerization. This SE process returns the photo-initiators to their ground state $|S_0\rangle$, preventing the generation of free radicals outside the central excitation region. Figure 3.3 illustrates the principle of STED-DLW.

The depletion efficiency depends on the intensity of the depletion laser (commonly CW laser at 532 nm of wavelength [171] or nanosecond pulsed laser [172]) and the competition among the different deactivation channels from the lower excited singlet state $|S_1\rangle$ (depopulation of the photo-initiator's excited state) [168], including fluorescence, ISC, and non-radiative decay. By carefully adjusting the depletion laser's power, it is possible to significantly reduce the polymerization volume, enabling precise control over the voxel geometry.

This combination of 2PP-DLW with STED enables the fabrication of microstructures with much finer details than those achievable by conventional DLW. It allows for printing speeds in the m/s range but requires very high depletion laser power [167]. Additionally, photoresists under SE eject energy from the system through photons, rather than relying on heat to complete polymerization.

3.2.2. RAPID lithography

Resolution augmentation through photo-induced deactivation (RAPID) also allows for surpassing the diffraction limit of conventional lithography [173]. Initially, RAPID was designed to support STED by incorporating special cationic dyes as photo-initiators [174]. A

common example is malachite green carbinol base (MGCB), which has a high extinction coefficient and absorbs at 620 nm, with an additional shoulder around 430 nm. 2PA of femtosecond pulses can excite MGCB to a higher singlet state $|S_1\rangle$, followed by non-radiative relaxation to a lower singlet state, with expected fluorescence emission around 700 nm (not shown in Figure 3.4) [167].

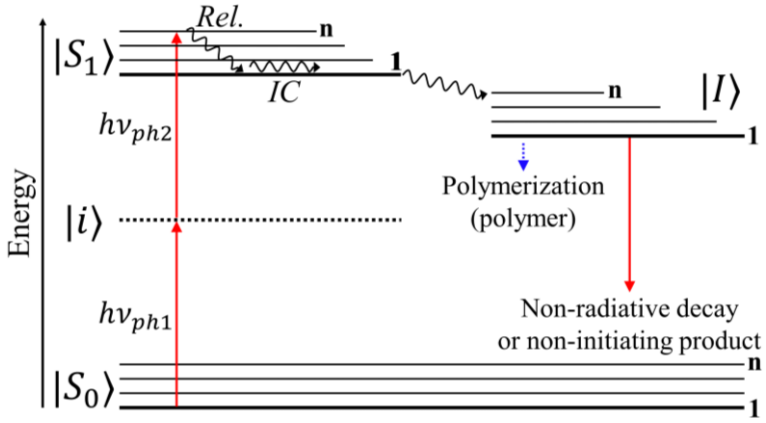

Figure 3.4: Schematic illustration of the molecular electronic states and transitions in RAPID lithography [1]. Upon CW laser exposure, the long-lived intermediate state $|I\rangle$ is deactivated. This deactivation can result in non-radiative decay or the formation of non-initiating products, which ultimately reduces the extent of cross-linking in the polymer.

RAPID lithography can be implemented using two lasers at the same wavelength: an ultrafast pulsed laser (200 fs) for excitation and a CW laser for deactivation. Figure 3.4 illustrates the principle of RAPID lithography. Although MGCB was initially expected to support STED, no luminescence has been detected. However, it was observed that depletion laser activation can effectively inhibit polymerization in MGCB-based photoresists [167]. This effect is attributed to the depletion of a long-lived intermediate state $|I\rangle$, enabling the use of a CW laser without requiring precise synchronization. The exact nature of this intermediate state remains undetermined, but it may involve weakly reactive radical pairs [173] or solvated electrons [174] that can recombine with the parent molecules through a photoinduced electron back-transfer.

The drawback of using MGCB is that it absorbs light across the 400-700 nm range, covering the entire visible spectrum. Other photo-initiators, such as malachite green carbinol hydrochloride (MGC-HCl), have also been used [174]. This photo-initiator is particularly sensitive, showing a depletion effect even with femtosecond pulses, but it becomes independent of printing speed and does not contribute to the effective resolution of the polymer when speed increases.

3.2.3. 2PII lithography

Two-color photo-initiation/inhibition (2PII) lithography is not based on the direct deactivation of an excited intermediate state of the photo-initiator but instead utilizes two independent and

opposing high-efficiency processes [175]. The photo-initiation process generates free radicals via 1PA driven by a CW laser, e.g., blue light (photo-initiation laser), while the photo-inhibition process is activated via 1PA using a second CW laser, e.g., UV light (photo-inhibition laser), in a Gauss-Laguerre "donut" mode [176], generating inhibiting species (weakly reactive radicals). These radical quenchers can efficiently scavenge free radicals and terminate the chain propagation process. 2PII allows for a reduction in the formation of insoluble cross-linked polymer chains. Figure 3.5 illustrates the principle of 2PII lithography.

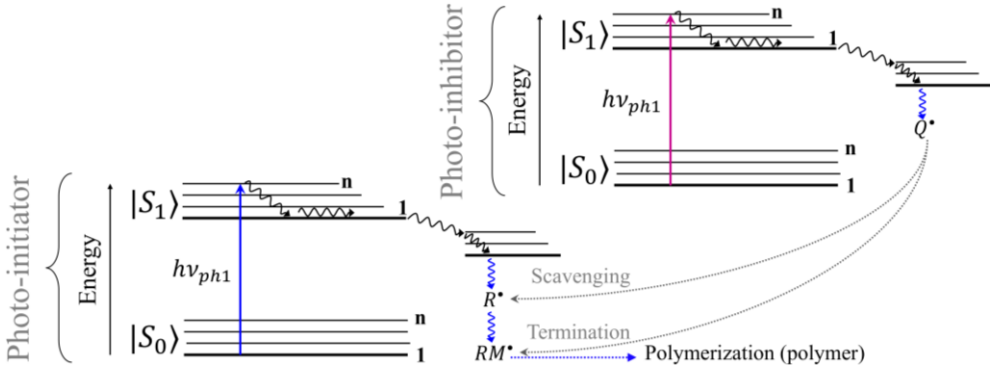

Figure 3.5: Schematic illustration of the molecular electronic states and transitions in 2PII lithography [1]. Deactivation is carried out by combining radical quenchers ($Q^\bullet$) with free radicals ($R^\bullet$) that scavenge the initiation process, and with chain-initiating radical ($RM^\bullet$) that terminate the propagation process.

Photo-initiators and photo-inhibitors must be activated separately by different wavelengths that do not cause interference, which requires preparing a specific photoresist to apply 2PII lithography. The photo-initiators, camphorquinone and ethyl 4-(dimethylamino)benzoate, and the photo-inhibitors, tetraethylthiuram disulfide, are combined with triethylene glycol dimethacrylate monomers to obtain a functional photoresist [176].

The advantage of 2PII lithography is that it confines effective excitation and also reduces excitation blurring caused by radical diffusion, which is particularly useful in low-viscosity photoresists [167]. However, a challenge in 2PII is the difficulty in fabricating complex 3D structures. When focusing deeper into the photoresist volume, beams from the photo-initiation laser and the photo-inhibition laser attenuate as they pass through the material, as they rely on the principle of 1PA, making the required laser powers highly depth-dependent. Additionally, this can lead to excessive consumption of the photo-initiator or photo-inhibitor and continuous heating of the photoresist throughout the entire cone of the focused laser beams [167].

3.2.4. Other depletion methods based on excited-state absorption

Depletion mechanisms based on excited-state absorption (ESA) can be alternative methods to improve resolution [30]. Photo-initiators are excited via 2PA, and ESA occurs directly from the lowest excited state $|S_1\rangle$ or from the triplet state $|T_1\rangle$. After light absorption, the system may

relax non-radiatively from highly excited states of $|S_2\rangle$ or $|T_2\rangle$ back to the ground state $|S_0\rangle$. Additionally, free radicals generated from $|T_1\rangle$ can absorb depletion light and contribute to the reduction of cross-linked polymers [177]. This method is referred to as ESA + non-radiative decay [167] and is illustrated in Figure 3.6-a.

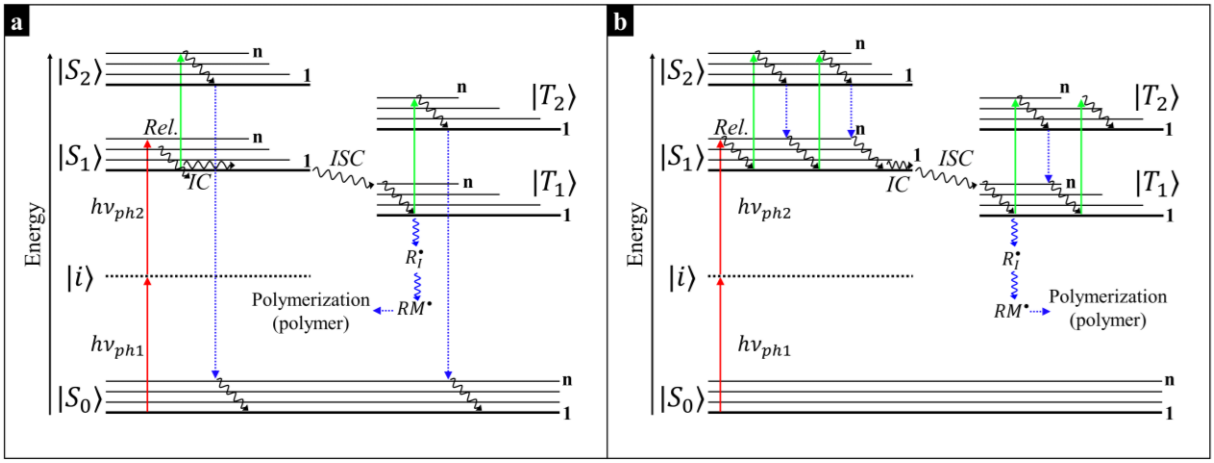

Figure 3.6: Schematic illustration of the molecular electronic states and transitions in ESA lithography [1]. (a) ESA + non-radiative decay. (b) ESA + Resist heating.

Another mechanism involves multiple excitations and rapid non-radiative relaxations to the same excited state, applying heat and leading to dominant thermal effects that enhance resolution ($|S_1\rangle \xrightarrow{\text{heat}} |S_2\rangle$) or ($|T_1\rangle \xrightarrow{\text{heat}} |T_2\rangle$). In other words, the efficiency decreases as the 2PA cross-section of a molecule can significantly drop with increasing temperature, which also decreases the quantum yield due to non-radiative decay in the lowest excited state $|S_1\rangle$ [178]. This method is referred to as ESA + resist heating [167] and is illustrated in Figure 3.6-b.

These thermal mechanisms require less laser power but limit writing speed, due to the long lifetime of triplet states $|T_1\rangle$ (~msec). In comparison, SE extracts energy from the system, which could make STED superior [167].

3.3. Challenges on 2PP-DLW

Submicron-scale 2PP-DLW printing is highly versatile, particularly for the precise functionalization of surfaces, but its slow printing speed limits its broader adoption in research and industry. The high resolution it offers is akin to the precision of sketching with a fine-tip pencil. Techniques have been developed to enhance the precision and accuracy of microstructures, such as shape pre-compensation, multipath scanning method, 2D slicing method, and improving surface roughness [2]. Printing time is influenced by voxel size, structure shape, and the limited field of view of high NA objective lens [179].

Recently, methods to accelerate manufacturing have been proposed [4], such as parallel fabrication with multiple foci generated by microlenses, diffractive optical elements (DOE)

[28], spatial light modulators (SLM) [31], [180], and digital micromirror devices (DMD) [181]. DMDs enable precise control of multiple foci, accelerating printing without compromising resolution. Additionally, when combined with high-power lasers, they facilitate the rapid printing of 3D structures without losing detail.

3.4. 2PP focusing configuration

2PP-DLW is carried out using custom and commercial systems, according to the optical design, photoresist properties, and light spread in the materials to reach higher resolution [32], [33], [182], [183]. Next, three main focusing configurations available to make micro/nanostructures are described.

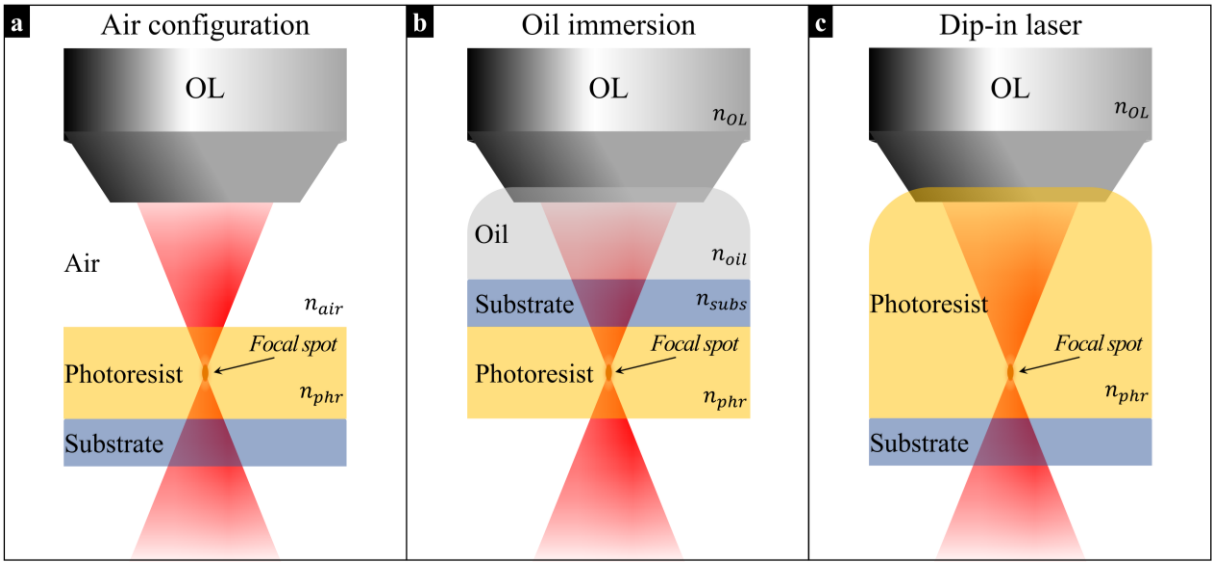

Figure 3.7: Comparison between air configuration (a), oil immersion (b), and dip-in laser (c). In illustrations (a) and (c), the refractive index of the substrate is irrelevant. However, if focusing is done directly on the substrate in the air configuration, the effects of the substrate's refractive index must be considered.

3.4.1. Air configuration

Air configuration is also referred to as free-immersion. The light from a laser source can be focused directly on the photoresist on any opaque or transparent substrate, or through the glass substrate. The focusing accuracy depends on the vertical position of the laser spot in the photoresist. The maximum structure height is defined by the working distance (WD) of the objective lens (OL) and the refractive indices of the materials. Figure 3.7-a illustrates a perspective of focusing using two propagation materials. The structures are limited by photoresist thickness if the laser is focused directly on the photoresist.

A disadvantage of this configuration is that an elongated voxel results from Snell's law when passing from one medium to another with a high refractive index ($n_{air} < n_{phr}$) at the

wavelength of the excitation light at a specific angle of incidence by the OL, and also, the changes in refractive indices can affect the position and accuracy of beam focusing.

3.4.2. Oil immersion

The laser is focused on the sample through a transparent substrate. In this configuration, only transparent substrates can be used, and the effect of the refractive index is negligible. Between the OL and the substrate, immersion oil is employed, which has a refractive index similar to that of the OL glass and the substrate ($n_{OL} \approx n_{oil} \approx n_{subs}$). This minimizes light scattering and reduces optical aberrations, allowing for an optimal focus at the substrate-resist interface. In addition, the refractive index of the photoresist should match that of the surrounding materials to avoid distortions and loss of resolution.

However, as the laser is focused deeper into the photoresist, spherical aberrations increase due to the light passing through different materials. These aberrations affect the focus quality, which can lead to reduced precision in the fabricated structures. Figure 3.7-b shows a schematic of this configuration. Therefore, the height limitations of the structures are determined by the WD of the OL and the substrate thickness.

3.4.3. Dip-in laser

In this configuration, the OL is directly immersed in the photoresist. Spherical aberrations are minimal and consistent throughout the thickness of the photoresist. Additionally, the heights of the structures are limited by the photoresist support. Figure 3.7-c shows the Dip-in laser.

The refractive indices of the OL and the photoresist are approximately matched ($n_{OL} \approx n_{phr}$). The issue with this configuration is that if other photoresists are used, they may damage the optical system of the OL or result in poor quality of the fabricated structures.

CHAPTER 4

4. Design and fabrication of a 2PP system

Two-photon polymerization direct laser writing (2PP-DLW) micro-fabrication can be performed using three different strategies:

(i) moving the samples across a fixed laser beam,

(ii) moving the laser beam within a fixed sample, or

(iii) moving both the sample and the laser beam sequentially.

In the first case, the sample is moved in three orthogonal directions with the help of three linear translational stages along the X, Y, and Z axes. In the second case, an optical scanner is used to rotate a set of mirrors to sweep the laser beam over an XY-plane, and a Z lineal translation stage is used to move the laser beam vertically. The third case is a hybrid combination of the previous two cases, allowing the system to have better printing features in terms printing area with high speed, and better resolution and precision.

In this section, a custom fabrication system gathering features of a hybrid system is described. It allows sequential movement in the XYZ dimensions using linear translational stages and galvanometric scanners, while considering the requirements and components necessary for the optical design and setup. This leads to the launch of the fully functional 2PP system for 3D micro/nanostructures. Additionally, an extension for one-photon polymerization direct laser writing (1PP-DLW) has been added for the simple calibration and optimization of the 2PP system without considering fine focusing on the photoresists for polymerization. A low-cost violet laser was incorporated to minimize optical path errors and improve positioning accuracy.

4.1. System requirements

The 2PP system combines control and synchronization features of XYZ nano-positioning stages, minimizing positioning errors at high speeds and synchronizing movements with the laser beam (shutter modulation and power light during the laser writing process).

The galvanometer-based optical scanners (galvos) are better suited for nanometric positioning in an XY-plane for fabrication of micro/nano-structures with complex geometry at extremely high scanning speeds (up to 3 m/s in Newson galvos [184]). Galvos are electro-mechanical systems composed of mirrors installed in an orthogonal configuration, on motors with very low

mechanical inertia, allowing swift rotation about their axes. This allows the beam to be scanned in two dimensions.

Galvos are very precise, with short latency times (few hundred microseconds). Fast scanning of mirrors in the kHz frequency domain with good angular resolution is therefore allowed. However, their field of view (FOV) is limited when a magnifying lens is used, significantly reducing and constraining its operation to small structures confined within of FOV. This is not an issue when manufacturing of larger structures, but stitching is required; however, it induces structural errors during the process of combination substructures made in smaller areas. Stitching forces the systems to use linear translational stages (linear stages) to move the sample in the XY-plane [33], and also along of the Z-axis to achieve real 3D fabrication [4].

Linear stages have the advantage of not being limited by the objective's FOV. They move the sample along all three axes, with a travel range that can exceed hundreds of millimeters in each direction. However, their printing speed is limited to up to 50 mm/s under conditioned load and power supply in Tecnotion linear motor [185]. As a result, linear stages tend to be significantly larger and heavier compared to galvos, which reduces acceleration. This results in a non-uniform displacement speed along the stage travel range, that implies some time is required to reach the printing speed, thereby adding extra printing time. Consequently, affecting the accuracy in nanometric positioning (>100 nm).

Nano-positioning forces the system to use piezoelectric transducer (piezo) to move the samples with high accuracy along the X, Y, and Z axes. It is advantageous for fine positioning with nanometric precision and resolution less than 1 nm.

Piezo is an actuator that uses the inverse piezoelectric effect to generate mechanical displacement of the piezoelectric material (usually quartz) when an electric field is applied. This displacement can be precisely controlled by the applied electric signal. When an electric voltage is applied, it causes the internal dipoles of the material to align, resulting in a physical expansion or contraction of the material, and producing linear movements directly proportional to the electric voltage.

Piezo has very high precision and resolution (0.3 nm), with high resonance frequency for movements of high dynamic response around of the kHz, over a travel range of a few hundreds of micrometers in Newport piezos [186]. However, it has limited load capacity due to deformation of the piezoelectric material, which reduces the resonance frequency under heavier loads, increases the rise time for applied signals, and consequently reduces the printing speed. This affect the performance and printing times, but it is not an issue when it is used just to move smaller loads for smaller trajectories, i.e. move a set of lenses along the Z-axis at up to 100µm/s.

Finally, all movements must be thoroughly synchronized with the laser beam. The laser is dependent of the printing times and speed, e.g. turn on/off and power light modulation. Ultrafast

pulsed laser beam can be manipulated by an acousto-optic modulator (AOM) or a half-wave plate (HWP).

The AOM has the advantage of diffracting the incoming light into several orders without turning on/off delays, with the majority of the laser beam intensity being diffracted into the 1st order. It utilizes the acousto-optic effect to diffract light in different directions (nth orders) by using sound waves created inside a material (like quartz or glass) attached to a piezoelectric material that vibrates in response to applied pure sinusoidal electrical signals. The main issue is that the rest of the light intensity is distributed in all diffraction orders, resulting in a waste of light of the laser beam source and reducing the diffraction efficiency in the best conditions up to 99 % in the 1st order in Gooch & Housego AOMs [187]. However, this is not an issue when the exposure of the laser beam is higher than the threshold intensity of the photoresists to be polymerized, as the printing speed and laser beam power can be adjusted accordingly.

HWPs can be used to adjust and control the polarization state of the laser beam. It is based on birefringent materials (such as quartz or calcite) that introduce a phase difference of π radians between two orthogonal components of linearly polarized light [188]. It can function as a continuously adjustable polarization rotator, but it requires the use of a rotary stage to precisely adjust the rotation. When coupled with a rotary stage, the HWP is particularly useful with a polarizer for attenuating the intensity of laser light [189], [190], which is often necessary for photoresists requiring varying levels of power for 2PP-DLW processes.

4.2. System components

The performance of the system is fundamentally characterized by:

(i) the capacity to control and synchronize combined movements of the motion stages (linear stages, rotary stage, galvos, and piezo),

(ii) the capacity to control and synchronize the motion stages along with the laser beam (shutter and power attenuation) for printing processes, and

(iii) the capacity to configure and program recipes to execute printing processes in any photoresists.

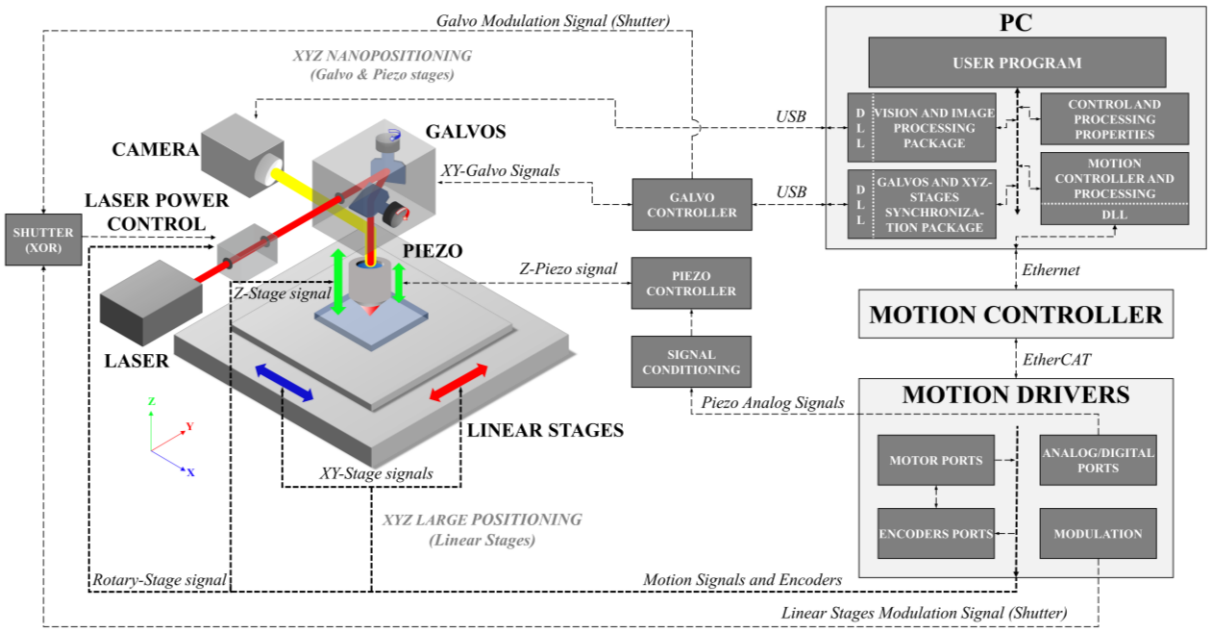

Figure 4.1: Block diagram of the electronic 2PP system.

Considering these points, the proposed control architecture is shown in Figure 4.1. The system provides processing pseudo-algorithms (settings and recipes) for polymerizing photoresists by custom software (user program) installed on the PC. These pseudo-algorithms are translated into interactions stored in the motion controller, which provides laser processing functionality. The interactions are algorithms executed in the buffers of the motion controller simultaneously, translating processing parameters and geometric objects (control and processing properties) into combined and synchronized movements of the stages, laser power control, modulations, and switching of the motion stages at execution rates of 20 kHz and synchronization times of 0.1 µs. In addition, a software package translates part of the galvo interactions executed in the galvo controller, providing synchronization to the deflectors (joint synchronization with the laser beam and the XY linear stages) at control rates of 100 kHz and up to 40 MHz laser activation. This allows for the execution of high dynamic parts. In addition, the galvo controller executes interactions that provide synchronization to the deflectors at control rates of 100kHz and up to 40 MHz laser activation.

The movements of the motion stages are fed back to their respective controllers in closed-loop operation mode, to provide precise positioning control with nanometric resolution. The piezo controller is connected to analog signal conditioning hardware, which in turn is connected to the motion drivers to calibrate and control the piezo movements through interactions executed in the motion controller. The synchronization of the linear stages and the piezo with respect to the galvos is ensured via the high-speed digital communication protocol (EtherCAT) to minimize potential desynchronization errors and movement delays.

The motion drivers and galvo controller manage the power modulation of the laser beam (shutter signal by galvos or linear stages) via two selective digital signals. For example, if the processing properties of the geometric objects are configured to be printed with the galvos, the galvo modulation signal is activated while the linear stages modulation signal is deactivated, but never both together. Additionally, the attenuation of the laser beam power is controlled by an HWP coupled to a rotary stage and a polarizer placed ahead the HWP. The motion drivers correctly synchronize the rotary stage to rotate the output polarization of the HWP and obtain the appropriate power at the output of the polarizer required by the printing processes programmed in the software recipes.

The galvo controller is correctly synchronized with the motion controller using a software package integrated into the user program (Galvos and XYZ stages Synchronization Package). Finally, a real-time vision and image processing software package has been integrated. This allows for inspecting all XYZ movements, focus adjustments, stage configurations, and calibration of the motion stages to correct XY surface deformations and stitching parameters.

Additionally, to provide a greater range for the Z-axis, the system is reconfigurable to include another linear Z stage, offering extended vertical travel range. This is advantageous when working with 3D structures that require vertical travel greater than the range the piezo stage can provide. It also enhances system scalability by allowing flexibility to change focusing lenses for different focal distances and surface mapping.

4.3. Optical design

4.3.1. Optical design for 2PP using near-infrared light

The design of the optical system is primarily characterized by a power control part and laser beam expansion.

Considering a high-performance laser source that emits ultrafast pulsed light, i.e., a laser beam with a very high polarization extinction ratio (PER) and beam quality (M^2) very close to 1, there is no need to modify it to enhance its propagation characteristics. This holds true if the divergence and aberrations of the light are negligible so the efficiency in the 2D and 3D 2PP-DLW processes is not reduced.

The laser beam power control consists of an AOM, a HWP, and a polarizer. The light is diffracted at the output of the AOM at different diffraction angles (nth orders) according to the Bragg condition, where the 1st order diffracted beam is used, while the non-1st orders are eliminated, as shown in Figure 4.2.

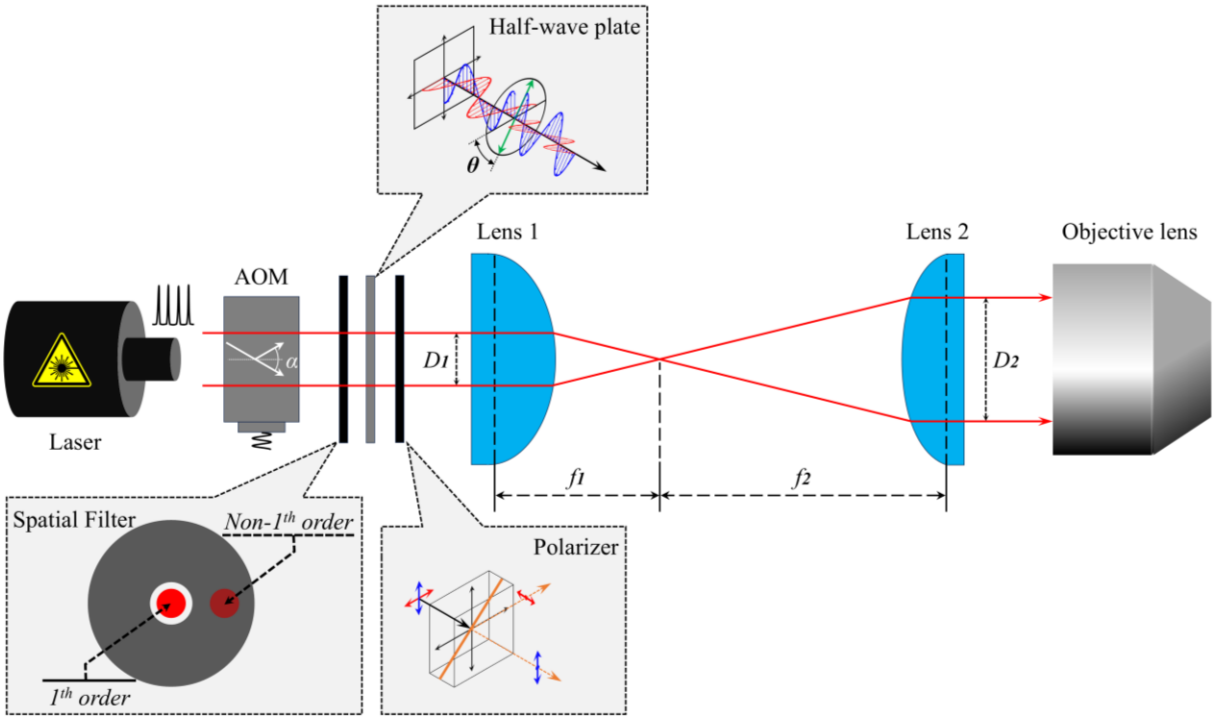

Figure 4.2: Simplified diagram of ultrafast pulsed near-infrared (N-IR) laser beam control and expansion. This design is used to induce 2PP via two-photon absorption (2PA).

Considering that the electric field of the beam is linearly polarized and that the light intensity remains constant during propagation, its intensity can be varied by modifying the polarization rotation and filtering it out through a polarizer [189], [190].

The HWP rotates the orthogonal components of the light by θ degrees on the plane of incidence. This causes the transmitted light to have different amplitudes according to θ, without phase shifts in p- and s-polarization, as shown in the Jones vector in Table 4.1. The polarizer is a filter that separates the orthogonal components of linearly polarized light, transmitting the electric field polarized parallel to the plane of incidence of the polarizer (p-polarization) and reflecting the component perpendicular to the plane of incidence (s-polarization).

The principle of operation for power control is based on Malus's law [190], where the intensity I of polarized light passing through the polarizer is given by:

$$I = I_o \cdot \cos^2(\theta) \tag{4.1}$$

where I_o is the input intensity and θ is the angle between the initial direction of the polarized beam and the fast axis of the HWP. The angle of the HWP allows continuous rotation in the polarization direction of the beam.

Table 4.1: Jones vectors description for spatial polarization state of light [189].

Linearly polarized wave	**Vector**	**Description**
Plane of polarization parallel in x axis ($\theta = 0°$)	$\begin{bmatrix}1\\0\end{bmatrix}$	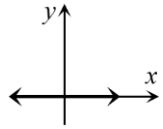
Plane of polarization perpendicular in x axis ($\theta = 90°$)	$\begin{bmatrix}0\\1\end{bmatrix}$	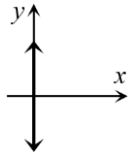
Plane of polarization making angle θ with x axis	$\begin{bmatrix}\cos\theta\\\sin\theta\end{bmatrix}$	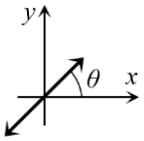

Eventually, the laser beam passes through the expansion set, which consists of a collimator with two lenses configured like an astronomical telescope, as depicted in its simplest form in Figure 4.2. The first lens must have a diameter larger than the input beam waist (D_1) to prevent clipping the beam. Similarly, the diameter of the output lens must be larger than the expanded beam waist (D_2).

The expansion geometry is based on a Keplerian telescope, which uses two plano-convex lenses with positive focal lengths [191]. The magnification of the system must satisfy the optical design requirements, according to the expression:

$$m = \frac{f_2}{f_1} = \frac{D_2}{D_1} \tag{4.2}$$

where f_1 and f_2 are the focal lengths of the respective lenses and the spacing between them is equal to the sum of the focal lengths ($f_1 + f_2$). To reduce aberrations, only the central part of the lenses should be used, i.e., D_1 and D_2 should be as small as possible about the optical axis of the system. However, for a large magnification (n times the input), the usable extended beam waist can be up to a maximum of 80 % of the total diameter of the lenses.

$$D_{1,2} \leq 0.8 \cdot \emptyset_{Lenses} \tag{4.3}$$

Furthermore, to avoid clipping at the end of the optical path of the system, the extended beam waist should not diverge from the exit of the second expansion lens to the entrance of the objective lens (OL). Ideally, this divergence should be less than 10^{-3} mrad and the extended beam waist should not exceed the entrance pupil diameter ($\emptyset_{EP}$) of the OL.

Both the OL and the additional lenses must adhere to the optical design specifications of the system. Specifically, the extended beam waist should occupy at least 80 % of the entire $\emptyset_{EP}$ of the OL, satisfying Equation (4.4):

$$0.8 \times \emptyset_{EP} \leq D_2 < \emptyset_{EP} \tag{4.4}$$

while $\emptyset_{EP}$ can be calculated using the Equation (4.5):

$$\emptyset_{EP} = 2 \cdot NA \cdot EFL \tag{4.5}$$

where EFL is the effective focal length of the OL and NA is its numerical aperture. Between Lens 2 and the OL shown in Figure 4.2, additional optical components, such as mirrors to define the optical path and galvos to move the laser beam on the photoresists, will be used.

4.3.2. Optical design for 1PP using violet light

This optical design is integrated into the 2PP system to calibrate and optimize the linear translational stages and galvanometric scanners due to the difficulty of applying 2PP directly at the substrate-photoresist interface without considering fine focusing on the photoresists for processes. This design is primarily characterized by a power control and collimation part of the laser beam.

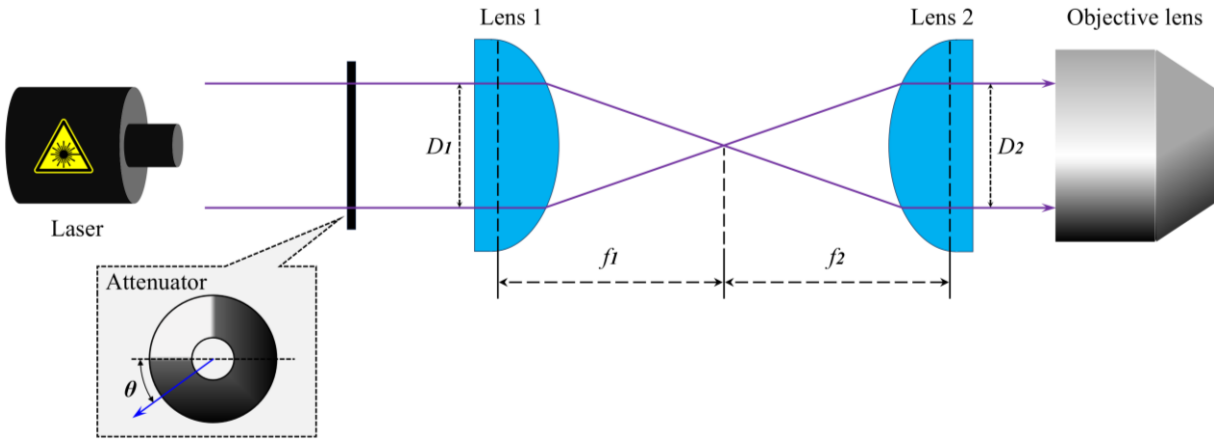

Figure 4.3: Simplified diagram of violet continuous-wave (CW) laser beam control and collimation. This design is used to induce 1PP via one-photon absorption (1PA).

Considering a laser diode as the continuous-wave (CW) emission source in the violet spectrum (~405 nm), it is only necessary to perform power control and beam homogenization for its projection at the entrance of the OL with no need to improve other characteristics of the propagation. Therefore, a low-cost laser diode can be the appropriate choice for high-resolution 1PP-DLW processes in 2D printing.

The laser beam power control is composed of a variable attenuator as shown in Figure 4.3, where the rotation angle (θ) determines the appropriate power for the used photoresists, given by:

$$I = I_o \cdot 10^{-OD(\theta)} \tag{4.6}$$

where I_o is the input power intensity and OD is the optical density of the attenuator as a function of the rotation angle.

Laser diodes typically emit light with a wider divergence than other laser sources, requiring collimation to make the photons highly directional and propagate nearly parallel to the optical axis of the system [191].

The geometry of the optical design consists of two plano-convex lenses with equal focal lengths ($f_1 = f_2$); hence the system magnification is 1×, according to Equation (4.2). They are separated by twice the focal length to avoid introducing divergence. Equations (4.3) and (4.4) also satisfy the system requirements to reduce aberrations. The diameters of the lenses D_1 and D_2 must be sufficiently large to avoid clipping of the beam, with D_2 ranging between 80–99% at the entrance of the OL. Finally, the optical components between Lens 2 and the OL will be the same as those mentioned in the optical design for 2PP.

4.3.3. Focusing and surface mapping design

The 2PP system is characterized by its focusing and surface mapping technique like an optical measurement tool using displacement lasers [192]. The design in Figure 4.4 consists of a single device emitting low-power red light and a sensor that detects the reflected light at an incidence point on the first layer of the photoresist. The device measures the distance between a point on the photoresist surface and the optical receiver [193]. This design requires moving the Z stage to find the OL focus, and the X and Y stages to construct a topography of the photoresist through multiple measurement points. This approach enables compensation for surface inclination errors and ensures the focusing precision in DLW processes. This design is based on air configuration mode, and the uniformity of the photoresist thickness is mandatory.

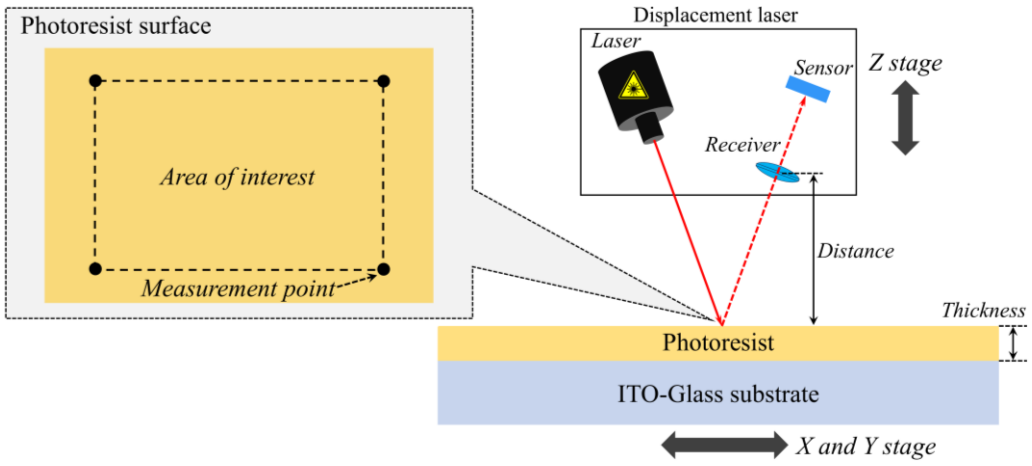

Figure 4.4: Simplified diagram of focusing and surface mapping design using a displacement laser. The measurement points may be captured by software, which also calculates the focus of the objective lens (OL) and the photoresist topography.

4.3.4. Vision design

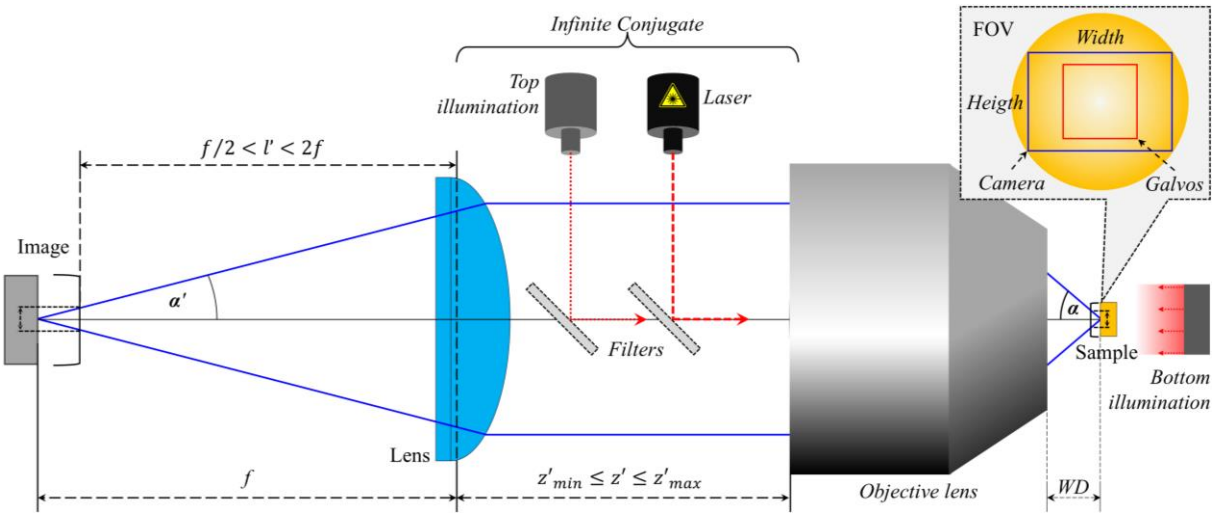

Figure 4.5: Simplified diagram of vision design (infinite conjugate microscope).

The vision system shown in Figure 4.5 indicate a conventional microscope setup. The focal length (l') can be adjusted up to 2 times the focal distance (f) of the tube lens to enhance the image quality of an object focused within the FOV of the system. This adjustment provides a linear zoom along the optical axis corresponding to the magnification of the OL.

The FOV of this vision design with a digital camera can be calculated by:

$$FOV = \frac{C_A \cdot s}{M_{OL} \cdot \frac{l'}{f_{OL}}} \tag{4.7}$$

where C_A is the size of the camera sensor in (height × width) pixels, s is the size of a single pixel, f_{OL} and M_{OL} are the focal length and the magnification of the OL. Depending on the technical parameters of the used OL, the FOV of the vision system can increase or decrease.

The galvos' FOV is not part of the vision design, but it must be considered in the design criteria. Galvos' FOV is defined by the separation between the last galvos mirror and OL and is limited by the technical parameters of the OL. Therefore, galvos' FOV must be smaller than the FOV of the vision system to avoid clipping the beam.

$$FOV_{galvos} < FOV_{vision} \tag{4.8}$$

The illumination within the vision design enables visualization of the DLW processes and focusing on the material plane. The 2PP system is equipped with two red light illumination sources: one from the bottom and one from the top.

The bottom illumination is a type of backlighting (e.g., Koehler illumination), where incident light floods the entire FOV under inspection from behind. This illumination does not require any additional lens, as it can be a bright and uniform source in the object plane.

The top illumination above the OL is collinear with the vision and laser beam, where incident light on the material in the object plane reaches at an angle due to the OL, resulting in a very compact illumination that is both intense and precise.

The optical design depicted in Figure 4.5 shows a system conjugate to infinity, i.e., the vision, illumination, and laser beam at the entrance pupil of the OL focused on a plane of the material are parallel and collinear (infinite focal length). This feature also allows varying magnification depending on the employed OL; based on this, the focal length (l') of the lens can be adjusted to produce a sharp image. Furthermore, this design allows for the introduction of additional optics in the infinite conjugate tube length (z'), such as beam-splitters and transparent filters in the visible spectrum to adjust light parallel to the optical axis of the vision.

Given that the Z-axis is variable in the 2PP system (due to focusing, surface mapping, or the OL used), the maximum distance between the OL and the tube lens (z'_{max}) can be determined by:

$$z'_{max} = \frac{\emptyset_L - \emptyset_{EP}}{C_A \cdot s} \cdot f_L \tag{4.9}$$

where $\emptyset_L$ and f_L are the diameter and focal length of the camera focus lens respectively.

4.4. System setup

4.4.1. 2PP setup

The combination of all stages and optical components is described in the setup of the 2PP nanofabrication system in Figure 4.6, and the technical specifications are summarized in Table 4.2.

The ultrafast pulsed laser source (femto laser) generates a pulsed beam with a high repetition rate in the order of MHz and a pulse width in the femtosecond range at a wavelength N-IR. The AOM diffracts the laser beam into the 1st diffraction order through sinusoidal signals generated by a modulator provided by the AOM. The iris diaphragm (I1) blocks the remaining components of the diffracted light coming from the AOM. An HWP and a polarizing beam-splitter (PBS) control the power of the linearly polarized laser beam.

The intensity of the laser beam for the 2PP setup can be expressed in terms of power ($P \propto I$). Therefore, Equation (4.1) becomes:

$$P = P_{max} \cdot \cos^2(2\theta - \varphi) \tag{4.10}$$

where P_{max} is the maximum power of the 1st order diffracted laser beam and φ is the offset angle of the fast principal axis of the HWP installed in the rotary stage of the optical path. The

beam dump absorbs the s-polarization of the laser beam, while the PBS transmits the p-polarization for the 2PP-DLW processes.

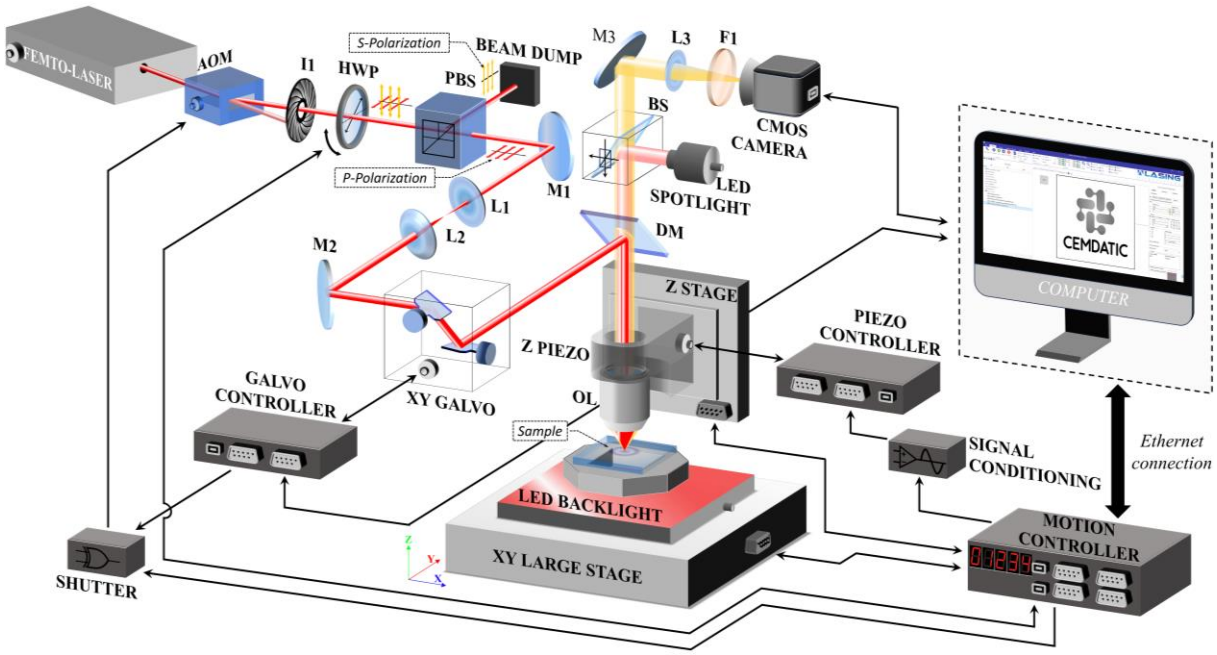

Figure 4.6: 2PP setup: A femtosecond laser source (femto laser), an acousto-optic modulator (AOM), an iris (I1), a half-wave plate (HWP), a polarizing beam-splitter (PBS), two plano-convex lenses (L1, L2), two mirrors (M1, M2), a XY galvanometer scanner (XY galvo), a dichroic mirror (DM), a piezoelectric stage (Z piezo), a Z stage, an objective lens (OL) and a XY large stage compose the nanofabrication part of the system. Two lighting sources (LED spotlight and backlight), the OL, the DM, a beam-splitter (BS), a mirror (M3), a plano-convex lens (L3), a filter (F1) and a CMOS camera compose the real-time monitoring part of the system. The motion, galvo and piezo controller manage XYZ micro/nano-positioning, while the AOM, HWP, and PBS control the increase or attenuation of the laser beam power. The CMOS camera is managed by software on the computer.

Two planoconvex lenses (L1, L2) with focal lengths of 25.0 mm and 100.0 mm respectively allow the laser beam to be expanded 4 times, resulting in an expanded beam waist (D_2) of 5.2 mm according to Equation (4.2), and satisfying the condition of Equation (4.3) for a diameter of ½" for both lenses, i.e., 5.2 mm ≤ (0.8 × 12.7) mm.

The setup also consists of a pair of high-reflectance mirrors (M1, M2) to route the laser beam toward the galvanometer scanner (XY galvo) input.

The laser beam is manipulated by the XY galvo to realize dimensional scanning in the XY-plane, and a piezoelectric stage (Z piezo) with a 100 µm travel range is used to move the focused laser beam vertically along the Z-axis. The XY large stage, with a 200 mm travel range in both the X- and Y-axes is used to realize long-range positioning with high micrometric precision and repeatability. The XYZ nano-positioning is composed by the XY galvo and the Z piezo to realize nanostructures with higher nanometric precision and resolution.

The XY large stage allows working on microstructures larger than the FOV of the XY galvo in the XY-plane. It enables the use of stitching techniques to utilize the entire scanning area, dividing the XY-plane into adjusted tiles within the FOV of the XY galvo. Furthermore, the Z piezo allows for laser focal spot adjustment (focusing) and XY-plane representative surface mapping of a photoresist.

A dichroic mirror (DM) is used as a short-pass filter to reflect the laser beam and transmit light in other bands, i.e., reflective for N-IR light and transparent in the visible light band-wide for the vision in the camera.

An OL infinite conjugate with magnification of 50×, a NA of 0.8, a working distance (WD) of 0.47 mm and effective focal length of 3.6 mm is used. Entrance pupil diameter ($\emptyset_{EP}$) was calculated as 5.76 mm, using Equation (4.5). According to Table 4.2, the diameter of the laser beam at the exit of the implemented femto laser is 1.3 mm. Therefore, the magnification (m) at the entrance pupil of the OL is 5.2 mm, satisfying Equation (4.4).

The customized 2PP system described in Figure 4.6 operates in air configuration mode, where the immersion medium is air. This mode allows the laser beam to be focused directly onto photoresists on either opaque or transparent substrates. Focusing and surface mapping are manipulated within the Z piezo travel range. However, for thicker substrates or larger photoresist thicknesses, an additional Z stage with a 25 mm travel range is employed, resulting in a total work volume of 200 × 200 × (0.1 + 25) mm³.

The 2PP setup includes a real-time monitoring part for visualizing the 2PP-DLW process on photoresists. This monitoring part is composed of two illumination sources (LED spotlight and LED backlight), a CMOS camera, a beam-splitter (BS), a camera focus lens (L3), and additional optics (F1, M3) that adjust the FOV on the camera sensor. The lighting sources ensure excellent uniformity, high intensity, and red-light variability without spectral components that could inadvertently polymerize photoresists. An optical short-pass filter (F1) is employed to block N-IR diffuse reflections from reaching the camera sensor, preventing pixel saturation or potential damage in the active region.

The FOV of the vision system was calculated as 135.16 × 101.37 μm², using Equation (4.7), based on the size of the digital CMOS camera sensor presented in Table 4.2.

The DM and the OL share the nanofabrication and the monitoring part of the system, whereas the motion controller executes the interaction for mechanical movement of the stages in the X Y and Z axes according to the geometric parameters of a CAD design in software recipes.

Table 4.2: Technical characteristics of the components for the 2PP setup.

Part	Component	Manufacturer	System specifications required	Ref.
Femto laser	Carmel X-780	Calmar Laser	Repetition rate of 80 MHz, pulse width of 90 fs, average power of 250 mW, pulse energy of 3 nJ, central wavelength of 780 nm and, output beam diameter of 1.3 mm.	[194]
AOM	AOMO 3080-122	Gooch & Housego	Operating wavelength range 780–850 nm, frequency of 80 MHz, Bragg angle of 7.9 mrad and diffraction efficiency of 85 % (at 830 nm).	[195]
HWP	WPH05M-780	Thorlabs	Operating wavelength of 780 nm, retardance of $\lambda/2$, reflectance 0.1 %, beam deviation of <10 arcsec.	[196]
PBS	CCM5-PBS202/M		Wavelength range 620–1000 nm, transmission efficiency (p-pol.) of 90 % and reflection (s-pol.) of 95 %.	
Beam dump	LB1/M		Wavelength range 400 nm – 2 µm, pulse laser type and max average power of 10 W.	
L1, L2, L3	LA1560-AB, LA1207-AB and AC254-150-A-ML		Focal length of 25.0 mm, 100.0 mm and 150 mm respectively. Wavelength ranges 400–1100 nm (L1, L2), diameter ½”. Wavelength range 400–700 nm (L3), diameter 1”.	
I1	ID12/M		Aperture range 1–12 mm	
M1, M2, M3	PF10-03-G01		Diameter of 1" and average reflectance of 71.3 % at 780 nm for 45° AOI S-polarization laser beam.	
XY galvo	2D-MSA-A10 MINI	Newson	Entrance beam diameter of 10 mm, resolution of repeatability 20bits, repeatability less than 3 µrad and optical angular range of 180 mrad (10.3°).	[197]
Galvo controller	CUA32-MST-AC		3 deflectors control at 20 bits resolution, synchronized deflector, usb and ethernet connection, and SDP transfer protocol support.	
Z piezo	NPO140SG	Newport	Close loop travel range of 100 µm, close loop resolution of 3 nm and typical repeatability of 3 nm.	[198]
Piezo controller	NPC3SG		3 piezoelectric stages control in close loop (position), stability of ± 0.1%, analog signal control.	
Z stage	LTA-HL		Travel range of 25 mm, bi-directional repeatability of ±1.0 µm and minimum incremental motion of 0.05 µm.	

Part	Component	Manufacturer	System specifications required	Ref.
XY large stage	LS-ONE-XY	Lasing S.A.	High speed analog encoders integrated, XY range travel of 200 mm and resolution of 10 nm.	[199]
DM	FF670-SDi01-25X36	Semrock	Average transmission greater than 90 % at 360–650 nm band, average reflection greater than 95 % at 685–1600 nm band and edge wavelength of 670 nm.	[200]
OL	MSPlan 50	Olympus	Numerical aperture of 0.8, magnification of 50×, infinite conjugate, lens tube focal length of 180 mm, working distance of 0.47 mm and effective focal length of 3.6mm.	[201]
Lighting sources	MV-I-R and ML-B50-R	Mvotem Optics	Red light at wavelength range 620–625 nm.	[202]
Camera	UI-1580LE-C-GL	IDS	CMOS Color sensor, pixel class of 5 MP, resolution of 2560x1920, pixel size of 2,2 μm and frame rate of 6,4 fps.	[203]
BS	CCM1-BS013/M	Thorlabs	Non-polarizing BS, wavelength range 400–700 nm and absolute transmission and reflection of 47 ± 10 %.	[196]
F1	FESH0750		Cut-off wavelength of 750 nm, transmission region (>90 %) 400–740 nm and rejection region 761–1200 nm.	
Motion controller	SPiiPlusEC (Motion controller)	ACS Motion Control	4 axis control, TCP/IP, Ethernet/IP host (PC) communication, EtherCAT cycle rate up to 5kHz, and network/motion-boost.	[204]
	NPMpm (Motion driver)		2 Axis control, 4 encoder channels (sin/cos), servo-boost and nanoPWM, motion-process synchronization.	
	UDMsd (Motion driver)		4 axis control, 4 encoder channels (AqB, abs), servo-boost, and motion-process synchronization.	

4.4.2. 1PP setup

1PP setup illustrated in Figure 4.7 is an extension of the optical components of the 2PP setup in the system for 1PP micro-fabrication, as summarized in Table 4.3.

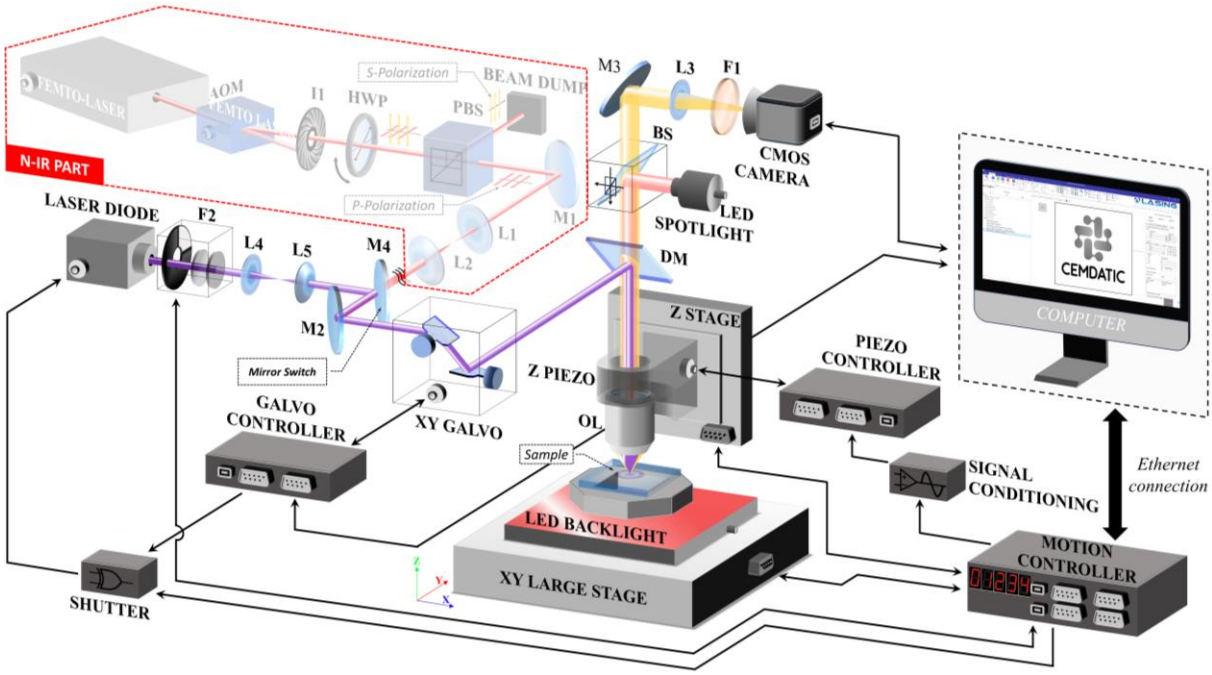

Figure 4.7: 1PP setup: A continuous-wave laser diode (CW laser), a spatial filter setup (F2), two plano-convex lenses (L4, L5), a mirror (M4) and a dichroic mirror (DM) compose the micro-fabrication part of the system. 1PP setup is an extended part of the 2PP setup.

The CW laser diode generates a beam at a wavelength in the violet visible spectrum (405 nm). The implemented power control consists of a set of three spatial filters (F2). The main filter (f_v) has a continuously variable neutral optical density (OD) that provides exponentially adjustable attenuation through rotation, while two secondary filters (f_{sub1}, f_{sub2}) have fixed ODs that allow constant attenuation. Thus, the intensity of the laser beam in Equation (4.6) can be expressed in terms of transmitted power, therefore:

$$P = P_{max} \cdot 10^{-OD(\theta)}, \quad 0° < \theta < 270° \tag{4.11}$$

where P_{max} is the maximum power transmission of the laser beam and θ belongs to the minimum and maximum OD of the main filter. Depending on the required exposure power to execute 1PP-DLW processes on various photoresists with varying sensitivity to the laser beam wavelength, F2 can be configured to adapt the transmission of the applied filters.

Two plano-convex lenses (L4, L5) with equal focal lengths are used to homogenize the laser beam along the optical axis of the optical path, satisfying the condition of Equation (4.3) for lens diameters of 25.0 mm. i.e., for the implemented CW laser, the output beam waist (D_2) is 5.8 mm ≤ (0.8×25.0) mm.

A highly reflective longpass dichroic mirror (DM) in the violet and ultra-violet (UV) spectrum, and highly transmissive in the visible spectrum has been implemented.

To satisfy Equation (4.4), an iris diaphragm installed in the optical path of the 1PP configuration reduces the beam waist to between 80 – 99% of the entrance pupil diameter ($\emptyset_{EP}$) of the OL.

Table 4.3: Technical characteristics of the components for the 1PP setup.

Part	**Component**	**Manufacturer**	**System specifications required**	**Ref.**
Laser diode	Laser diode	Unknown	Average power of 500 mW, wavelength of 405 nm and, output beam diameter of 5.8 mm	--
F2	NDC-100C-2 (f_v)	Thorlabs	Optical density range 0.04 – 2.0, coating radial angle 270° ± 5°, reflectance of 0.53 % for 8° AOI laser beam at 405nm.	[196]
	ND10B (f_{sub1})		Optical density of 1.0, transmission of 9.7 % at 405 nm and diameter of 25.0 mm	
	ND30B (f_{sub2})		Optical density of 3.0, transmission of 0.098 % at 405 nm and diameter of 25.0 mm	
L4, L5	LA1252		Focal length of 25.4 mm, wavelength ranges 350–2000 nm and diameter of 25.0 mm.	
M4	PF10-03-G01		Diameter of 1" and average reflectance of 89 % at 405 nm for 45° AOI unpolarized laser beam.	
DM	DMLP425R		Transmission lower than 1.1 % and reflection greater than 97.4 % at 380–410 nm band and cut-on wavelength of 425 nm.	

4.5. Ad-hoc design of hardware components and 2PP system

The customized 2PP system was previously designed using high-performance CAD design software before fabrication and assembly. All optical and electronic devices described in Figure 4.6 and Figure 4.7 meet the optical design requirements of the 2PP and 1PP setups precisely as described.

The model in Figure 4.8 simulates the assembly of optical devices and stages to ensure their dynamics and proper functionality. Additionally, this model ensures the reduction of time, correction of design errors, and enhancement of the final system's quality through detailed documentation provided by the company Lasing S.A. to meet industrial regulations and quality standards [199].

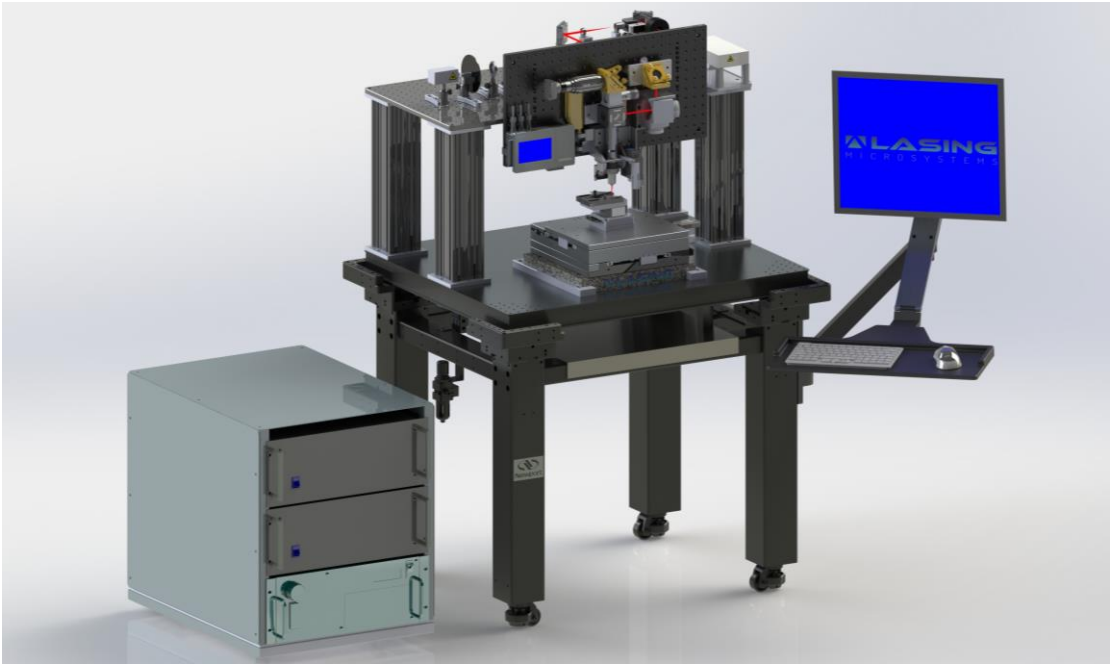

Figure 4.8: CAD design of the 2PP system assembly.

Positioning of the optical components in Figure 4.9 involves assembling the 2PP setup for ultrafast pulsed N-IR laser beam emission (780 nm, 90 fs) by a laser head [194], power control, beam waist expansion, and routing of the polarized laser beam. Meanwhile, Figure 4.10 shows the assembly of the 1PP setup for continuous violet laser beam (405 nm) by a laser diode, power control, collimation, and routing of the laser beam.

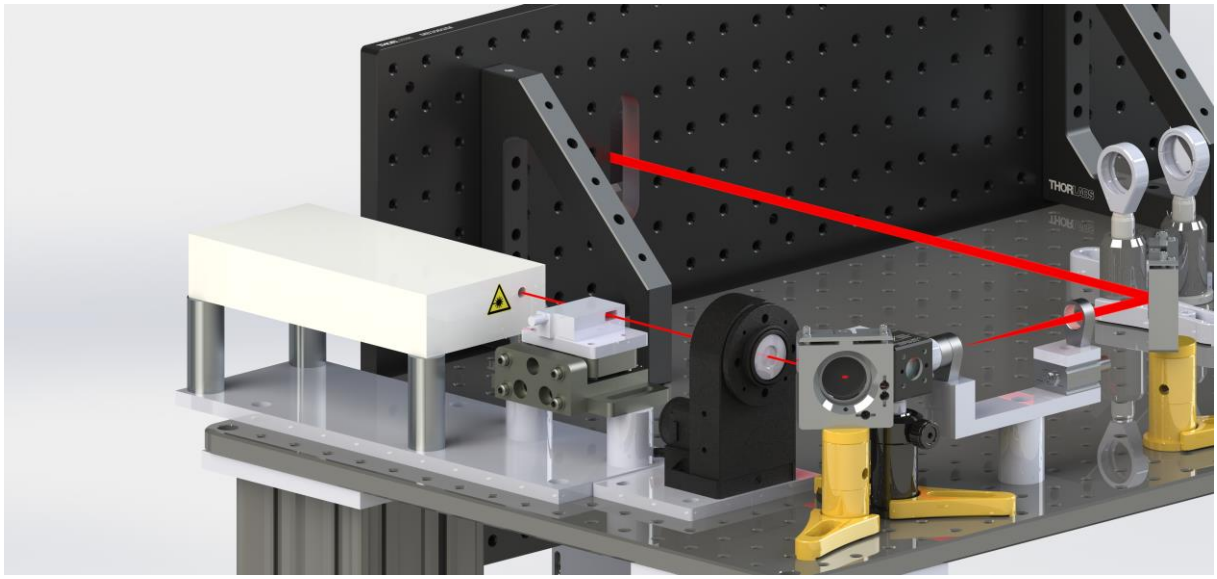

Figure 4.9: CAD simulation of the 2PP setup assembly.

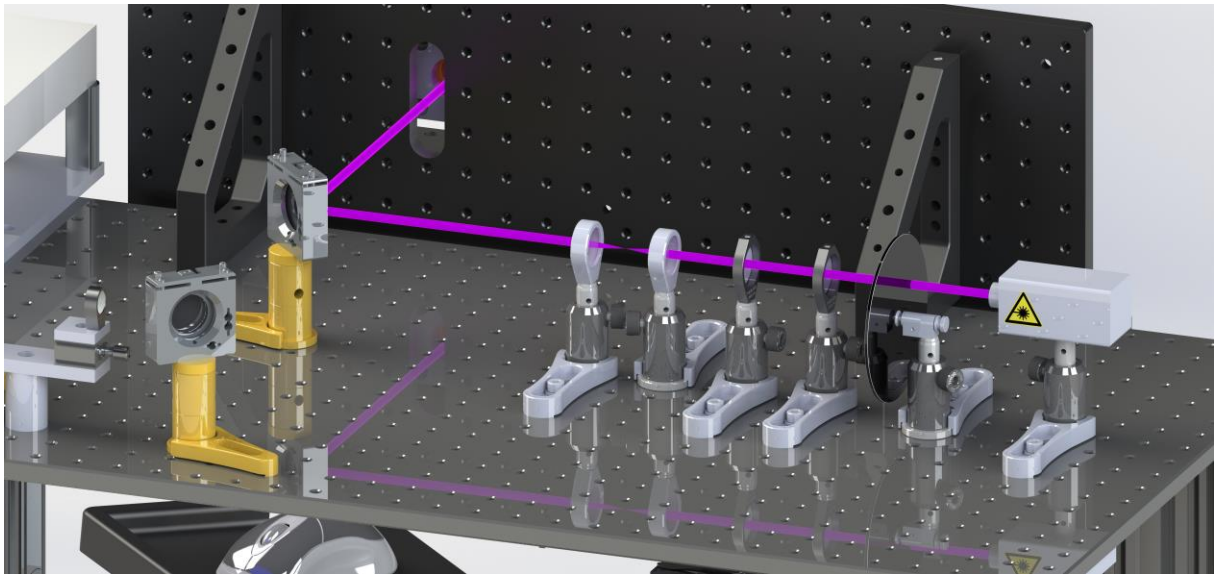

Figure 4.10: CAD simulation of 1PP setup assembly.

Only one laser beam is permitted to perform DLW processes. Both laser beams acting simultaneously are not allowed, because the customized system is not characterized for polymerizing photoresists using both one-photon absorption (1PA) and two-photon absorption mechanisms (2PA). The laser beams are generated separately by their sources and directed towards the main optical path up to the entrance pupil of the OL. Therefore, the optical switch (M4 in Figure 4.9) acts as a reflector for the violet laser when the system operates in 1PP-DLW mode, keeping the ultrafast pulsed light off, and vice versa for 2PP-DLW mode without M4. Additionally, different dichroic mirrors (DM) are implemented for each laser wavelength according to the technical requirements in Table 4.2 and Table 4.3 for each 1PP-DLW and 2PP-DLW process.

A vertical platform allows positioning of the optical components and XYZ nano-positioning stages (XY-galvos and Z-piezo) in the main optical path, as well as all vision optical components, ensuring they are collinear with the laser beams (violet and N-IR) along the Z-axis of the customized 2PP system. Figure 4.11 shows a comprehensive simulation to prevent manufacturing and assembly errors.

Finally, Figure 4.12 and Figure 4.13 depict the XY large stage and the integrated control electronics rack (controllers, computer, and power supply) required for the system operation.

The system is implemented on an anti-vibration floating table isolated by injected air pressure to prevent external perturbations that may be transmitted to the 2PP system, thereby affecting the 1PP- and 2PP-DLW processes and reducing the resolution of critical micro/nanostructures for photonic devices and applications.

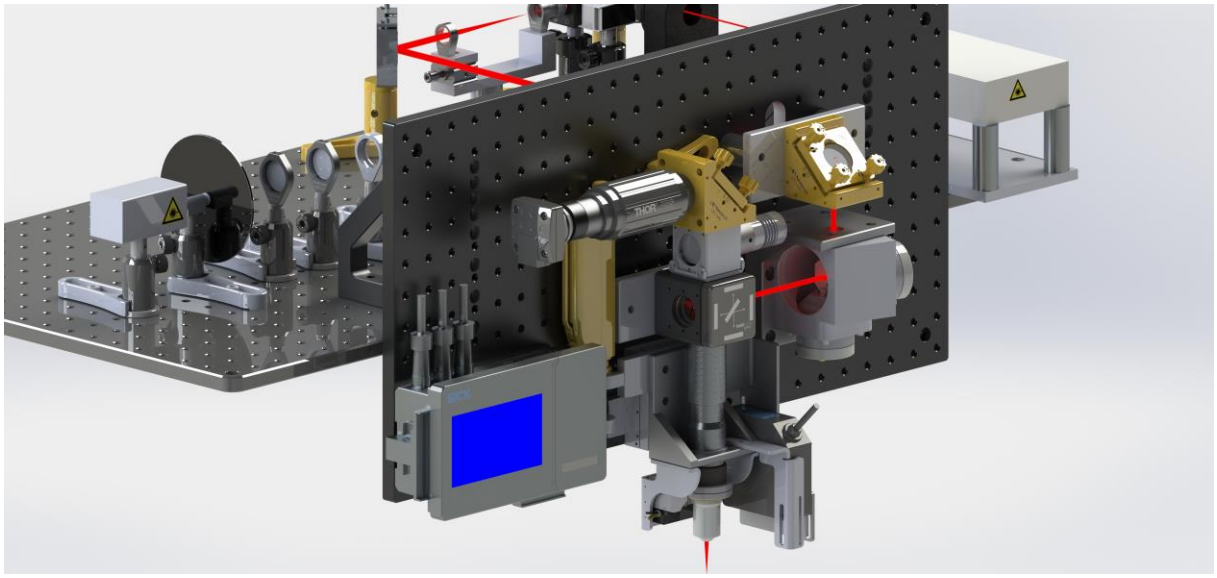

Figure 4.11: CAD simulation of the vision and XYZ nano-positioning of the system.

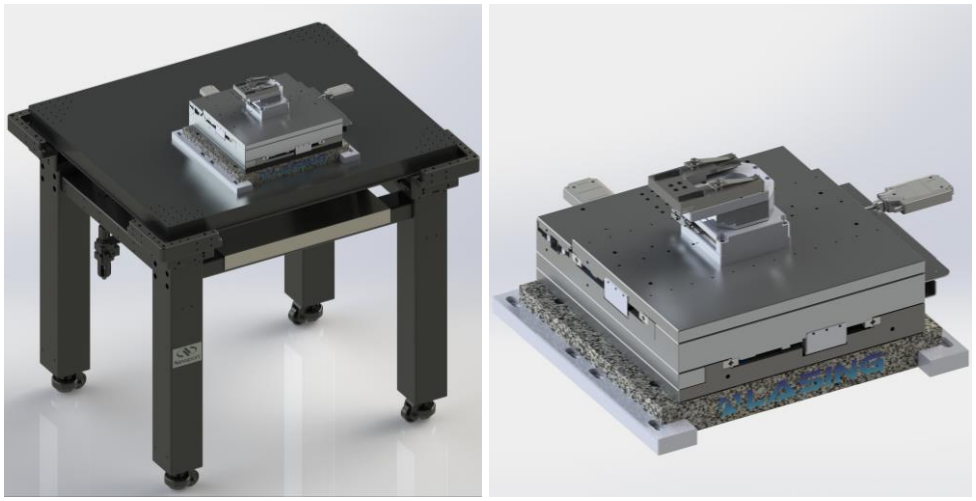

Figure 4.12: CAD simulation of XY large stage assembly on anti-vibration table.

Figure 4.13: CAD simulation of the control rack assembly.

4.6. 2PP System Assembly

The final assembly of the 2PP system is shown in Figure 4.14, where each component is carefully designed and manufactured to meet the criteria of the CAD simulations from Figure 4.8 to Figure 4.13.

The 2PP system has been thoroughly tested, and the XYZ linear stages and rotary stage have been tuned using the SPiiPlus MMI Application Studio software from ACS Motion Control [204], and Lasing Processing Software (LPS) is thoroughly programmed and installed on the computer with the respective configurations and calibrations for controlling the entire hardware of the 2PP system [199].

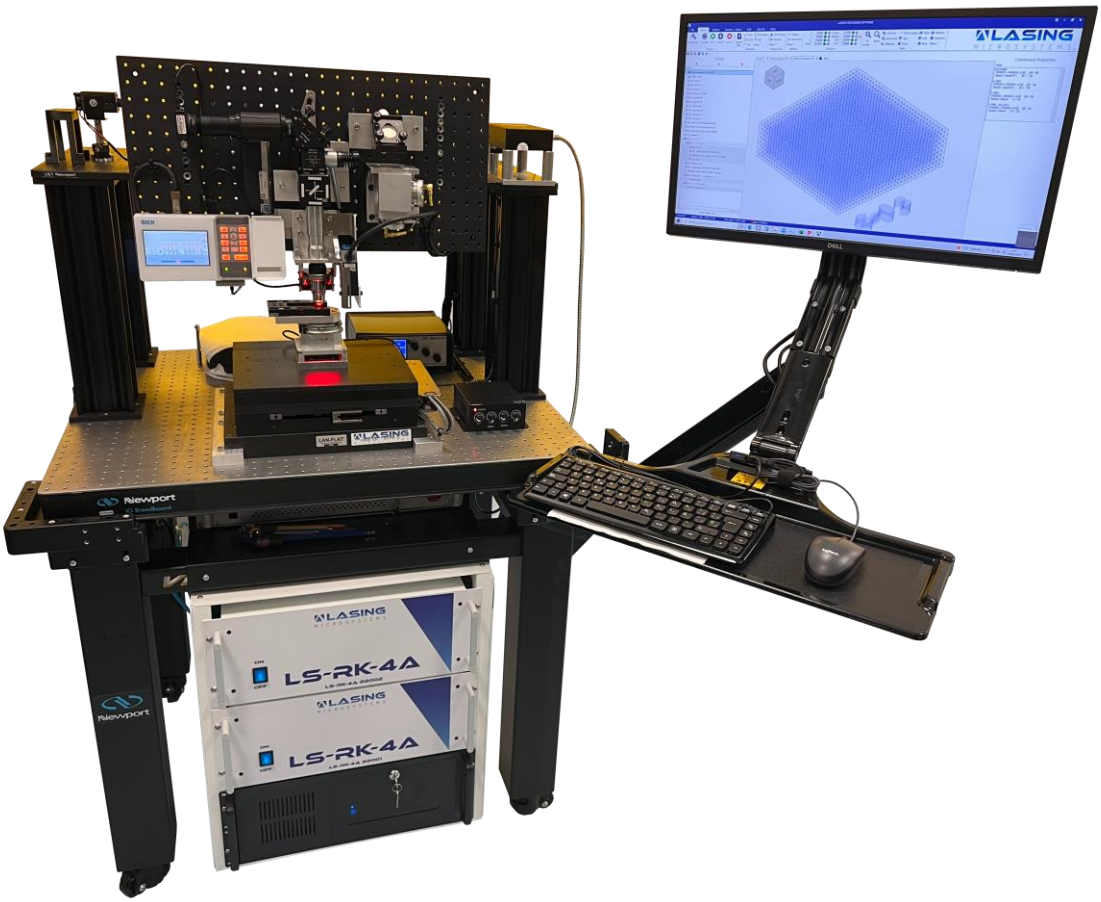

Figure 4.14: Final view of the assembled 2PP system.

The optical components and assembly mounts of the 2PP system are organized on three platforms (optical tables from Newport and Thorlabs). The top platform is shown in Figure 4.15, while the vertical platform and the anti-vibration floating table are shown in Figure 4.16. 1PP and 2PP setups are completely labeled in the figures with optical path of the laser beams.

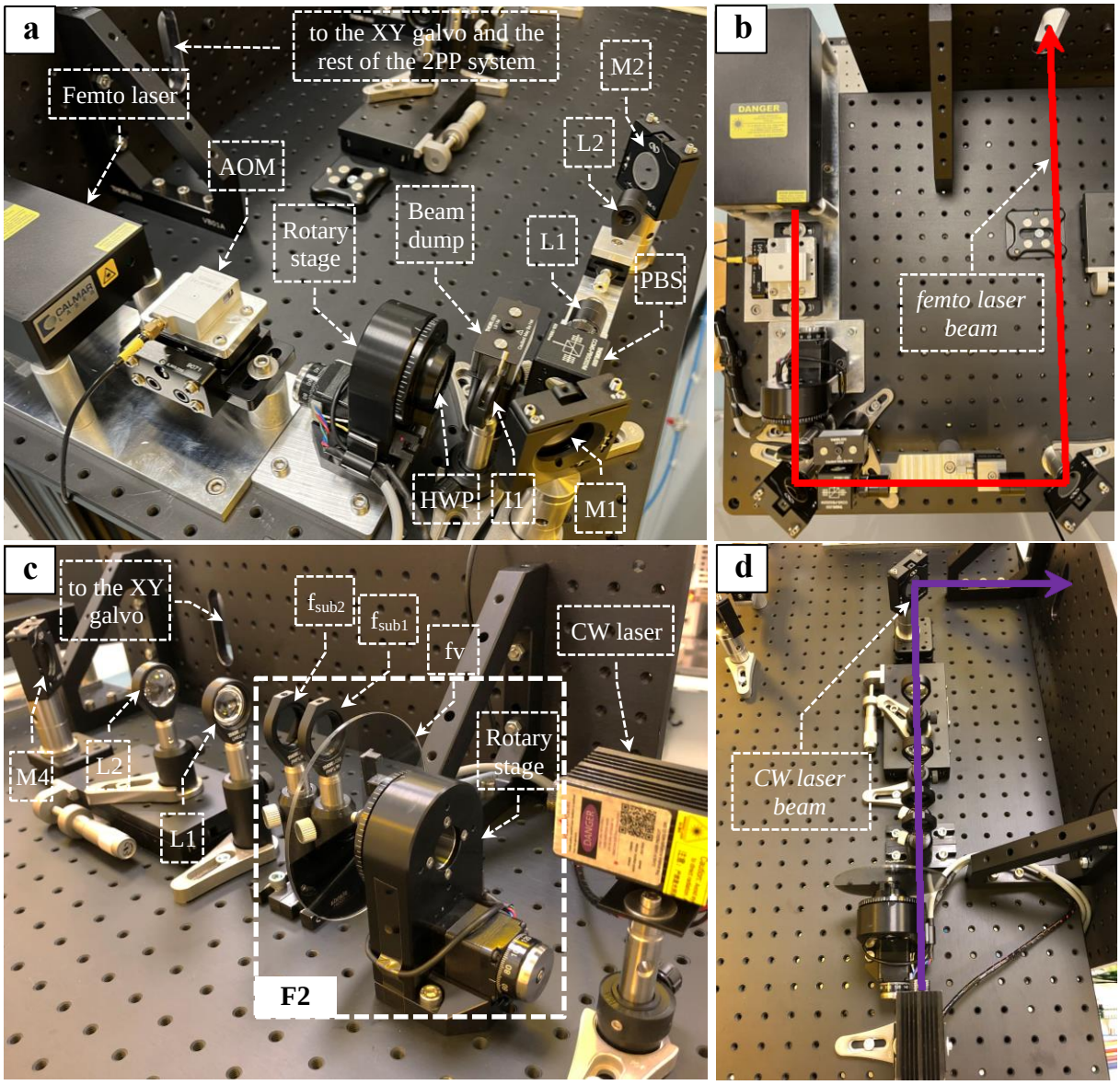

Figure 4.15: Top platform of the assembled 2PP system. a) View of the assembled 2PP setup. b) Optical path of the assembled 2PP setup. c) View of the assembled 1PP setup. d) optical path of the assembled 1PP setup.

Vision design and light optical design (N-IR and violet light) are shown in Figure 4.16. All assembly mounts used for this 2PP system are acquired from Newport and Thorlabs stock, while other nonstandard mounts are designed and manufactured according to the CAD simulations.

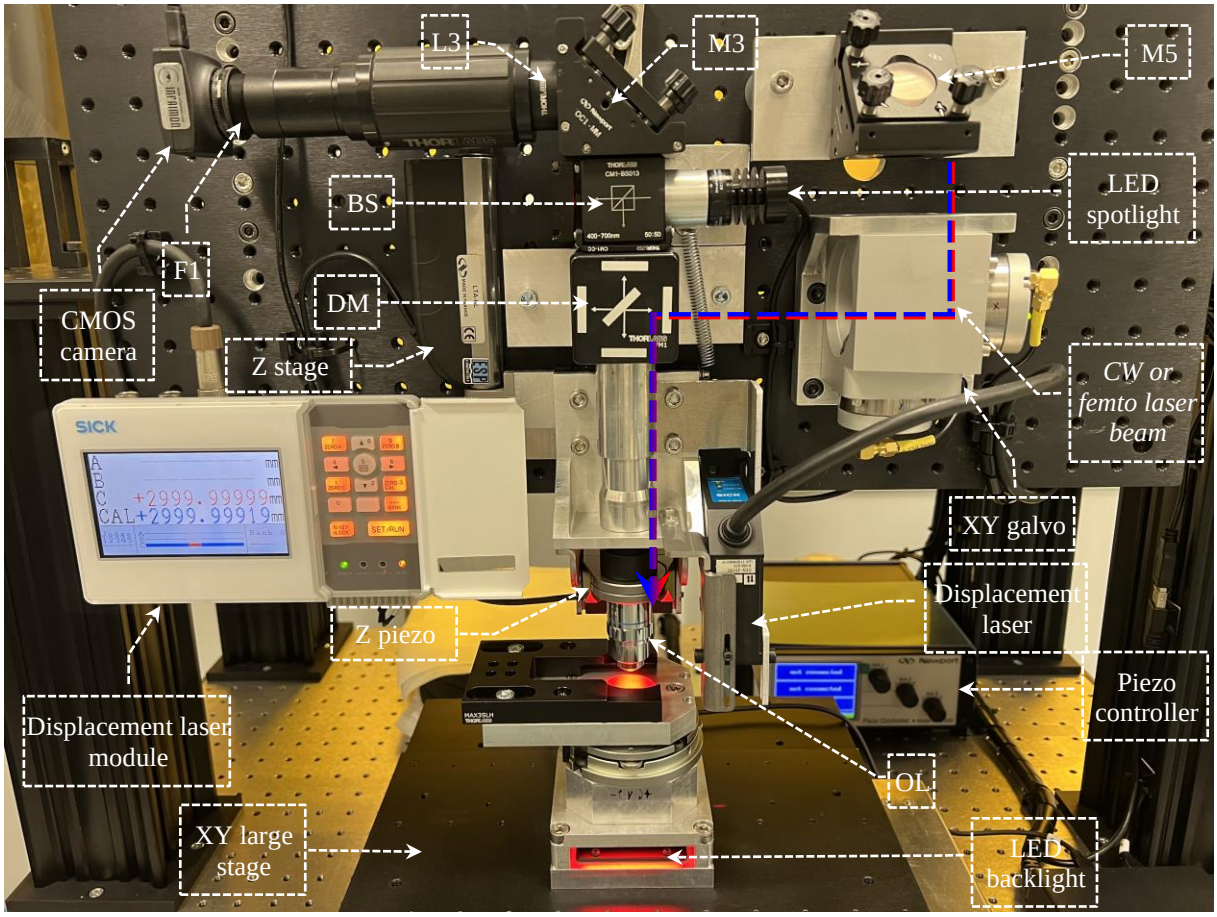

Figure 4.16: View of the vertical platform and anti-vibration floating table of the assembled 2PP system. An additional mirror (M5) has been used to redirect the laser beam to the XY galvo, and a displacement laser module to manage focusing and surface mapping data from displacement laser [205].

In practice, optical aberrations, laser quality, and laser alignment can influence the efficiency of the 2PP system during DLW processes. The volume formed by the focal spot of the focused beam in the photoresists, particularly the voxel size created by a femto laser beam, is affected, aside from the properties of the photoresist which can also alter voxel dimensions. Therefore, the 2PP system must be correctly assembled and tuned prior to the fabrication of micro/nanostructures.

The electronic components are organized in three cases inside the control rack: control, power supply and computer case, as depicted in Figure 4.17-a. The control case, depicted in Figure 4.17-b, is composed of galvo and motion controllers, a shutter, an AOM module, and signal conditioning, while the power supply case consists of DC power supplies of +5 volts, +24 volts, and +48 volts to provide the necessary tension and current for the entire 2PP system. All electric and coaxial cables used for the connections are fully distributed among all electronic components in the 2PP system.

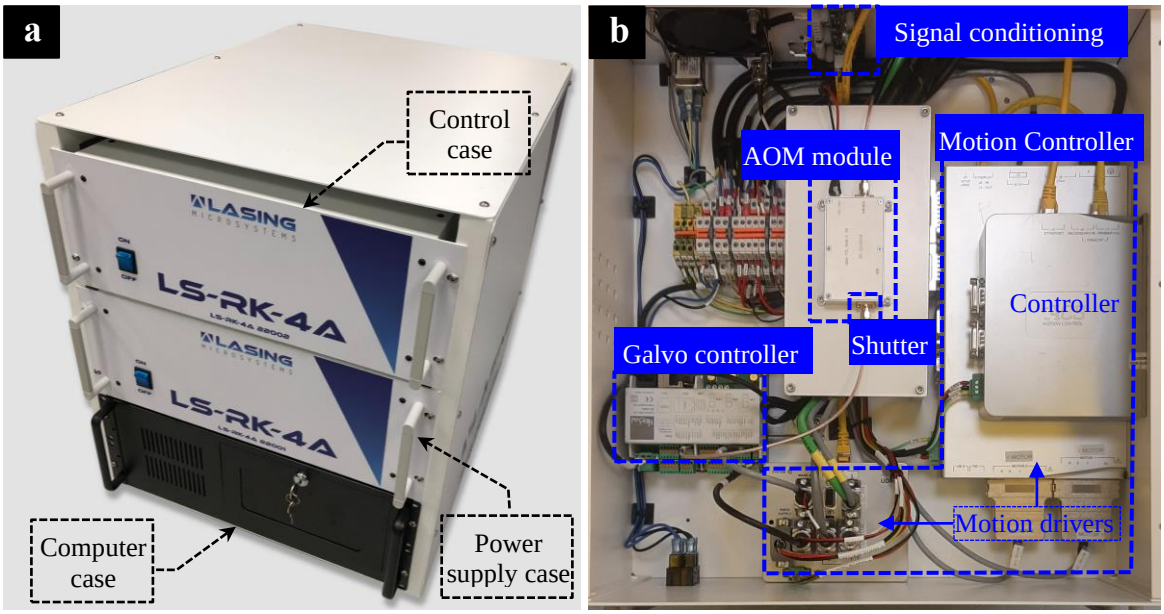

Figure 4.17: View of the entire control rack of the assembled 2PP system. a) Organization of the cases of all electronic components. b) Inside view of the control case.

CHAPTER 5

5. Results: Initial commissioning and optimization of the system

The exposure power and marking/scanning speed are parameters to be optimized in photolithographic systems for the fabrication of 2D and 3D micro/nanostructures for photonic devices with the best achievable precision and resolution [27]. Two-photon polymerization (2PP) is the most versatile technique for achieving high-resolution micro/nanostructures smaller than 100 nm [158], [206]. Therefore, an optimization of the 2PP system to achieve the desired resolution in commercial photoresist must be carried out, similar to commercial systems for micro-fabrication based on 2PP [32], [33], [34].

This chapter presents the commissioning and optimization results of the customized 2PP system. Optimization is divided into two steps.

Optimization of direct laser writing (DLW) using one-photon polymerization (1PP-DLW) and 2PP-DLW in thin layers of negative-tone photoresist, followed by a comparison of their commissioning results.

2PP-DLW optimization in thin and thick layers of positive-tone and negative-tone photoresists for voxel characterization in the customized 2PP system.

1PP-DLW is used to calibrate and optimize the 2PP system without considering fine focusing on the photoresist surfaces. This is because polymerization in 2PP-DLW is more complicated when positioning or optical path errors occur during the 2PP system start-up. Also, it allows for thin-layer 2D lithography with a resolution above one micron.

5.1. 1PP-DLW optimization on SU-8 photoresist

The 1PP-DLW process uses the one-photon absorption (1PA) mechanism to polymerize photoresists. This technique is commonly used to fabricate 2D microstructures (usually in thin layers) for photonic devices and applied optics [8], [207]. The molecules absorb the necessary amount of energy, above the polymerization threshold without over-exposing the exposure area. The exposure time and the photon energy ($h\nu_{ph}$) that induce the transition from the ground state to the excited state, along with the laser photon emission rate (photons/time), are key parameters of the process. Therefore, the laser beam power and scanning speed contribute to

the optimization of the polymerization reaction within the micrometric area formed about the focal point of the objective lens (OL) [155].

In this context, the optimized power is determined by the angle θ of the attenuator in the filter setup (F_2). This has been described in the 1PP setup of Figure 4.7 and expressed in Equation (4.11). It can be rewritten as follows:

$$P = P_{max} \cdot T_{losses} \cdot 10^{\left(\left[-OD_{max}-\left(\frac{OD_{min}-OD_{max}}{250°}\right)\cdot\theta\right]-OD_{sub1}-OD_{sub2}\right)} \tag{5.1}$$

where P_{max} = 500 mW is the maximum average power output of the continuous-wave laser (CW laser), OD_{min} = 0.04 and OD_{max} = 2.0 are the minimum and maximum optical densities of the variable attenuator disk (f_v), $OD_{sub1} = 1.01$ and $OD_{sub2} = 3.01$ are the optical densities of the fixed filters f_{sub1} and f_{sub2} respectively, θ is determined within the defined attenuation region of f_v as $\{0° \leq \theta \leq 250°\}$, and T_{losses} represents the remaining optical transmissions after accounting for the optical losses of all components at a wavelength of 405 nm. It is defined as follows:

$$T_{losses} = 1 - \sum_{i=1}^{M}(1 - R_i) + \sum_{j=1}^{L}(1 - T_j) \tag{5.2}$$

where R_i represents the reflection losses of all mirrors, and T_j represents the transmission losses of all lenses along the optical path of the system.

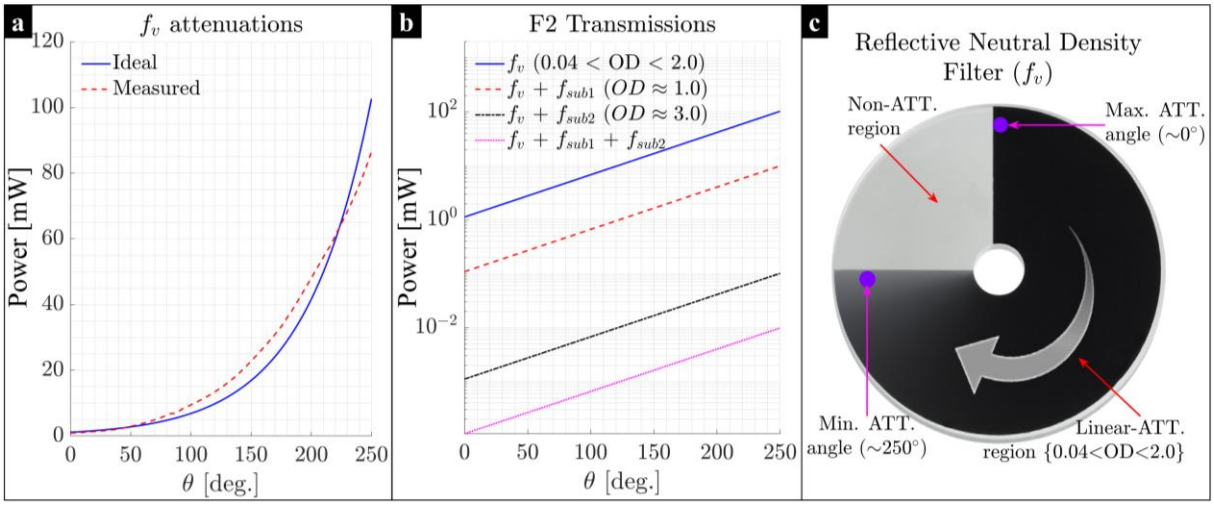

Figure 5.1: a) Characteristic average powers of the 1PP setup measured and calculated from the attenuator disk (f_v). b) Power of the CW laser applying the filter setup ($F_2 = f_v + f_{sub1} + f_{sub2}$). The dashed lines represent the powers obtained using the fixed filters (f_{sub1} and f_{sub2}) for their respective transmissions (ND10B and ND30B from Thorlabs) at λ = 405 nm. c) Representation of the variable attenuator f_v (NDC-100C-2 from Thorlabs).

Figure 5.1-a represents the measured and calculated powers corresponding to the optical design of the 1PP setup. The CW laser power was measured at the entrance pupil of the OL using a

power meter equipped with a Newport photodetector (1936-R and 918D-SL-OD3R). The total powers in Figure 5.1-b are determined based on the combination of filters applied for polymerization. Figure 5.1-c shows the descriptive profile of the attenuator disk (f_v) in the filter setup (F_2). The attenuation region is linear with rotation, where ($OD \approx 2.0|\theta = 0°$) and ($OD \approx 0.04|\theta = 250°$) determine the maximum and minimum attenuation limits in the system as obtained in Figure 5.1-a and -b. The non-attenuation region ($P_{out} > P_{max}$) represents the uncontrolled power region and has not been considered for system optimization.

5.1.1. Methods and materials

The system is designed to photopolymerize photoresists deposited on silicon, quartz, or glass substrates.

In this chapter, commercial 0.7 mm-thick glass indium-tin oxide (ITO) coated slides are used as substrates. The ITO layer is nominally 130 nm-thick and provides good and uniform adherence of the photoresists. The CW-laser beam is focused inside the photoresist using a 50× microscope OL with numerical aperture (NA) of 0.80. Negative-tone photoresist can selectively be polymerized using the Equation (5.1) by 1PA explained in Chapter 2.

Prior to 1PP-DLW meticulous substrate cleaning process was carried out in the clean-room of the UPM´s CEMDATIC [208]. First, the substrates are immersed in commercial acetone/2-propanol for 1 minute and cleaned with lint-free cloths. Subsequently, ultrasonic cleaning of the substrates is performed for 30 minutes immersed in deionized water. Afterwards, the substrates are thoroughly dried with nitrogen flow. Finally, high-temperature baking at 200 °C for 120 minutes eliminates any remaining adsorbed water.

Before dispensing the photoresist onto the ITO-glass substrates, they are placed under deep cleaning using an ultra-violet-ozone cleaner (UVO-Cleaner) for 10 minutes to eliminate any organic material (oils, greases and other waste). This step also makes the substrates surface more hydrophilic, improving the adhesion of the deposited photoresist.

Photoresist is drop-casted onto the ITO-glass surface (1 ml of photoresist for each 25×25 mm² surface) for spin-coating. The used photoresist is SU-8 TF 6002 negative-tone photoresist (Kayaku Advanced Materials) obtained from Micro Resist Technology GmbH. SU-8 photoresist is spin-coated in two steps. Firstly for 10 seconds at 500 rpm to achieve a uniform distribution of the material on the substrate; in the second step, the sample is rotated for 30 seconds at 3000 rpm to reach the desired thickness. In both steps, acceleration ramps of 500 rpm/s. are used. This creates a photoresist layer of approximately 2 µm of thickness. Finally, the spin-coated photoresist is immediately soft-baked at 110 °C for 3 minutes to get it ready for the 1PP-DLW processes. Pre- and post-exposure parameters are summarized in "Appendix A: Cleaning and spin-coating processes".

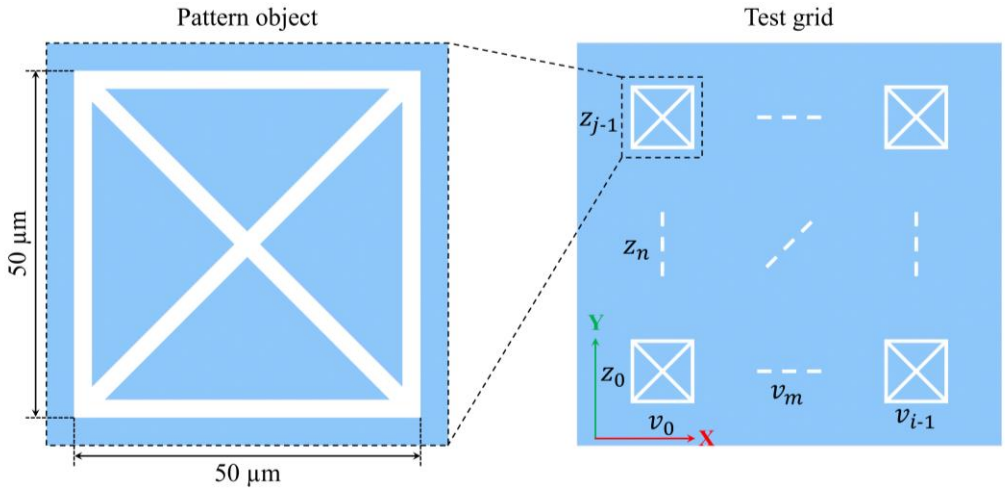

Figure 5.2: A pattern object for the 1PP-DLW process and a test grid to optimize the scanning speeds.

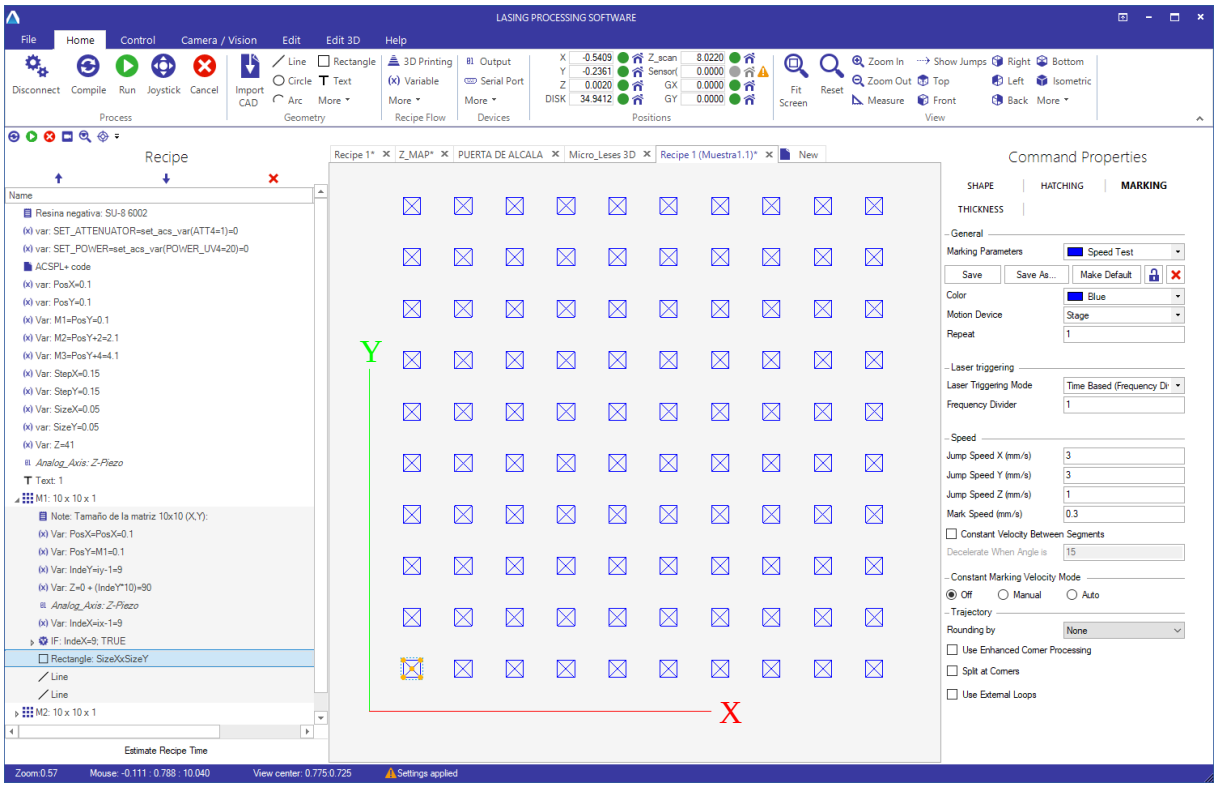

Figure 5.3: Programming and configuration of pattern objects on the LPS software front panel. The displayed test grid is processed at an average laser power. For other laser powers, the test grid is repeated multiple times on the same substrate.

The 1PP-DLW process is implemented using the Lasing Processing Software (LPS) provided by the company Lasing S.A. [199]. LPS software is based on programmable recipes and features an intuitive interface for obtaining optimized parameters. Hence, a pattern object has been programmed in LPS software to be polymerized. The pattern object is a simple geometric shape measuring 50×50 µm², as depicted in Figure 5.2. In addition, a test grid of $m \times n$ pattern objects have been configured.

Each pattern object of the test grid is programmed with different parameters, where $\{v_m|v_0, v_1, \dots, v_{i-1}\}$ represent the increments in scanning speeds of the motion stages, while $\{z_n|z_0, z_1, \dots, z_{j-1}\}$ represent the increments in heights along the Z-axis of the motion stages. Therefore, a pattern object $(v_i; z_j)$ is associated to a specific scanning speed and Z jumping. Z jumping is used to define the smallest possible linewidth on the spin-coated SU-8 layer thickness (maximum resolution) in 1PP-DLW process.

Optimization is directly related to the ability of configuring parameter properties to generate laser processing pseudo-algorithms contained within a Recipe in LPS software. Figure 5.3 shows the interface and the programming command list with their respective system configurations.

SU-8 is commonly used to form 2D structures through 1PA induced by a CW laser beam [155]. 1PP-DLW is governed by applying an appropriate exposure energy/time during the process. The characterized power shown in Figure 5.1 is used to define the polymerization threshold levels together with the focused CW laser beam scanning speed in the XY-plane of the substrates. Therefore, the absorption probability is linear and proportional to the beam intensity [40]. However, the absorption may be more complex, and 1PA might not be the dominant mechanism because of complex energy activation in SU-8, where the energy distribution and deep effects are relevant.

The spin-coated SU-8 substrates are placed into the system to process the entire test grid of pattern objects shown in Figure 5.3. Pseudo-algorithms generated in LPS software are downloaded to the controllers of the 2PP system. These interpret the X and Y axes speeds, laser power control, synchronization, and other specific programming properties, such as vector positioning, field of view (FOV) adjustment, surface mapping, stitching, etc.

The printing and focusing mode of the 2PP system is designed in air configuration mode, described in Chapter 4. Prior to optimization, the focusing was calibrated with initial, non-extreme precision. Initially, the focal spot of the OL was adjusted on the photoresist surface by moving the Z stage. This adjustment must ensure that the separation between the surface and the OL matched the working distance (WD) of the OL. The system's vision camera has been used to meticulously set the WD with micrometer precision (step one in Figure 5.4). Next, a displacement laser was assembled and calibrated to its operational distance. The laser used is the OD5-25T01 (Sick Sensor Intelligence), a red laser sensor designed for focusing. According to the sensor specifications, the distance to obtain 90 % of the reflectance on the surface is 25 mm, with accuracy of 0.02 µm of the measuring range of sensor (24–26 mm) [205]. This operational distance was meticulously calibrated, and the displacement laser should remain untouched to ensure that the OL's WD is consistently the same for all processes (step two in Figure 5.4). When a new spin-coated SU-8 substrate is placed into the 2PP system, the sensor measures the distance again to detect any deviation (WD ± Δ). The system then moves the Z

stage to minimize this deviation ($\Delta \approx 0$), ensuring that OL's WD must be the ideal by automatically setting the operational distance to 25 mm by reading the analog values of the sensor in LPS software (step three in Figure 5.4). This means that focusing is performed by reading the sensor, not by the system's vision. Finally, the OL and the displacement laser move together as a single block (Z head). This method may be referred to as coarse focusing.

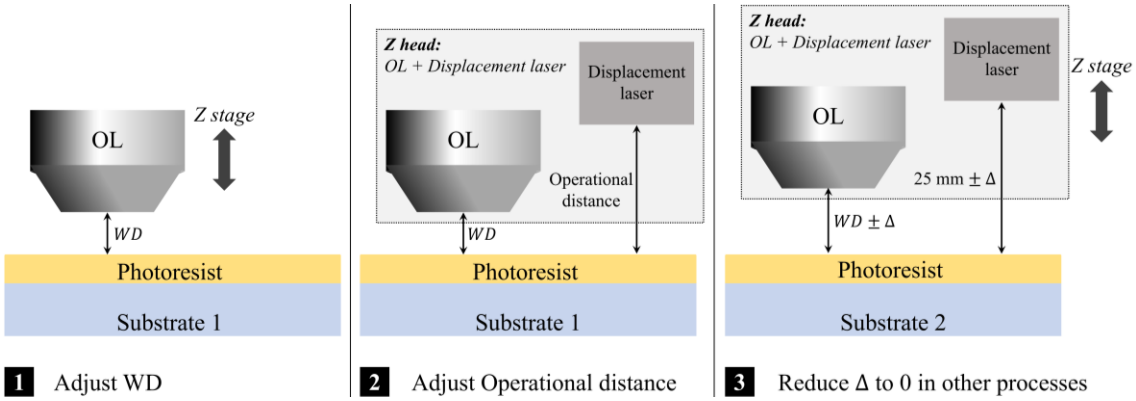

Figure 5.4: Steps for initial focusing in the 2PP system: After calibrating the distance of the objective lens (OL) and displacement laser, the Z stage is moved along the z-axis to ensure the operational distance to 25 mm throughout the processes. The sensor's range is between 24 mm and 26 mm, and measurements outside this range are not assured. The OL and displacement lasers are mounted on a Z head, which is moved by the linear Z translation stage.

After coarse focusing, the test grid shown in Figure 5.3 was processed, and repeated several times on the same spin-coated SU-8 substrate, with different scanning speeds, as well as variations in Z-axis positions, to achieve better precision and gather more comprehensive data.

The experiments have been repeated several times with different powers of the CW laser beam per substrate to empirically determine the minimum permissible power. For each exposed power value on the SU-8, different polymerization results have been obtained, and consequently, different resolutions.

After the 1PP-DLW process, the substrates are immediately post-baked at 110 °C for 2 minutes to complete the polymerization process, according to the SU-8 technical datasheet [71].

Finally, the substrates are developed by submerging them in SU-8 developer (PGMEA) for 3 minutes, then cleaned with 2-propanol for 30 seconds, and dried using a nitrogen flow. The post-exposure processes used in this work are summarized in "Appendix A: Cleaning and spin-coating processes".

5.1.2. Results

The position errors of the stages were mitigated by tuning all motion stages and adjusting the optical path of the CW laser to avoid aberrations and clipping the beam. This was continuously

verified to ensure the correct formation of the polymerized pattern objects for the presented results.

The exposure time to polymerize SU-8 is an unknown value for the energy transfer required within the volume formed by the incident area (focused laser beam area) along the thickness of SU-8 (Z-direction). Hence, the power was determined by observing the lines after the development process using an optical microscope. Multiple test grids on the same substrate were processed, each with a different average laser power. In the experiments of the 1PP-DLW processes, an average laser power from 0.1 µW to 10.3 µW and scanning speeds from 50 µm/s to 600 µm/s were applied to simplify the analysis. Therefore, for this laser power range, polymerized microstructures in SU-8 were observed at a scanning speed of 300 µm/s and summarized in Table 5.1.

Table 5.1: Classification of powers in 1PP-DLW processes at a scanning speed of 300 µm/s.

Average power applied [µW]	**1PP-DLW linewidth resolution [µm]**
0.10 – 1.65	No results were reliable (Un-polymerized)
1.85 – 5.15	~ 1.0 (Polymerized)
5.15 – 6.39	> 1.5 (Polymerized)
6.39 – 10.3	> 2.5 (Polymerized)
>10.3	> 3.0 (Over-exposed)

At a scanning speed of 300 µm/s and an average power of 1.85 µW, according to Equation (5.1), the best achieved resolution observed was 1.106 µm, as shown in Figure 5.5. Different results have been observed at other scanning speeds, where the polymerized objects were not reliable. Outside of the mentioned range of the average laser power and scanning speed, no promising results were observed. The entire test grid corresponding to the experiments carried out in Figure 5.5 is depicted in “Appendix C: Results in optimization processes”.

Pattern objects have been analyzed using a field emission scanning electron microscope SEM (EVO 10, ZEISS group). Prior to imaging, a 100 nm aluminum layer was deposited on the samples, and an electron beam voltage of 4 kV was applied.

The SU-8 exhibited completely polymerized lines. In some cases, pattern objects exhibited broken shapes due to the polymerization being below the threshold. Consequently, the bonding of polymer chains was not successfully completed throughout the entire photoresist thickness, leaving some areas soluble to the SU-8 developer, as depicted in Figure 5.5.

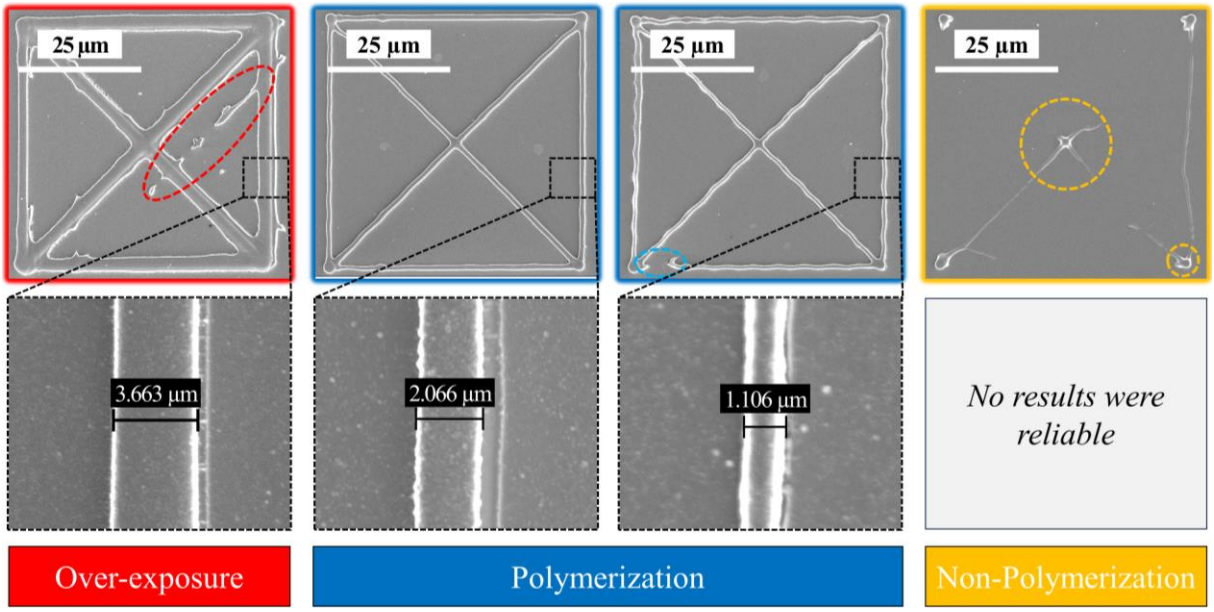

Figure 5.5: SEM images of pattern objects exposed to 1.85 µW. The measurements obtained on the over-exposed, polymerized, and non-polymerized pattern objects correspond to different scanning speeds for a single test grid in 1PP-DLW processes.

Non-polymerization results in either non-polymerized pattern objects, or blurred and indistinguishable pattern objects due to insufficient photon absorption throughout the entire thickness of SU-8, i.e., the exposure dose is far below the threshold (see Figure 5.5). The laser intensity attenuates exponentially for small exposure doses as it penetrates in depth, as shown in Equation (2.3), leading to insufficient excitation of the photo-initiators required for photopolymerization throughout the entire thickness. As a result, these non-polymerized objects are unlikely to be observable during SEM analysis. Furthermore, the polymerized points depicted in non-polymerization micrograph of the Figure 5.5 are the result of double exposure during the 1PP-DLW processes and the (de-)accelerations of the motion stages.

The over-exposure exhibits unfavorable outcomes with line widths exceeding 3 µm due to the uncontrolled chain reaction of monomer-radicals near the exposed area. Another issue with over-exposure is the effects of back reflections (multiple refraction/reflection of the laser beam within the substrate layers), causing undesired polymerizations and consequently reducing the precision and resolution of the polymerized microstructures.

Different levels of polymerization are achieved with different scanning speeds, i.e., for average powers of 1.70 µW, 1.85 µW, and 2.68 µW, different results in polymerized linewidths have been obtained. The linewidths in Figure 5.6 exhibit exponential decays with increasing scanning speeds for the three mentioned power levels. Linewidths below 1 µm are not appreciable due to the dispersion of the data measured in the SEM. Linewidths exceeding 2 µm are also unacceptable due to over-exposure effects, which further increase variability in the SEM measurements. Therefore, well-polymerized pattern objects were successfully created in

the scanning speed range of 100 µm/s to 400 µm/s at 1.85 µW of laser power during this optimized 1PP-DLW process.

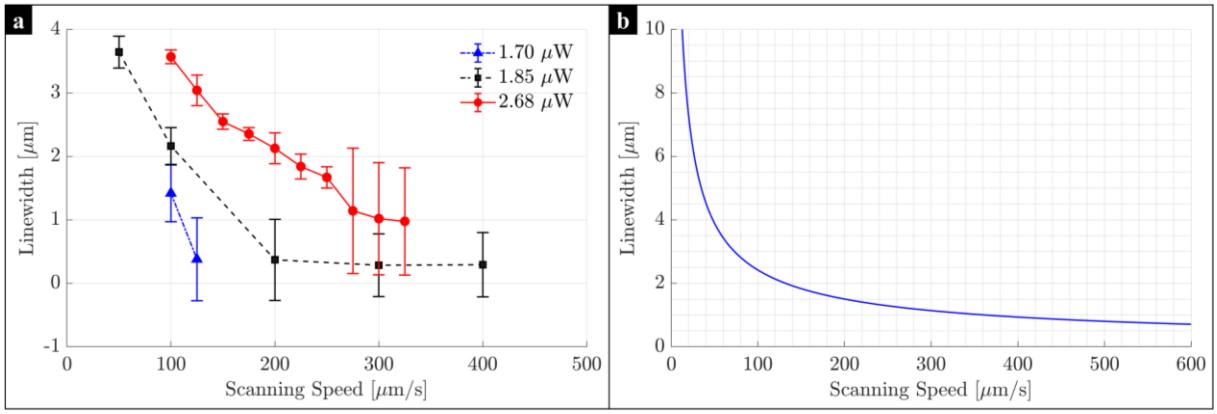

Figure 5.6: a) Linewidths measured at three power values in 1PP-DLW processes. b) Fitted data corresponding to 1.85 µW.

5.2. 2PP-DLW optimization on SU-8 photoresist

The 2PP-DLW process uses the two-photon absorption (2PA) mechanism to polymerize SU-8 [72], [209]. This technique is commonly used to fabricate high-resolution 2D and 3D nanostructures, achieving approximately 30 nm resolution in SU-8 [72], or less than 25 nm in other photoresists [23]. It is employed in the fabrication of micro-scaffolds [149], nano-needles [144], micro-lenses [105], liquid crystal alignment [93], and in-situ 2PP for medical applications [146].

After minimizing positioning and optical path errors in 1PP-DLW. The appropriate exposure time allows achieving maximum resolution in the nanometric volume formed by the laser spot (voxel) in the 2PP system. Therefore, optimization of scanning speed and beam power is primordial.

The optimized femtosecond laser (femto laser) beam power is determined by the angle θ of the half-wave plate (HWP) in the 2PP setup shown in Figure 4.6 and expressed in Equation (4.10). It can be rewritten as follows:

$$P = P_{max} \cdot T_{losses} \cdot \cos^2(2\theta - \varphi) \tag{5.3}$$

where $P_{max} = 250\ mW$ is the maximum average power, $\varphi = 97.4°$ is the offset angle for the fast principal axis of the HWP installed in the 2PP system, and T_{losses} represents optical losses in the total transmission through all lenses and mirrors at the wavelength of 780 nm, defined by Equation (5.2).

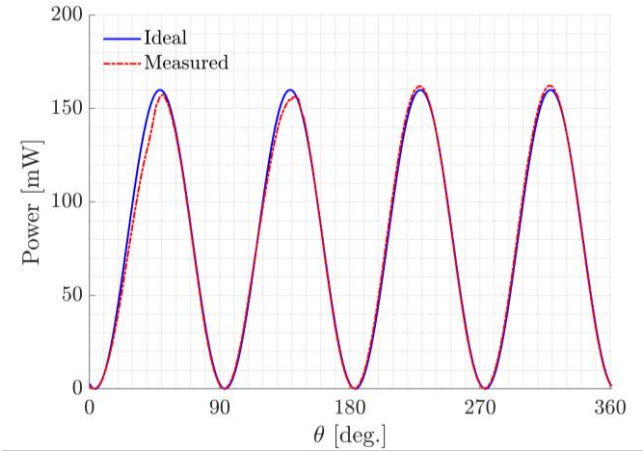

Figure 5.7: Characteristic average powers of the 2PP setup measured and calculated from the control stage consisting of the half-wave plate (HWP) and polarizing beam-splitter (PBS).

Figure 5.7 shows the measured and calculated femto laser beam powers using Equation (5.3). The beam power was measured at the entrance pupil of the OL using a Newport power meter (1936-R and 918D-SL-OD3R). To control the beam power, only 25 % of the total rotation range of the HWP has been utilized, which ranges from 0° to 45°, corresponding to a power range of 0 mW to 160 mW in this 2PP system.

5.2.1. Methods and materials

Commercial 0.7 mm-thick glass ITO coated slides are also used as substrates. The 2PP setup description is provided in Chapter 4, where the femto laser beam is focused on the interface between the ITO and the SU-8 using the 50× OL with a NA of 0.80.

The cleaning process is described in Section 5.1.1. Substrates are pre-cleaned using commercial acetone/2-propanol and ultrasonic immersion cleaning, dried with a nitrogen flow, baked at 200 °C, and undergo deep cleaning with a UVO-Cleaner. SU-8 is then drop-cast onto the ITO-coated glass surface for spin-coating, followed by a final soft-bake at 110 °C, as summarized in “Appendix A: Cleaning and spin-coating processes”.

The same test grid of m×n pattern objects is used under identical conditions and configurations in LPS software for the 2PP-DLW process (see Figure 5.2 and Figure 5.3). The beam power required to cross the polymerization threshold is determined by Equation (5.3). The absorption probability of photons is proportional to the square of the incident intensity, making 2PA highly likely within the voxel of the focused laser beam rather than outside it (confined photons energy).

Fine focusing into the photoresist in the air configuration of the 2PP system was employed. In the 2PP-DLW process, the focal spot of the OL must be placed between ITO-glass substrate and the spin-coated photoresist. The voxel starts polymerization at this interface and prevents

the polymerized objects from floating into the photoresist volume, avoiding the risk that they might be removed during the washing of the photoresist and that no result is obtained. Therefore, to achieve this focusing, coarse focusing is performed by moving the Z stage to find the OL's WD with Δ close to 0 (step one in Figure 5.8). This method has been used in 1PP-DLW to locate the focal spot on the photoresist surface. Then, the 2PP system calculates a fine factor (*H'*) to adjust the OL position downward until the laser spot is aligned with the photoresist-substrate interface, taking into consideration the thickness of the photoresist and the refractive indices of both air and the photoresist at the wavelength of the femto laser beam (step two in Figure 5.8).

Fine focusing is specifically used to determine how far the laser spot needs to move downward for thicker spin-coated photoresists, ranging from a few microns to several hundred microns in air configurations mode. In "Appendix B: Fine focusing", the description of fine focusing by the 2PP system is provided for better comprehension.

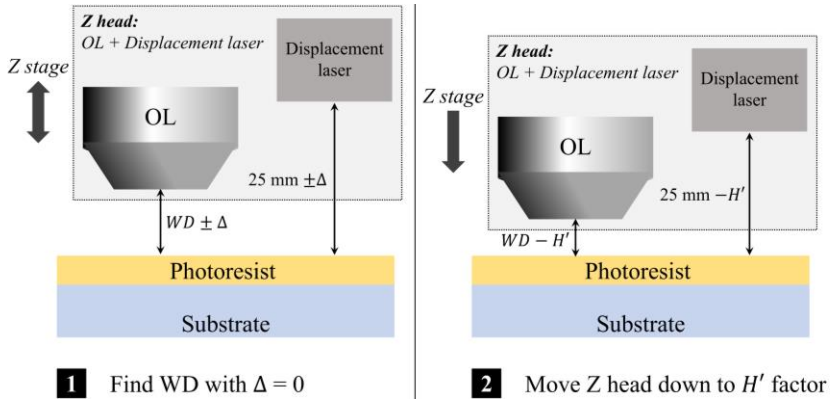

Figure 5.8: Steps for fine focusing in the 2PP system: After determining the working distance (WD) of the objective lens (OL) by moving the Z stage, the 2PP system computes the factor (H') to adjust the position of the OL until the laser spot is correctly positioned at the photoresist-substrate interface.

After fine focusing, 2PP-DLW is performed to polymerize the pattern objects on a substrate. The test grid has been repeated several times on a single substrate to obtain more measurement data. Several substrates with the same parameters have been subjected to different laser beam powers to optimize 2PP-DLW process in SU-8.

Finally, the substrates are baked at 110 °C to complete the SU-8 polymerization processes, then developed with PGMA by immersion, cleaned with 2-propanol, and dried with nitrogen flow, as summarized in "Appendix A: Cleaning and spin-coating processes".

5.2.2. Results

The beam powers required to polymerize SU-8 in 2PP-DLW differ from the optimization values for 1PP-DLW in Section 5.1.2, for several reasons. First, the energy of a photon in near-infrared

(N-IR) is approximately half that of a photon at violet wavelengths [206]. Second, two photons must be simultaneously absorbed to excite the SU-8 photo-initiator molecules. Finally, the spatial and temporal concentration of photons (ultrafast pulsed beam) and high laser intensity increase the probability of absorption. This demands a very powerful laser beam to surpass the absorption threshold within the voxel volume. An average laser power from 1 mW to 160 mW and scanning speeds from 100 µm/s to 1000 µm/s were applied, where 300 µm/s was chosen to analyze the results in this section. Therefore, for this scanning speed and laser power range, polymerized microstructures in SU-8 were observed and summarized in Table 5.2.

Table 5.2: Classification of powers in 2PP-DLW processes at a scanning speed of 300 µm/s.

Average power applied [mW]	**2PP-DLW linewidth resolution [µm]**
1.0 – 88.0	No results were reliable (Un-polymerized)
95.0 – 115.0	< 0.5 (Polymerized)
115.0 – 150.0	> 0.5 (Polymerized)
>150.0	~ 1.0 (Over-exposed)

It has been found that a laser beam power of 95 mW is appropriate to polymerize SU-8 at a speed of 300 µm/s, achieving a resolution of 301.7 nm, as depicted in Figure 5.9. The SEM images were obtained using an electron beam voltage of 4 kV. A 100 nm aluminum layer was deposited on all samples by physical vapor deposition. A complete test grid corresponding to the experiments is depicted in "Appendix C: Results in optimization processes".

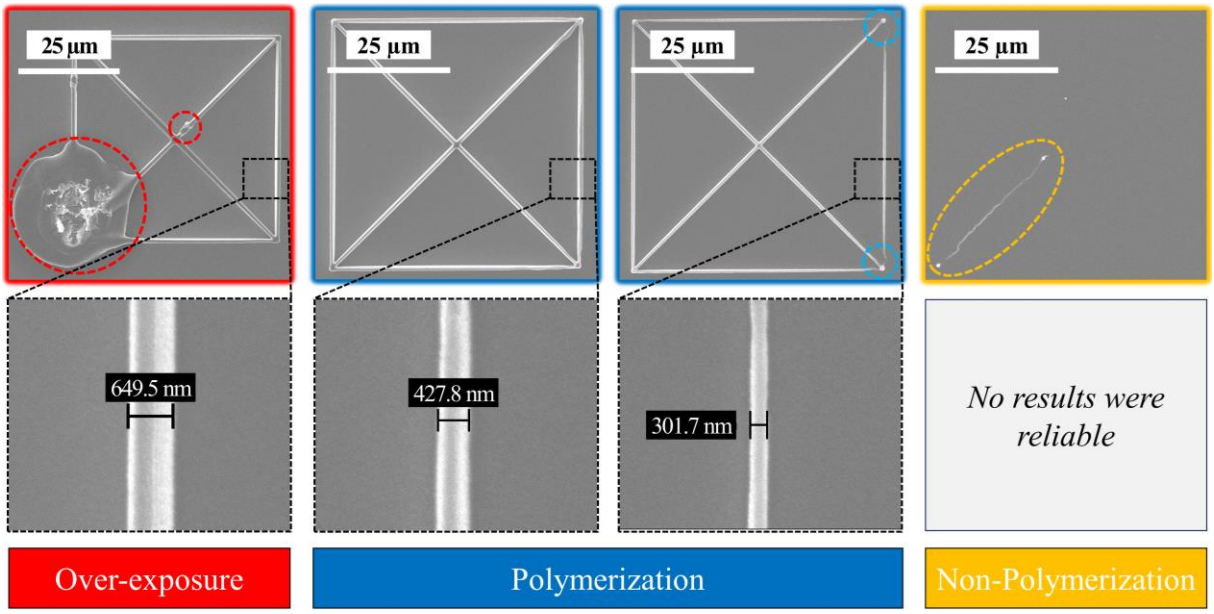

Figure 5.9: SEM images of pattern objects exposed to 95 mW. The measurements obtained on the over-exposed, polymerized, and non-polymerized pattern objects correspond to different scanning speeds for a single test grid in 2PP-DLW processes.

Over-exposure yields unfavorable results with linewidths exceeding 600 nm due to excessive photon absorption, leading to uncontrolled chain reactions of monomer radicals formed within the voxel and extending beyond it. Moreover, at very high exposure times, excessively absorbed energy can lead to bubble formation or even voxel bursting, as illustrated in Figure 5.9, due to non-uniform temperature gradients toward the voxel center. Additionally, reflection effects can cause energy distributions in undesired areas of the SU-8. All these factors reduce the precision and resolution of the microstructures.

Non-polymerization occurs when the absorbed intensity is reduced below the SU-8 threshold, defined as the maximum intensity at $1/e^2$ of the half waist of a gaussian beam [39], [67], [210]. In these conditions, the probability of photon absorption to excite the photo-initiators is very low, consequently failing to initiate propagation of monomer-radicals in the exposed region. Furthermore, optical adjustments in the 2PP system can affect 2PP-DLW processes. For example, misalignment of the field of view (FOV) angle of the galvos can lead to beam clipping at the entrance pupil of the OL. This reduces exposure energy, resulting in non-polymerized areas near the edges of the OL FOV, as illustrated in Figure 5.9 for well-defined polymerized lines.

Figure 5.10 shows three experiments conducted at average powers of 90 mW, 95 mW, and 115 mW at the previously mentioned range of scanning speeds. The measured linewidth undergoes exponential decay with increasing scanning speed for a given power. Linewidths greater than 0.8 µm may exhibit burnt SU-8, whereas widths less than 300 nm may indicate incomplete SU-8 polymerization.

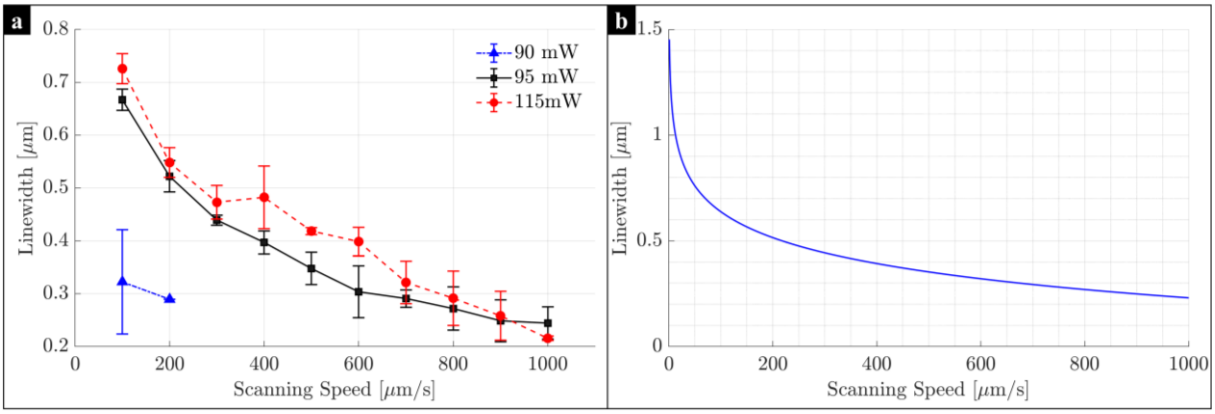

Figure 5.10: a) Linewidths measured at three power values in 2PP-DLW processes. b) Fitted data corresponding to 95 mW.

5.3. SU-8 resolution comparison 1PP vs 2PP

Polymerization in 1PP-DLW is uniform throughout the entire thickness of SU-8 in the experiments carried out, whereas in 2PP-DLW, polymerization is very high within the voxel volume due to the high density of spatially and temporally confined photons. This enables

achieving high resolutions in nanoscale dimensions with appropriate exposure times, where the non-linear matter-light interactions is a dominant factor in SU-8.

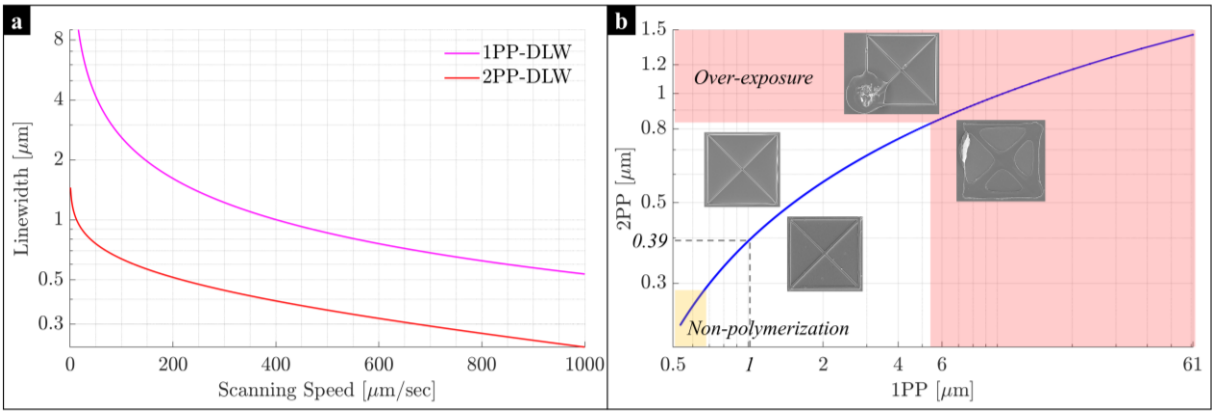

Figure 5.11: SU-8 resolution comparison of the optimization experiments. a) Linewidth of 1PP-DLW vs. 2PP-DLW. b) Resolution relationship between 2PP & 1PP at the same scanning speed of 300 µm/s.

The concentration of photo-initiators in SU-8 strongly absorbs light in the UV and violet light spectrum. In high optical density, the light intensity distribution undergoes exponential decay across the layer thickness as the light penetrates from top to bottom in 1PA. This leads to a limitation in the SU-8 layer thickness, approximately 2 µm in these 1PP experiments.

When the incident light intensity is above the threshold, absorption causes a uniform light intensity distribution along the optical axis (thickness) of the thin SU-8 layer. This also occurs for low optical density interactions explained in Chapter 3. Conversely, very low light intensity decreases until extinction from top to bottom of the layer thickness, leading to non-polymerized SU-8 in the 1PP experiments.

Figure 5.11-a shows the results of linewidth measurements from previously conducted experiments. Both processes were subjected to different laser powers (1.85 µW for 1PP-DLW and 95 mW for 2PP-DLW) due to their absorption conditions, but with the same scanning speeds. This allowed for comparison to observe the resolution difference in SU-8. For example, the average resolution achieved in 2PP-DLW is 0.39 µm compared to 1 µm in 1PP-DLW, highlighting a significant difference in spatial resolution between the two techniques, as depicted in Figure 5.11-b.

The over-exposure and non-polymerization regions indicate that the results are unfavorable for both processes, where the non-polymerization region and the over-exposure region unachievable for extremely low and extremely high times, respectively. Additionally, the relationship exhibits a non-linear trend, while 1PP increases exponentially compared to 2PP. Therefore, it has been demonstrated that 2PP exhibits a logarithmic decrease as:

$$2PP_{res} = a \cdot \log_{10}(b \cdot 1PP_{res}) \tag{5.4}$$

where a and b are experimentally defined resolution factors for different scanning speeds, and average laser powers at given wavelength, independent of the intrinsic properties of the photoresist.

5.4. 2PP-DLW optimization on photoresists

2PP-DLW is widely used for fabricating micro/nanostructures in commercial photoresists other than SU-8, such as the IP-series [93], [106], ORMO series [96], [211], SZ2080 [212], and SCR500 [23], among others summarized by Rajabasadi et al. [11]. Customized photoresists also utilize 2PP-DLW, demonstrating promising results [66], [213]. However, there are no reports on voxel sizes for other types of commercial photoresists, either negative-tone or positive-tone. This section presents optimizations of 2PP-DLW for S1800 series, Epo-Core, and mr-DWL photoresists, including SU-8 (2000 and 6000).

5.4.1. Methods and materials

Cleaned ITO-glass substrates are used to spin-coat photoresists, following the technical protocol for each photoresist from their datasheets, to obtain the desired thickness. "Appendix A: Cleaning and spin-coating processes" summarizes all steps of the spin-coating and baking preparation: photoresist deposition, spin cycle, thickness definition, bake times and temperatures, relaxation times and developing solutions.

S1805 and S1818 positive-tone photoresists as well as SU-8 TF 6002, SU-8 2015, EpoCore 5, and mr-DWL 40 negative-tone photoresists have been used. All of these were obtained from Kayaku Advanced Materials and Micro Resist Technology GmbH [71], [80].

Negative-tone photoresists generate well-defined nanostructures with high resolution upon exposure to a laser beam. The cross-linked polymers produced by the 2PP-DLW process exhibit high resistance, while the unexposed portions are highly soluble in developing solutions [80].

Positive-tone photoresists are efficient in manufacturing hollow structures, requiring relatively low insolation energy and facilitating easy removal of the exposed photoresist during development (breaking the cross-linked polymers by 2PP-DLW process) [71].

A new recipe was configured in LPS software to introduce new polymerization parameters. In this case, n test grids have been created within a single recipe. Each test grid is associated with a single scanning speed, and consists of m pattern objects programmed with different power values.

Figure 5.12 shows the pattern objects to be designed in the LPS software. Figure 5.13, shows the test grids programed in LPS software. In Table 5.3, the applied scanning speeds for all photoresists and average laser powers in these experiments can be observed.

Table 5.3: Processing parameters for photoresists printing.

Photoresist	Scanning speed [µm/s]	Femto laser beam power
S1805	100 – 1600	1.6 – 160 mW
S1818	100 – 1600	
SU-8 TF 6002	100 – 1600	
SU-8 2015	100 – 800	
mr-DWL 40	300 – 2400	
EpoCore 5	20 – 160	

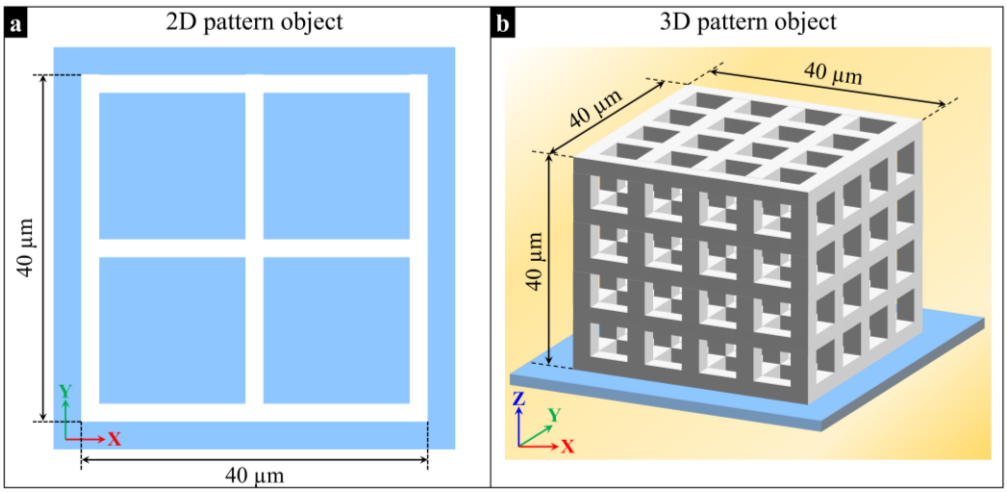

Figure 5.12: 2D and 3D pattern objects to be polymerized for voxel characterization.

For thin layers of spin-coated photoresists, specifically S1805, S1818, and SU-8 TF 6002, the recipe depicted in Figure 5.13 was executed to polymerize 2D pattern objects with sizes of 40×40 µm² (see design in Figure 5.12-a). Meanwhile, for thick layers of photoresist, specifically SU-8 2015, mr-DLW-40, and EpoCore 5, the recipe from Figure 5.13 was reconfigured to program 3D pattern objects with sizes of 40×40×40 µm³ (see design in Figure 5.12-b).

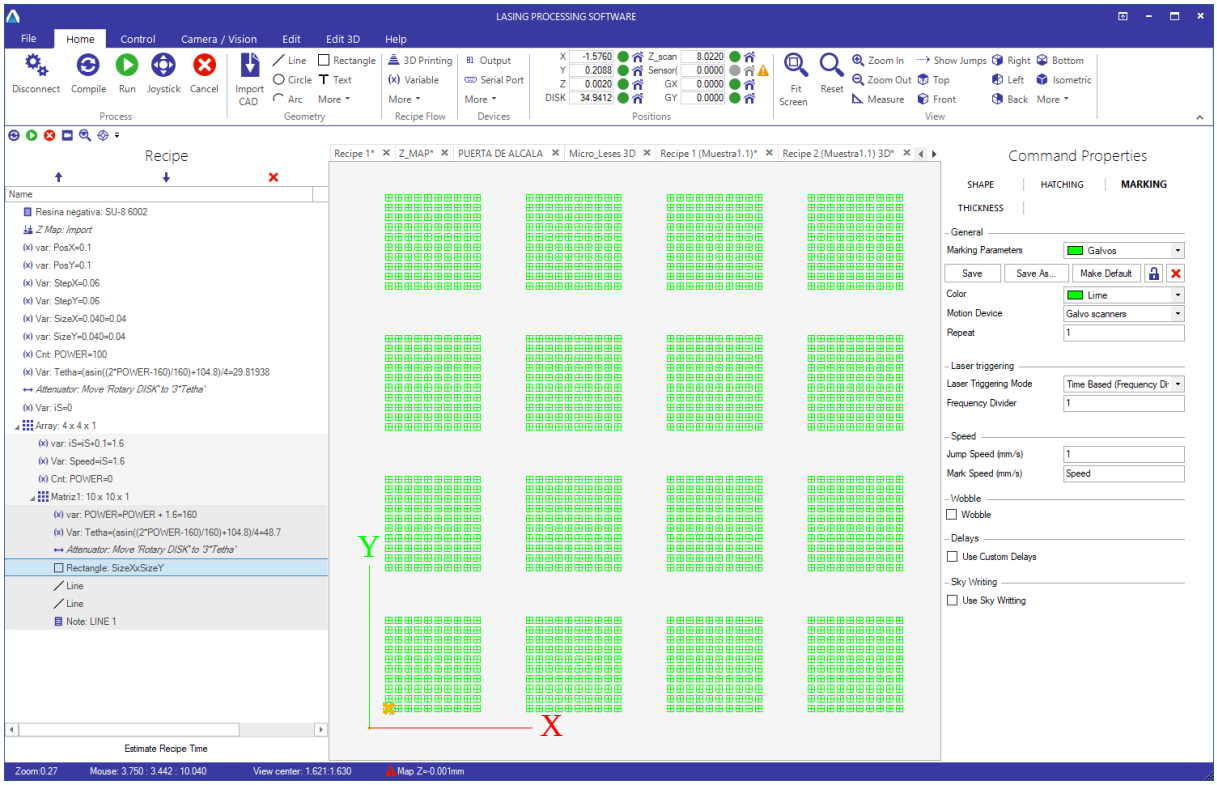

Figure 5.13: Programming and configuration of test grids on the LPS software front panel.

After the 2PP-DLW process, the photoresists were post-baked, developed, and cleaned to obtain the solidified microstructures. Negative-tone photoresists were developed with PGMEA or mr-DEV 600 developers, while positive-tone photoresists are developed with a microposit developer.

5.4.2. Results

The 2PP-DLW processes have shown positive results in all experiments, with well-defined microstructures in both 2D and 3D.

Different polymerization and over-exposure thresholds have been identified for each used photoresist, depending on their intrinsic properties. For instance, S1805 and S1818 are the same material (photoactive compound and monomers), both highly sensitive to radiation [214]. However, the measured thresholds vary with thickness under standard spin-coating conditions (viscosity): 0.5 µm in S1805, and 1.8 µm in S1818. In comparison, S1818 has more photon-absorbing material, making it more prone to burning at high powers levels under the same scanning speed conditions as S1805. Nevertheless, measured linewidth results are nearly identical for both photoresists.

SU-8 TF 6002 and SU-8 2015 cannot be compared because they differ in their formulations, despite their common Epoxy base, such as viscosity, additives, and reactive components to exposure light. Therefore, exposure times vary in polymerization and over-exposure thresholds.

The microstructures obtained on each substrate were metallized with a 50 nm thick aluminum deposition. Subsequently, the 2D and 3D pattern objects were analyzed using a SEM (EVO 10, ZEISS group), applying an electron beam voltage of 5 kV for more sensitive photoresists in Figure 5.15, Figure 5.16, and Figure 5.17, and 8 kV in Figure 5.18 and Figure 5.19 (for less sensitive photoresists).

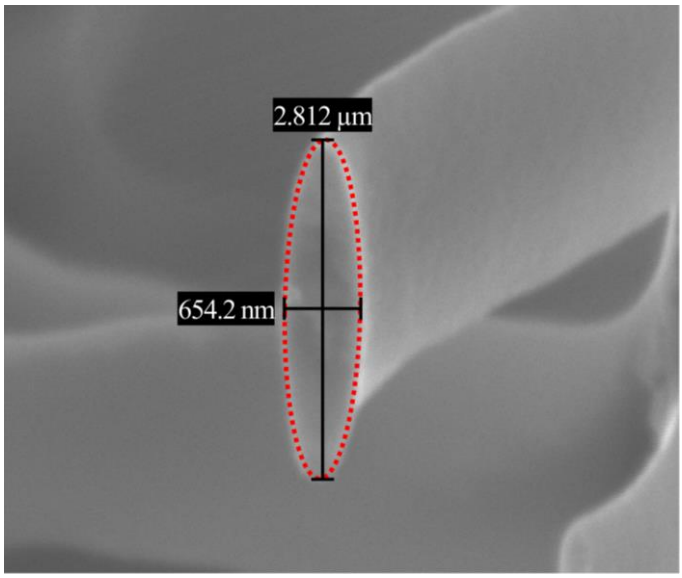

Figure 5.14: Measurement of lateral and axial voxel dimensions in 2PP. The lateral voxel size (xy-plane) is 654.2 nm, and the axial voxel size (z-direction) is 2.812 µm.

The linewidths of the polymerized 2D pattern objects have been measured in all experiments and represent the sizes of xy sectioned voxels. In contrast, the z-voxel has been obtained by measuring the height of polymerized lines in negative-tone photoresists. The measured polymerized lines in 3D pattern objects must be separated from the ITO-Glass surface and supported horizontally by vertical micro-pillars, each 40 µm high at both ends and the center, to achieve well-defined microstructures and obtain an accurate z-voxel measurement, as depicted in Figure 5.18-a and Figure 5.19-a.

The experimental voxel data versus laser power is compared with the results from numerical integration for curve fitting. Error bars represent the standard deviation of the averaged linewidths in the xy-, and z-voxel to obtain adjusted data representing the 3D voxel size trend across the entire power range for each scanning speed. An example of voxel size is depicted in Figure 5.14, where the 2PP-DLW process was carried out within negative-tone photoresists.

Within the non-polymerization region (yellow region in the plots), no polymerized lines have been observed. Additionally, near the edge of this region, polymerized lines have been evident but were not sufficiently vertical to be measured. On the other hand, within the over-exposure region (red region in the plots), voxel bursts have occurred, although not uniformly across the polymerized pattern objects (e.g., see Figure 5.9).

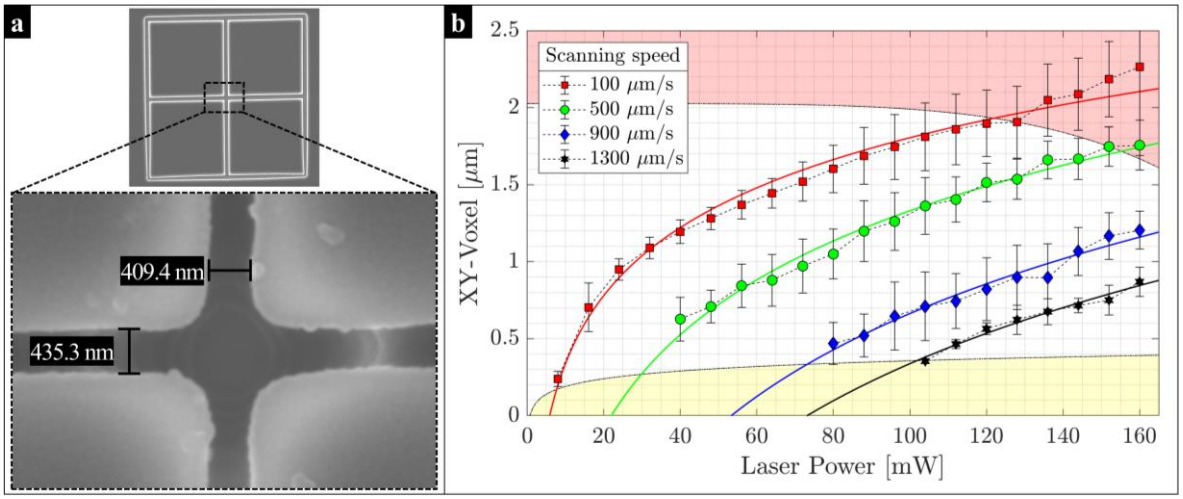

Figure 5.15: Experimental data of the S1805 photoresist optimization. a) SEM images of 2D pattern object polymerized. b) xy-voxel vs. laser power.

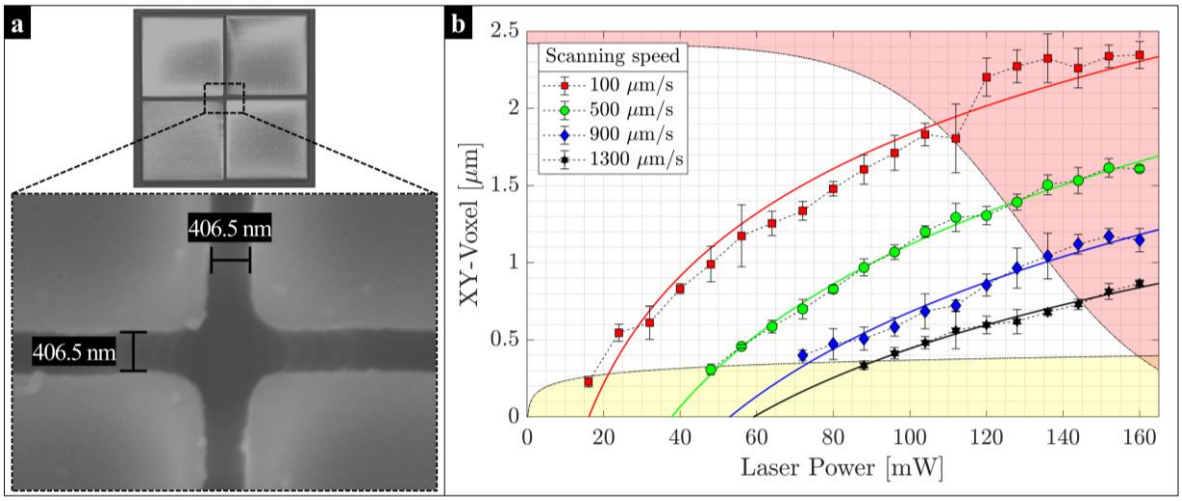

Figure 5.16. Experimental data of the S1818 photoresist optimization. a) SEM images of 2D pattern object polymerized. b) xy-voxel vs. laser power.

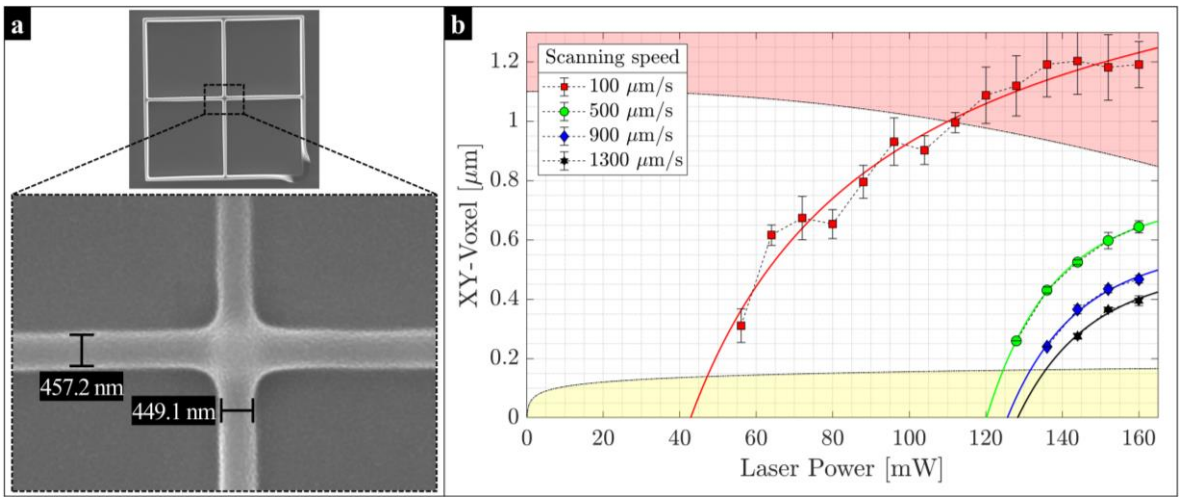

Figure 5.17: Experimental data of the SU-8 TF 6002 photoresist optimization. a) SEM images of 2D pattern object polymerized. b) xy-voxel vs. laser power.

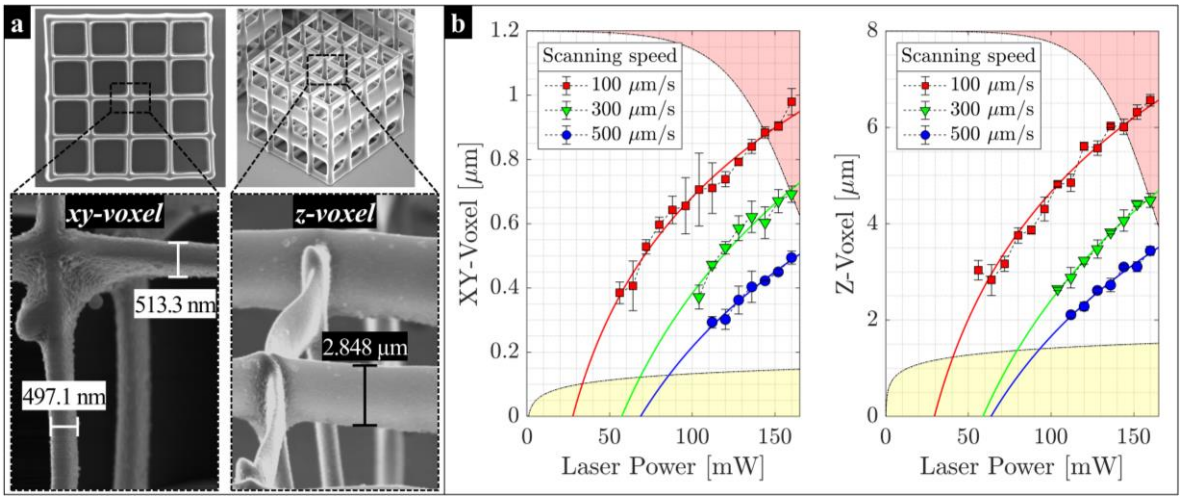

Figure 5.18: Experimental data of the SU-8 2015 photoresist optimization. a) SEM images of 3D pattern object polymerized. b) xy- and z-voxel vs. laser power.

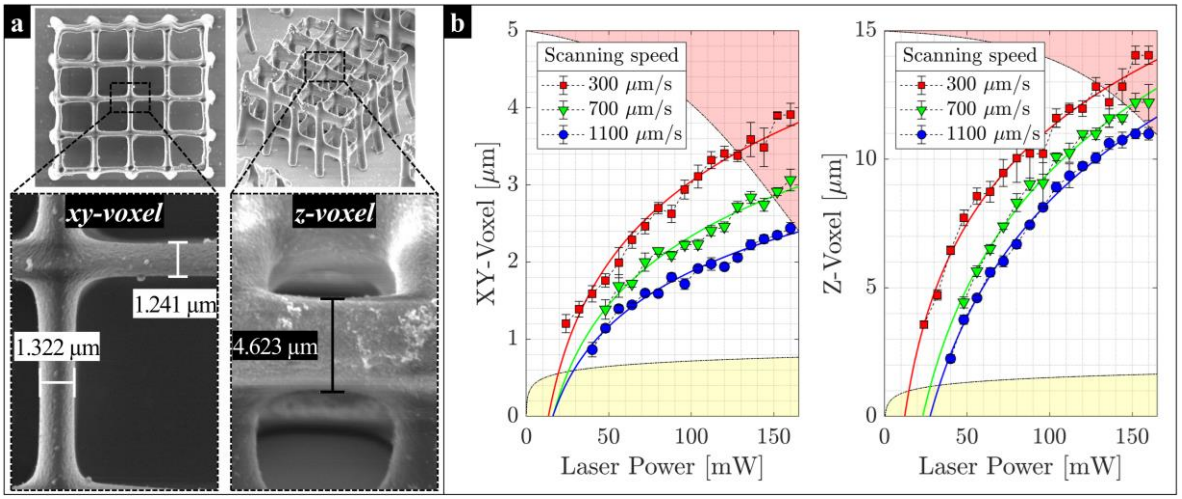

Figure 5.19: Experimental data of the mr-DWL 40 photoresist optimization. a) SEM images of 3D pattern object polymerized. b) xy- and z-voxel vs. laser power.

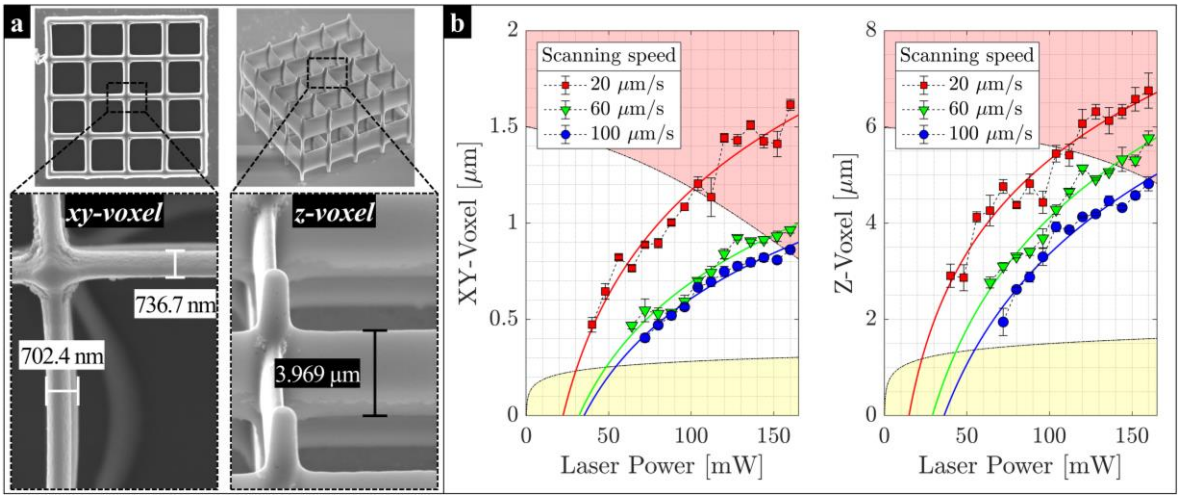

Figure 5.20: Experimental data of the EpoCore 5 photoresist optimization. a) SEM images of 3D pattern object polymerized. b) xy- and z-voxel vs. laser power.

The gathered experimental data show that most of the photoresists experienced voxel bursting. This occurred because the exposed photo-initiators absorbed excessive photon energy beyond what they could withstand during the 2PP-DLW process, except for mr-DWL 40. This is because it is a chemically amplified photoresist, robust, and optimized for optical applications [80].

mr-DWL 40 exhibits very large linewidths without experiencing voxel bursting at high powers from 100 µm/s. The intrinsic properties of the photoresist (high absorption or scattering) cause excessive energy distributions, resulting in polymerization outside the voxel. Additionally, the high concentration of photo-initiators increases the probability of photon absorption, leading to uncontrolled polymer bonding. In contrast, EpoCore 5 shows unpolymerized microstructures at scanning speeds higher than 150 µm/s. To avoid this, the scanning speed was decreased (i.e., higher exposure time) to obtain reliable polymerized linewidths, avoiding burnt voxels during experiments at speeds starting from 20 µm/s. Therefore, the over-exposure edge in mr-DWL 40 and EpoCore 5 photoresists has been represented as a sigmoidal distribution ($xyz\text{-}voxel/(1 + exp\,\{\alpha(x - \beta)\})$) of the maximum permissible voxel size with increasing scanning speed for manufacturing nanostructures using the maximum available laser beam power. This edge represents a limit value that can be exceeded without considering the resolution of microstructures with extremely elongated features.

In “Appendix C: Results in optimization processes”, all SEM measurements of the polymerized 2D and 3D pattern objects from the optimization experiments conducted in this chapter can be seen. Additionally, characterized xy- and z-voxels over a wider range of scanning speeds for all photoresists are presented in “Appendix D: Voxels characterization”.

5.5. Associated challenges of the 2PP system

During the commissioning of the 2PP system, several challenges were encountered that hindered the optimization of nano-positioning control systems and laser beam synchronization. In its first phase, the system was consisted of:

- A non-motorized linear stage for manual focusing.
- A controller for two linear axes.
- Piezoelectric stages for nano-positioning in X and Y.
- An acousto-optic modulator (AOM) for beam control.

Additionally, limitations were identified, including instability caused by external vibrations, defocusing, and the lack of micrometric control, which negatively impacted direct laser writing (DLW) processes.

5.5.1. Improvements Implemented

1. Focus Optimization

The manual focus with the non-motorized linear stage made it difficult to maintain precision between substrates. To address this, a 25 mm micrometric motorized linear stage was installed on the Z-axis, complementing the existing Z piezoelectric stage. This allowed for automatic focus adjustment and significantly improved the lithography processes at the substrate-photoresist interfaces.

2. Controller Scalability

The integration of additional motorized stages made the initial controller insufficient, as it could not manage multiple axes. It was replaced with a higher-capacity controller capable of managing up to 8 linear or piezoelectric axes, enabling the integration of more advanced nano-positioning systems.

3. Replacement of Piezoelectric Axes

The piezoelectric stages exhibited synchronization issues with the laser beam at speeds over 100 µm/s, affecting repeatability and causing errors in microfabrication. These were replaced with galvanometric mirrors, which provide nanometric positioning with low inertia, eliminating synchronization problems. This change allowed for an increase in lithography speed up to 2.3 mm/s in photoresist like mr-DWL 40.

4. Laser Beam Control Improvements

The initial acousto-optic modulator (AOM) had insufficient efficiency, delivering only 47% of the laser power and limiting the maximum focus power to 78 mW. It was replaced with a higher-efficiency AOM, resulting in an 85 % increase in power, reaching a maximum focus power of 160 mW.

5.5.2. Proposals for the Second Phase

To develop a fully commercial 2PP system, the following aspects must be addressed:

1. Structural and Stability Improvements

Implement structures designed for optical microscopy or metal alloys resistant to vibrations and thermal expansion.

2. Resolution and Focus Optimization

Incorporate immersion objective lenses that allow for automatic changes without compromising focus quality or the optical path.

3. Laser Power Increase

Replace the current laser with one of higher capacity that can process low-sensitivity materials and expand the system's material database.

4. Field of View Expansion

Relocate the galvanometric scanners closer to the objective lens to expand the field of view, currently limited to 40 µm.

CHAPTER 6

6. Results: Manufacturing of 2D sub-micrometric structures

In recent decades, two-photon polymerization (2PP) has become the most attractive technique for producing functionalized devices [210]. Usually, these are produced with specific customized design features for their application fields. For example, nano-grids for manipulating THz waves in spectroscopy [215], aligned ridges in neural models [216], optical elements for manipulating light [217], [218], [219], and surface patterning for liquid crystals (LC) devices [93].

This chapter presents arbitrary surface alignment in complex patterns on thin layers of negative-tone and positive-tone photoresist to create patterned polarizers in dye doped LC, which is one of the many applications that can be achieved using 2PP direct laser writing (2PP-DLW). The assembled cell based on nematic LC doped with black dichroic dyes are assessed employing additional standard polarizers.

6.1. An example of 2PP application: Liquid crystal alignment

LC alignment has been carried out for a wide range of applications in optical devices [220]. Surface alignment is commonly employed to control the LC molecular orientation [221]. Any alignment method that results in aligned LC or polymerized reactive mesogen films may serve in various applications, such as spatial geometric phase modulators [222], since the alignment layer provides precise control of 2D and 3D molecular orientation in LC cells [223]. Adding dichroic dyes or fluorescent dyes to the LC opens up for more applications [224], [225], [226].

The 2PP-DLW technique may be employed for curing photoresists and creating microstructures that align LCs [133], [227]. 2PP-DLW enhances the dimensional characteristics of 2D and 3D microstructures with nanometric resolution [9], [125].

2PP-DLW has been used to study the behavior and quality of LC alignment surfaces [93], [228], aiming to enhance the optical properties of cholesteric LCs [229] and explore innovative techniques for alignment in 3D structures in LC cells [227], [230].

Anchoring and periodicity evaluation of nematic LC alignment surfaces has been carried out using 2PP-DLW to create complex patterns on thin layers of commercial negative-tone photoresists [93], and even on titanium layers on glass substrates [231]. A compartmentalized

alignment method for polymeric ribbons in LC has been developed [232], allowing the creation of relief gratings on surfaces. This method enables the production of arbitrary configurations of curved shapes and checkerboard patterns in microstructures.

2PP-DLW has proven instrumental in maximizing the capacity to modify the morphological geometry of LC structures [233]. Notably, multi-layered LC cells (2-3 layers) have been designed and surface-aligned to create 3D spatial light modulators, resulting in significantly improved response times when compared to conventional single-layer counterparts [134]. A compact and transmissive multi-layer polymer-based LC device with 3D switching capabilities has been developed for generating holograms through voltage-induced modulation [228]. Finally, configurable patterns for image encryption and encoding through 2PP-DLW in LCs have been used in authentication and security applications. For instance, a rewriting technique employing 2PP-DLW and applied voltage to encode the features of a fully assembled polymerizable LC was employed [135]. This method ensures the local orientation of the director along the laser beam direction at different voltage amplitudes.

Surface alignments are involved in many applications, particularly in the context of the geometric phase known as the Pancharatnam-Berry phase. Several contributions have been involved to create interesting planar optics devices. For example, compact see-through near-eye displays [234], augmented reality (AR) near-eye displays based on Pancharatnam-Berry phase lenses [235], holographic cholesteric LC reflective lenses with high efficiency and polarization selectivity [236], coexisting superstructures with opposite chirality for Pancharatnam-Berry phase inversion in cholesteric LCs (generating reflective optical vortices) [237], and 2D geometric phase LC diffraction gratings (generating arrays of equi-energetic optical vortices) [238]. These devices, many of which are already employed in the industry are costly manufactured using conventional techniques [239], can be produced with 2PP-DLW technique, at a lower cost with increased reliability of the complex alignment in LC [108].

6.1.1. Liquid crystal aligning methods

There are various methods of obtaining LC alignment, i.e., homeotropic, homogeneous, pretilted and intermediate alignment.

Homeotropic alignment –i.e., an alignment where molecules align perpendicularly to the surface– may be achieved in several different ways. For example, coating the surface with a surfactant such as lecithin, which can be dissolved in ethanol or 2-propanol. The lecithin layer may be created by simply wiping a cloth soaked in the solution over the surface, leaving the polar hydrophilic parts adhered to the substrate and the hydrophobic tails perpendicular to the surface. Consequently, the LC molecules align parallel to the hydrophobic tails, i.e., aligning vertically with the surface [240]. Conventional dip- or spin-coating is adequately applied in labs for hydrophobic polyimide alignment [241].

Homogeneous alignment –i.e., an alignment where molecules align parallelly to the surface in a specific direction– can be carried out with various methods to align the LC molecules planarly on substrates. Rubbing is a commonly used mechanical method to align LC. A polyimide layer is coated onto a substrate and then uniformly rubbed using a roller wrapped with a velvet cloth. The LC that come into contact with the polyimide adopt a degenerative azimuthal angle of the director within the plane of the substrate, i.e., in the direction in which the polyimide is rubbed [242]. Rubbing can also be accompanied by a surface pretilt, known as pretilted alignment, depending on the direction of the rubbing process, the type of polyimide used, and the LC. The pretilt angle is generally between 0° and 10° [221]. Alternatively, evaporation is a non-contact alignment method. It involves the oblique deposition of silicon oxide using a vacuum chamber. The uniform alignment direction is achieved by defining the azimuthal angle of the evaporation direction [243]. Thirdly, Photo-alignment is a common method used to generate customized patterns on alignment surfaces [244]. This technique employs polymers sensitive to ultra-violet (UV) radiation. When the polymer layer is exposed to polarized UV light, it becomes anisotropic, thereby inducing homogeneous alignment.

Intermediate alignment is a method that combines homeotropic and planar alignment by employing various strategies. For example, creating a solution of two polymers that can individually form regions separated in phases through solvent evaporation [245]. Another common method involves creating patterned alignments. This non-uniform alignment is achieved by manipulating the surface to generate patterns with varying azimuthal alignment directions within either a homeotropic or planar alignment layer. Photo-alignment can create patterns on a single surface using a mask [246], [247], while a focused UV laser beam on the substrate creates smaller regions capable of aligning LC in the direction of the recording beam [248]. Therefore, one-photon polymerization DLW (1PP-DLW) can produce complex patterns without a mask, whereas 2PP-DLW adds enhanced features introduced earlier, as the central focus of this chapter.

Additionally, complex surface alignment of LC has involved combining photo-alignment and 2PP-DLW. In this case, a uniform UV exposure has been used to orient a liquid crystalline conjugated polymer, and 2PP-DLW has been employed to write patterns in a dye, successfully transferring patterns to the film through thermotropic reorientation and solidification at room temperature [133]. These advancements underscore the versatility and potential of 2PP in the realm of surface alignment and LC-based device manufacturing.

6.1.2. Liquid crystal aligning by microgrooves

LC alignment by 2PP-DLW allows for the fabrication of efficiently aligned microgrooves. The desired configuration of the microgrooves causes them to behave as effective physical guides for orientation [93]. Periodicity can also be used to achieve a balance between elastic energy

and anchoring of LC molecules [249]. Furthermore, depth and spacing can provide robust alignments (potential for LC reorientation from other alignment directions towards the microgroove direction) [250].

Therefore, the period of the microgrooves on a surface is a crucial factor that affects the direction and alignment quality. By controlling the period and depth of the microgrooves, the alignment of LCs can be designed and manipulated to create arbitrary polarizers with practical contrast [241]. In this chapter, periodic microgrooves of 1 µm with spacing and microgrooves depth half the period have been designed, as shown in Figure 6.1. Moreover, pretilted azimuthal angles of the microgrooves enable control over molecule orientations to modulate transmitted light in a complex pattern of a LC cell.

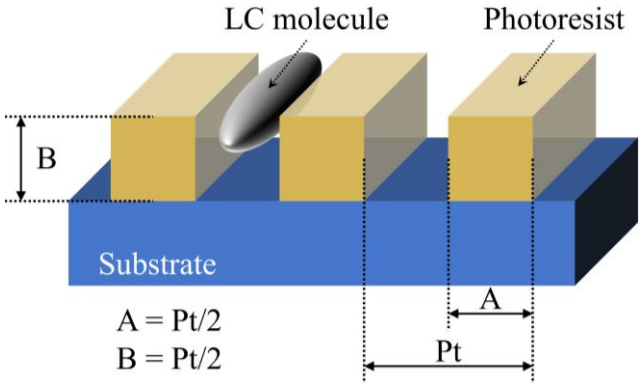

Figure 6.1: Microgroove requirements in LC surface alignment by 2PP-DLW, where B is the thickness of the photoresist or microgrooves depth, A is the width of microgroove or linewidth, and Pt is the period of the microgrooves.

6.2. Manufacturing methods and materials

The patterned alignment surfaces were prepared by spin-coating photoresist on commercial 0.7 mm-thick glass ITO-coated substrates. The indium-tin oxide (ITO) layer is nominally 130 nm-thick and provides good and uniform adherence of the photoresist.

Prior to spin-coating, a meticulous cleaning process was carried out. First, the substrates were cleaned with lint-free cloths and immersed in 2-propanol/acetone for 1 minute, followed by ultrasonic cleaning in deionized water for 30 minutes. They were then rinsed with deionized water, dried with a nitrogen flow, baked at high temperature (200 °C) for 120 minutes, and finally placed under deep ultra-violet light (UVO-Cleaner) for 10 minutes to eliminate any organic material on the substrate surface. This step makes the surface more hydrophilic, improving the adhesion of the deposited photoresist.

Photoresists were drop-casted onto the ITO-glass substrate for spin-coating. A volume of approximately 1 ml of photoresist for each 25×25 mm² substrate was deposited manually in the center of the substrate using graduated pipettes. Two different types of photoresists were used:

SU-8 TF 6002 (SU-8) negative-tone photoresist and Shipley 1805 G2 (S1805) positive-tone photoresist, both obtained from Micro Resist Technology GmbH.

The required thickness of the photoresist layer ($B = 0.5$ µm) must be at least five times less than the ideal voxel depth (axial resolution) along the optical axis as described by:

$$z\text{-}voxel = \frac{2\lambda\eta}{NA^2} \tag{6.1}$$

where NA is the numerical aperture of the objective lens (OL), and n is the refractive index (n_{air} =1.00027, $n_{SU\text{-}8}$ =1.58098, and n_{S1805} =1.62451) at the wavelength of the femtosecond laser (femto laser) in the 2PP system.

The SU-8 was mixed with cyclopentanone (C_5H_8O) solvent to reduce the viscosity of the photoresist. A mixture containing 75 wt% of C_5H_8O was used to achieve a thickness of ~0.5 µm, as shown in Figure 6.2. To get this thickness the solution was ramped slowly at 100 rpm/s up to 500 rpm, where it spins for 5 seconds. Subsequently, it was ramped up at 500 rpm/s to 3000 rpm and spun for 30 seconds to achieve the desired thickness.

S1805 is specifically designed to achieve a thickness of 0.5 µm, according to the technical datasheet [71]. Therefore, it was spin-coated as supplied at 3500 rpm for 30 seconds, with acceleration ramps of 500 rpm/s. Finally, the photoresists were soft-baked at 115 °C for 1 minute to get it ready for the 2PP-DLW. Spin-coating and baking parameters of both photoresists are summarized in Table 6.1.

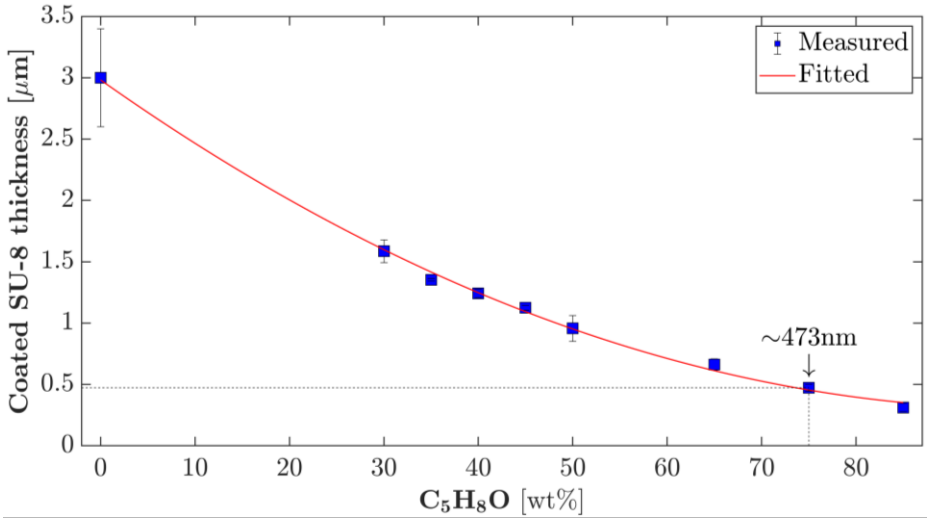

Figure 6.2: Thickness of SU-8 photoresist spin-coated onto an ITO-glass substrate.

The LC surface alignments were fabricated by adjusting the 2PP system to setup the printing parameters to obtain the desired voxel diameter (xy-size) for the linewidth ($A = 0.5$ µm) requirement in this 2PP-DLW process. Hence, the femto laser beam with a wavelength of 780 nm was focused on the air-photoresist interface using a 50× OL with an NA of 0.80, as depicted in Figure 6.3.

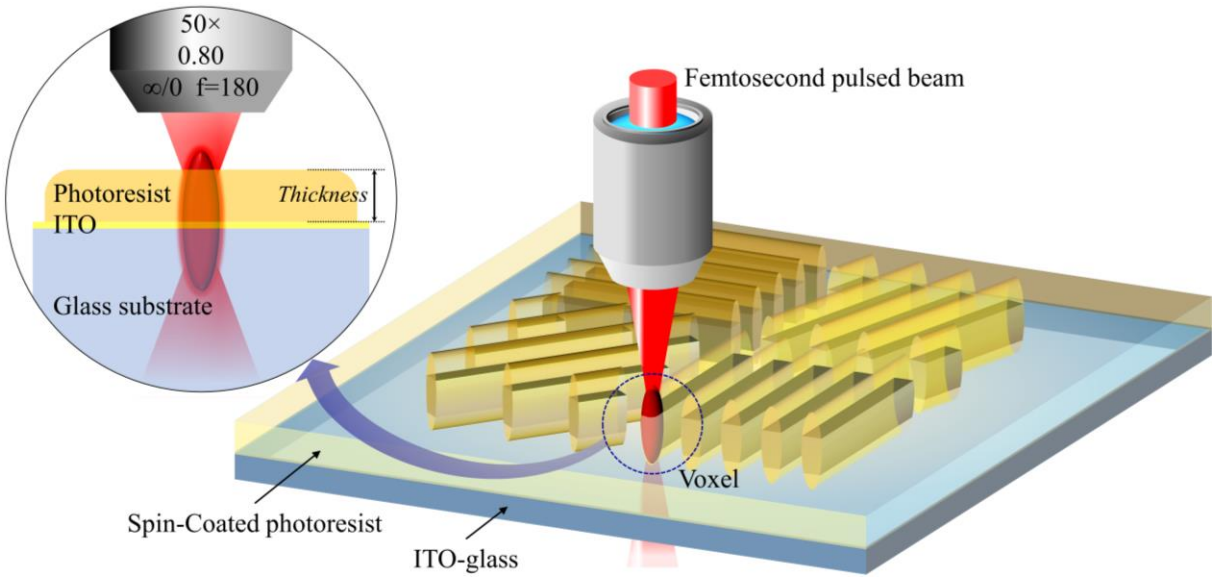

Figure 6.3: Schematic illustration of photoresist orientation using the two-photon polymerization direct laser writing (2PP- DLW).

SU-8 has previously been used for LC alignment [232], [233]. Upon polymerization, it generates well-defined 3D microgrooves with high resolution and high aspect-ratio once exposed to the laser beam [72], [75], [251]. It exhibits high resistance to solvent, while the unexposed portion is highly soluble in developing solutions. S1805 is efficient in manufacturing hollow lines, requiring relatively small insolation energy and easy removal of the exposed part of the material when developed [71].

The S1805 results in structures inverse to those generated with SU-8 when the same exposure pattern is used. Both may serve as direct aligning pattens or as master molds for creating, via nanoimprint, LC alignment surfaces in other materials [4], [252]. Both photoresists share the property of being practically transparent in the visible spectrum [214]. Furthermore, SU-8, is thermally stable [9], [71].

The laser exposure energy was optimized to match the polymerization threshold levels by adjusting the voxel travel speed in the XY-plane and controlling the average laser power. This process ensures the generation of truncated voxels for both photoresists, as depicted in Figure 6.3. Optimization steps are described in Chapter 5 to ensure the appropriate polymerization of the entire thickness of the photoresist.

To execute the 2PP-DLW process, the designed patterns were loaded and programmed on Lasing Processing Software (LPS) based on programmable Recipes. LPS software allows patterning parameters on photoresists in function of scanning speed and average laser power.

After the polymerization, SU-8 was post-baked at 115 °C for 4 minutes in order to complete the cross-linking process. The S1805 does not need any post-bake, although it can be used to

harden unexposed photoresist before the developing process. The post-exposure processes were determined empirically and summarized in Table 6.1.

Table 6.1: Spin-coating and baking parameters of photoresists and polyimide deposition.

Material	Spin-coating parameters				Baking parameters	
	steps	Speed (rpm)	Acceleration (rpm/s)	Time (sec)	Soft-bake	Post-bake
SU-8 + C5H8O	1/2	500	100	5	1 minute at 115 °C	4 minutes at 115 °C
	2/2	3000	500	30		
S1805	1/1	3500	500	30	1 minute at 115 °C	4 minutes at 115 °C
PI2525	1/2	500	100	5	5 minutes at 80 °C	60 minutes at 250 °C
	2/2	2500	500	30		

Finally, the substrates were developed by submerging them into photoresist developer (PGMEA developer for SU-8 and Shipley developer for S1805) for 10 seconds and 30 seconds respectively, then cleaned for 30 seconds (2-propanol for SU-8 and deionized water for S1805) and dried using nitrogen flow.

6.3. Development of liquid crystal patterned polarizers

Alignment patterns with a pitch (Pt) of 1 µm and a linewidth (A) of ~0.5µm in 25×25 µm² area per pattern, as shown in Figure 6.4, are employed. The chosen microline aspect ratio, width and pitch has previously been employed in the group for nano-imprint alignment of LC. The microlines of a printed pattern were generated using vectorial plotting at any given alignment angles (φ) resulting in nicely define structures as seen in Figure 6.5 and Figure 6.6.

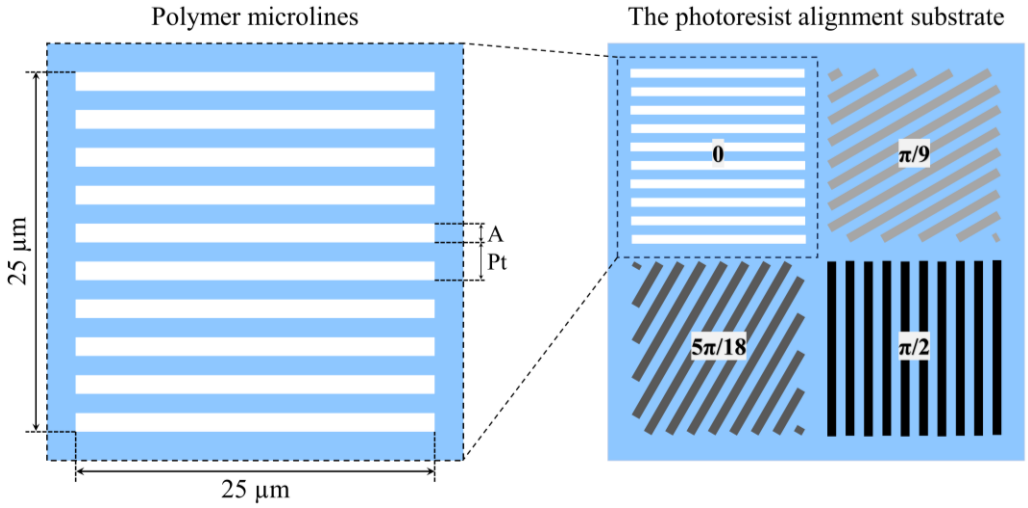

Figure 6.4: Definition of pitch (Pt) and linewidth (A).

To assess the fidelity of the polymerized surface, the actual widths of the fully resolved microlines/microgrooves were previously measured using electronic microscopy. In order to

analyze the actual topology of the alignment layer, a 100 nm thick layer of gold was deposited on all polymerized photoresist, and an electron beam voltage of 8 kV was applied.

The photoresist exhibited perfectly polymerized microlines with a repetitive periodicity (~1 µm) in all directions, as depicted in Figure 6.5 and Figure 6.6. In Figure 6.7, perfectly defined microlines are observed in the printing directions of 0 and $\pi/2$ radians (90°) on both photoresists, while in the other directions, microlines exhibit slightly less perfection. The scanning electron micrographs show patterns with microgrooves of 0.5 µm width and polymer microlines with a depth of 0.5 µm, and a pitch of 1 µm. These structures enable the arbitrary surface alignment of patterned LC. Fully patterned surfaces in both photoresists were measured for polymerized microline/microgroove patterns, as shown in "Appendix E: Results in surface alignment".

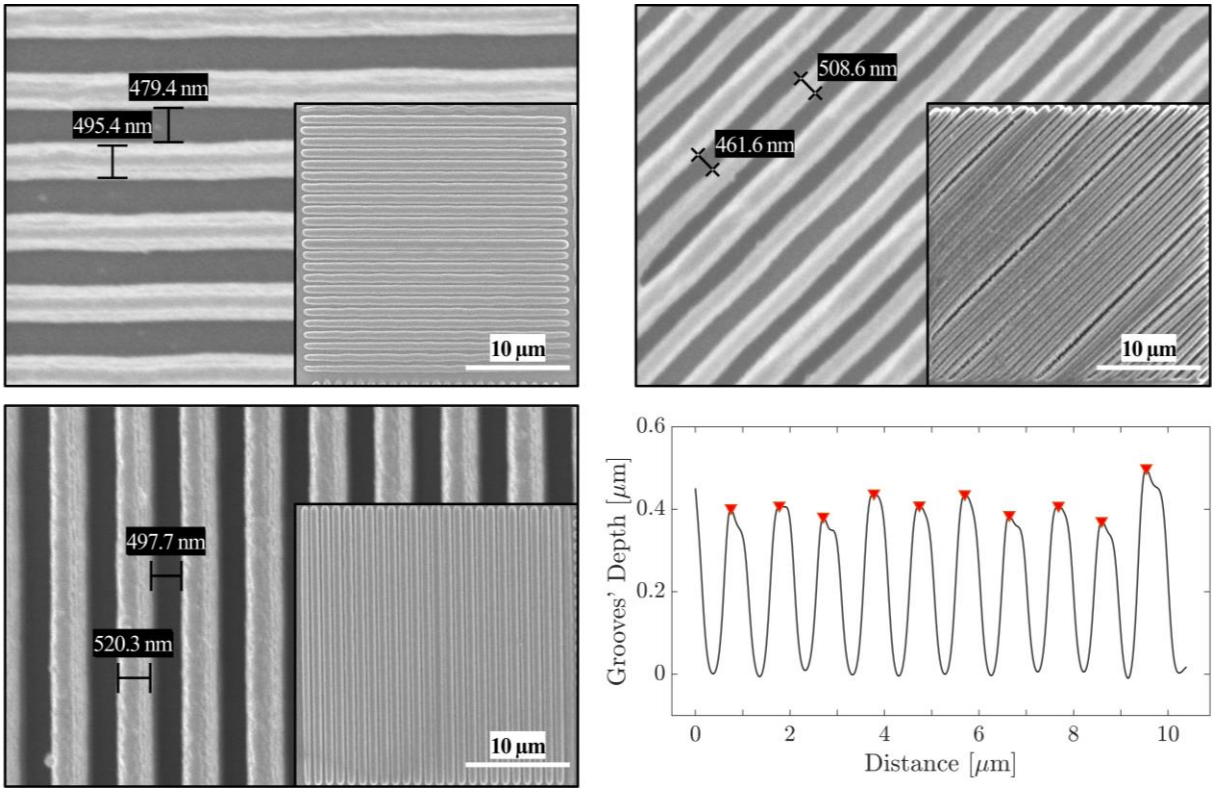

Figure 6.5: Scanning electron micrographs of polymerized microline patterns in directions of 0, $2\pi/9$ (20º) and $\pi/2$ (90º) on SU-8 photoresist.

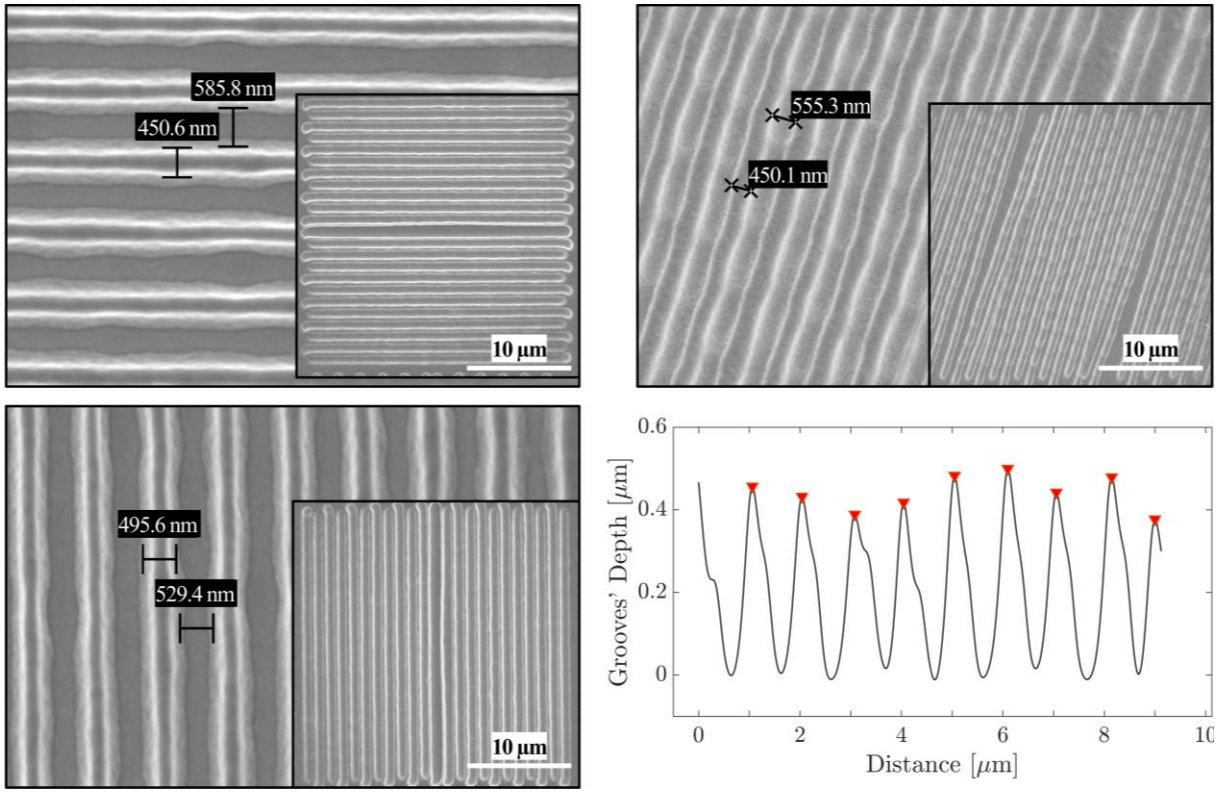

Figure 6.6: Scanning electron micrographs of polymerized microgroove patterns in directions of 0, $7\pi/18$ (70º) and $\pi/2$ (90º) on S1805 photoresist.

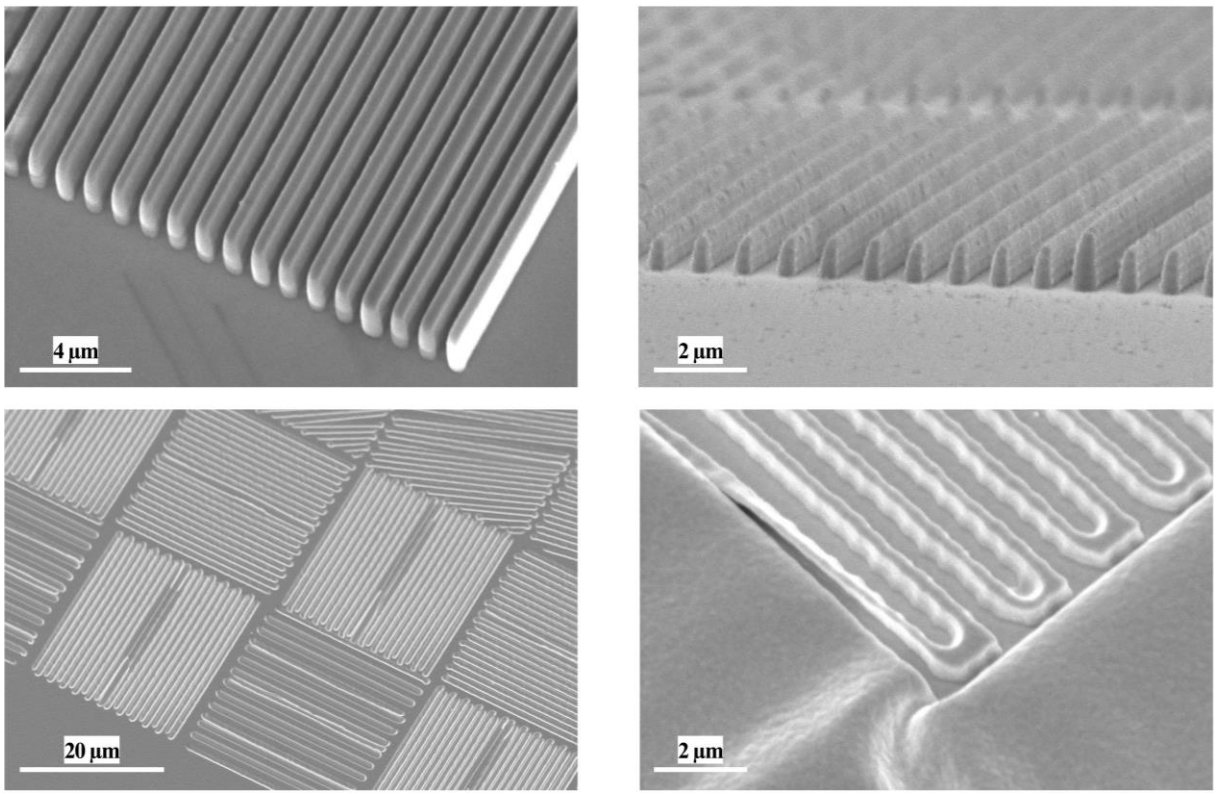

Figure 6.7: Scanning electron micrographs in 3D visualization of the printed patterns for both photoresists (top: SU-8, bottom: S1805).

6.3.1. Patterned polarizer design

Patterned polarizers have been prepared with the 2PP-DLW printing microlines and microgrooves at different angles defining the molecular orientation (φ). Nematic LC (5CB, Merck) doped with 2.0 wt% of black dichroic dye (D8, Mitsui Chemical Inc.) was used. LC cells were fabricated by assembling two ITO-glass substrates. One of the substrates was patterned using 2PP-DLW, while the other was coated unidirectionally rubbed polyimide (PI2525) to achieve a homogeneous planar orientation. The polyimide was spin-coated to obtain an average 200 nm uniform layer thickness, followed by soft-baking at 80 °C for 5 minutes, and cured by post-baking at 250 °C for 60 minutes. The spin-coating conditions for all aligning surfaces are listed in Table 6.1.

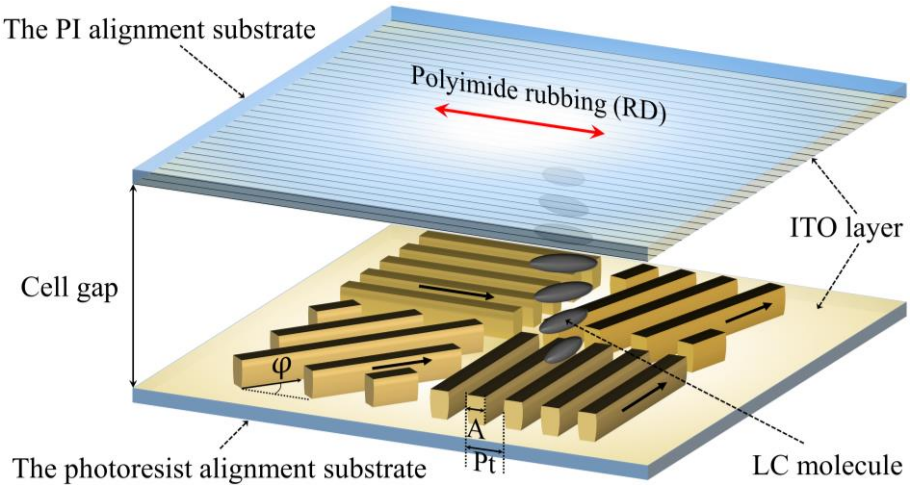

Figure 6.8: Representation of an assembled LC cell.

A simple cell structure with an LC alignment pattern is shown in Figure 6.8, where 2PP-DLW printed microline directions are shown on the lower substrate, while the polyimide rubbing direction is indicated on the top substrate. The 2PP-DLW aligned LC molecules, parallel to the microgrooves in the lower substrate, and the LC molecules aligned parallel to the polyimide rubbing direction on the top will generally cause twist orientations of the LC in different patterns of the cell. This configuration resembles to some extent a conventional twist-nematic cell [253], although the device is actually a guest-host system [254].

The cell gap was determined by silica bead spacers of 14 µm, which must obey the Mauguin condition for the thickness of the LC cell, where:

$$\frac{2d\Delta n}{\lambda} \gg 1 \Leftrightarrow \frac{\lambda}{2} \ll d\Delta n \tag{6.2}$$

where d is the cell thickness and $\Delta n = n_e - n_o$ is the birefringence of LC 5CB at the wavelength of light incident on the LC cell, in this case within the sensitive range of the human eye.

The cells were filled with the LC and sealed and examined under a polarized microscope (MDi8, Leica) equipped with a digital camera (D3400, Nikon) and standard linear polarizers.

6.3.2. Results in SU-8

Cells with dichroic dye-doped LC, mounted as sketched in Figure 6.8, scale transmission images when linearly polarized light is incident on the 2PP-patterned surface. The uniformly rubbed surface, with known LC alignment direction, confirmed that the absorbing polarization coincided with the LC director. When the alignment angle of the LC (φ), and thus the guest dichroic dye, coincides with that of incident light polarization, a minimum light will be transmitted [254], while if the incident polarization is perpendicular to the alignment angle, a maximum of light will be transmitted. For any other φ an intermediate fraction of the light will be transmitted.

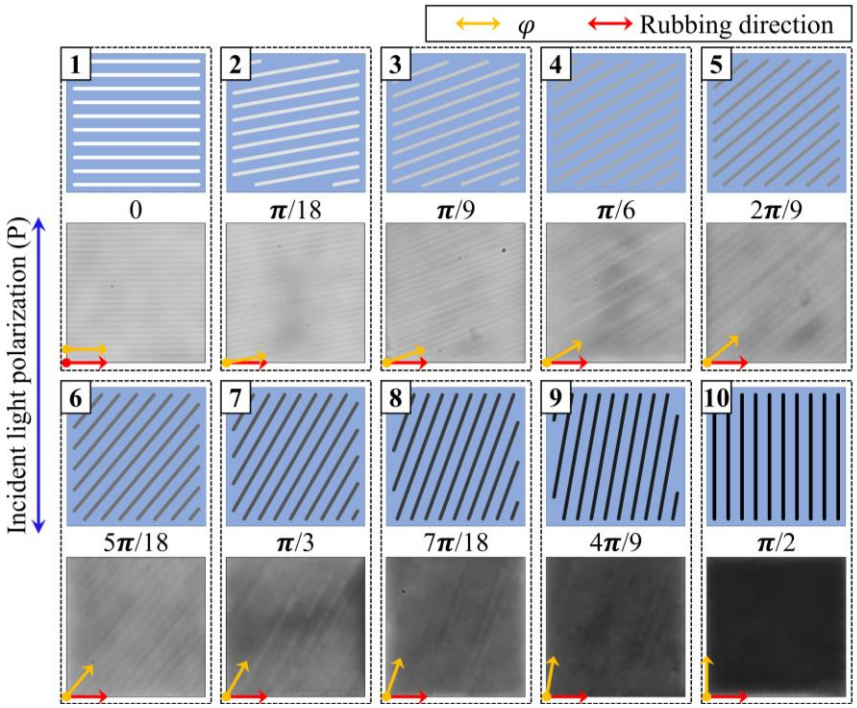

Figure 6.9: Comparison of a set of the 10 patterns of a SU-8 aligned patterned polarizer that defines 10 grayscale levels in LC cells as a function of the alignment angles (φ) with incoming vertical polarization for all patterns.

In a single LC cell, 10 distinct patterns of parallel microlines have been defined and printed under identical conditions. Each pattern, n, is characterized by an alignment angle $\varphi_n = \left(\frac{\pi}{18}\right) \times \{(n-1) | 1 \leq n \leq 10\}$, as shown in Figure 6.9. The 10 different φ_n values result in varying light transmission of the assembled cell when illuminated by linearly polarized white light from the patterned side. The nanostructured texture is reflected in visible variations in the light transmission, confirming that the dye and LC are aligning parallel to the engraved microlines, as seen in previous studies [232], [233].

The 2PP structure in SU-8 exhibits good alignment of the LC with a high repeatability in all directions uniformly across the individual alignment patterns. The transmitted intensities of the patterns, shown in Figure 6.9, were measured, and the grayscale transmission obeys Malus' law, defined in the Equation (4.1), as shown in Figure 6.10. The measurements were taken with the patterned polarized backlit with vertically polarized light. The polyimide rubbing direction (RD) of the other substrate (RD) does not affect the transmission of the light.

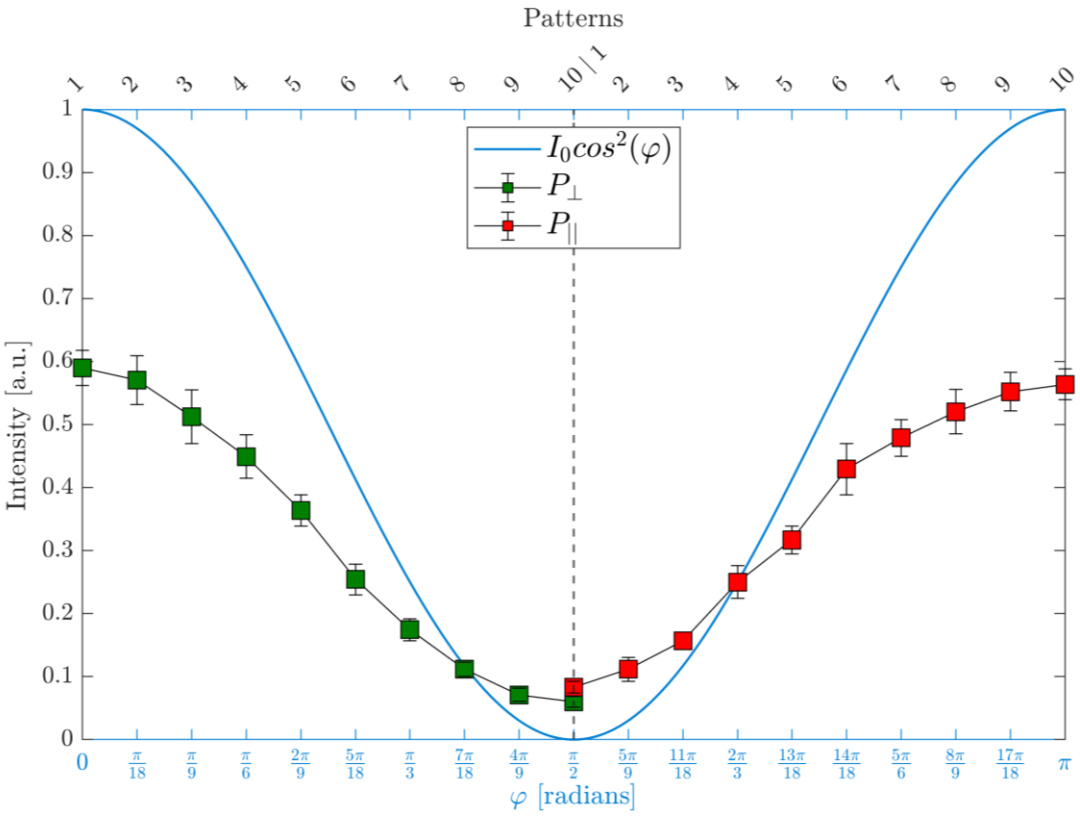

Figure 6.10: Condition of Malus' law for the measured patterns of an LC cell in SU-8. Crossed polarization ($P_\perp$) of the standard polarizer with respect to the rubbed polyimide substrate implies that the patterns obey the equation $I_0\, cos^2(\varphi)$, while parallel polarization ($P_{||}$) of the standard polarizer with respect to the rubbed polyimide substrate for the same patterns follows the phase-shifted equation $I_0\, cos^2(\varphi + \pi/2)$.

In Figure 6.11, a patterned polarizer with patterns arranged in a chessboard-like configuration is shown, together with ascending/descending grayscales. A visible edge between adjacent patterns can be appreciated, corresponding to the inter pattern space in the design as seen in Figure 6.4.

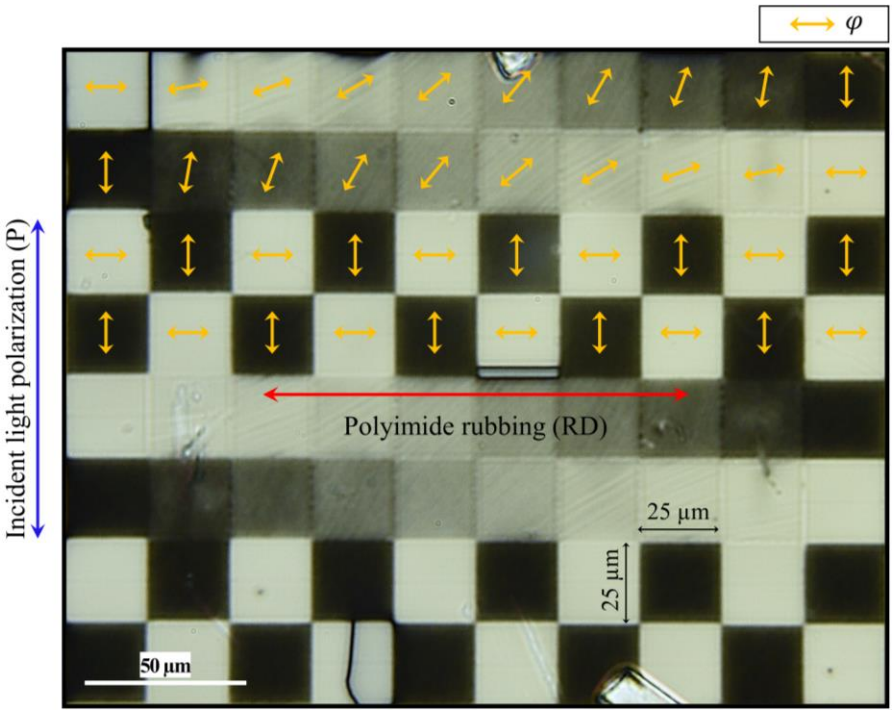

Figure 6.11: Optical micrograph of the entire pattern employed in the dichroic dye-doped LC cell with chessboard pattern and the 10-step grayscale repeated twice. The grayscale of the transmitted light of the patterns was defined by the alignment angle (φ).

The quality of the patterned polarizers in the LC cells has been quantified by the contrast ratio (CR) [93]. The transmitted light intensities were quantified using a NIKON D3400 camera configured with sensibility ISO-400, with exposure time of 1/125 seconds and 1/30 seconds. Subtracting the average minimum intensity transmitted by the standard crossed polarizers, denoted as ($\bar{I}_{bkgr}$), with the microscope precisely focused onto a glass surface, the following CR was calculated:

$$CR = \frac{\left(\bar{I}_{max,meas} - \bar{I}_{bkgr}\right)}{\left(\bar{I}_{min,meas} - \bar{I}_{bkgr}\right)} \tag{6.3}$$

where $\bar{I}_{max,meas}$ is the average transmitted light intensity by the brightest pattern, and $\bar{I}_{min,meas}$ is the minimum average transmitted light intensity by the darkest pattern. This resulted in a normalized CR of 14 for SU-8.

The uniformity of the pattern in the LC cells has been analyzed by employing image entropy (H) [255]. This parameter measures the disorder in the intensity distribution and provides insights into uniformity of the molecular orientation within the microgrooves formed after 2PP-DLW. The disorder was calculated using the Shannon expression:

$$S(I) = \sum_{I=0}^{N} P(I) \times log_2\big(P(I)\big) \tag{6.4}$$

where $P(I)$ is the probability of the occurrence of intensity I within the pixel pattern area and N is the number of intensities measured within the same pixel pattern area.

The uniformity distribution is normalized, dividing the $S(I)$ computed as disorder measured by the maximum entropy of pixel pattern $max(S(I))$ when all intensities are equally likely to occur ($P(I) = 1/N$). Thus Equation (6.4) becomes:

$$H(I) = -\frac{S(I)}{log_2(N)} \times 100\% \tag{6.5}$$

Here, $H \approx 0\,\%$ denotes perfect uniformity, while $H \approx 100\,\%$ shows a random intensity variation of the image pixels. Figure 6.12 shows the uniformity of each of the 10-pixel patterns. All the patterns show similar disorder under both parallel and crossed polarization, although each introduces a different twist in the LC cell, indicating a strong azimuthal anchoring.

H was calculated over an area of 25×25 μm² corresponding to 200×200 pixels² per pattern. The degree of disorder H is approximately 35 %, representing around 65 % of the uniformity.

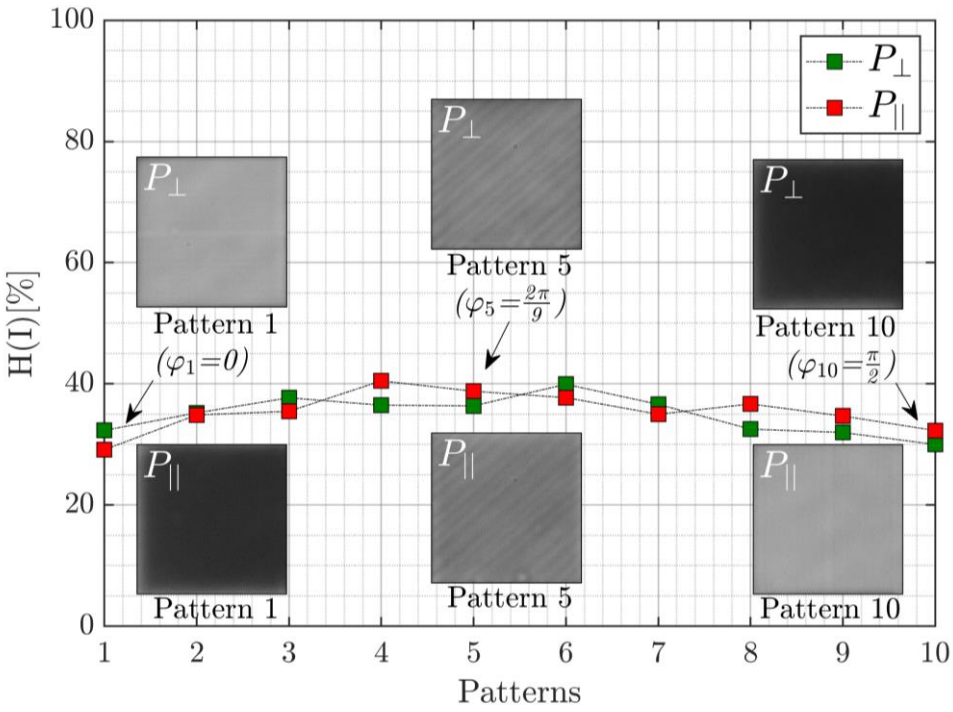

Figure 6.12: Grayscale pattern entropy (H) of dichroic dye-doped LC cell in SU-8 aligned patterned polarizer. Parallel polarization ($P_{||}$) and crossed ($P_\perp$) of the standard polarizer with respect to the rubbed substrate.

6.3.3. Results in S1805

The same cell structure and analysis have been performed on S1805. In this case a 3.2×3.2 mm² logotype of CEMDATIC of UPM has been patterned instead of the checkerboard structure. The alignment of the LC molecules and dye is parallel to the orientation of the microgrooves cut in the S1805.

Figure 6.13 shows photos of the dichroic dye-doped LC cell backlit with polarized light incident onto the uniformly rubbed and patterned alignment surfaces respectively. The discrete 2PP aligned areas are clearly visible, with a visibly high contrast. In Figure 6.14, the original pixelated image and measurements of the transmitted light intensities in the doped cell are shown with the incident light polarization parallel to the alignment direction in the text (appearing dark text on bright background) or perpendicular hereto (appearing bright text on dark background).

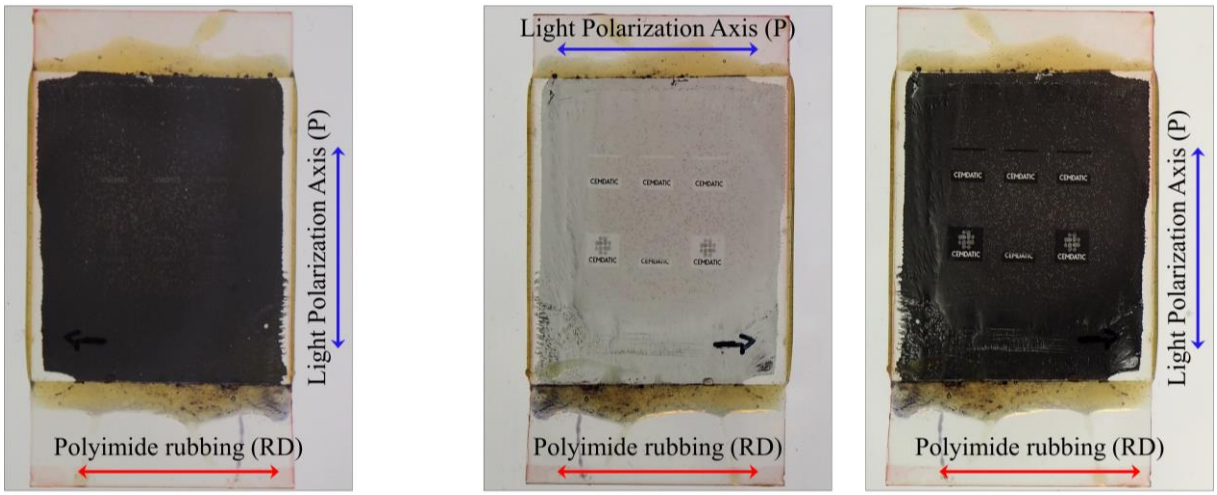

Figure 6.13: Photos taken of the sample backlit with polarized light. Left: Light incident onto the uniformly rubbed surface. Middle and Right: Light incident onto the patterned surface, where recognizable features are clearly visible in separate aligned regions.

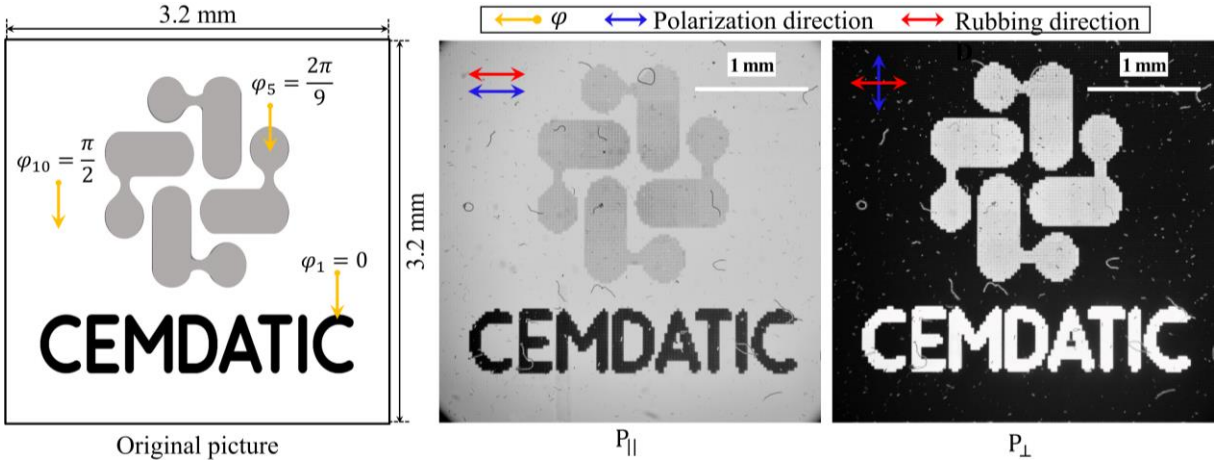

Figure 6.14: Original logotype used in the LC cell, and optical micrograph with a standard polarizer placed in parallel ($P_{||}$) and crossed ($P_\perp$). The alignment angles (φ_n) are labeled to distinguish the grayscale of the transmitted light of the patterns.

The normalized contrast ratio (CR) was of 37 for the measurements using Equation (6.3).

As Equation (6.5) the normalized Shannon entropy (H) of the intensity distribution of grayscale patterns, has been used to assess the alignment quality. In this case H was also calculated over an area of 25×25 μm² (200×200 pixels²/pattern).

Figure 6.15 shows the degree of disorder in the intensity distributions, approximately 37 %, representing 63 % of the uniformity in the doped LC. The repetition rate of the laser pulses was too slow for the scanning rate, leading to imperfect alignment microgrooves. Even so the resulting structure aligned the LC. Table 6.2 presents a summary of the alignment quality for S1805 compared with its counterpart SU-8, both subjected to the same analysis conditions.

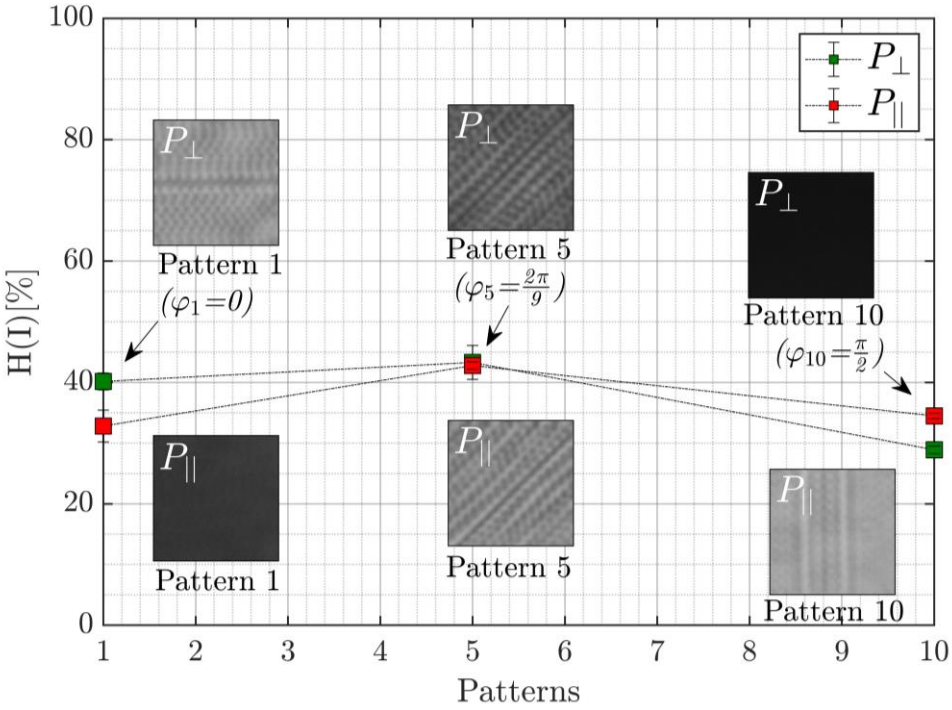

Figure 6.15: Grayscale pattern entropy (H) of LC cell in S1805 aligned patterned polarizer. Parallel polarization ($P_{||}$) and crossed ($P_\perp$) of the standard polarizer with respect to the rubbed substrate.

Table 6.2: Alignment quality comparison (CR and H) for both SU-8 and S1805 alignment surface.

Alignment Quality	**SU-8 alignment**	**S1805 alignment**
Normalized CR	14	37
Entropy (H)	35 ±3.1 % 65 % of uniformity	37 ±5.3 % 63 % of uniformity

S1805 photoresist is an option for creating patterned polarizers in doped LCs. The patterning processes in large-sized LC cells is significantly faster in S1805 due to its high photo sensitivity (62 minutes of 2PP-DLW processing at a scanning speed of 6 mm/s) compared to SU-8 photoresist for the same CEMDATIC logotype (205 minutes at 1 mm/s).

CHAPTER 7

7. Results: Manufacturing of 3D sub-micrometric structures

Printing at extremely high resolutions for creating complex polymeric structures for nanoscale applications and advanced photonic devices [156] is a challenging task. Two-photon polymerization (2PP) is the most precise technique employed for manufacturing micro/nanostructures with resolution below 50 nm [158]. Thus, the 2PP direct laser writing (2PP-DLW) method has commonly been used to fabricate complex 3D microstructures in a variety of polymers, ceramics, and acrylates [19], [22], [256]. Photosensitive materials such as polymers, nanocomposites, and hydrogels have been synthesized, developed, and widely used to fabricate functional 3D components [24], [257]. Additionally, dimensional manipulation of materials using 2PP-DLW is key to 2.5D and 3D manufacturing processes [2], [99].

In this chapter, manufacturing of high-resolution microstructures in polymeric negative-tone photoresist is revised. The microstructures are fabricated using both 2.5D conventional printing technology (layer-by-layer) and true 3D printing technology. The nanoscale feature sizes achieved with the custom 2PP system can be used for advanced applications such as photonic integrated circuits, optical coupling, micro-scaffolds, micromachines, and many others.

7.1. 2.5D microstructures results

The 2PP system illustrated so far in this work was used for manufacturing 2D microstructures by 2PP-DLW for surface alignment in liquid crystal polarizers, as developed in Chapter 6. Three-dimensional microstructures are widely explored in long wide of applications e.g. microfluidic [139], [145], [149], photonic wire bonding [117], [118], [119], and microlenses [103], [104]. The spatial resolution of the microstructures inside the photoresists is key to the photo-chemical reaction technique [39], [67], [175], [258], [259], 2PP processes [260], [261], and focusing configurations [31], [181]. The nanostructures molded by 2PP-DLW can be considered as an orderly arrangement of interconnected volumetric pixels (voxels) in space, formed by the beam focused inside the photoresist [156]. The shape of the voxel, often spheroidal, depends on the numerical aperture (NA) of the objective lens and can be regarded as the fundamental building block of a manufactured microstructure. The effect of the NA, which increases the resolution of the microstructures, is described in Chapter 3.

Manufacturing of 2.5D microstructures was made using slicing, layer-by-layer scanning technology. This traditional technology, commonly applied by commercial systems such as Nanoscribe [32] or UpNano [34], employs the displacements of the Z stage along the optical axis of the microstructure.

2.5D polymeric microstructures created by computer-aided design are often used. Laser processing software (LPS) used so far is designed to be fed into the custom 2PP system, featuring the transcription of 2.5D design data. The process of converting 2.5D design data in LPS software is called slicing. This process involves dividing a microstructure into layers in the XY-plane, which can then be used to recreate the 3D microstructures. The two-dimensional data from design layers define the movement of the focused laser beam across the field of view (FOV) of the system, with processing properties that enable the creation of accurate 3D microstructures.

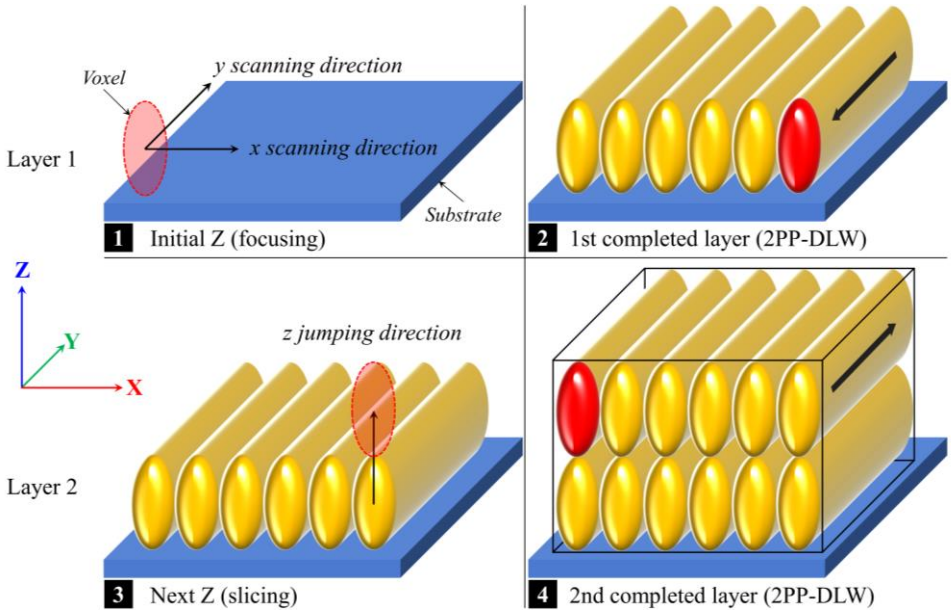

Figure 7.1: An example of layer-by-layer scanning description in 2PP-DLW. The red voxel represents the progression of the laser during the fabrication of microstructures.

During the 2PP-DLW processes shown in Figure 7.1, the layers are fabricated through x- and y-axis movements while the laser is synchronized and turned on/off between layers of the microstructure. After each completed layer, the voxel moves up along the optical axis, jumping the distance between layers. This leads to a slow progression of fabrication.

In the processes described in Figure 7.1, the laser focus spot is directed to the interface between the substrate and the photoresist, as depicted in step one. The laser is then turned on, and the voxel moves along the length and width of the first layer (in the XY-plane) at a defined scanning speed, as depicted in step two. After completing the layer, the laser is turned off, and the laser focus spot is adjusted to the next layer, as shown in step three. The laser is turned on again, and the voxel moves along the second layer. These processes are repeated as many times as needed

to complete the entire 3D microstructure, whether using just the contour method or the filled method in LPS software, as depicted in step four.

7.1.1. Design of 2.5D microstructures

A WordArt block was designed for these experiments. A recipe file generated by the LPS software contains pseudo-algorithms of the CAD design shown in Figure 7.2-b. This design was selected to demonstrate the ability of the 2PP-DLW processes to create solid 3D microstructures with high filled surface roughness.

In these experiments, the 2.5D microstructure consists of layers that were repeated three times along the Z-axis to be fabricated. Each layer was designed to produce a solid microstructure by filling the layer with lines – a process known as hatching. The hatching consists of lines repeated and distributed equally within the layer. The hatching factor within the layers is defined by the voxel resolution in the x- and y-dimensions, while the distance between layers is determined by the z-height of the defined voxel – also referred to as voxel depth.

The microstructure layers were controlled by adjusting the average laser power and scanning speed. The xyz-voxel sizes used to define the hatching parameters for SU-8, mr-DWL, and other photoresists are summarized in "Appendix D: Voxels characterization" for microstructure designs and replotted in Figure 7.3 for these experiments.

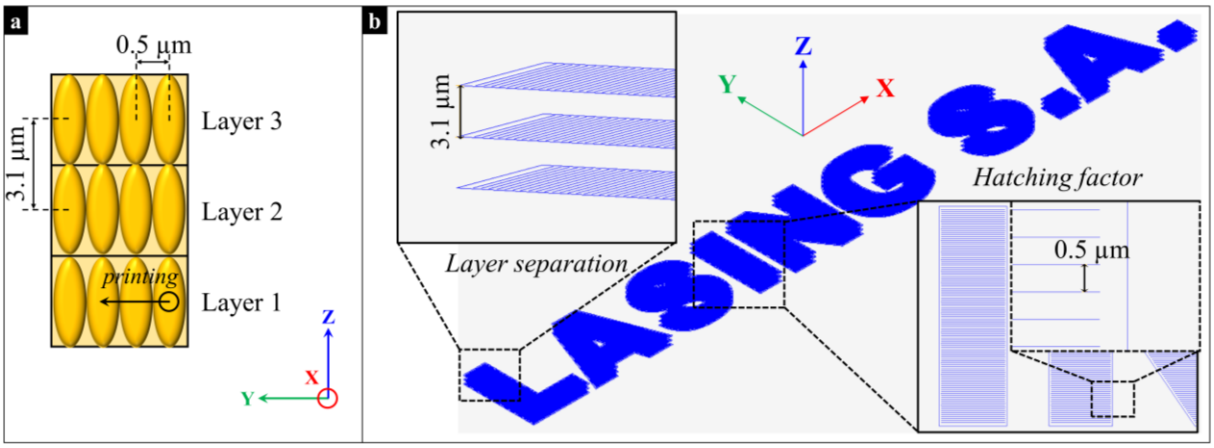

Figure 7.2: 2.5D microstructure in LPS software. a) Description of printing layers with a hatching factor of 0.5 µm and a z-jump factor (layer separation) of 3.1 µm, defined by the voxel diameter and depth. b) Design of a 2.5D microstructure (letters: LASING S.A.) used for the experiments. The design dimensions are 500×57×9.3 µm³, applying the hatching factor and layer separation.

Prior to being exposed to the 2PP-DLW processes, ITO-glass substrates are meticulously cleaned and then spin-coated with photoresist, which is applied by drop-casting onto the ITO layer. Two types of photoresists were used: SU-8 2015 (SU-8) and mr-DWL 40 (mr-DWL). Both were spin-coated to achieve a thickness of 40 µm on substrates. Substrate preparation

parameters for both photoresists are provided in “Appendix A: Cleaning and spin-coating processes”.

SU-8 is commonly used to create 3D microstructures with high aspect-ratio [75], while mr-DWL, which is chemically similar to SU-8 [262], has been specifically tested for 3D microstructure polymerization using commercial 2PP systems [71]. Both photoresists are highly transparent to visible light and thermally stable.

During the 2PP-DLW process, the microstructures were replicated several times on the same substrate. The resolution in voxels can be determined by precisely controlling the average laser power and scanning speed. This parameter (resolution in voxels) differs from one photoresist to another. In order to quantify the achievable voxel size, the scanning speed of the XY-plane was set to 100 µm/s in SU-8 and 300 µm/s in mr-DWL. This resulted in an xy-voxel size of 0.5 µm and a z-voxel size of 3.1 µm for both photoresists, as shown in Figure 7.2-a. The characterized voxel size of SU-8, corresponding to these experiments, is illustrated in Figure 7.3. The jumping speed in the Z direction was set to 100 µm/s. This value may differ because the z-jump factor, defined by the distance between two consecutive layers, is related to the z-voxel size at scanning speed of the XY plane. The average power was set to 70 mW in SU-8 and 22 mW in mr-DWL for the fixed scanning speed.

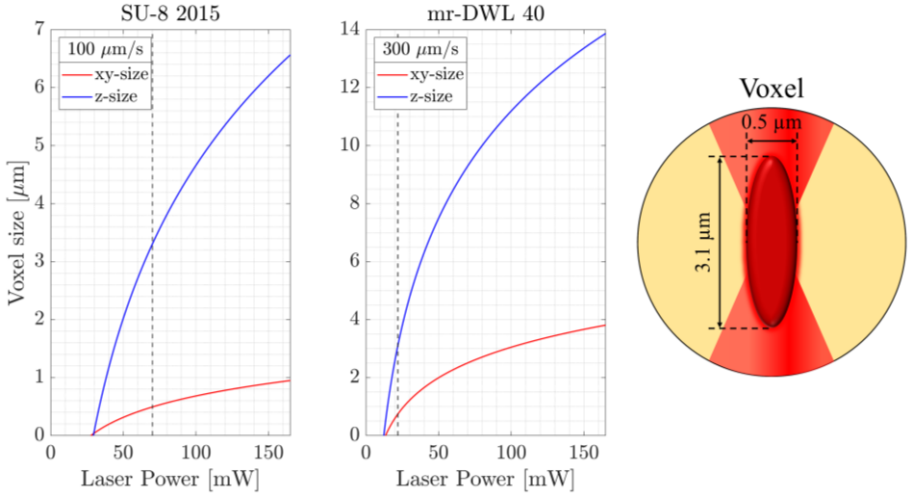

Figure 7.3: Definition of voxel size in SU-8 and mr-DWL photoresists for these experiments, using a 50× objective lens with a numerical aperture (NA) of 0.8. The expressed voxel resolution in the plots is defined at 100 µm/s and 300 µm/s for SU-8 and mr-DWL photoresists.

After the polymerization, the samples were placed on a hotplate to complete the polymerization of the microstructures through post-baking. Relaxation times following soft-baking and post-baking in mr-DWL photoresist are needed [80], with cooling at room temperature, approximately 21 °C and 40–60 % relative humidity. The substrates were then washed to remove the unexposed photoresist by submerging them in PGMEA for SU-8 and mr-DEV 600 for mr-DWL.

7.1.2. Scanning electron microscopy characterization

The substrates were coated with a 50 nm layer of aluminum by physical vapor deposition before being measured using scanning electron microscopy (SEM) at 8 kV in SU-8 and 5kV in mr-DWL photoresist, taking care not to burn the samples (EVO 10, ZEISS group).

The hatching factor was evaluated in the microstructures, and the xy-voxel size was measured, yielding values for the characterized voxels of both photoresists. Figure 7.4 shows the voxel sizes on the coated surface of a photoresist, with an xy-size of 592 ± 60.21 nm. The values are close to that of the defined in Figure 7.3.

SEM micrographs of the resulting SU-8 microstructure show correctly polymerized 2.5D microstructures, with the measured dimensions shown in Figure 7.5.

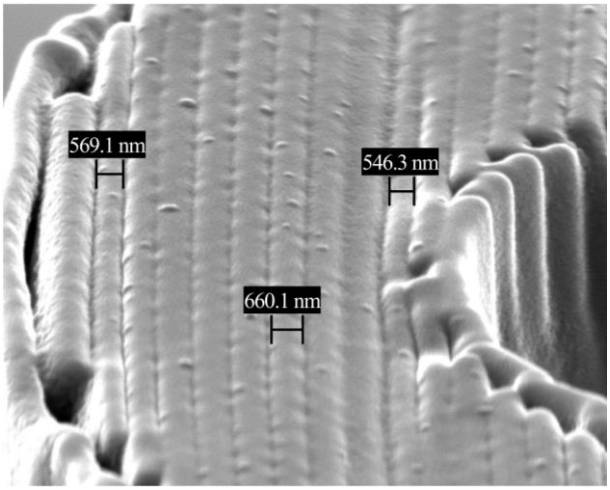

Figure 7.4: Measurements of the hatching factor (xy-voxel size) in SU-8 photoresist.

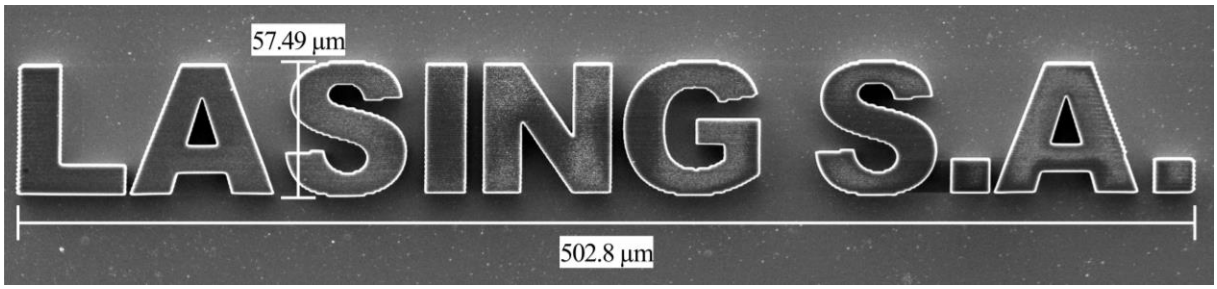

Figure 7.5: Scanning electron micrographs of an entire 2.5D microstructure in SU-8 2015.

The xy dimensional characterization was measured, showing sizes as predicted in the CAD design in Figure 7.2. The voxel shape predicted by the microstructure was also observed to become more deeper (> 3.1 µm), and the height of the entire structure resulted higher than the CAD design (> 9.3 µm). This was because the presence of travel errors in the Z stage (piezoelectric), which resulted in a displacement of approximately 1.5 µm for every micron of movement in the Z-axis. Additionally, hatching can cause an accumulation of energy outside the voxel, leading to polymerized structures that are thicker than expected.

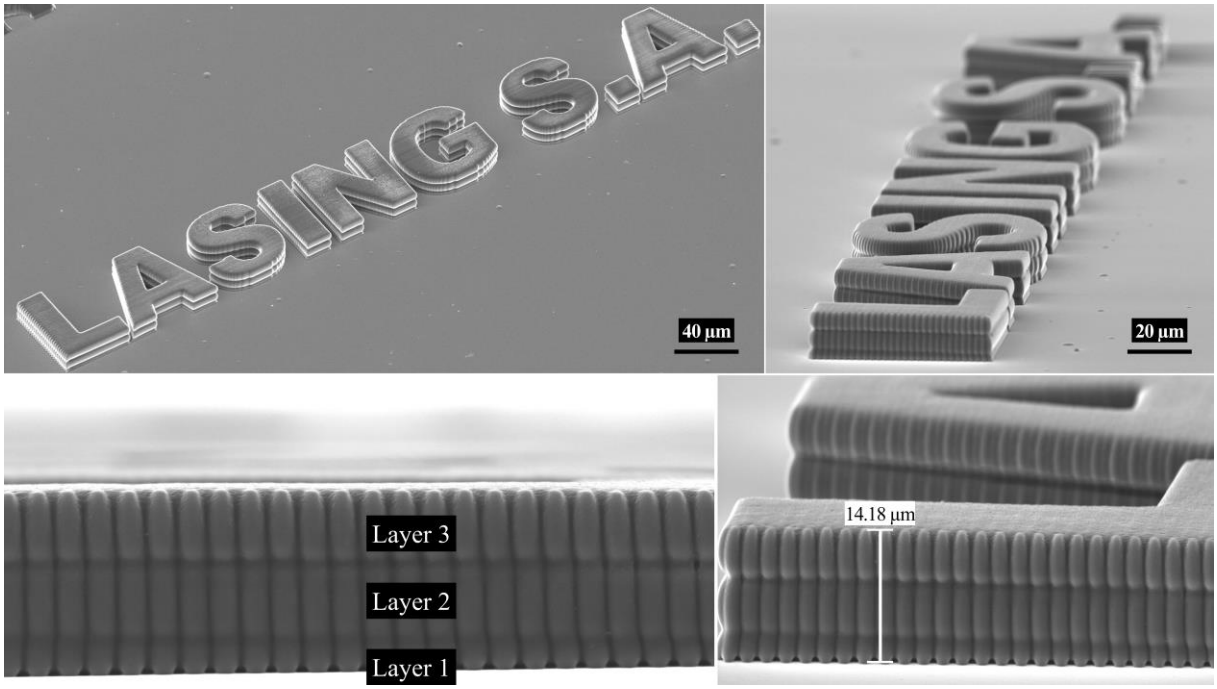

Figure 7.6: Scanning electron micrographs of the measured 2.5D microstructure with the applied voxel sizes in SU-8 2015.

Figure 7.6 shows a well-polymerized 2.5D microstructure. Approximately half of the first layer was polymerized because the laser focus spot was placed at the interface between the ITO-glass and the photoresist.

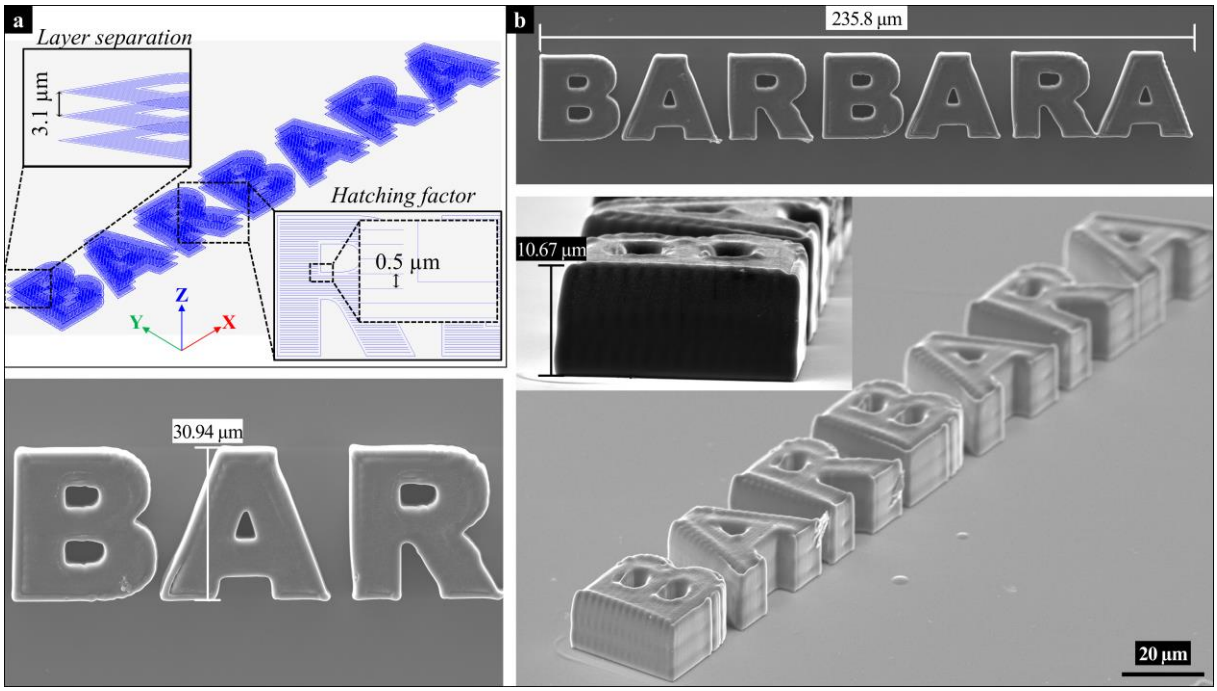

Figure 7.7: 2.5D microstructure used for the experiments. a) The design dimensions are 232×29×9.3 µm³, with a hatching factor of 0.5 µm and a z-jump factor (layer separation) of 3.1 µm. b) Scanning electron micrographs of an entire 2.5D microstructure in mr-DWL. The design was developed in LPS software.

The custom 2PP system was adjusted based on the measurement results. A new WordArt block was designed under the same conditions for layer separations and voxel size as defined in Figure 7.3 in LPS software for experiments using the mr-DWL photoresist, as shown in Figure 7.7-a.

SEM micrographs of the mr-DWL photoresist also show well-polymerized microstructures. The xyz dimensional characteristics were measured, and the sizes correspond to those predicted, as shown in Figure 7.7-b.

Table 7.1: XYZ dimensions measurements of the microstructure in both photoresists.

Photoresist	**Design [µm]**	**Measured [µm]**
SU-8	x = 500 y = 57 z = 9.3	x = 501.4 ± 1.97 y = 57.2 ± 0.33 z = 11.7 ± 4.03
mr-DWL	x = 232 y = 29 z = 9.3	x = 233.9 ± 2.68 y = 29.9 ± 1.37 z = 9.98 ± 0.96

Table 7.1 summarizes the designed and standard deviation of measured dimensions of the microstructure in the X, Y, and Z axes for both photoresists.

7.1.3. Surface roughness analysis

In the 2PP-DLW process, SU-8 and mr-DWL photoresists were cured during the voxel tracing, and 2.5D microstructures on substrates were analyzed by measuring the roughness on the microstructure surface. The voxel tracing is the primary parameter that affects surface roughness [263]. The distance between voxels during polymerization, defined by the hatching factor, allows surface roughness to be controlled by adjusting the voxel diameter. Thus, an atomic force microscope (AFM) was used to quantify the surface roughness (PicoLE, Molecular Imaging). Measurements were taken at selected depths using a 10 nm radius silicon tip on each 2.5D microstructure. Scanned surfaces were 5×5 µm with a resolution of 256×256 points. Three measures per each scanned microstructure were carried out.

The surface roughness is defined by three parameters in this work: average roughness, root-mean-square roughness, and skewness roughness.

The average roughness (R_a) represents the mean value of the absolute values of the height deviations of the surface relative to a mean value over the evaluation length [264], given by:

$$Ra = \frac{1}{N}\sum_{i=1}^{N}|z_i - \bar{z}| \tag{7.1}$$

where N is the number of surface points of a total scanned surface, z_i is the height of each point, and $\bar{z}$ is the mean height of the surface.

The root-mean-square roughness (R_q) is the standard deviation of the height values of the surface relative to the mean value over the evaluation length and is given by:

$$Rq = \sqrt{\frac{1}{N}\sum_{i=1}^{N}(z_i - \bar{z})^2} \tag{7.2}$$

The skewness roughness (R_{sk}) is a statistic parameter and describes the distribution asymmetry of the heights with respect to the mean value, given by:

$$R_{sk} = \frac{1}{R_q^3 N}\sum_{i=1}^{N}(z_i - \bar{z})^3 \tag{7.3}$$

The roughness reveals a surface characterized by nanogrooves fabricated by lines due to the voxel effect of a femtosecond laser (femto laser), inherent to the hatching factor in the manufacturing process. Nevertheless, the roughness can be reduced by adjusting the laser tracing with an adapted exposure dose and incorporating roughness parameters (e.g., R_{sk} and R_a) into the 2PP system, allowing for the control of smooth surfaces in 2.5D and 3D microstructures, achieving values close to those of highly commercial systems in 2PP lithography (< 10 nm). In Table 7.2, the roughness of both photoresists used in these experiments can be observed, showing lower values in SU-8 compared to mr-DLW subjected to the same voxel conditions. Figure 7.8 shows the surface roughness measurement on SU-8 microstructures.

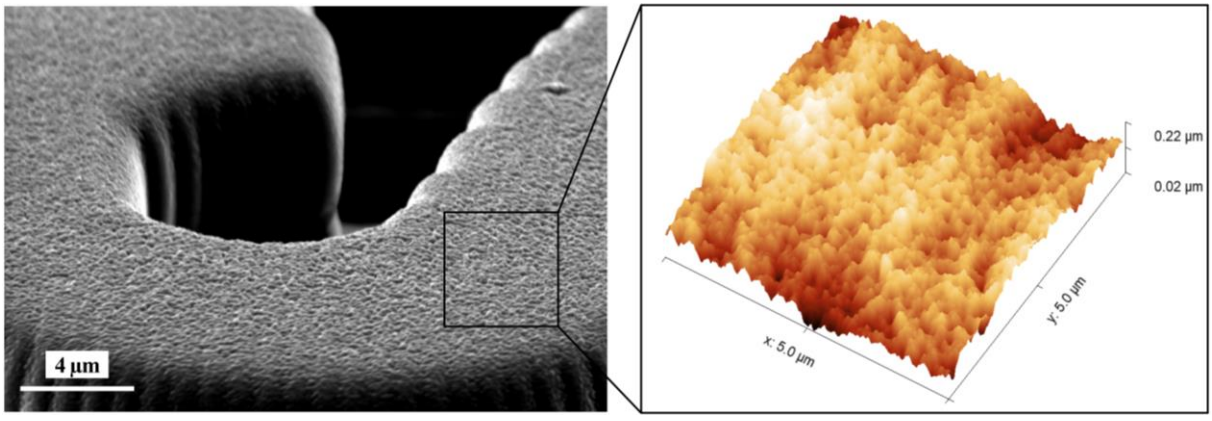

Figure 7.8: Micrographs taken from surfaces of microstructures polymerized with SU-8 photoresist. SEM micrographs (left); AFM micrographs for measuring roughness (right).

Table 7.2: Roughness evaluation of the 2.5D microstructure surfaces.

Roughness	**SU-8**	**mr-DWL**
R_a	22.72 nm	45.61 nm
R_q	28.98 nm	57.74 nm
R_{sk}	-0.3751	0.1229

The evaluation difference between the two photoresists is related to their intrinsic properties, which are not evaluated in this work, but may be considered to increase accuracy in obtaining microstructures more efficiently.

7.2. 3D microstructure results

High viscosity of the photoresists is one of the keys to producing true 3D microstructures that float within the photoresists during photopolymerization processes [160] exploited for manufacturing using 2PP-DLW. Consequently, three-dimensional movements of the voxel freely inside the volume of the photoresist can be applied, eliminating the traditional layer-by-layer printing technology and ensuring the microstructure architecture [9], [125], [164], [265], [266].

The process of converting 3D design data is called volumetric additive manufacturing (VAM) [267], which may be easily carried out [268], using 3D 2PP-DLW. This novel manufacturing process allows rapid, freeform, layer-less 3D printing.

3D microstructures can be manufactured at all points within the photoresist volume, involving three-dimensional vectorial processing. The 3D design data in LPS software defines the movements of the focused laser beam at any point to start the 2PP-DLW process, with processing properties to recreate the 3D microstructure.

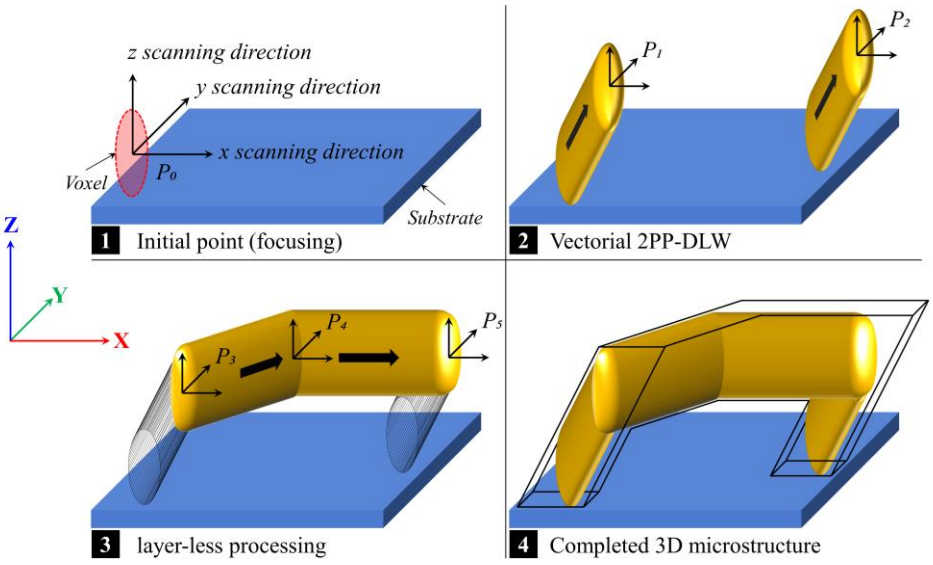

Figure 7.9: An example of 3D scanning description in 2PP-DLW. The point represents the initial and final progression of the laser during the fabrication of microstructures.

In the simple process described in Figure 7.9, the laser focus spot might start at any point directly at the interface between the substrate and the photoresist, as depicted in step one. However, it could also be initiated from any vectorial point defined by the 3D design far from the substrate (as shown in step three). The laser is then turned on, and the voxel is moved along

the spin-coated photoresist volume (xyz scanning directions), as depicted in steps two and three. The laser is correctly synchronized to turn on and off at the processing of vectorial points (P_0 – P_5) of the microstructure to avoid unwanted polymerized parts. The voxel follows all points, connecting them with polymerized microlines, which describe the 3D design of the microstructure, as depicted in step four.

7.2.1. Design of 3D microstructures

Applying the concept of 3D 2PP-DLW to microstructures, the CAD designs illustrated in Figure 7.2 and Figure 7.7 were redesigned. In this case, the layers were tilted 35º and 90º with respect to the y-axis (surface substrate), as depicted in Figure 7.10. The layer dimensions in 35º tilted microstructures were kept in both photoresists, while the layer dimensions in the 90º tilted microstructures were reduced to confine the designs within the spin-coated photoresist volume. In the 90° tilted microstructures, fourteen layers were added to prevent collapse during the development process due to their aspect ratio, which is approximately 10:1 [269]. The printing strategy applied to make 3D microstructures is illustrated in Figure 7.10-a and -b. This approach allows defining the xyz printing directions of all points in the designs at a defined tilt angle. Each tilted layer used the hatching method, as defined by the voxel sizes shown in Figure 7.3 for both SU-8 and mDWL photoresists. The separation between tilted layers was defined by the voxel depth of 3.1 µm for the 35º tilted microstructure, depicted in Figure 7.11-a, and by the voxel diameter of 0.5 µm for the 90° tilted microstructure, depicted in Figure 7.11-b.

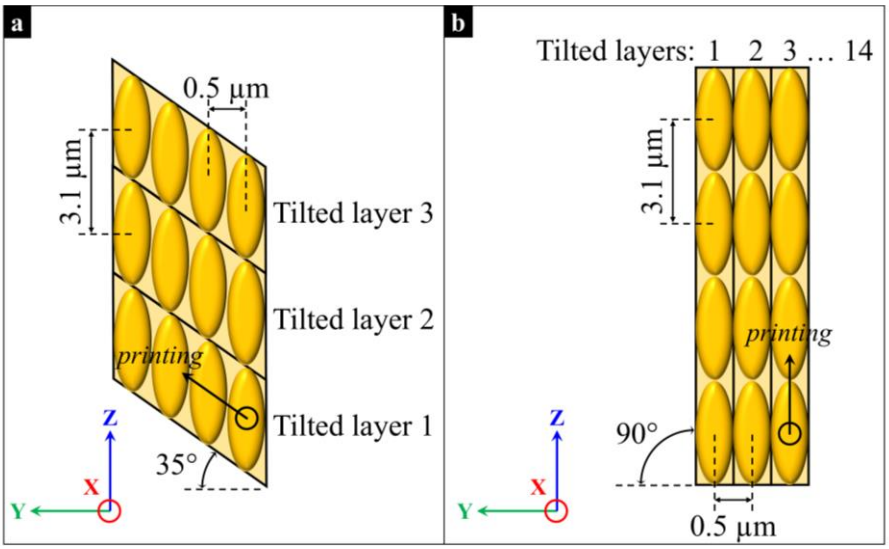

Figure 7.10: Description of printing layers (2.5D microstructure strategy) with a hatching factor of 0.5 µm and a z-jump factor (layer separation) of 3.1 µm, defined by the voxel diameter and depth.

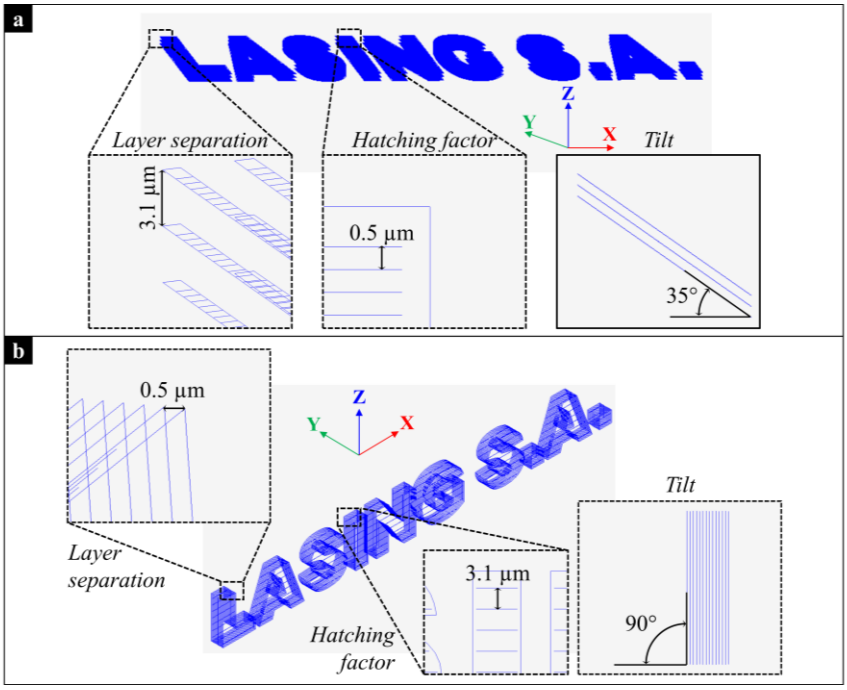

Figure 7.11: Redesign of a 3D microstructure (WordArt: LASING S.A.) used for the experiments: a) 35º and b) 90º tilted microstructure. The design was developed in LPS software with the applied hatching factor (voxel sizes) in SU-8 2015 and mr-DWL 40 photoresist.

7.2.2. Scanning electron microscopy characterization

SEM micrographs show well-polymerized 3D microstructures. The angles of the tilted layers were measured, and the values are close to those predicted by the CAD design, as shown in Figure 7.12. Table 7.3 summarizes the angle measurements and the standard deviations of the tilted layers of the microstructures for both photoresists. Completed SEM micrographs of 3D microstructures and their dimension measurements can be found in "Appendix F: Results in 3D microstructures".

Table 7.3: Angle measurements of the tilted microstructure in both photoresists.

Photoresist	Design [deg.]	Measured [deg.]
SU-8	35	36.9 ± 2.61
	90	89.5 ± 0.78
mr-DWL	35	35.6 ± 0.85
	90	90.7 ± 0.92

It can be concluded that the custom 2PP system developed in this project effectively produces 2D, 2.5D, and 3D microstructures. The standard deviations of the dimensional structures are minimized, and the variability depends on the calibration of the system, especially the mechanical stages. These introduce errors in positioning and (de-)accelerations of the stages during the printing processes. Hence, they must be thoroughly calibrated to ensure 100% reliability of the system, both in hardware and software.

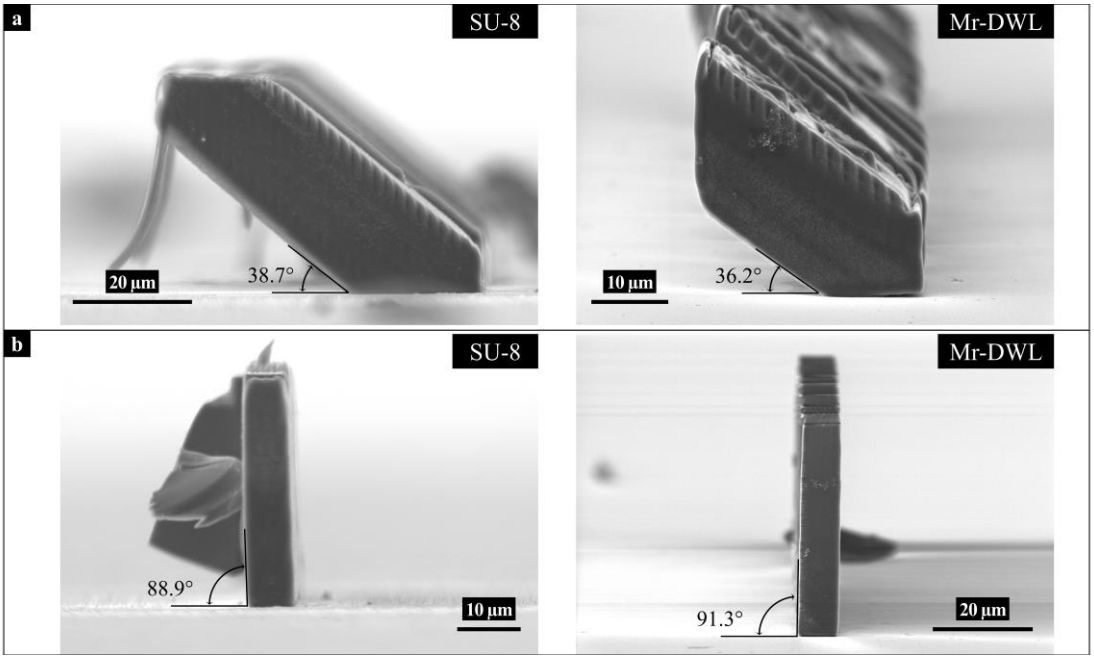

Figure 7.12: 3D microstructure measurements in both SU-8 and me-DWL photoresists. a) The tilted layer is at 35º. b) The tilted layer is at 90º.

7.3. Micro-scaffolds for bio-applications

Micro-scaffolds are widely used, with mechanical and chemical resistance being crucial features for specific applications, such as in biological and medical fields [15], [149], [270], [271]. They are also useful for evaluating new polymers for photonic devices [272]. For this reason, micro-scaffolds cannot be overlooked, and are designed to pave the way to systematic studies of multidisciplinary applications, aligning with the research interests of the UPM and the company Lasing S.A. These include micro-fluidics and tissue engineering applications [273], [274], [275], using the custom 2PP system presented in this project.

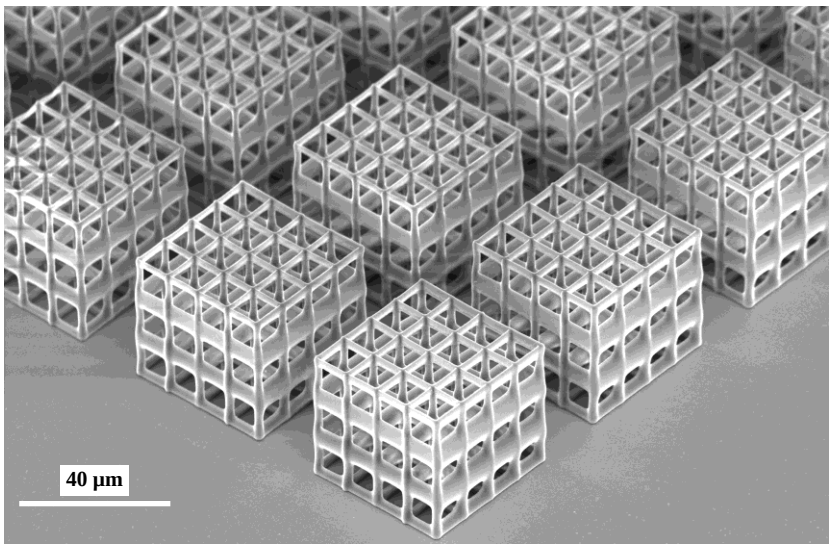

Figure 7.13: Micro-scaffolds for test grids optimization (40×40×40 µm³) in SU-8 carried out in Chapter 5.

Micro-scaffolds for characterizing voxel sizes were previously introduced in Chapter 5. The obtained results serve as an introduction to the design of 3D microstructures, as depicted in Figure 7.13. To extend the 3D polymeric microstructures, the mr-DWL photoresist was used. In this case, grids of orthogonal rods in the XY-plane and interconnected rods in the Z direction were designed. As depicted in Figure 7.14-a, the micro-scaffold consists of bi-dimensional grids with a stacking sequence that repeats every n times in the Z direction.

Micro-scaffolds have also been created out of micro-rings. In Figure 7.14-b, the micro-scaffold consists of bi-dimensional ring grids with a stacking sequence that repeats every n times in the Z direction. Within each 2D ring grid, the rings are sequential in the X and Y directions with each one having a radius (r).

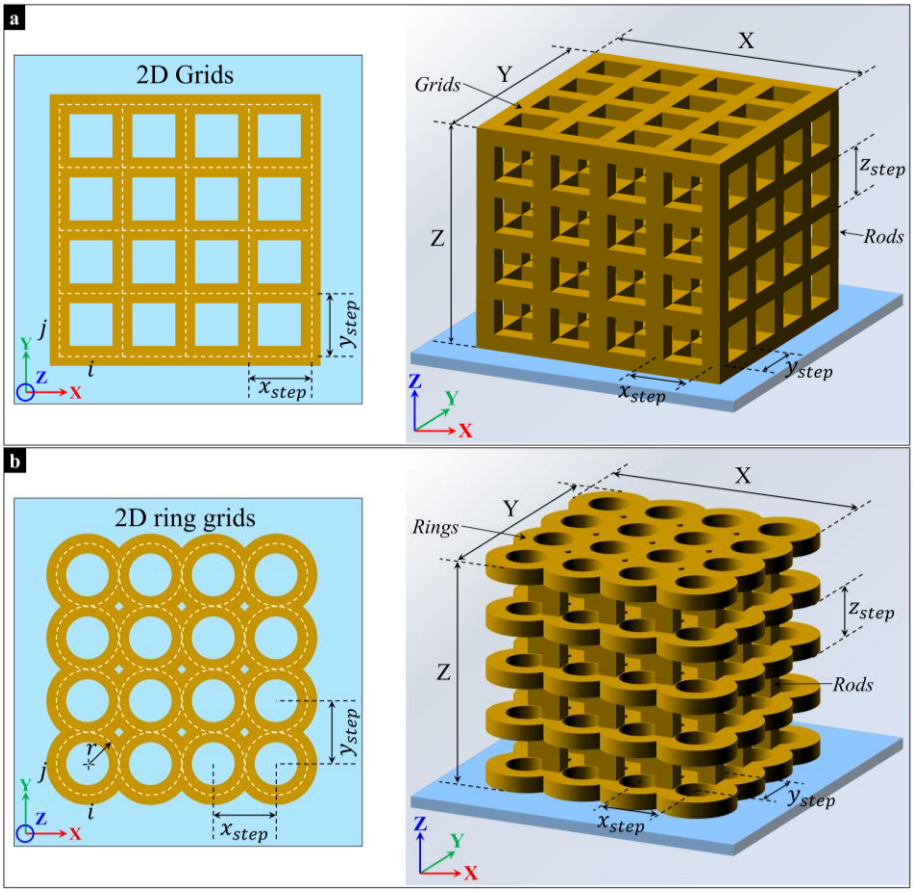

Figure 7.14: Schematic illustration of 3D microstructures. a) Micro-scaffolds composed by 2D grids. b) Micro-scaffolds composed by 2D ring grids.

The micro-scaffolds depicted in Figure 7.14 were designed on LPS software applying the design conditions previously described. Figure 7.15-a shows, on the left, micro-scaffolds composed of 2D grid designs with dimensions of 160×160×37.5 μm³, and on the right, micro-scaffolds composed of 2D ring grids with dimensions of 200×200×37.5 μm³. The thin lines in the designs are transferred into voxels with a depth of about 2 μm and a diameter of 0.5 μm. The 2D grids and rings were fabricated with an average laser power of 18 mW under a constant scanning

speed of 300 µm/s. The vertical rods of both designs were constructed by increasing the exposure time to achieve higher mechanical stability, using a scanning speed of 200 µm/s at the same applied average laser power. Figure 7.15-b shows the realization of the micro-scaffolds, corresponding to the designs in Figure 7.15-a. The micro-scaffolds were replicated several times on the same substrate to obtain more structural analysis. The first level of the microstructure, near the substrate surface, is only partially written due to some inaccuracy in focusing on this specific structure.

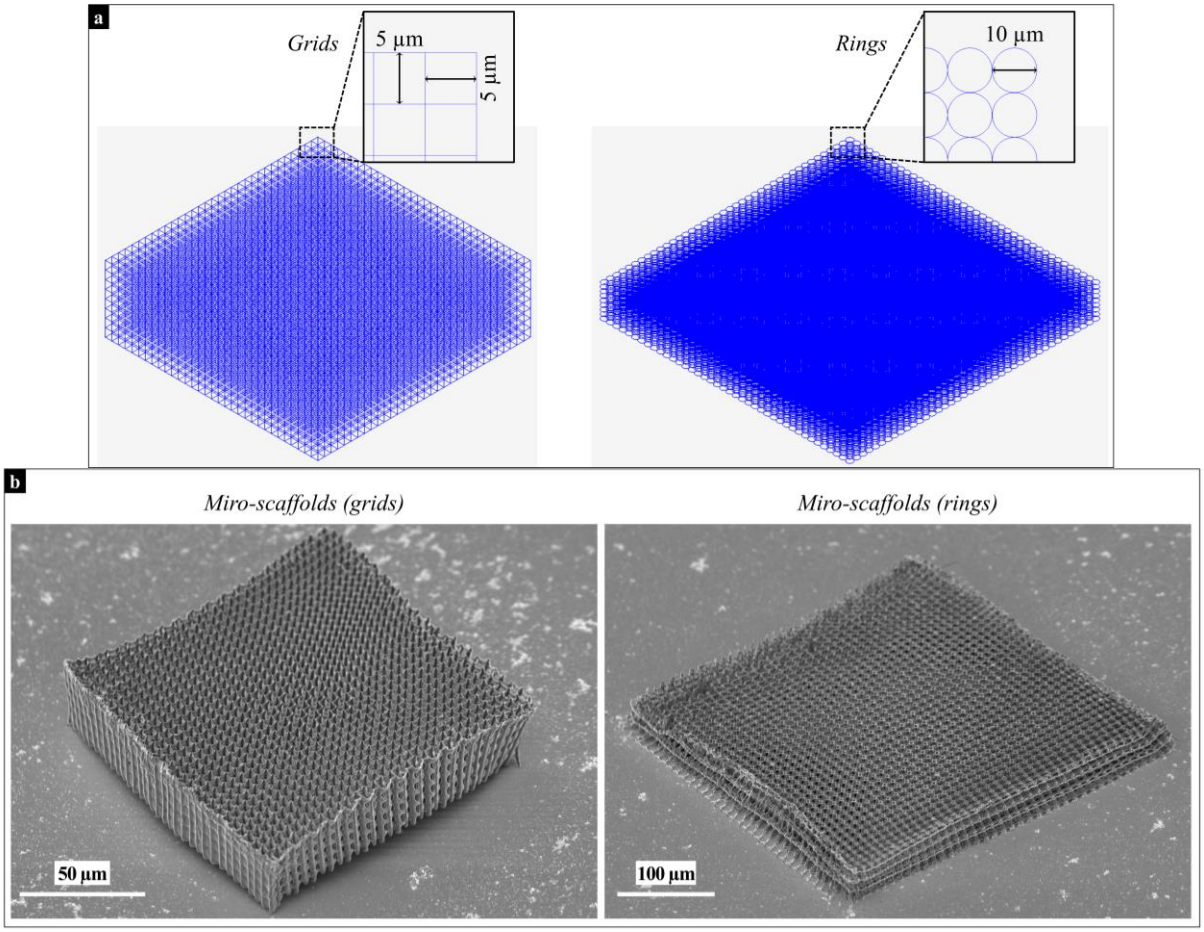

Figure 7.15: a) Micro-scaffolds design on LPS software. b) SEM micrographs of the micro-scaffolds fabricated.

The 2D grids of rods formed square micro-pores in the micro-scaffolds in the design. The square pores defined by (x_{step} & y_{step}) are 5×5 µm² in size, with an approximate linewidth of 0.5 µm, while the rings pores defined by ($2r = x_{step}$ & y_{step}) are approximately 78 µm² in size (πr^2) with 0.5 µm of linewidth, The diameter of the rings is approximately 10 µm ($2r$), satisfying the design conditions of the micro-scaffolds.

Finally, the fabrication of micro-scaffolds with well-defined geometry was successfully achieved through 2PP-DLW processes. The SEM micrographs of the fabricated microstructures

are shown in Figure 7.16-a and -b. A complete set of results of this analysis is presented in "Appendix F: Results in 3D microstructures".

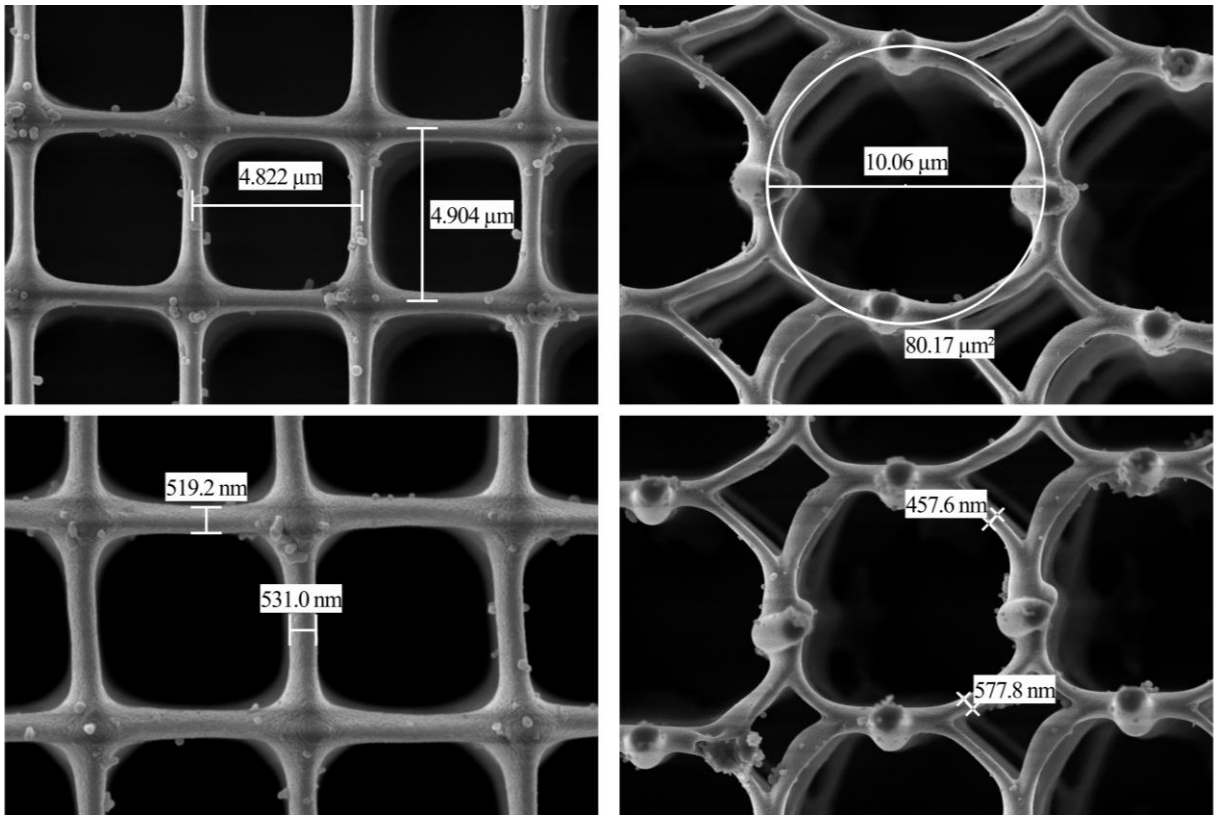

Figure 7.16: Analysis of the measurement of micro-scaffolds in both designs in mr-DWL photoresist.

7.4. High Resolution samples

High resolution in 3D microstructures was achieved. For example, during the fabrication of 3D test grids, the smallest polymerized linewidth measured by SEM was 280 nm in mr-DWL 40 photoresist (Figure 7.17-a) and 378 nm in EpoCore 5 (Figure 7.17-b). Additionally, by applying the characterized voxel criteria, high resolution was also achieved in the design of micro-scaffolds, with linewidths of 333 nm and 357 nm in the 2D ring of 3D microstructures (Figure 7.17-c and -d).

The highest resolution can be achieved by applying effective techniques to reach values well below 50 nm, such as depletion microscopy applied to lithography to overcome the diffraction limit. These techniques can involve combining methods such as voxel tracing strategies in 3D vectorial movements, adding inhibitors to the photoresists, and using two-color lasers [163], [172].

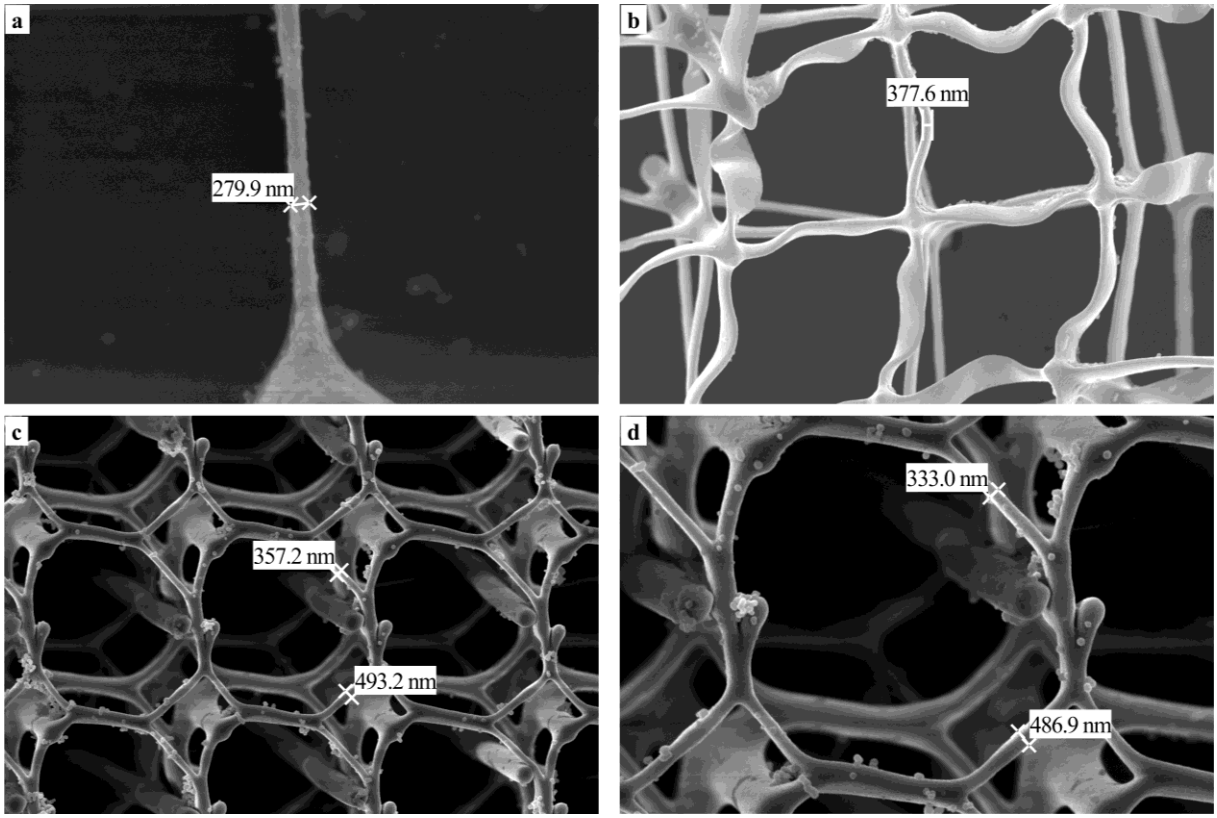

Figure 7.17: Maximum resolution reached in 3D microstructures designs.

CHAPTER 8

8. Conclusions and future works

8.1. Conclusions

The main aim of this Thesis was the design and development of a customized system capable of manufacturing microphotonic devices using the 2PP technique. This goal has been achieved, meticulously optimized, and is now fully operational in the cleanroom of the Grupo de Fotónica Aplicada (GFA) at CEMDATIC, UPM.

1. A customized 2PP system has been designed and assembled with various components and modules to create a compact, low-cost open-hardware system with performance similar to current commercial systems. This direct laser writing (2PP-DLW) equipment is suitable for the micro-fabrication of 2D and 3D structures and includes the firmware programming of the system.
2. Additionally, a setup for single-photon polymerization direct laser writing (1PP-DLW) for calibration and 2PP system optimization in conventional lithography has been integrated.
3. The characteristic voxel of commercial negative-tone and positive-tone photoresists was tested and characterized, providing a database for the micro-fabrication of structures with controlled resolution based on programmable scanning speed and laser power parameters in the system's software.
4. Patterned polymeric surfaces composed of microgrooves or microlines (~0.5 μm) were successfully fabricated and used for liquid crystal alignment. By employing dichroic dye-doped liquid crystals, advanced arbitrarily patterned polarizers were generated.
5. The equipment has demonstrated its capacity to produce 2.5D (layer-by-layer) and true 3D sub-micrometric structures.
6. Complex micro-scaffolds with a typical resolution of approximately 500 nm for bioengineering applications were also manufactured.

8.2. Future works

1. The development of new structures, such as photonic wire bonding, micro-lenses, micro-optic spiral phase plates, and micro-antennas, is proposed.

2. From the wide variety of existing photoresists, several of the most relevant ones have been used. This study could be extended to other photoresists specifically designed for 2PP, particularly those that produce fluorescence or index changes when illuminated, which would improve focusing precision.
3. Post-curing effects on 3D micro/nanostructures need to be analyzed in greater depth to assess the accuracy and repeatability of the 2PP system after manufacturing.
4. Modification of the objective holder is proposed for easier changes of the objective lens for testing the 2PP system in oil immersion configuration and dip-in laser lithography.
5. An improvement in focus is proposed by applying more sophisticated analysis techniques, such as using nanometric measurement lasers collinear with the femtosecond laser or employing advanced image processing with the system's vision camera.
6. Redesigning the system's assembled structure with thermal expansion-resistant alloys and granite is suggested to increase its resistance to variations or vibrations.

Finally, further sophistication of the 2PP system for micro-fabrication can be pursued, for example:

1. Surpassing the Abbe's diffraction limit for ultra-high resolution. Although a maximum resolution of ~280 nm has been achieved in this work, it has not been repeatable. Therefore, it is possible to apply advanced lithography techniques, such as stimulated emission depletion (STED) microscopy integrated to 2PP-DLW, to further enhance resolution in the nanofabrication of photonic devices with features as small as 10 nm.
2. Multi-beam generators for simultaneous fabrication of multiple microstructures using spatial light modulators, diffractive optical elements, or digital micromirror devices.
3. Micro-fabrication in other materials such as hybrid sol-gel for photonic materials, or material subtraction in metals. These would largely spread the number of application fields.

References

[1] J. Fischer, “Three-dimensional optical lithography beyond the diffraction limit,” Institut für Angewandte Physik (APH), 2012. doi: 10.5445/IR/1000028704.

[2] X. Zhou, Y. Hou, and J. Lin, “A review on the processing accuracy of two-photon polymerization,” *AIP Advances*, vol. 5, no. 3, p. 030701, Mar. 2015, doi: 10.1063/1.4916886.

[3] C. Xiong *et al.*, “Optical Fiber Integrated Functional Micro-/Nanostructure Induced by Two-Photon Polymerization,” *Front. Mater.*, vol. 7, Oct. 2020, doi: 10.3389/fmats.2020.586496.

[4] A. Balena, M. Bianco, F. Pisanello, and M. De Vittorio, “Recent Advances on High-Speed and Holographic Two-Photon Direct Laser Writing,” *Advanced Functional Materials*, vol. 33, no. 39, p. 2211773, 2023, doi: 10.1002/adfm.202211773.

[5] *NMR 3D Analysis Photopolymerization*, vol. 170. in Advances in Polymer Science, vol. 170. Berlin, Heidelberg: Springer, 2004. doi: 10.1007/b12766.

[6] S. Maruo, O. Nakamura, and S. Kawata, “Three-dimensional microfabrication with two-photon-absorbed photopolymerization,” *Opt. Lett., OL*, vol. 22, no. 2, pp. 132–134, Jan. 1997, doi: 10.1364/OL.22.000132.

[7] A. S. López, C. Maibohm, O. F. Silvestre, and J. B. Nieder, “Polimerización de Dos Fotones, una tecnología interdisciplinar: de la innovación en investigación biomédica a los dispositivos fotónicos integrados,” *Revista Española de Física*, vol. 34, no. 2, Art. no. 2, Jun. 2020.

[8] S. Achenbach, S. Hengsbach, J. Schulz, and J. Mohr, “Optimization of laser writer-based UV lithography with high magnification optics to pattern X-ray lithography mask templates,” *Microsyst Technol*, vol. 25, no. 8, pp. 2975–2983, Aug. 2019, doi: 10.1007/s00542-018-4161-2.

[9] V. Harinarayana and Y. C. Shin, “Two-photon lithography for three-dimensional fabrication in micro/nanoscale regime: A comprehensive review,” *Optics & Laser Technology*, vol. 142, p. 107180, Oct. 2021, doi: 10.1016/j.optlastec.2021.107180.

[10] L. Zheng *et al.*, "Fabrication of sub-150 nm structures by two-photon polymerization for plasmon excitation," in *2017 Progress In Electromagnetics Research Symposium - Spring (PIERS)*, May 2017, pp. 3402–3405. doi: 10.1109/PIERS.2017.8262348.

[11] F. Rajabasadi, L. Schwarz, M. Medina-Sánchez, and O. G. Schmidt, "3D and 4D lithography of untethered microrobots," *Progress in Materials Science*, vol. 120, p. 100808, Jul. 2021, doi: 10.1016/j.pmatsci.2021.100808.

[12] G. Zhao, A. Ambrosi, and M. Pumera, "Self-propelled nanojets via template electrodeposition," *Nanoscale*, vol. 5, no. 4, pp. 1319–1324, Feb. 2013, doi: 10.1039/C2NR31566A.

[13] C. Acikgoz, M. A. Hempenius, J. Huskens, and G. J. Vancso, "Polymers in conventional and alternative lithography for the fabrication of nanostructures," *European Polymer Journal*, vol. 47, no. 11, pp. 2033–2052, Nov. 2011, doi: 10.1016/j.eurpolymj.2011.07.025.

[14] V. F. Paz *et al.*, "Development of functional sub-100 nm structures with 3D two-photon polymerization technique and optical methods for characterization," *Journal of Laser Applications*, vol. 24, no. 4, p. 042004, Jul. 2012, doi: 10.2351/1.4712151.

[15] A. J. G. Otuka, N. B. Tomazio, K. T. Paula, and C. R. Mendonça, "Two-Photon Polymerization: Functionalized Microstructures, Micro-Resonators, and Bio-Scaffolds," *Polymers*, vol. 13, no. 12, Art. no. 12, Jan. 2021, doi: 10.3390/polym13121994.

[16] C. N. LaFratta and T. Baldacchini, "Two-Photon Polymerization Metrology: Characterization Methods of Mechanisms and Microstructures," *Micromachines (Basel)*, vol. 8, no. 4, p. 101, Mar. 2017, doi: 10.3390/mi8040101.

[17] A. K. Nguyen and R. J. Narayan, "Two-photon polymerization for biological applications," *Materials Today*, vol. 20, no. 6, pp. 314–322, Jul. 2017, doi: 10.1016/j.mattod.2017.06.004.

[18] Z. Huang, G. C.-P. Tsui, Y. Deng, and C.-Y. Tang, "Two-photon polymerization nanolithography technology for fabrication of stimulus-responsive micro/nano-structures for biomedical applications," *Nanotechnology Reviews*, vol. 9, no. 1, pp. 1118–1136, Jan. 2020, doi: 10.1515/ntrev-2020-0073.

[19] A. Ovsianikov, *Investigation of Two-Photon Polymerization Technique for Applications in Photonics and Biomedicine*. Göttingen, Universidad de Hannover, 2009. Accessed: May 22, 2024. [Online]. Available: https://cuvillier.de/de/shop/publications/1104

[20] G. Liu *et al.*, “Additive manufacturing of structural materials,” *Materials Science and Engineering: R: Reports*, vol. 145, p. 100596, Jul. 2021, doi: 10.1016/j.mser.2020.100596.

[21] S. C. Ligon, R. Liska, J. Stampfl, M. Gurr, and R. Mülhaupt, “Polymers for 3D Printing and Customized Additive Manufacturing,” *Chem. Rev.*, vol. 117, no. 15, pp. 10212–10290, Aug. 2017, doi: 10.1021/acs.chemrev.7b00074.

[22] X. Chen, Q. Cao, T. Chen, D. Wang, Y. Fan, and W. Xing, “3D printing for precision construction of ceramic membranes: Current status, challenges, and prospects,” *Advanced Membranes*, vol. 3, p. 100068, Jan. 2023, doi: 10.1016/j.advmem.2023.100068.

[23] D. Tan *et al.*, “Reduction in feature size of two-photon polymerization using SCR500,” *Applied Physics Letters*, vol. 90, no. 7, p. 071106, Feb. 2007, doi: 10.1063/1.2535504.

[24] A. Ovsianikov and B. N. Chichkov, “Two-Photon Polymerization – High Resolution 3D Laser Technology and Its Applications,” in *Nanoelectronics and Photonics: From Atoms to Materials, Devices, and Architectures*, A. Korkin and F. Rosei, Eds., New York, NY: Springer, 2008, pp. 427–446. doi: 10.1007/978-0-387-76499-3_12.

[25] M. Vaezi, H. Seitz, and S. Yang, “A review on 3D micro-additive manufacturing technologies,” *Int J Adv Manuf Technol*, vol. 67, no. 5, pp. 1721–1754, Jul. 2013, doi: 10.1007/s00170-012-4605-2.

[26] X. Wang, M. Jiang, Z. Zhou, J. Gou, and D. Hui, “3D printing of polymer matrix composites: A review and prospective,” *Composites Part B: Engineering*, vol. 110, pp. 442–458, Feb. 2017, doi: 10.1016/j.compositesb.2016.11.034.

[27] S. M. Thompson, L. Bian, N. Shamsaei, and A. Yadollahi, “An overview of Direct Laser Deposition for additive manufacturing; Part I: Transport phenomena, modeling and diagnostics,” *Additive Manufacturing*, vol. 8, pp. 36–62, Oct. 2015, doi: 10.1016/j.addma.2015.07.001.

[28] C. Maibohm, O. F. Silvestre, J. Borme, M. Sinou, K. Heggarty, and J. B. Nieder, “Multi-beam two-photon polymerization for fast large area 3D periodic structure fabrication for bioapplications,” *Sci Rep*, vol. 10, no. 1, p. 8740, May 2020, doi: 10.1038/s41598-020-64955-9.

[29] L. Zheng *et al.*, “Nanofabrication of High-Resolution Periodic Structures with a Gap Size Below 100 nm by Two-Photon Polymerization,” *Nanoscale Res Lett*, vol. 14, no. 1, p. 134, Apr. 2019, doi: 10.1186/s11671-019-2955-5.

[30] R. Wu, Q. Zhan, H. Liu, X. Wen, B. Wang, and S. He, “Optical depletion mechanism of upconverting luminescence and its potential for multi-photon STED-like

microscopy," *Opt. Express, OE*, vol. 23, no. 25, pp. 32401–32412, Dec. 2015, doi: 10.1364/OE.23.032401.

[31] K. Obata, J. Koch, U. Hinze, and B. N. Chichkov, "Multi-focus two-photon polymerization technique based on individually controlled phase modulation," *Opt. Express, OE*, vol. 18, no. 16, pp. 17193–17200, Aug. 2010, doi: 10.1364/OE.18.017193.

[32] "Nanoscribe GmbH & Co. KG." Accessed: May 26, 2024. [Online]. Available: https://www.nanoscribe.com/en/

[33] "Heidelberg Instruments," Heidelberg Instruments. Accessed: May 26, 2024. [Online]. Available: https://heidelberg-instruments.com/

[34] "UpNano GmbH." Accessed: May 26, 2024. [Online]. Available: https://www.upnano.at/

[35] "Microlight3D," Microlight3D. Accessed: May 26, 2024. [Online]. Available: https://www.microlight3d.com/

[36] "Moji-Nano Technology Co., Ltd." Accessed: May 26, 2024. [Online]. Available: https://www.moji-nano.com/

[37] "FEMTIKA," FEMTIKA. Accessed: May 26, 2024. [Online]. Available: https://femtika.com/

[38] R. Menzel, Ed., "Nonlinear Interactions of Light and Matter with Absorption," in *Photonics: Linear and Nonlinear Interactions of Laser Light and Matter*, Berlin, Heidelberg: Springer, 2007, pp. 263–358. doi: 10.1007/978-3-540-45158-7_5.

[39] E. Skliutas *et al.*, "Polymerization mechanisms initiated by spatio-temporally confined light," *Nanophotonics*, vol. 10, no. 4, pp. 1211–1242, Jan. 2021, doi: 10.1515/nanoph-2020-0551.

[40] R. Menzel, Ed., "Linear Interactions Between Light and Matter," in *Photonics: Linear and Nonlinear Interactions of Laser Light and Matter*, Berlin, Heidelberg: Springer, 2007, pp. 93–171. doi: 10.1007/978-3-540-45158-7_3.

[41] G. S. He, *Nonlinear Optics and Photonics*. OUP Oxford, 2014.

[42] Y. E. S. Said, "Linear and Non-Linear Optical Phenomena of Glasses (Photonics-Photo Chromic-Electro and Magneto Optics): A Review," *Solid State Phenomena*, vol. 207, pp. 1–35, 2014, doi: 10.4028/www.scientific.net/SSP.207.1.

[43] G. S. Maciel *et al.*, "Two-Photon Processes: Dynamics and Applications," in *Multiphoton and Light Driven Multielectron Processes in Organics: New Phenomena, Materials and Applications*, F. Kajzar and M. V. Agranovich, Eds., Dordrecht: Springer Netherlands, 2000, pp. 21–30. doi: 10.1007/978-94-011-4056-0_2.

[44] D. Kang, S. Zhu, D. Liu, S. Cao, and M. Sun, “One- and Two-Photon Absorption: Physical Principle and Applications,” *The Chemical Record*, vol. 20, no. 9, pp. 894–911, 2020, doi: 10.1002/tcr.202000038.

[45] N. V. Tkachenko, “Chapter 1 - Introduction,” in *Optical Spectroscopy*, N. V. Tkachenko, Ed., Amsterdam: Elsevier Science, 2006, pp. 1–14. doi: 10.1016/B978-044452126-2/50025-3.

[46] J. Fourkas, “5 - Multiphoton lithography, processing and fabrication of photonic structures,” in *Laser Growth and Processing of Photonic Devices*, N. A. Vainos, Ed., in Woodhead Publishing Series in Electronic and Optical Materials. , Woodhead Publishing, 2012, pp. 139–161. doi: 10.1533/9780857096227.2.137.

[47] M. Rumi and J. W. Perry, “Two-photon absorption: an overview of measurements and principles,” *Adv. Opt. Photon., AOP*, vol. 2, no. 4, pp. 451–518, Dec. 2010, doi: 10.1364/AOP.2.000451.

[48] M. Göppert-Mayer, “Über Elementarakte mit zwei Quantensprüngen,” *Annalen der Physik*, vol. 401, no. 3, pp. 273–294, 1931, doi: 10.1002/andp.19314010303.

[49] W. Kaiser and C. G. B. Garrett, “Two-Photon Excitation in CaF2: Eu2+,” *Phys. Rev. Lett.*, vol. 7, no. 6, pp. 229–231, Sep. 1961, doi: 10.1103/PhysRevLett.7.229.

[50] Y. Pao and P. M. Rentzepis, “LASER-INDUCED PRODUCTION OF FREE RADICALS IN ORGANIC COMPOUNDS,” *Applied Physics Letters*, vol. 6, no. 5, pp. 93–95, Mar. 1965, doi: 10.1063/1.1754182.

[51] S. Pascal, S. David, C. Andraud, and O. Maury, “Near-infrared dyes for two-photon absorption in the short-wavelength infrared: strategies towards optical power limiting,” *Chem. Soc. Rev.*, vol. 50, no. 11, pp. 6613–6658, Jun. 2021, doi: 10.1039/D0CS01221A.

[52] N. V. Tkachenko, Ed., “Appendix C - Two photon absorption,” in *Optical Spectroscopy*, Amsterdam: Elsevier Science, 2006, pp. 293–294. doi: 10.1016/B978-044452126-2/50043-5.

[53] P. Liu, W. L. Smith, H. Lotem, J. H. Bechtel, N. Bloembergen, and R. S. Adhav, “Absolute two-photon absorption coefficients at 355 and 266 nm,” *Phys. Rev. B*, vol. 17, no. 12, pp. 4620–4632, Jun. 1978, doi: 10.1103/PhysRevB.17.4620.

[54] F. Wang and X. Liu, “1.18 - Rare-Earth Doped Upconversion Nanophosphors,” in *Comprehensive Nanoscience and Technology*, D. L. Andrews, G. D. Scholes, and G. P. Wiederrecht, Eds., Amsterdam: Academic Press, 2011, pp. 607–635. doi: 10.1016/B978-0-12-374396-1.00146-X.

[55] Y. Gao and M. J. Potasek, "Effects of excited-state absorption on two-photon absorbing materials," *Appl. Opt., AO*, vol. 45, no. 11, pp. 2521–2528, Apr. 2006, doi: 10.1364/AO.45.002521.

[56] Y. Zeng, C. Wang, F. Zhao, M. Qin, Y. Zhou, and X. Huang, "Two-photon induced excited-state absorption and optical limiting properties in a chiral polymer," *Applied Physics Letters*, vol. 102, no. 4, p. 043308, Feb. 2013, doi: 10.1063/1.4790391.

[57] S.-J. Chung, K.-S. Kim, T.-C. Lin, G. S. He, J. Swiatkiewicz, and P. N. Prasad, "Cooperative Enhancement of Two-Photon Absorption in Multi-branched Structures," *J. Phys. Chem. B*, vol. 103, no. 49, pp. 10741–10745, Dec. 1999, doi: 10.1021/jp992846z.

[58] M. Altarelli and D. L. Dexter, "Cooperative energy transfer and photon absorption," *Optics Communications*, vol. 2, no. 1, pp. 36–38, May 1970, doi: 10.1016/0030-4018(70)90025-8.

[59] K. C. Mishra, J. K. Berkowitz, E. A. Dale, T. P. Das, and K. H. Johnson, "Cooperative two-photon luminescence," *Journal of Luminescence*, vol. 46, no. 4, pp. 209–215, May 1990, doi: 10.1016/0022-2313(90)90016-5.

[60] S. O'Halloran, A. Pandit, A. Heise, and A. Kellett, "Two-Photon Polymerization: Fundamentals, Materials, and Chemical Modification Strategies," *Advanced Science*, vol. 10, no. 7, p. 2204072, 2023, doi: 10.1002/advs.202204072.

[61] R. Menzel, Ed., "Lasers," in *Photonics: Linear and Nonlinear Interactions of Laser Light and Matter*, Berlin, Heidelberg: Springer, 2007, pp. 359–531. doi: 10.1007/978-3-540-45158-7_6.

[62] L. H. Foo-Gregory and S. L, "Analysis of Two-Photon Polymerization for the Development of a Reconfigurable Micro-Device Manufacturing System.," Thesis, 2012. Accessed: Jun. 08, 2024. [Online]. Available: http://deepblue.lib.umich.edu/handle/2027.42/96099

[63] T. Asavei, T. A. Nieminen, N. R. Heckenberg, and H. Rubinsztein-Dunlop, "Fabrication of microstructures for optically driven micromachines using two-photon photopolymerization of UV curing resins," *J. Opt. A: Pure Appl. Opt.*, vol. 11, no. 3, p. 034001, Jan. 2009, doi: 10.1088/1464-4258/11/3/034001.

[64] M. Pawlicki, H. A. Collins, R. G. Denning, and H. L. Anderson, "Two-Photon Absorption and the Design of Two-Photon Dyes," *Angewandte Chemie International Edition*, vol. 48, no. 18, pp. 3244–3266, 2009, doi: 10.1002/anie.200805257.

[65] D. B. Fullager, G. D. Boreman, and T. Hofmann, "Infrared dielectric response of nanoscribe IP-dip and IP-L monomers after polymerization from 250 cm^{-1} to 6000

cm^{-1}," *Opt. Mater. Express, OME*, vol. 7, no. 3, pp. 888–894, Mar. 2017, doi: 10.1364/OME.7.000888.

[66] T. Wloka, M. Gottschaldt, and U. S. Schubert, "From Light to Structure: Photo Initiators for Radical Two-Photon Polymerization," *Chemistry – A European Journal*, vol. 28, no. 32, p. e202104191, 2022, doi: 10.1002/chem.202104191.

[67] C. Martineau, R. Anémian, C. Andraud, I. Wang, M. Bouriau, and P. L. Baldeck, "Efficient initiators for two-photon induced polymerization in the visible range," *Chemical Physics Letters*, vol. 362, no. 3, pp. 291–295, Aug. 2002, doi: 10.1016/S0009-2614(02)01073-4.

[68] T. W. Lim, S. H. Park, and D.-Y. Yang, "Contour offset algorithm for precise patterning in two-photon polymerization," *Microelectronic Engineering*, vol. 77, no. 3, pp. 382–388, Apr. 2005, doi: 10.1016/j.mee.2005.01.022.

[69] J. Ma *et al.*, "Coherent quantum control of two-photon absorption and polymerization by shaped ultrashort laser pulses," *Laser Phys. Lett.*, vol. 10, no. 8, p. 085304, Jul. 2013, doi: 10.1088/1612-2011/10/8/085304.

[70] M. Duocastella *et al.*, "Improving the Spatial Resolution in Direct Laser Writing Lithography by Using a Reversible Cationic Photoinitiator," *J. Phys. Chem. C*, vol. 121, no. 31, pp. 16970–16977, Aug. 2017, doi: 10.1021/acs.jpcc.7b03591.

[71] "Kayaku Advanced Materials, Inc." Accessed: Feb. 13, 2024. [Online]. Available: https://kayakuam.com/

[72] S. Juodkazis, V. Mizeikis, K. K. Seet, M. Miwa, and H. Misawa, "Two-photon lithography of nanorods in SU-8 photoresist," *Nanotechnology*, vol. 16, no. 6, p. 846, Apr. 2005, doi: 10.1088/0957-4484/16/6/039.

[73] M. K. Ghantasala, J. P. Hayes, E. C. Harvey, and D. K. Sood, "Patterning, electroplating and removal of SU-8 moulds by excimer laser micromachining," *J. Micromech. Microeng.*, vol. 11, no. 2, p. 133, Mar. 2001, doi: 10.1088/0960-1317/11/2/308.

[74] M. Suter *et al.*, "Superparamagnetic microrobots: fabrication by two-photon polymerization and biocompatibility," *Biomed Microdevices*, vol. 15, no. 6, pp. 997–1003, Dec. 2013, doi: 10.1007/s10544-013-9791-7.

[75] W. H. Teh, U. Dürig, U. Drechsler, C. G. Smith, and H.-J. Güntherodt, "Effect of low numerical-aperture femtosecond two-photon absorption on (SU-8) resist for ultrahigh-aspect-ratio microstereolithography," *Journal of Applied Physics*, vol. 97, no. 5, p. 054907, Feb. 2005, doi: 10.1063/1.1856214.

[76] S. Puce *et al.*, "3D-microfabrication by two-photon polymerization of an integrated sacrificial stencil mask," *Micro and Nano Engineering*, vol. 2, pp. 70–75, Mar. 2019, doi: 10.1016/j.mne.2019.01.004.

[77] B. Ganazhapa, J. Pereiro-García, X. Q. Arregui, M. A. Geday, G. Guadaño, and M. Caño-García, "Generation of arbitrarily patterned polarizers using 2-photon polymerization," *Sci Rep*, vol. 14, no. 1, p. 22550, Sep. 2024, doi: 10.1038/s41598-024-73946-z.

[78] "JSR Corporation." Accessed: Aug. 17, 2024. [Online]. Available: https://www.jsr.co.jp/jsr_e/

[79] K. Takada, K. Kaneko, Y.-D. Li, S. Kawata, Q.-D. Chen, and H.-B. Sun, "Temperature effects on pinpoint photopolymerization and polymerized micronanostructures," *Applied Physics Letters*, vol. 92, no. 4, p. 041902, Jan. 2008, doi: 10.1063/1.2834365.

[80] "Microresist technology." Accessed: Jul. 12, 2024. [Online]. Available: https://www.microresist.de/en/

[81] V. Prajzler, M. Neruda, P. Jašek, and P. Nekvindová, "The properties of free-standing epoxy polymer multi-mode optical waveguides," *Microsyst Technol*, vol. 25, no. 1, pp. 257–264, Jan. 2019, doi: 10.1007/s00542-018-3960-9.

[82] A. Elmogi, E. Bosman, J. Missinne, and G. Van Steenberge, "Comparison of epoxy- and siloxane-based single-mode optical waveguides defined by direct-write lithography," *Optical Materials*, vol. 52, pp. 26–31, Feb. 2016, doi: 10.1016/j.optmat.2015.12.009.

[83] N. T. Benéitez, "Imprinted Micro- and Nanophotonic Sensors".

[84] E. Toomey, M. Colangelo, and K. K. Berggren, "Investigation of ma-N 2400 series photoresist as an electron-beam resist for superconducting nanoscale devices," *Journal of Vacuum Science & Technology B*, vol. 37, no. 5, p. 051207, Sep. 2019, doi: 10.1116/1.5119516.

[85] N. Støvring, B. Rezaei, A. Heiskanen, J. Emnéus, and S. S. Keller, "Fabrication of pyrolytic carbon interdigitated microelectrodes by maskless UV photolithography with epoxy-based photoresists SU-8 and mr-DWL," *Micro and Nano Engineering*, vol. 23, p. 100257, Jun. 2024, doi: 10.1016/j.mne.2024.100257.

[86] "MicroChemicals GmbH," MicroChemicals GmbH. Accessed: Aug. 17, 2024. [Online]. Available: https://www.microchemicals.com/

[87] C. C. J. Alcântara *et al.*, "3D Fabrication of Fully Iron Magnetic Microrobots," *Small*, vol. 15, no. 16, p. 1805006, 2019, doi: 10.1002/smll.201805006.

[88] I. Bernardeschi, O. Tricinci, V. Mattoli, C. Filippeschi, B. Mazzolai, and L. Beccai, "Three-Dimensional Soft Material Micropatterning via Direct Laser Lithography of Flexible Molds," *ACS Appl. Mater. Interfaces*, vol. 8, no. 38, pp. 25019–25023, Sep. 2016, doi: 10.1021/acsami.6b08872.

[89] S. Biswas, "Advanced processing of vertically aligned nanodevices." Lund University, 2013. Accessed: Jul. 15, 2024. [Online]. Available: https://www.lunduniversity.lu.se/lup/publication/3737105

[90] Y. Liu, J. H. Campbell, O. Stein, L. Jiang, J. Hund, and Y. Lu, "Deformation Behavior of Foam Laser Targets Fabricated by Two-Photon Polymerization," *Nanomaterials*, vol. 8, no. 7, Art. no. 7, Jul. 2018, doi: 10.3390/nano8070498.

[91] Y. Li *et al.*, "UV to NIR optical properties of IP-Dip, IP-L, and IP-S after two-photon polymerization determined by spectroscopic ellipsometry," *Opt. Mater. Express, OME*, vol. 9, no. 11, pp. 4318–4328, Nov. 2019, doi: 10.1364/OME.9.004318.

[92] M. Hasan and S. Blair, "Maximizing transmittance in two-photon 3D printed materials for micro-optics in the visible," *Opt. Mater. Express, OME*, vol. 12, no. 3, pp. 895–906, Mar. 2022, doi: 10.1364/OME.448819.

[93] U. Jagodič, M. Vellaichamy, M. Škarabot, and I. Muševič, "Surface alignment of nematic liquid crystals by direct laser writing of photopolymer alignment layers," *Liquid Crystals*, vol. 50, no. 13–14, pp. 1999–2009, Nov. 2023, doi: 10.1080/02678292.2023.2242297.

[94] F. Qiu *et al.*, "Noncytotoxic artificial bacterial flagella fabricated from biocompatible ORMOCOMP and iron coating," *J. Mater. Chem. B*, vol. 2, no. 4, pp. 357–362, Dec. 2013, doi: 10.1039/C3TB20840K.

[95] X. Zheng, K. Cheng, X. Zhou, J. Lin, and X. Jing, "A method for positioning the focal spot location of two photon polymerization," *AIP Advances*, vol. 7, no. 9, p. 095318, Sep. 2017, doi: 10.1063/1.4986102.

[96] J. Serbin *et al.*, "Femtosecond laser-induced two-photon polymerization of inorganic–organic hybrid materials for applications in photonics," *Opt. Lett., OL*, vol. 28, no. 5, pp. 301–303, Mar. 2003, doi: 10.1364/OL.28.000301.

[97] S. Zhang *et al.*, "Ultrafast, high-resolution and large-size three-dimensional structure manufacturing through high-efficiency two-photon polymerization initiators," *Additive Manufacturing*, vol. 47, p. 102358, Nov. 2021, doi: 10.1016/j.addma.2021.102358.

[98] L. Jiang *et al.*, "Performance comparison of acrylic and thiol-acrylic resins in two-photon polymerization," *Opt. Express, OE*, vol. 24, no. 12, pp. 13687–13701, Jun. 2016, doi: 10.1364/OE.24.013687.

[99] M. Malinauskas, M. Farsari, A. Piskarskas, and S. Juodkazis, "Ultrafast laser nanostructuring of photopolymers: A decade of advances," *Physics Reports*, vol. 533, no. 1, pp. 1–31, Dec. 2013, doi: 10.1016/j.physrep.2013.07.005.

[100] Y. Shao, Y. Zhao, H. Ma, M. Chen, Y. Lian, and J. Shao, "An easy method to improve efficiency of multi-photon polymerization: Introducing solvents with nonlinear optical absorption into photoresist," *Optics & Laser Technology*, vol. 151, p. 108008, Jul. 2022, doi: 10.1016/j.optlastec.2022.108008.

[101] A. El-Tamer, U. Hinze, and B. N. Chichkov, "Two-Photon Polymerization in Optics, Microfluidics, and Biomedicine," in *Handbook of Laser Micro- and Nano-Engineering*, K. Sugioka, Ed., Cham: Springer International Publishing, 2020, pp. 1–44. doi: 10.1007/978-3-319-69537-2_35-1.

[102] H. Wang *et al.*, "Two-photon polymerization lithography for imaging optics," *Int. J. Extrem. Manuf.*, vol. 6, no. 4, p. 042002, Apr. 2024, doi: 10.1088/2631-7990/ad35fe.

[103] M. Marini *et al.*, "Microlenses Fabricated by Two-Photon Laser Polymerization for Cell Imaging with Non-Linear Excitation Microscopy," *Advanced Functional Materials*, vol. 33, no. 39, p. 2213926, 2023, doi: 10.1002/adfm.202213926.

[104] R. Guo, S. Xiao, X. Zhai, J. Li, A. Xia, and W. Huang, "Micro lens fabrication by means of femtosecond two photon photopolymerization," *Opt. Express, OE*, vol. 14, no. 2, pp. 810–816, Jan. 2006, doi: 10.1364/OPEX.14.000810.

[105] K. Vanmol, A. Kandeel, G. Y. Belay, H. Thienpont, H. Ottevaere, and J. Van Erps, "Two-Photon Polymerization-based Direct Laser Writing and Characterization of Micro-Lenses for Optical Interconnect Applications," in *2021 26th Microoptics Conference (MOC)*, Sep. 2021, pp. 1–2. doi: 10.23919/MOC52031.2021.9598125.

[106] K. Vanmol, A. A. A. Nazar, H. Thienpont, F. Ferranti, and J. V. Erps, "Fabrication of multilevel metalenses using multiphoton lithography: from design to evaluation," *Opt. Express, OE*, vol. 32, no. 6, pp. 10190–10203, Mar. 2024, doi: 10.1364/OE.514237.

[107] T. Gissibl, S. Thiele, A. Herkommer, and H. Giessen, "Two-photon direct laser writing of ultracompact multi-lens objectives," *Nature Photon*, vol. 10, no. 8, pp. 554–560, Aug. 2016, doi: 10.1038/nphoton.2016.121.

[108] Z. Wang, Y. Wu, D. Qi, W. Yu, and H. Zheng, "Two-photon polymerization for fabrication of metalenses for diffraction-limited focusing and high-resolution imaging," *Optics & Laser Technology*, vol. 169, p. 110128, Feb. 2024, doi: 10.1016/j.optlastec.2023.110128.

[109] A. Vyatskikh, S. Delalande, A. Kudo, X. Zhang, C. M. Portela, and J. R. Greer, "Additive manufacturing of 3D nano-architected metals," *Nat Commun*, vol. 9, no. 1, p. 593, Feb. 2018, doi: 10.1038/s41467-018-03071-9.

[110] Y. YUANJUN, "Fabrication of 3D metamaterials using two-photon polymerization and selective silver electroless plating," Thesis, 2011. Accessed: Aug. 18, 2024. [Online]. Available: https://scholarbank.nus.edu.sg/handle/10635/31616

[111] G. Panusa, Y. Pu, J. Wang, C. Moser, and D. Psaltis, "Fabrication of Sub-Micron Polymer Waveguides through Two-Photon Polymerization in Polydimethylsiloxane," *Polymers*, vol. 12, no. 11, Art. no. 11, Nov. 2020, doi: 10.3390/polym12112485.

[112] H. Wei, A. K. Amrithanath, and S. Krishnaswamy, "3D Printing of Micro-Optic Spiral Phase Plates for the Generation of Optical Vortex Beams," *IEEE Photonics Technology Letters*, vol. 31, no. 8, pp. 599–602, Apr. 2019, doi: 10.1109/LPT.2019.2903151.

[113] E. Brasselet, M. Malinauskas, A. Žukauskas, and S. Juodkazis, "Photopolymerized microscopic vortex beam generators: Precise delivery of optical orbital angular momentum," *Applied Physics Letters*, vol. 97, no. 21, p. 211108, Nov. 2010, doi: 10.1063/1.3517519.

[114] K. Zeng, S. He, X. Wang, and H. Luo, "Generation of Vector Vortex Beams Based on the Optical Integration of Dynamic Phase and Geometric Phase," *Photonics*, vol. 10, no. 2, Art. no. 2, Feb. 2023, doi: 10.3390/photonics10020214.

[115] M. Plidschun, M. Zeisberger, J. Kim, T. Wieduwilt, and M. A. Schmidt, "Fiber-based 3D nano-printed holography with individually phase-engineered remote points," *Sci Rep*, vol. 12, no. 1, p. 20920, Dec. 2022, doi: 10.1038/s41598-022-25380-2.

[116] C. Liberale *et al.*, "Micro-Optics Fabrication on Top of Optical Fibers Using Two-Photon Lithography," *IEEE Photonics Technology Letters*, vol. 22, no. 7, pp. 474–476, Apr. 2010, doi: 10.1109/LPT.2010.2040986.

[117] V. Rosborough *et al.*, "Photonic wire bonding via two-photon polymerization laser lithography for hybrid integration," in *Integrated Optics: Devices, Materials, and Technologies XXVII*, SPIE, Mar. 2023, pp. 147–151. doi: 10.1117/12.2647641.

[118] N. Lindenmann *et al.*, "Photonic wire bonding: a novel concept for chip-scale interconnects," *Opt. Express, OE*, vol. 20, no. 16, pp. 17667–17677, Jul. 2012, doi: 10.1364/OE.20.017667.

[119] M. R. Billah *et al.*, "Hybrid integration of silicon photonics circuits and InP lasers by photonic wire bonding," *Optica, OPTICA*, vol. 5, no. 7, pp. 876–883, Jul. 2018, doi: 10.1364/OPTICA.5.000876.

[120] S. J. Chowdhury *et al.*, "On-chip hybrid integration of swept frequency distributed-feedback laser with silicon photonic circuits using photonic wire bonding," *Opt. Express, OE*, vol. 32, no. 3, pp. 3085–3099, Jan. 2024, doi: 10.1364/OE.510036.

[121] N. Lindenmann *et al.*, "Connecting Silicon Photonic Circuits to Multicore Fibers by Photonic Wire Bonding," *Journal of Lightwave Technology*, vol. 33, no. 4, pp. 755–760, Feb. 2015, doi: 10.1109/JLT.2014.2373051.

[122] W. Lee, S. a. Pruzinsky, and P. v. Braun, "Multi-Photon Polymerization of Waveguide Structures Within Three-Dimensional Photonic Crystals," *Advanced Materials*, vol. 14, no. 4, pp. 271–274, 2002, doi: 10.1002/1521-4095(20020219)14:4<271::AID-ADMA271>3.0.CO;2-Y.

[123] S. John, "Strong localization of photons in certain disordered dielectric superlattices," *Phys. Rev. Lett.*, vol. 58, no. 23, pp. 2486–2489, Jun. 1987, doi: 10.1103/PhysRevLett.58.2486.

[124] C. C. Cheng and A. Scherer, "Fabrication of photonic band-gap crystals," *Journal of Vacuum Science & Technology B: Microelectronics and Nanometer Structures Processing, Measurement, and Phenomena*, vol. 13, no. 6, pp. 2696–2700, Nov. 1995, doi: 10.1116/1.588051.

[125] M. Thiel, M. Decker, M. Deubel, M. Wegener, S. Linden, and G. von Freymann, "Polarization Stop Bands in Chiral Polymeric Three-Dimensional Photonic Crystals," *Advanced Materials*, vol. 19, no. 2, pp. 207–210, 2007, doi: 10.1002/adma.200601497.

[126] J. Wang *et al.*, "Remote manipulation of micronanomachines containing magnetic nanoparticles," *Opt. Lett., OL*, vol. 34, no. 5, pp. 581–583, Mar. 2009, doi: 10.1364/OL.34.000581.

[127] H. Xia *et al.*, "Ferrofluids for Fabrication of Remotely Controllable Micro-Nanomachines by Two-Photon Polymerization," *Advanced Materials*, vol. 22, no. 29, pp. 3204–3207, 2010, doi: 10.1002/adma.201000542.

[128] T. Asavei, "Optically Fabricated and Driven Micromachines," 2010. Accessed: Jul. 12, 2024. [Online]. Available: https://espace.library.uq.edu.au/view/UQ:217548

[129] S. Maruo and H. Inoue, "Optically driven micropump produced by three-dimensional two-photon microfabrication," *Applied Physics Letters*, vol. 89, no. 14, p. 144101, Oct. 2006, doi: 10.1063/1.2358820.

[130] K. Kunzler, "Two-Photon Polymerization Used to Fabricate Electrothermal MEMS Actuators and Rotational Parts," May 2023, Accessed: Aug. 18, 2024. [Online]. Available: https://hdl.handle.net/2346/96387

[131] L. Ivy and A. Lal, “Solderable Multisided Metal Patterns Enables 3D Integrable Direct Laser Written Polymer MEMS,” in *2023 35th International Conference on Microelectronic Test Structure (ICMTS)*, Mar. 2023, pp. 1–6. doi: 10.1109/ICMTS55420.2023.10094101.

[132] S. Sikulskyi, R. Srinivasaraghavan Govindarajan, T. Stark, Z. Ren, N. Reed, and D. Kim, “Two-photon polymerized wetting morphologies for tunable external and internal electrode micropatterning,” *Additive Manufacturing*, vol. 86, p. 104220, Apr. 2024, doi: 10.1016/j.addma.2024.104220.

[133] Y. Shi *et al.*, “Two-Photon Laser-Written Photoalignment Layers for Patterning Liquid Crystalline Conjugated Polymer Orientation,” *Advanced Functional Materials*, vol. 31, no. 7, p. 2007493, 2021, doi: 10.1002/adfm.202007493.

[134] Y.-H. Lee *et al.*, “Two-photon polymerization enabled multi-layer liquid crystal phase modulator,” *Sci Rep*, vol. 7, no. 1, Art. no. 1, Nov. 2017, doi: 10.1038/s41598-017-16596-8.

[135] C. C. Tartan *et al.*, “Read on Demand Images in Laser-Written Polymerizable Liquid Crystal Devices,” *Advanced Optical Materials*, vol. 6, no. 20, p. 1800515, 2018, doi: 10.1002/adom.201800515.

[136] L. FRIGHETTO, “Parallelization of the two-photon polymerization technique by the use of a spatial light modulator,” Italy, 2017. Accessed: Aug. 18, 2024. [Online]. Available: https://www.politesi.polimi.it/handle/10589/135813

[137] R. J. Winfield, B. Bhuian, S. O’Brien, and G. M. Crean, “Fabrication of grating structures by simultaneous multi-spot fs laser writing,” *Applied Surface Science*, vol. 253, no. 19, pp. 8086–8090, Jul. 2007, doi: 10.1016/j.apsusc.2007.02.100.

[138] S. Reede, I. Eichhorn, M. Oellers, A. Schander, and M. J. Vellekoop, “Two-Photon Polymerized Flow Sensor Integrated in a Microfluidic Channel with Optoelectronic Readout,” in *2020 IEEE SENSORS*, Oct. 2020, pp. 1–4. doi: 10.1109/SENSORS47125.2020.9278690.

[139] C. Plamadeala, S. R. Gosain, S. Purkhart, B. Buchegger, W. Baumgartner, and J. Heitz, “Three-Dimensional Photonic Structures Fabricated by Two-Photon Polymerization for Microfluidics and Microneedles,” in *2018 20th International Conference on Transparent Optical Networks (ICTON)*, Jul. 2018, pp. 1–4. doi: 10.1109/ICTON.2018.8473647.

[140] J. Wang *et al.*, “Embellishment of microfluidic devices via femtosecond laser micronanofabrication for chip functionalization,” *Lab Chip*, vol. 10, no. 15, pp. 1993–1996, Aug. 2010, doi: 10.1039/C003264F.

[141] D. Serien, H. Kawano, A. Miyawaki, K. Midorikawa, and K. Sugioka, "Femtosecond Laser Direct Write Integration of Multi-Protein Patterns and 3D Microstructures into 3D Glass Microfluidic Devices," *Applied Sciences*, vol. 8, no. 2, Art. no. 2, Feb. 2018, doi: 10.3390/app8020147.

[142] N. Nekrasov, N. Yakunina, V. Nevolin, I. Bobrinetskiy, P. Vasilevsky, and A. Y. Gerasimenko, "Two-Photon Polymerization of Albumin Hydrogel Nanowires Strengthened with Graphene Oxide," *Biomimetics*, vol. 6, no. 4, Art. no. 4, Dec. 2021, doi: 10.3390/biomimetics6040066.

[143] C. Yi, S. Qu, Y. Wang, H. Qi, Y. Zhang, and G. J. Cheng, "Optical force brush enabled free-space painting of 4D functional structures," *Science Advances*, vol. 9, no. 38, p. eadg0300, Sep. 2023, doi: 10.1126/sciadv.adg0300.

[144] S. D. Gittard, A. Ovsianikov, B. N. Chichkov, A. Doraiswamy, and R. J. Narayan, "Two-photon polymerization of microneedles for transdermal drug delivery," *Expert Opinion on Drug Delivery*, vol. 7, no. 4, pp. 513–533, Apr. 2010, doi: 10.1517/17425241003628171.

[145] K. S. Worthington *et al.*, "Two-photon polymerization for production of human iPSC-derived retinal cell grafts," *Acta Biomaterialia*, vol. 55, pp. 385–395, Jun. 2017, doi: 10.1016/j.actbio.2017.03.039.

[146] C. Xin *et al.*, "Light-triggered multi-joint microactuator fabricated by two-in-one femtosecond laser writing," *Nat Commun*, vol. 14, no. 1, p. 4273, Jul. 2023, doi: 10.1038/s41467-023-40038-x.

[147] M. Farsari and B. N. Chichkov, "Two-photon fabrication," *Nature Photon*, vol. 3, no. 8, pp. 450–452, Aug. 2009, doi: 10.1038/nphoton.2009.131.

[148] *Principles of Tissue Engineering*. 2020. Accessed: Aug. 19, 2024. [Online]. Available: https://shop.elsevier.com/books/principles-of-tissue-engineering/lanza/978-0-12-818422-6

[149] P. Tayalia, C. R. Mendonca, T. Baldacchini, D. J. Mooney, and E. Mazur, "3D Cell-Migration Studies using Two-Photon Engineered Polymer Scaffolds," *Advanced Materials*, vol. 20, no. 23, pp. 4494–4498, 2008, doi: 10.1002/adma.200801319.

[150] W. Wang *et al.*, "Two-photon polymerization-based 3D micro-scaffolds toward biomedical devices," *Chemical Engineering Journal*, vol. 493, p. 152469, Aug. 2024, doi: 10.1016/j.cej.2024.152469.

[151] J. Mačiulaitis *et al.*, "Preclinical study of SZ2080 material 3D microstructured scaffolds for cartilage tissue engineering made by femtosecond direct laser writing lithography,"

Biofabrication, vol. 7, no. 1, p. 015015, Mar. 2015, doi: 10.1088/1758-5090/7/1/015015.

[152] R. J. Narayan, A. Doraiswamy, D. B. Chrisey, and B. N. Chichkov, "Medical prototyping using two photon polymerization," *Materials Today*, vol. 13, no. 12, pp. 42–48, Dec. 2010, doi: 10.1016/S1369-7021(10)70223-6.

[153] M. Hunt *et al.*, "Harnessing Multi-Photon Absorption to Produce Three-Dimensional Magnetic Structures at the Nanoscale," *Materials*, vol. 13, no. 3, Art. no. 3, Jan. 2020, doi: 10.3390/ma13030761.

[154] A. Grabulosa, J. Moughames, X. Porte, and D. Brunner, "Combining one and two photon polymerization for accelerated high performance (3 + 1)D photonic integration," *Nanophotonics*, vol. 11, no. 8, pp. 1591–1601, Mar. 2022, doi: 10.1515/nanoph-2021-0733.

[155] M. T. Do, Q. Li, T. T. N. Nguyen, H. Benisty, I. Ledoux-Rak, and N. D. Lai, "High aspect ratio submicrometer two-dimensional structures fabricated by one-photon absorption direct laser writing," *Microsyst Technol*, vol. 20, no. 10, pp. 2097–2102, Oct. 2014, doi: 10.1007/s00542-014-2096-9.

[156] C. Woo Ha, P. Prabhakaran, and K.-S. Lee, "Versatile applications of three-dimensional objects fabricated by two-photon-initiated polymerization," *MRS Communications*, vol. 9, no. 1, pp. 53–66, Mar. 2019, doi: 10.1557/mrc.2018.218.

[157] V. Nathan, A. H. Guenther, and S. S. Mitra, "Review of multiphoton absorption in crystalline solids," *J. Opt. Soc. Am. B, JOSAB*, vol. 2, no. 2, pp. 294–316, Feb. 1985, doi: 10.1364/JOSAB.2.000294.

[158] M. Emons, K. Obata, T. Binhammer, A. Ovsianikov, B. N. Chichkov, and U. Morgner, "Two-photon polymerization technique with sub-50 nm resolution by sub-10 fs laser pulses," *Opt. Mater. Express, OME*, vol. 2, no. 7, pp. 942–947, Jul. 2012, doi: 10.1364/OME.2.000942.

[159] D. Li and K. Du, "Ultrashort Pulse Lasers," in *Handbook of Laser Micro- and Nano-Engineering*, K. Sugioka, Ed., Cham: Springer International Publishing, 2021, pp. 331–365. doi: 10.1007/978-3-030-63647-0_58.

[160] S. Maruo and K. Ikuta, "Three-dimensional microfabrication by use of single-photon-absorbed polymerization," *Applied Physics Letters*, vol. 76, no. 19, pp. 2656–2658, May 2000, doi: 10.1063/1.126742.

[161] E. Rebollar and M. Castillejo, "Laser Interactions with Organic/Polymer Materials," in *Handbook of Laser Micro- and Nano-Engineering*, K. Sugioka, Ed., Cham: Springer International Publishing, 2021, pp. 165–212. doi: 10.1007/978-3-030-63647-0_13.

[162] E. Abbe, “Beiträge zur Theorie des Mikroskops und der mikroskopischen Wahrnehmung,” *Archiv f. mikrosk. Anatomie*, vol. 9, no. 1, pp. 413–468, Dec. 1873, doi: 10.1007/BF02956173.

[163] Z. Gan, Y. Cao, R. A. Evans, and M. Gu, “Three-dimensional deep sub-diffraction optical beam lithography with 9 nm feature size,” *Nat Commun*, vol. 4, no. 1, p. 2061, Jun. 2013, doi: 10.1038/ncomms3061.

[164] S.-F. Liu, Z.-W. Hou, L. Lin, Z. Li, and H.-B. Sun, “3D Laser Nanoprinting of Functional Materials,” *Advanced Functional Materials*, vol. 33, no. 39, p. 2211280, 2023, doi: 10.1002/adfm.202211280.

[165] S. Zhang *et al.*, “High-efficiency two-photon polymerization initiators based on coumarin derivatives for additive manufacturing with sub-wavelength resolution,” *Materials Today Chemistry*, vol. 30, p. 101599, Jun. 2023, doi: 10.1016/j.mtchem.2023.101599.

[166] S. H. Park, T. W. Lim, D.-Y. Yang, R. H. Kim, and K.-S. Lee, “Improvement of spatial resolution in nano-stereolithography using radical quencher,” *Macromol. Res.*, vol. 14, no. 5, pp. 559–564, Oct. 2006, doi: 10.1007/BF03218724.

[167] J. Fischer and M. Wegener, “Three-dimensional optical laser lithography beyond the diffraction limit,” *Laser & Photonics Reviews*, vol. 7, no. 1, pp. 22–44, 2013, doi: 10.1002/lpor.201100046.

[168] J. M. Otón and E. Otón, *Harnessing light: some notes on photonics*, 09/05/2022 ed. UPM-Press.

[169] T. A. Klar, S. Jakobs, M. Dyba, A. Egner, and S. W. Hell, “Fluorescence microscopy with diffraction resolution barrier broken by stimulated emission,” *Proceedings of the National Academy of Sciences*, vol. 97, no. 15, pp. 8206–8210, Jul. 2000, doi: 10.1073/pnas.97.15.8206.

[170] T. A. Klar, R. Wollhofen, and J. Jacak, “Sub-Abbe resolution: from STED microscopy to STED lithography,” *Phys. Scr.*, vol. 2014, no. T162, p. 014049, Sep. 2014, doi: 10.1088/0031-8949/2014/T162/014049.

[171] R. Wollhofen, J. Katzmann, C. Hrelescu, J. Jacak, and T. A. Klar, “120 nm resolution and 55 nm structure size in STED-lithography,” *Opt. Express, OE*, vol. 21, no. 9, pp. 10831–10840, May 2013, doi: 10.1364/OE.21.010831.

[172] A. I. Akash, J. E. Johnson, F. C. Arentz, and X. Xu, “Two-color 3D printing for reduction in femtosecond laser printing power,” *Opt. Express, OE*, vol. 32, no. 15, pp. 25892–25905, Jul. 2024, doi: 10.1364/OE.525826.

[173] L. Li, R. R. Gattass, E. Gershgoren, H. Hwang, and J. T. Fourkas, "Achieving λ/20 Resolution by One-Color Initiation and Deactivation of Polymerization," *Science*, vol. 324, no. 5929, pp. 910–913, May 2009, doi: 10.1126/science.1168996.

[174] M. P. Stocker, L. Li, R. R. Gattass, and J. T. Fourkas, "Multiphoton photoresists giving nanoscale resolution that is inversely dependent on exposure time," *Nature Chem*, vol. 3, no. 3, pp. 223–227, Mar. 2011, doi: 10.1038/nchem.965.

[175] R. R. McLeod, B. A. Kowalski, and M. C. Cole, "Two-color photo-initiation/inhibition lithography," in *Advanced Fabrication Technologies for Micro/Nano Optics and Photonics III*, SPIE, Feb. 2010, pp. 9–16. doi: 10.1117/12.845850.

[176] T. F. Scott, B. A. Kowalski, A. C. Sullivan, C. N. Bowman, and R. R. McLeod, "Two-Color Single-Photon Photoinitiation and Photoinhibition for Subdiffraction Photolithography," *Science*, vol. 324, no. 5929, pp. 913–917, May 2009, doi: 10.1126/science.1167610.

[177] E. Rittweger, B. R. Rankin, V. Westphal, and S. W. Hell, "Fluorescence depletion mechanisms in super-resolving STED microscopy," *Chemical Physics Letters*, vol. 442, no. 4, pp. 483–487, Jul. 2007, doi: 10.1016/j.cplett.2007.06.017.

[178] L. De Boni, E. Piovesan, L. Misoguti, S. C. Zílio, and C. R. Mendonca, "Two-Photon Absorption Dependence on the Temperature for Azoaromatic Compounds: Effect of Molecular Conformation," *J. Phys. Chem. A*, vol. 111, no. 28, pp. 6222–6224, Jul. 2007, doi: 10.1021/jp0716684.

[179] G. Zyla and M. Farsari, "Frontiers of Laser-Based 3D Printing: A Perspective on Multi-Photon Lithography," *Laser & Photonics Reviews*, vol. 18, no. 7, p. 2301312, 2024, doi: 10.1002/lpor.202301312.

[180] L. Yang *et al.*, "Projection two-photon polymerization using a spatial light modulator," *Optics Communications*, vol. 331, pp. 82–86, Nov. 2014, doi: 10.1016/j.optcom.2014.05.051.

[181] Q. Geng, D. Wang, P. Chen, and S.-C. Chen, "Ultrafast multi-focus 3-D nano-fabrication based on two-photon polymerization," *Nat Commun*, vol. 10, no. 1, p. 2179, May 2019, doi: 10.1038/s41467-019-10249-2.

[182] S. Mckee *et al.*, "3D Printing by Two-Photon Polymerization," in *2020 Italian Conference on Optics and Photonics (ICOP)*, Sep. 2020, pp. 1–3. doi: 10.1109/ICOP49690.2020.9300308.

[183] E. E. Morales-Delgado, L. Urio, D. B. Conkey, N. Stasio, D. Psaltis, and C. Moser, "Three-dimensional microfabrication through a multimode optical fiber," *Opt. Express, OE*, vol. 25, no. 6, pp. 7031–7045, Mar. 2017, doi: 10.1364/OE.25.007031.

[184] “Rhothor, the ideal high speed smart deflector in beam deflection,” Rhothor Deflector. Accessed: Jun. 11, 2024. [Online]. Available: https://www.newson.be/rhothor_SmartDeflector.htm

[185] “Motor simulation tool,” Tecnotion. Accessed: Jun. 11, 2024. [Online]. Available: https://www.tecnotion.com/simulation-tool/

[186] “Objective NanoFocusing Stages.” Accessed: Jun. 11, 2024. [Online]. Available: https://www.newport.com/f/nanofocusing-objective-lens-mount

[187] “Acousto-Optic Modulator (AOM),” Modulators. Accessed: Jun. 24, 2024. [Online]. Available: https://gandh.com/products/acousto-optics/modulators

[188] “Mounted Zero-Order Half-Wave Plates.” Accessed: Jun. 11, 2024. [Online]. Available: https://www.thorlabs.com

[189] B. E. A. Saleh and M. C. Teich, “Polarization and Crystal Optics,” in *Fundamentals of Photonics*, John Wiley & Sons, Ltd, 1991, pp. 193–237.

[190] E. Hecht, *Optics*, 5th edition. Pearson, 2015.

[191] Office of the CTO, *MKS Instruments Handbook - Principles and Applications in Photonics Technologies*, MKS Instruments, Inc. 2019. Accessed: Jun. 18, 2024. [Online]. Available: https://www.newport.com/photonics-handbook

[192] T. Huang, S. Liu, P. Yi, and T. Shi, “Focusing and leveling system for optical lithography using linear CCD,” in *2008 International Conference on Optical Instruments and Technology: Optoelectronic Measurement Technology and Applications*, SPIE, Feb. 2009, pp. 767–772. doi: 10.1117/12.808083.

[193] SICK Sensor Intelligence, “Operating Instructions OD Precision - Displacement Sensor.” Accessed: Jun. 18, 2024. [Online]. Available: https://www.sick.com/es/en/s/downloads?category=g568283

[194] “Femtosecond Fiber Laser Technology from Calmar Laser,” Calmar Laser. Accessed: Jun. 22, 2024. [Online]. Available: https://www.calmarlaser.com/

[195] “G&H Products,” Gooch & Housego. Accessed: Jun. 24, 2024. [Online]. Available: https://gandh.com/

[196] “Thorlabs, Inc. - Your Source for Fiber Optics, Laser Diodes, Optical Instrumentation and Polarization Measurement & Control,” Thorlabs, Inc. Accessed: Jun. 22, 2024. [Online]. Available: https://www.thorlabs.com

[197] “Newson - Moving Optics, the freedom to build great laser machines,” Newson. Accessed: Jun. 22, 2024. [Online]. Available: https://www.newson.be/

[198] “Newport - Photonics Solutions for Extending the Frontiers of Science,” Newport Corporation. Accessed: Jun. 22, 2024. [Online]. Available: https://www.newport.com/

[199] “Lasing, S.A.” Accessed: Feb. 13, 2024. [Online]. Available: https://www.lasing.com/

[200] “IDEX Health & Science, Your Partner to Engineer Optofluidics,” IDEX Health & Science. Accessed: Jun. 22, 2024. [Online]. Available: https://www.idex-hs.com

[201] “Olympus Life Science Solutions,” Olympus Microscopy. Accessed: Jun. 22, 2024. [Online]. Available: https://www.olympus-lifescience.com/en/

[202] “Mvotem Optics - Leader of intelligent imaging optical system,” Mvotem Optics. Accessed: Jun. 22, 2024. [Online]. Available: https://en.mvotem.com/

[203] “IDS - Industrial cameras,” IDS Imaging Development Systems GmbH. Accessed: Jun. 22, 2024. [Online]. Available: https://en.ids-imaging.com/

[204] “ACS Motion Control,” ACS Motion Control. Accessed: Jun. 24, 2024. [Online]. Available: https://www.acsmotioncontrol.com/

[205] “SICK Sensor Intelligence.” Accessed: Jul. 11, 2024. [Online]. Available: http://www.sick.com

[206] Z. Faraji Rad, P. Prewett, and G. Davies, “High-resolution two-photon polymerization: the most versatile technique for the fabrication of microneedle arrays,” *Microsystems and Nanoengineering*, vol. 7, no. 1, Art. no. 1, Jan. 2021, doi: 10.1038/s41378-021-00298-3.

[207] A. Roncaglia, “Advanced Lithography,” in *Springer Handbook of Semiconductor Devices*, M. Rudan, R. Brunetti, and S. Reggiani, Eds., Cham: Springer International Publishing, 2023, pp. 279–308. doi: 10.1007/978-3-030-79827-7_8.

[208] “CEMDATIC – CEMDATIC web page.” Accessed: Jul. 12, 2024. [Online]. Available: https://cemdatic.upm.es/

[209] Y. Yan and A. A. Bettiol, “Selective electro-less plating of SU-8 microstructures fabricated using two-photon polymerization,” in *2010 Photonics Global Conference*, Dec. 2010, pp. 1–4. doi: 10.1109/PGC.2010.5705980.

[210] A. Jaiswal, C. K. Rastogi, S. Rani, G. P. Singh, S. Saxena, and S. Shukla, “Two decades of two-photon lithography: Materials science perspective for additive manufacturing of 2D/3D nano-microstructures,” *iScience*, vol. 26, no. 4, Apr. 2023, doi: 10.1016/j.isci.2023.106374.

[211] S. Schlie *et al.*, “Three-Dimensional Cell Growth on Structures Fabricated from ORMOCER® by Two-Photon Polymerization Technique,” *J Biomater Appl*, vol. 22, no. 3, pp. 275–287, Nov. 2007, doi: 10.1177/0885328207077590.

[212] L. Pertoldi, V. Zega, C. Comi, and R. Osellame, "Dynamic mechanical characterization of two-photon-polymerized SZ2080 photoresist," *Journal of Applied Physics*, vol. 128, no. 17, p. 175102, Nov. 2020, doi: 10.1063/5.0022367.

[213] A. Desponds, A. Banyasz, G. Montagnac, C. Andraud, P. Baldeck, and S. Parola, "Microfabrication by two-photon lithography, and characterization, of SiO2/TiO2 based hybrid and ceramic microstructures," *J Sol-Gel Sci Technol*, vol. 95, no. 3, pp. 733–745, Sep. 2020, doi: 10.1007/s10971-020-05355-3.

[214] S. Biswas, "Advanced processing of vertically aligned nanodevices." Lund University, 2013. Accessed: Feb. 13, 2024. [Online]. Available: https://www.lunduniversity.lu.se/lup/publication/3737105

[215] Y. Chen, J. Wang, Z. Hu, T. Gao, W. Zhu, and X. Wang, "Fabrication of large-scale freestanding THz wire grid polarizers by femtosecond laser micromachining," *Optik*, vol. 212, p. 164655, Jun. 2020, doi: 10.1016/j.ijleo.2020.164655.

[216] A. Marino *et al.*, "Two-Photon Polymerization of Sub-micrometric Patterned Surfaces: Investigation of Cell-Substrate Interactions and Improved Differentiation of Neuron-like Cells," *ACS Appl. Mater. Interfaces*, vol. 5, no. 24, pp. 13012–13021, Dec. 2013, doi: 10.1021/am403895k.

[217] Q. Song, "Design of synthetic diffractive structures for 3D visualization applications and their fabrication by a novel parallel-write two-photon polymerization process," phdthesis, Ecole nationale supérieure Mines-Télécom Atlantique, 2020. Accessed: Jul. 15, 2024. [Online]. Available: https://theses.hal.science/tel-02945442

[218] Z. Wang, Y. Wu, D. Qi, W. Yu, and H. Zheng, "Two-photon polymerization for fabrication of metalenses for diffraction-limited focusing and high-resolution imaging," *Optics & Laser Technology*, vol. 169, p. 110128, Feb. 2024, doi: 10.1016/j.optlastec.2023.110128.

[219] T. T. N. Nguyen, "Fabrication and optimization of polymer-based photonic structures and applications to nonlinear optics," phdthesis, École normale supérieure de Cachan - ENS Cachan, 2015. Accessed: Jul. 15, 2024. [Online]. Available: https://theses.hal.science/tel-01221694

[220] S. Ishihara and M. Mizusaki, "Alignment control technology of liquid crystal molecules," *Journal of the Society for Information Display*, vol. 28, no. 1, pp. 44–74, 2020, doi: 10.1002/jsid.825.

[221] L. P. Jones, "Alignment Properties of Liquid Crystals," in *Handbook of Visual Display Technology*, J. Chen, W. Cranton, and M. Fihn, Eds., Berlin, Heidelberg: Springer, 2012, pp. 1387–1402. doi: 10.1007/978-3-540-79567-4_86.

[222] J. Kim, Y. Li, M. N. Miskiewicz, C. Oh, M. W. Kudenov, and M. J. Escuti, "Fabrication of ideal geometric-phase holograms with arbitrary wavefronts," *Optica, OPTICA*, vol. 2, no. 11, pp. 958–964, Nov. 2015, doi: 10.1364/OPTICA.2.000958.

[223] Y. Guo *et al.*, "High-Resolution and High-Throughput Plasmonic Photopatterning of Complex Molecular Orientations in Liquid Crystals," *Advanced Materials*, vol. 28, no. 12, pp. 2353–2358, 2016, doi: 10.1002/adma.201506002.

[224] G. Myhre, "Patterned Liquid Crystal Polymer Retarders, Polarizers, and Sources," The university of Arizona, 2012. Accessed: Feb. 13, 2024. [Online]. Available: https://ui.adsabs.harvard.edu/abs/2012PhDT.....71M

[225] W. Shen, H. Zhang, Z. Miao, and Z. Ye, "Recent Progress in Functional Dye-Doped Liquid Crystal Devices," *Advanced Functional Materials*, vol. 33, no. 6, p. 2210664, 2023, doi: 10.1002/adfm.202210664.

[226] Y. Won, H. S. Shin, M. Jo, Y. J. Lim, R. Manda, and S. H. Lee, "An electrically switchable dye-doped liquid crystal polarizer for organic light emitting-diode displays," *Journal of Molecular Liquids*, vol. 333, p. 115922, Jul. 2021, doi: 10.1016/j.molliq.2021.115922.

[227] Y. Yang, L. Wang, H. Yang, and Q. Li, "3D Chiral Photonic Nanostructures Based on Blue-Phase Liquid Crystals," *Small Science*, vol. 1, no. 6, p. 2100007, 2021, doi: 10.1002/smsc.202100007.

[228] J. Sandford O'Neill *et al.*, "3D Switchable Diffractive Optical Elements Fabricated with Two-Photon Polymerization," *Advanced Optical Materials*, vol. 10, no. 7, p. 2102446, 2022, doi: 10.1002/adom.202102446.

[229] H. Yoshida, "Functionalisation of cholesteric liquid crystals by direct laser writing," *Liquid Crystals Today*, vol. 21, no. 1, pp. 3–19, Jan. 2012, doi: 10.1080/1358314X.2012.656392.

[230] M. del Pozo, J. A. H. P. Sol, A. P. H. J. Schenning, and M. G. Debije, "4D Printing of Liquid Crystals: What's Right for Me?," *Advanced Materials*, vol. 34, no. 3, p. 2104390, 2022, doi: 10.1002/adma.202104390.

[231] I. A. Pavlov *et al.*, "High-quality alignment of nematic liquid crystals using periodic nanostructures created by nonlinear laser lithography," *Journal of Molecular Liquids*, vol. 267, pp. 212–221, Oct. 2018, doi: 10.1016/j.molliq.2018.02.058.

[232] Z. Ji *et al.*, "Compartmentalized liquid crystal alignment induced by sparse polymer ribbons with surface relief gratings," *Opt. Lett., OL*, vol. 41, no. 2, pp. 336–339, Jan. 2016, doi: 10.1364/OL.41.000336.

[233] Z. He, G. Tan, D. Chanda, and S.-T. Wu, "Novel liquid crystal photonic devices enabled by two-photon polymerization [Invited]," *Opt. Express*, vol. 27, no. 8, p. 11472, Apr. 2019, doi: 10.1364/OE.27.011472.

[234] Y.-H. Lee, G. Tan, K. Yin, T. Zhan, and S.-T. Wu, "Compact see-through near-eye display with depth adaption," *Journal of the Society for Information Display*, vol. 26, no. 2, pp. 64–70, 2018, doi: 10.1002/jsid.635.

[235] S. Moon *et al.*, "Augmented reality near-eye display using Pancharatnam-Berry phase lenses," *Sci Rep*, vol. 9, no. 1, Art. no. 1, Apr. 2019, doi: 10.1038/s41598-019-42979-0.

[236] M. Stebryte, I. Nys, J. Beeckman, and K. Neyts, "Chiral liquid crystal based holographic reflective lens for spectral detection," *Opt. Express, OE*, vol. 30, no. 24, pp. 42829–42839, Nov. 2022, doi: 10.1364/OE.472821.

[237] L. Zhu *et al.*, "Pancharatnam–Berry phase reversal via opposite-chirality-coexisted superstructures," *Light Sci Appl*, vol. 11, no. 1, Art. no. 1, May 2022, doi: 10.1038/s41377-022-00835-3.

[238] D. Marco, María. M. Sánchez-López, A. Cofré, A. Vargas, and I. Moreno, "Geometric-phase grating as an optical vortex generator and detector," vol. 11354, p. 1135430, Apr. 2020, doi: 10.1117/12.2565547.

[239] "BEAM Co." Accessed: Feb. 13, 2024. [Online]. Available: https://www.beamco.com/

[240] A. A. Sonin, *The surface physics of liquid crystals*. Australia; United States: Gordon and Breach Publishers, 1995.

[241] K. Takatoh, M. Hasegawa, M. Koden, N. Itoh, R. Hasegawa, and M. Sakamoto, *Alignment Technology and Applications of Liquid Crystal Devices*. Taylor & Francis, 2005.

[242] A. Rastegar, M. Škarabot, B. Blij, and Th. Rasing, "Mechanism of liquid crystal alignment on submicron patterned surfaces," *Journal of Applied Physics*, vol. 89, no. 2, pp. 960–964, Jan. 2001, doi: 10.1063/1.1335649.

[243] J. L. Janning, "Thin film surface orientation for liquid crystals," *Applied Physics Letters*, vol. 21, no. 4, pp. 173–174, Aug. 1972, doi: 10.1063/1.1654331.

[244] Z. Yan, J. Yao, Y. Hou, J. Zhou, J. Sun, and X. Huang, "Polarized optical properties in liquid crystals devices with photoaligned metal nanoparticle gratings," *Appl. Phys. A*, vol. 127, no. 2, p. 82, Jan. 2021, doi: 10.1007/s00339-020-04240-8.

[245] F. S. Yeung *et al.*, "Variable liquid crystal pretilt angles by nanostructured surfaces," *Applied Physics Letters*, vol. 88, no. 5, p. 051910, Jan. 2006, doi: 10.1063/1.2171491.

[246] K. Yin, J. Xiong, Z. He, and S.-T. Wu, “Patterning Liquid-Crystal Alignment for Ultrathin Flat Optics,” *ACS Omega*, vol. 5, no. 49, pp. 31485–31489, Dec. 2020, doi: 10.1021/acsomega.0c05087.

[247] T. Seki, “New strategies and implications for the photoalignment of liquid crystalline polymers,” *Polym J*, vol. 46, no. 11, Art. no. 11, Nov. 2014, doi: 10.1038/pj.2014.68.

[248] M. N. Miskiewicz and M. J. Escuti, “Direct-writing of complex liquid crystal patterns,” *Opt. Express, OE*, vol. 22, no. 10, pp. 12691–12706, May 2014, doi: 10.1364/OE.22.012691.

[249] B. Zhang, F. K. Lee, O. K. C. Tsui, and P. Sheng, “Liquid Crystal Orientation Transition on Microtextured Substrates,” *Phys. Rev. Lett.*, vol. 91, no. 21, p. 215501, Nov. 2003, doi: 10.1103/PhysRevLett.91.215501.

[250] W. Kim, D. S. Kim, and D. K. Yoon, “Surface-induced orientation of liquid crystal phases,” *Giant*, p. 100324, Jul. 2024, doi: 10.1016/j.giant.2024.100324.

[251] F. Qi, Y. Li, D. Tan, H. Yang, and Q. Gong, “Polymerized nanotips via two-photon photopolymerization,” *Opt. Express, OE*, vol. 15, no. 3, pp. 971–976, Feb. 2007, doi: 10.1364/OE.15.000971.

[252] H.-B. Sun and S. Kawata, “Two-Photon Photopolymerization and 3D Lithographic Microfabrication,” in *NMR • 3D Analysis • Photopolymerization*, N. Fatkullin, T. Ikehara, H. Jinnai, S. Kawata, R. Kimmich, T. Nishi, Y. Nishikawa, and H.-B. Sun, Eds., in Apvances in Polymer Science. , Berlin, Heidelberg: Springer, 2004, pp. 169–273. doi: 10.1007/b94405.

[253] C. H. Gooch and H. A. Tarry, “Optical characteristics of twisted nematic liquid-crystal films,” *Electronics Letters*, vol. 10, no. 1, pp. 2–4, Jan. 1974, doi: 10.1049/el:19740002.

[254] C. Carrasco-Vela, X. Quintana, E. Otón, M. Geday, and J. Otón, “Security devices based on liquid crystals doped with a colour dye,” *Opto-Electronics Review*, vol. 19, no. 4, pp. 496–500, Dec. 2011, doi: 10.2478/s11772-011-0049-8.

[255] H. Y. D. Sigaki, R. F. de Souza, R. T. de Souza, R. S. Zola, and H. V. Ribeiro, “Estimating physical properties from liquid crystal textures via machine learning and complexity-entropy methods,” *Phys. Rev. E*, vol. 99, no. 1, p. 013311, Jan. 2019, doi: 10.1103/PhysRevE.99.013311.

[256] A. Ovsianikov, B. Chichkov, P. Mente, N. A. Monteiro-Riviere, A. Doraiswamy, and R. J. Narayan, “Two Photon Polymerization of Polymer–Ceramic Hybrid Materials for Transdermal Drug Delivery,” *International Journal of Applied Ceramic Technology*, vol. 4, no. 1, pp. 22–29, 2007, doi: 10.1111/j.1744-7402.2007.02115.x.

[257] S. Maruo, "Stereolithography and Two-Photon Polymerization," in *Handbook of Laser Micro- and Nano-Engineering*, K. Sugioka, Ed., Cham: Springer International Publishing, 2021, pp. 1375–1399. doi: 10.1007/978-3-030-63647-0_24.

[258] S. H. Park, T. W. Lim, D.-Y. Yang, R. H. Kim, and K.-S. Lee, "Improvement of spatial resolution in nano-stereolithography using radical quencher," *Macromol. Res.*, vol. 14, no. 5, pp. 559–564, Oct. 2006, doi: 10.1007/BF03218724.

[259] W.-E. Lu, X.-Z. Dong, W.-Q. Chen, Z.-S. Zhao, and X.-M. Duan, "Novel photoinitiator with a radical quenching moiety for confining radical diffusion in two-photon induced photopolymerization," *J. Mater. Chem.*, vol. 21, no. 15, pp. 5650–5659, Mar. 2011, doi: 10.1039/C0JM04025H.

[260] K.-S. Lee, R. H. Kim, D.-Y. Yang, and S. H. Park, "Advances in 3D nano/microfabrication using two-photon initiated polymerization," *Progress in Polymer Science*, vol. 33, no. 6, pp. 631–681, Jun. 2008, doi: 10.1016/j.progpolymsci.2008.01.001.

[261] N. Tsutsumi, K. Nagata, and W. Sakai, "Two-photon laser fabrication of three-dimensional silver microstructures with submicron scale linewidth," *Appl. Phys. A*, vol. 103, no. 2, pp. 421–426, May 2011, doi: 10.1007/s00339-011-6356-6.

[262] M. R. Haq and H. Schift, "Vertical sidewalls in thick epoxy resists – a challenge for laser-based direct write lithography," *Micro and Nano Engineering*, vol. 19, p. 100210, Jun. 2023, doi: 10.1016/j.mne.2023.100210.

[263] "Manufacturing of substrates with different surface roughness for cell migration test by two-photon polymerization method - ScienceDirect." Accessed: Aug. 02, 2024. [Online]. Available: https://www.sciencedirect.com/science/article/pii/S221282711830653X

[264] M. Khayet, "Characterization Of Membrane Distillation Membranes By Tapping Mode Atomic Force Microscopy," in *Recent Advances in Multidisciplinary Applied Physics*, A. Méndez-Vilas, Ed., Oxford: Elsevier Science Ltd, 2005, pp. 141–148. doi: 10.1016/B978-008044648-6.50023-9.

[265] G. Lemercier *et al.*, "Two-photon absorption: from optical power limiting to 3D microfabrication," *Comptes Rendus Chimie*, vol. 8, no. 8, pp. 1308–1316, Aug. 2005, doi: 10.1016/j.crci.2004.11.038.

[266] C. Barner-Kowollik *et al.*, "3D Laser Micro- and Nanoprinting: Challenges for Chemistry," *Angewandte Chemie International Edition*, vol. 56, no. 50, pp. 15828–15845, 2017, doi: 10.1002/anie.201704695.

[267] D. J. Whyte, E. H. Doeven, A. Sutti, A. Z. Kouzani, and S. D. Adams, “Volumetric additive manufacturing: A new frontier in layer-less 3D printing,” *Additive Manufacturing*, vol. 84, p. 104094, Mar. 2024, doi: 10.1016/j.addma.2024.104094.

[268] J. Madrid-Wolff *et al.*, “A review of materials used in tomographic volumetric additive manufacturing,” *MRS Communications*, vol. 13, no. 5, pp. 764–785, Oct. 2023, doi: 10.1557/s43579-023-00447-x.

[269] L. Amato *et al.*, “Fabrication of high-aspect ratio SU-8 micropillar arrays,” *Microelectronic Engineering*, vol. 98, pp. 483–487, Oct. 2012, doi: 10.1016/j.mee.2012.07.092.

[270] N. A. Bakhtina, M. Müller, H. Wischnewski, R. Arora, and C. Ciaudo, “3D Synthetic Microstructures Fabricated by Two-Photon Polymerization Promote Homogeneous Expression of NANOG and ESRRB in Mouse Embryonic Stem Cells,” *Advanced Materials Interfaces*, vol. 8, no. 6, p. 2001964, 2021, doi: 10.1002/admi.202001964.

[271] G. Weisgrab *et al.*, “3D Printing of large-scale and highly porous biodegradable tissue engineering scaffolds from poly(trimethylene-carbonate) using two-photon-polymerization,” *Biofabrication*, vol. 12, no. 4, p. 045036, Sep. 2020, doi: 10.1088/1758-5090/abb539.

[272] B. Jia, D. Buso, J. Li, and M. Gu, “Nonlinear nanocomposites for three-dimensional photonic crystals using two-photon polymerization,” in *Conference on Lasers and Electro-Optics 2010 (2010), paper JWA18*, Optica Publishing Group, May 2010, p. JWA18. doi: 10.1364/QELS.2010.JWA18.

[273] J. Heitz *et al.*, “Three-dimensional photonic structures on transparent substrates fabricated by two-photon polymerization for use as cell substrates and for wetting experiments,” in *2016 18th International Conference on Transparent Optical Networks (ICTON)*, Jul. 2016, pp. 1–4. doi: 10.1109/ICTON.2016.7550521.

[274] J. Song, C. Michas, C. S. Chen, A. E. White, and M. W. Grinstaff, “From Simple to Architecturally Complex Hydrogel Scaffolds for Cell and Tissue Engineering Applications: Opportunities Presented by Two-Photon Polymerization,” *Advanced Healthcare Materials*, vol. 9, no. 1, p. 1901217, 2020, doi: 10.1002/adhm.201901217.

[275] A. Z. Zabidi *et al.*, “Computational mechanical characterization of geometrically transformed Schwarz P lattice tissue scaffolds fabricated via two photon polymerization (2PP),” *Additive Manufacturing*, vol. 25, pp. 399–411, Jan. 2019, doi: 10.1016/j.addma.2018.11.021.

Appendix A: Cleaning and spin-coating processes

Cleaning processes carried out on all used substrates, as well as spin-coating and baking processes applied to the photoresists used in this work.

Table A.1: Cleaning processes on ITO-Glass substrates.

N.	Process	Times [minutes]
1	Immersion in Acetone	1
2	Immersion in 2-propanol	1
3	Ultrasonic	30
4	Nitrogen flow drying	No specific times*
5	Baking @ 200 °C	> 120
6	Cooling to room temperature	30
7	UVO-Cleaning	10

Table A.2: Spin-coating and baking parameters of photoresists in this thesis.

	S1800	SU-8 TF 6002	SU-8 2015	mr-DWL 40	EpoCore 5
Film thickness [µm]	0.5 (S1805) 1.8 (S1818)	2.0	38.0	40.0	15.0
Spin-coating	3500 rpm, 500 rpm/s, 30 sec	500 rpm, 100 rpm/s, 5 sec 3000 rpm, 500 rpm/s, 30 sec	500 rpm, 100 rpm/s, 5 sec 1000 rpm, 300 rpm/s, 30 sec	1500 rpm, 500 rpm/s, 60 sec	1000 rpm, 500 rpm/s, 30 sec
Soft-Bake	1 min @ 115 °C	3 min @ 110 °C	4 min @ 95 °C	2 min @ 50 °C 5 min @ 90 °C	2 min @ 50 °C 4 min @ 90 °C
Relaxation	--	--	--	30 min	--
Exposure	2PP	1PP & 2PP	2PP	2PP	2PP
Post-bake	Not needed	2 min @ 110 °C	6 min @ 95 °C	5 min @ 50 °C 5 min @ 90 °C	2 min @ 50 °C 4 min @ 85 °C
Relaxation	--	--	--	2 hrs	30 min
Develop-ment	30 sec (Microposit)	3 min (PGMEA)	5 min (PGMEA)	5 ±1 min (mr-Dev 600)	1 min (mr-Dev 600)

Appendix B: Fine focusing

Calculation of the factor H' for fine focusing on the air configuration of the custom 2PP system.

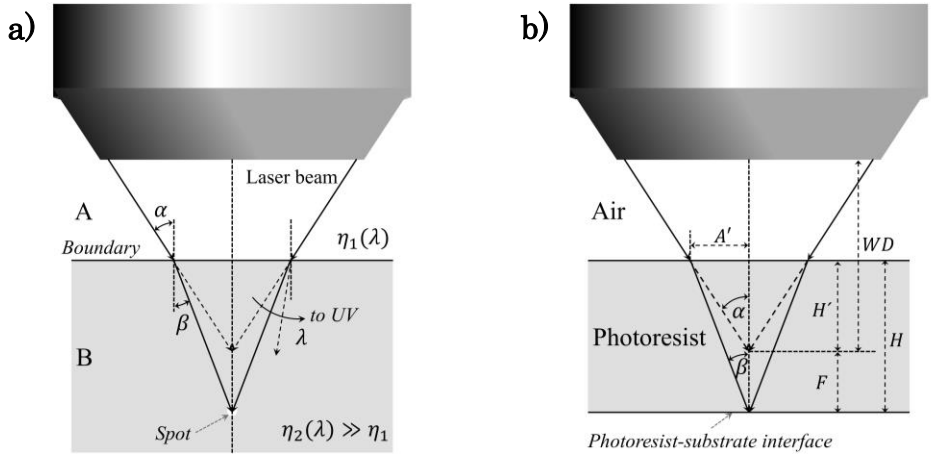

Figure B.1: a) Description of light propagation in two media with different refractive indices at the wavelength of the light. b) Derivation of the focal spot of the light within the photoresist for focusing at the photoresist-substrate interface.

Law of Snell:

$$n_1 \sin\alpha = n_2 \sin\beta$$

Numerical aperture (NA) of objective lens (OL) in the air configuration:

$$NA = n_{air} \sin\alpha$$

$$NA = n_{phr} \sin\beta$$

Beam waist on photoresist surface:

$$\tan\alpha = \frac{A'}{H'}$$

$$\tan\beta = \frac{A'}{H}$$

Deduction of factor H':

$$H' \tan\alpha = H \tan\beta$$

$$H' = H \frac{\tan\beta}{\tan\alpha}$$

By applying the identity $\sin^2\theta + \cos^2\theta = 1$ to factor H' and simplifying $\tan\theta$, where θ is the angle for the respective medium, the factor H' can be rewritten as:

$$H' = H\sqrt{\frac{n_{air}^2 - NA^2}{n_{phr}^2 - NA^2}}$$

Assigning, $Z = \sqrt{\frac{n_{air}^2 - NA^2}{n_{phr}^2 - NA^2}}$

$$H' = Z\,H$$

Therefore,

$$\frac{dH'}{dH} = Z$$

That means, if the thickness H of the photoresist increases in micron units, the factor H' increases in Z inside of the photoresist. Finally,

$$F = H - H'$$
$$F = H(1 - Z)$$
$$\frac{dF}{dH} = 1 - Z$$

That mean, when H increases, the focal spot (F) of the laser beam increases $1 - Z$. This assures that the focusing may occur at the photoresist-substrate interface when H varies.

Therefore, H' and F also depends on the refractive index of both air and the photoresist and used OL. The NA of the OL is a constant commonly given by the fabricant, but refractive index is calculated using Cauchy's equation to define how much the path of light is bent in the medium at wavelength (λ) of the light. This expression is commonly given by the photoresist fabricant, and is expressed by:

$$n(\lambda) = A + \frac{B}{\lambda^2} + \frac{C}{\lambda^4} + \cdots$$

where, A, B and C are coefficients of the material. Table B.1 summarized the coefficients of photoresists used in this work.

Table B.1: Coefficients of the air and photoresists, and refractive indices at $\lambda = 405$ nm and 780 nm.

Material	**A**	**B**	**C**	$\boldsymbol{n(\lambda = 405)}$	$\boldsymbol{n(\lambda = 780)}$
air	1.00027262	1.53271037	1.319296e+4	1.00028245	1.00027517
S1800	1.5935	1.8854e+4	4.1211e+6	1.70859906	1.62450061
SU-8 2000	1.5660	7.96e+3	1.4e+8	1.61973284	1.57946172
SU-8 6000	1.5674	8.03e+3	1.4e+8	1.62155960	1.58097678
mr-DWL	1.5700	8.20e+3	3.5e+8	1.63300150	1.58442353
EpoCore	1.5730	7.50e+3	4.7e+8	1.63619413	1.58659717

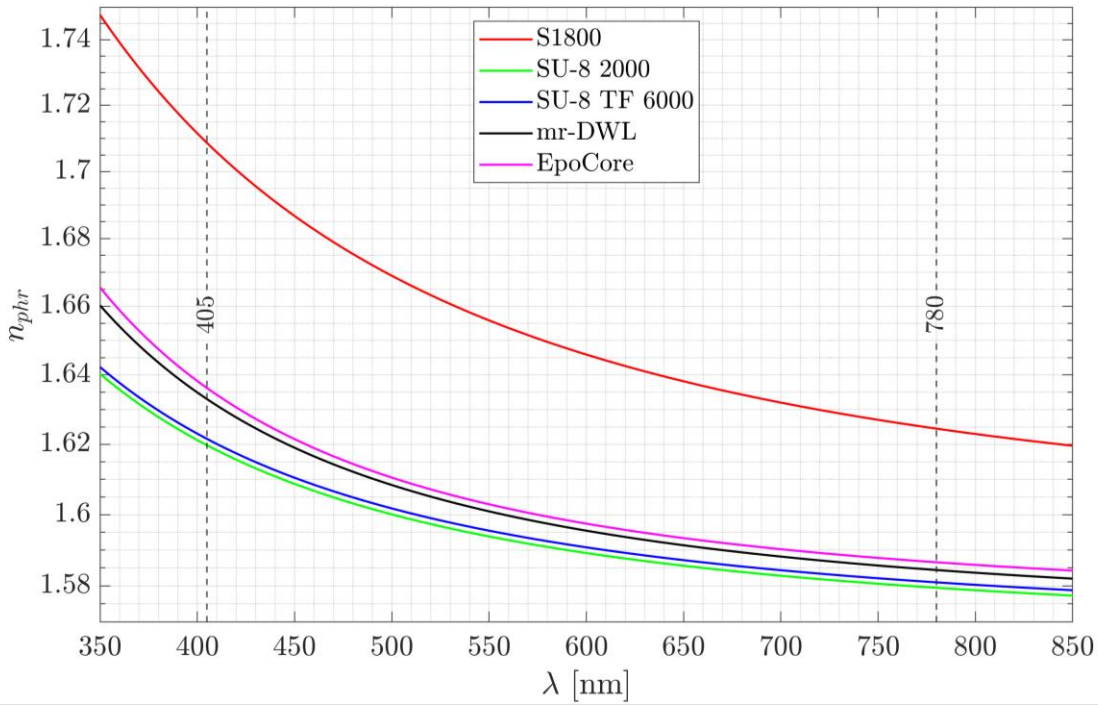

Figure B.2: Refractive indices of used photoresists in this work.

Appendix C: Results in optimization processes

SEM results of the polymerized 2D and 3D patterned objects from the optimization experiments in 1PP-DLW and 2PP-DLW processes.

a)

b)

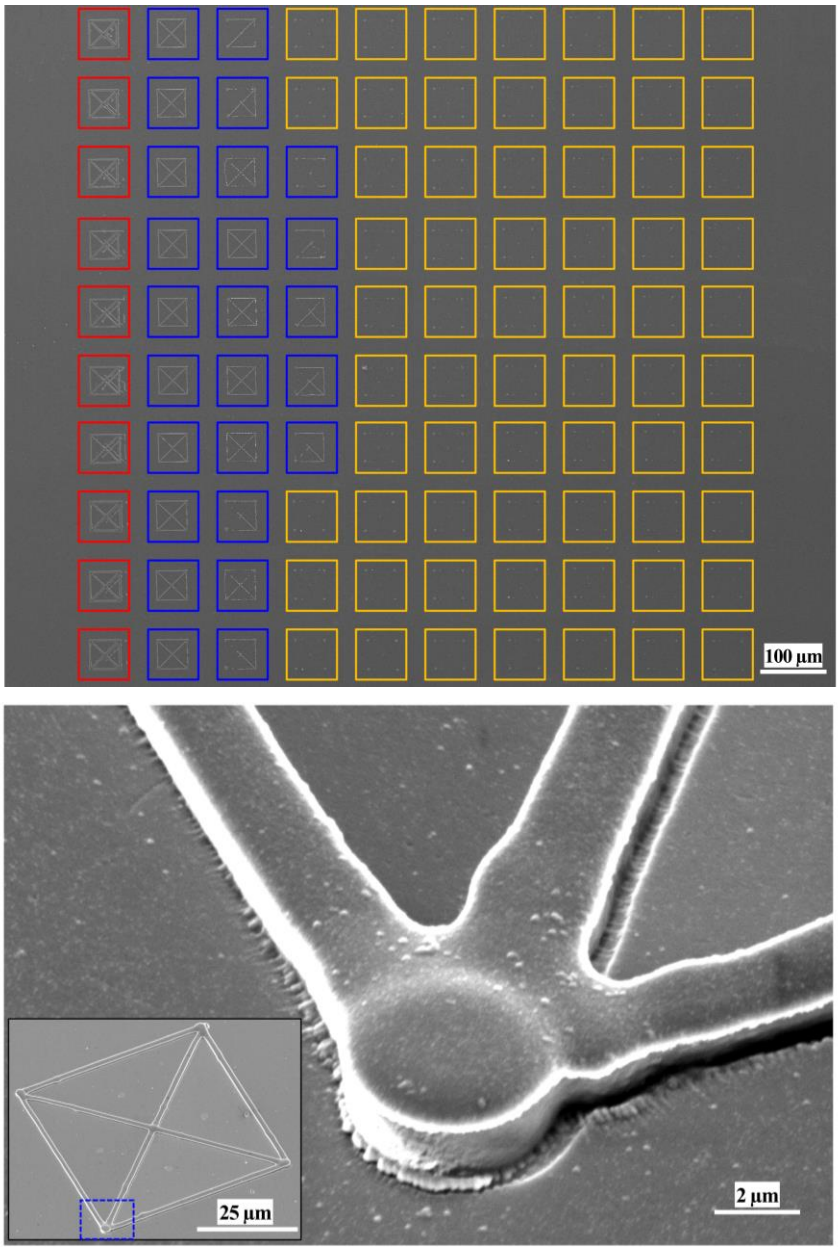

Figure C.1: a) SEM images of an entire polymerized test grid in 1PP-DLW process optimization. The red squares are over-exposed objects, the blue ones are polymerized, and the yellow ones are non-polymerized. b) SEM images of an entire polymerized pattern object in SU-8.

a)

b)

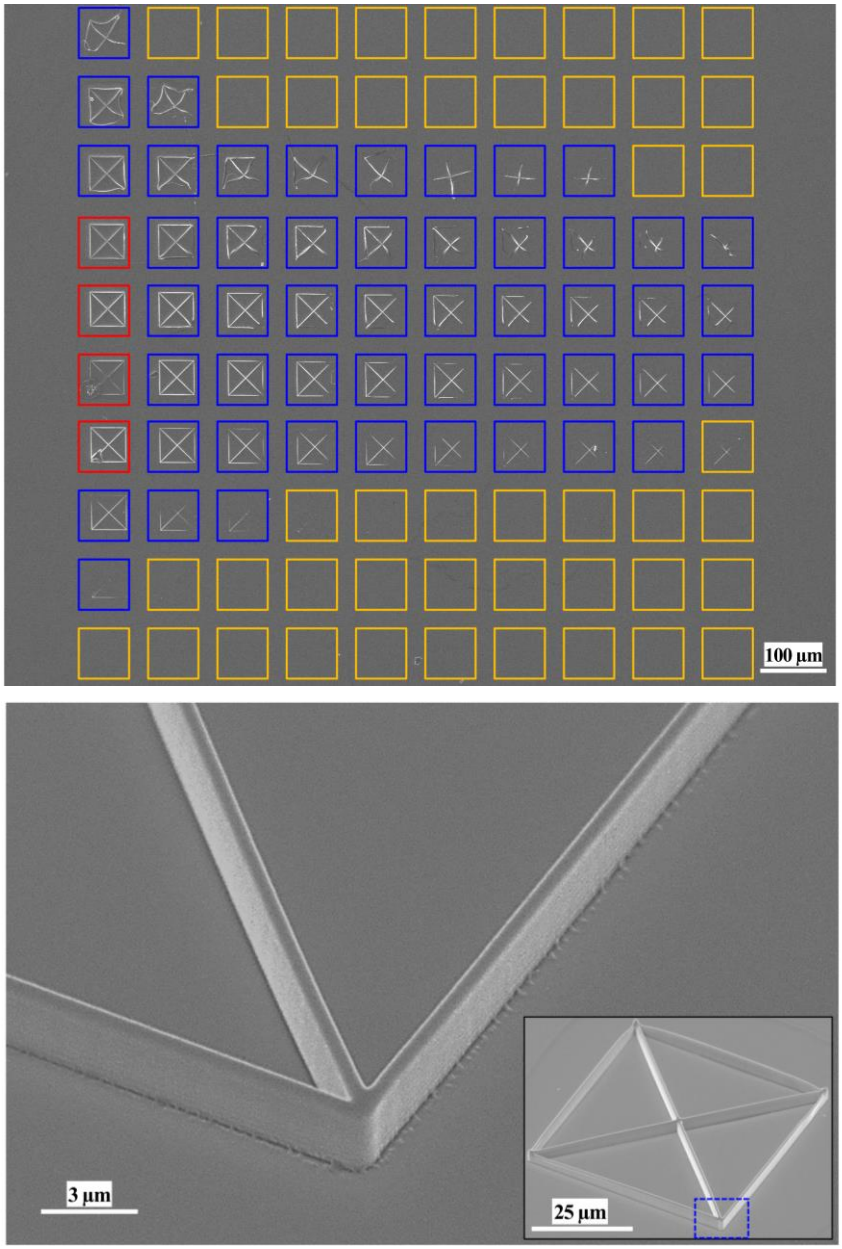

Figure C.2: a) SEM images of an entire polymerized test grid in 2PP-DLW process optimization. The red squares are over-exposed objects, the blue ones are polymerized, and the yellow ones are non-polymerized. b) SEM images of an entire polymerized pattern object in SU-8.

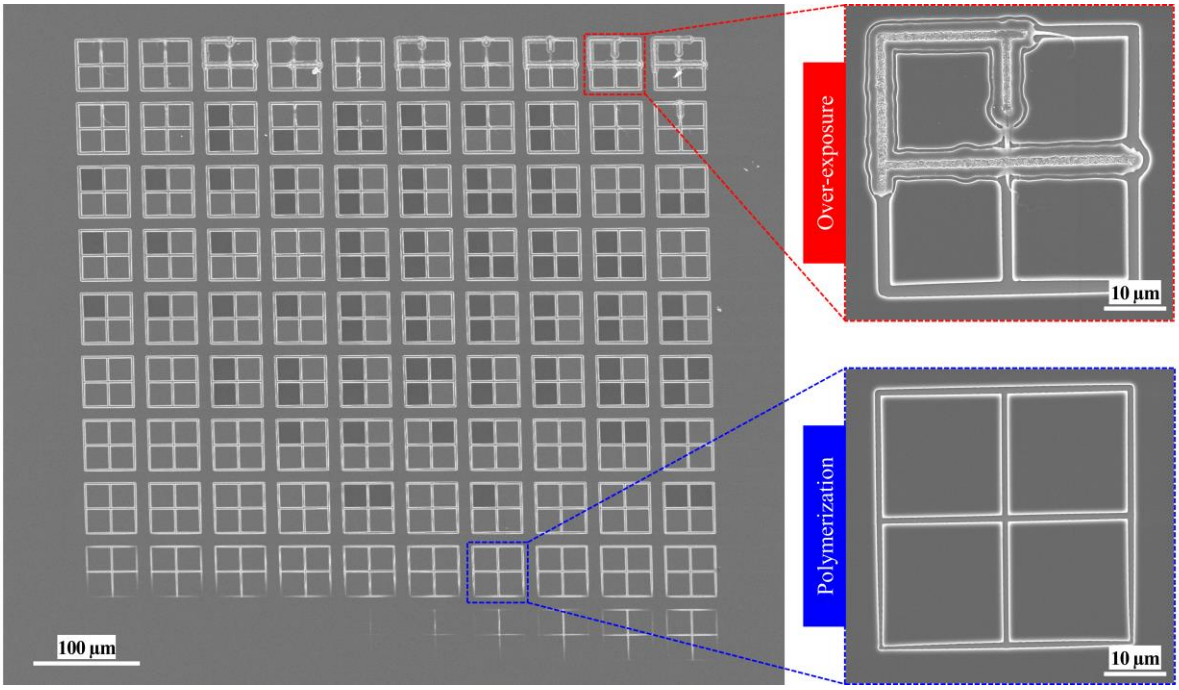

Figure C.3: SEM images of an entire polymerized test grid in 2PP-DLW for voxel characterization in positive-tone photoresist S1805.

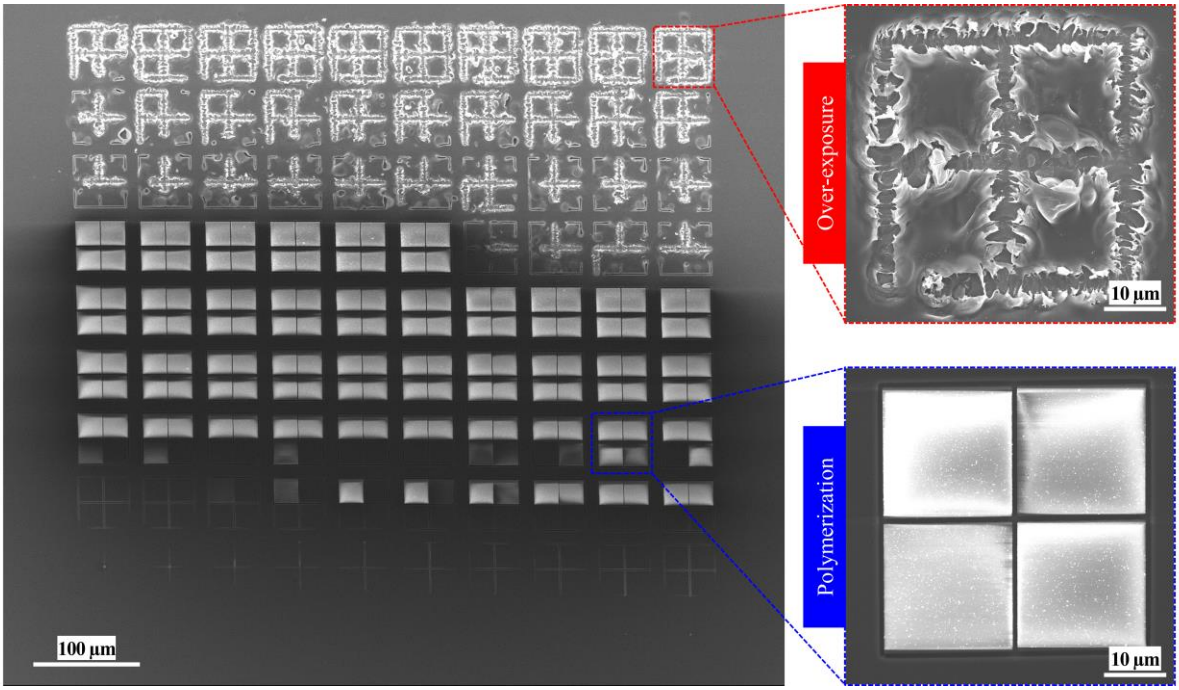

Figure C.4: SEM images of an entire polymerized test grid in 2PP-DLW for voxel characterization in positive-tone photoresist S1818.

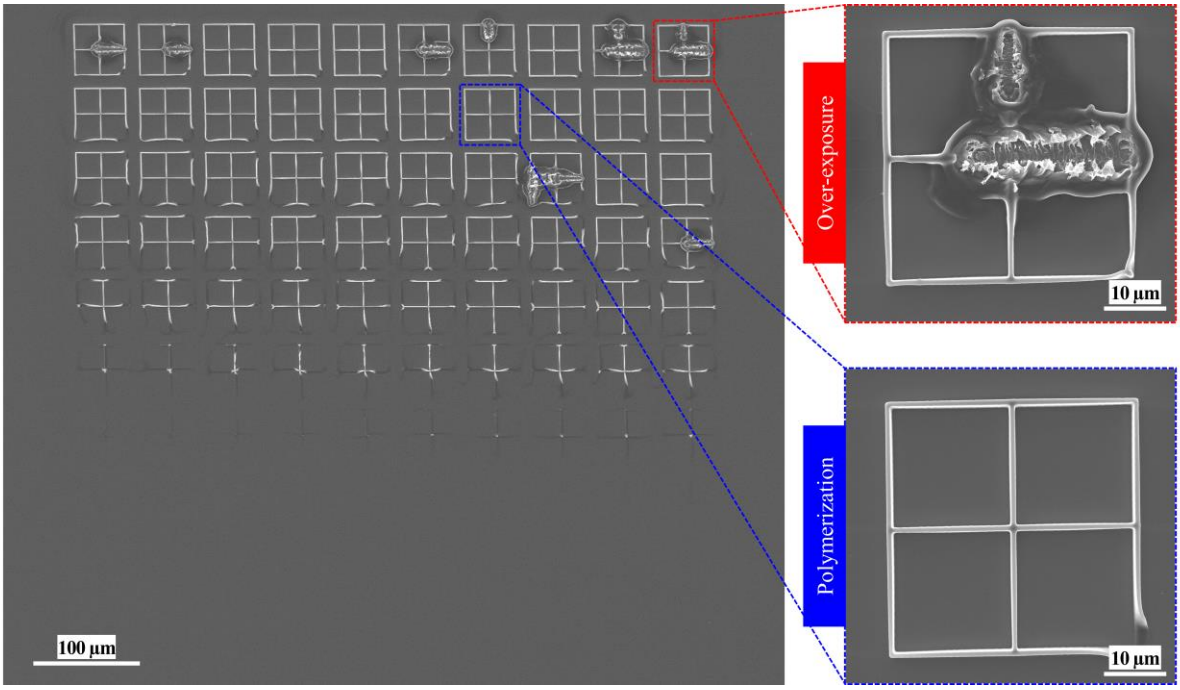

Figure C.5: SEM images of an entire polymerized test grid in 2PP-DLW for voxel characterization in negative-tone photoresist SU-8 TF 6002.

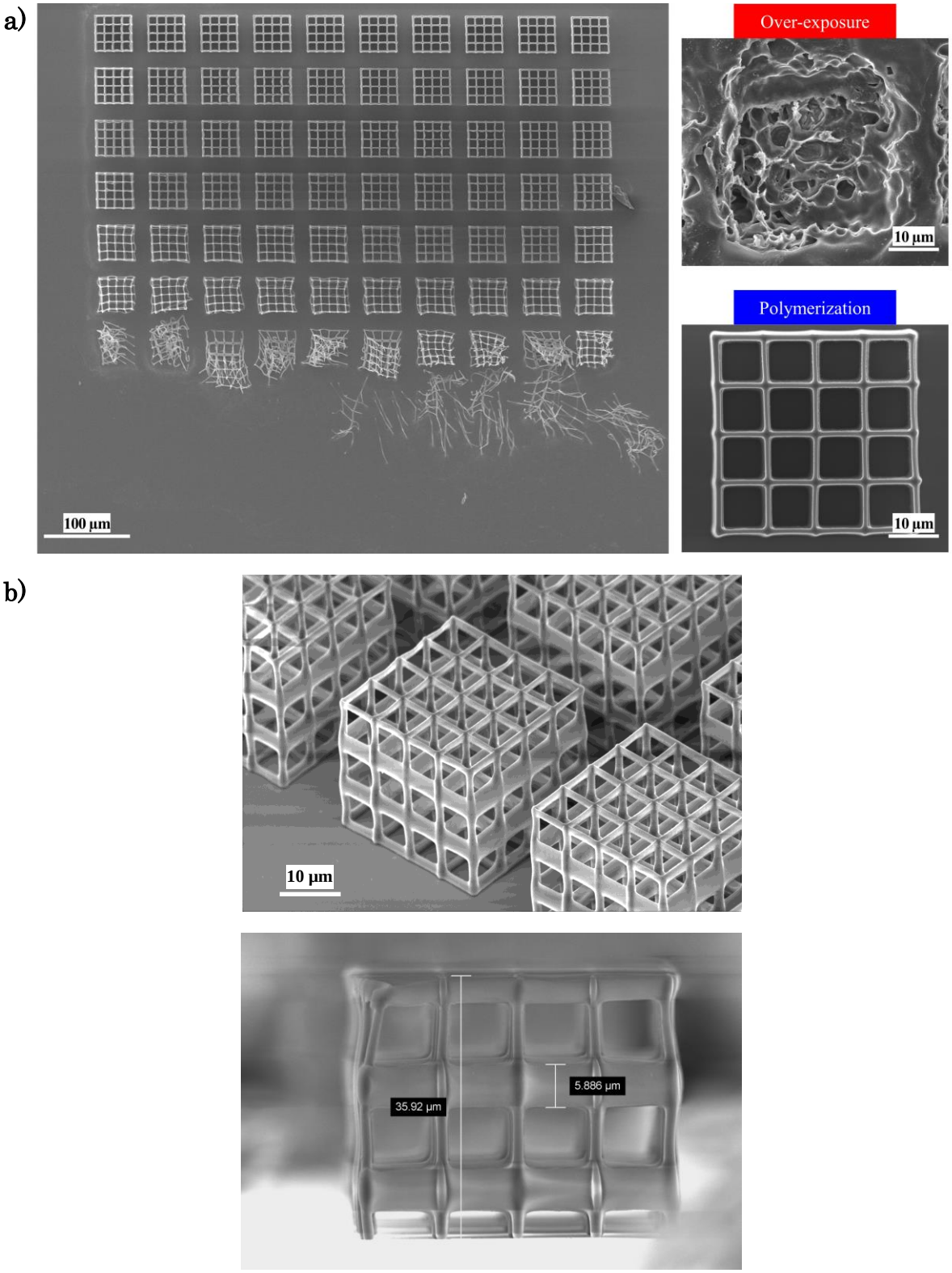

Figure C.6: a) SEM images of an entire polymerized test grid in 2PP-DLW for voxel characterization in negative-tone photoresist SU-8 2015. b) View of one 3D pattern object.

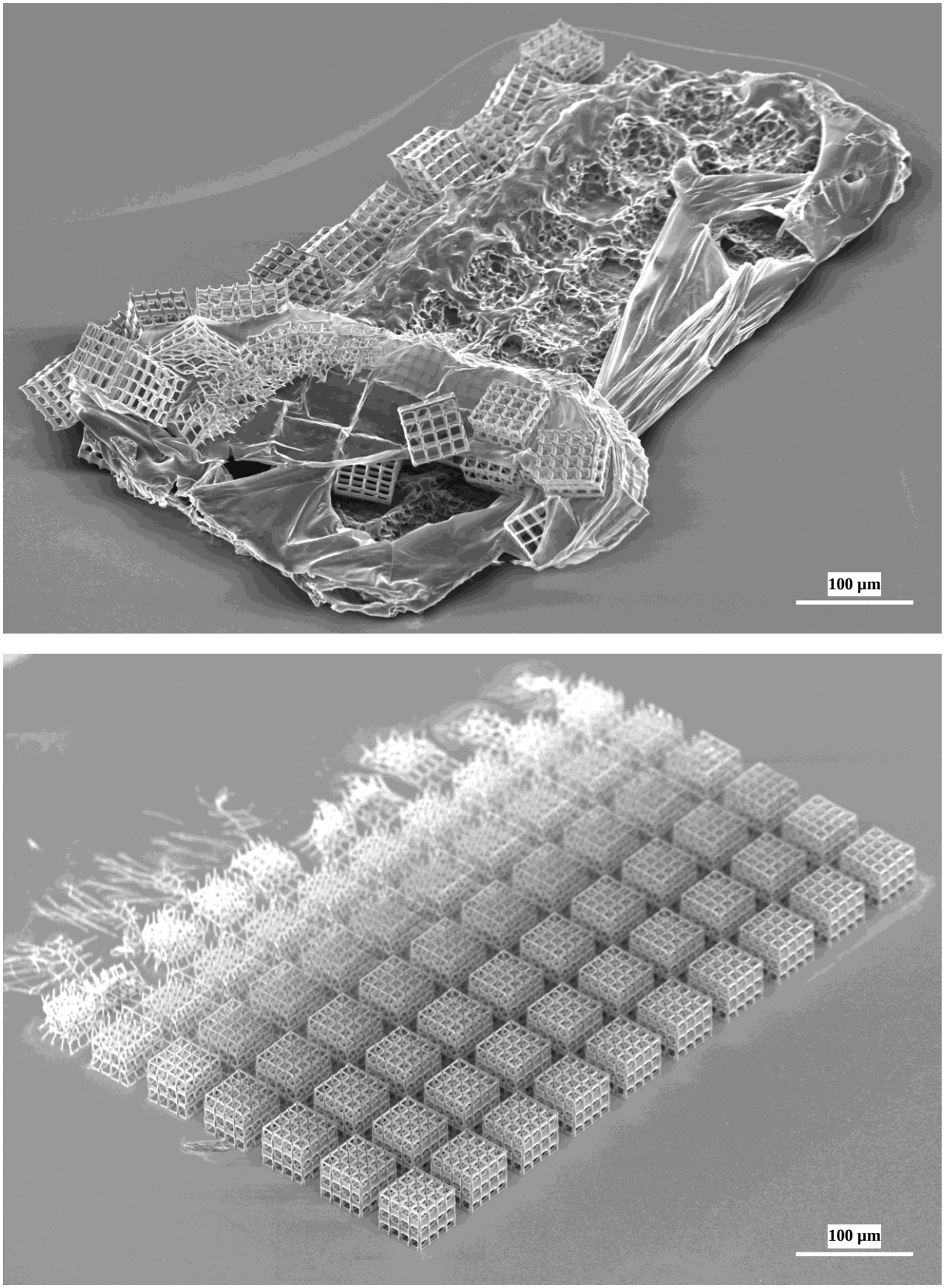

Figure C.7: 3D-view of the test grid where one is completely burned, and the other one is perfectly polymerized.

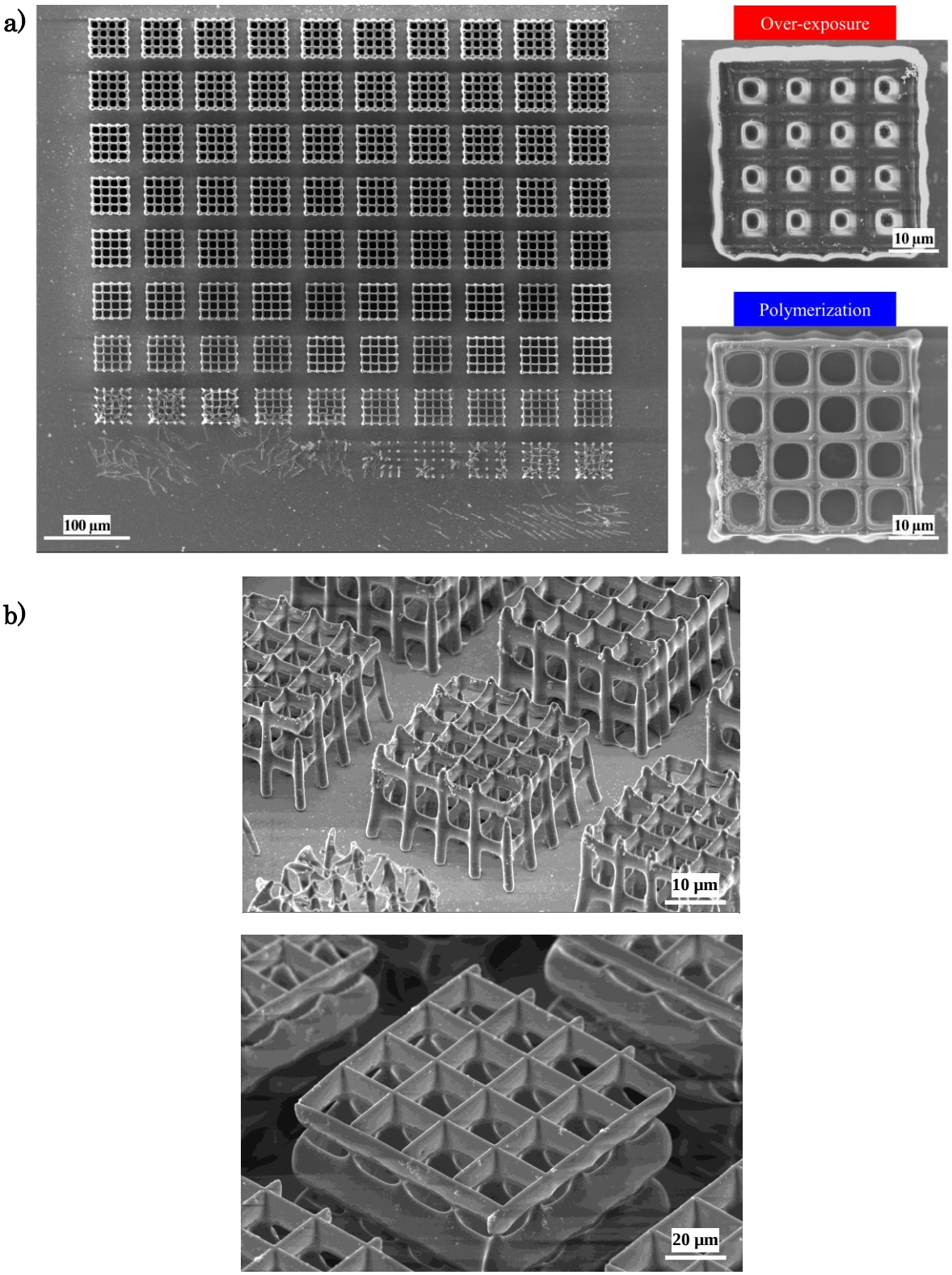

Figure C.8: a) SEM images of an entire polymerized test grid in 2PP-DLW for voxel characterization in negative-tone photoresist mr-DWL 40. b) View of two 3D pattern object.

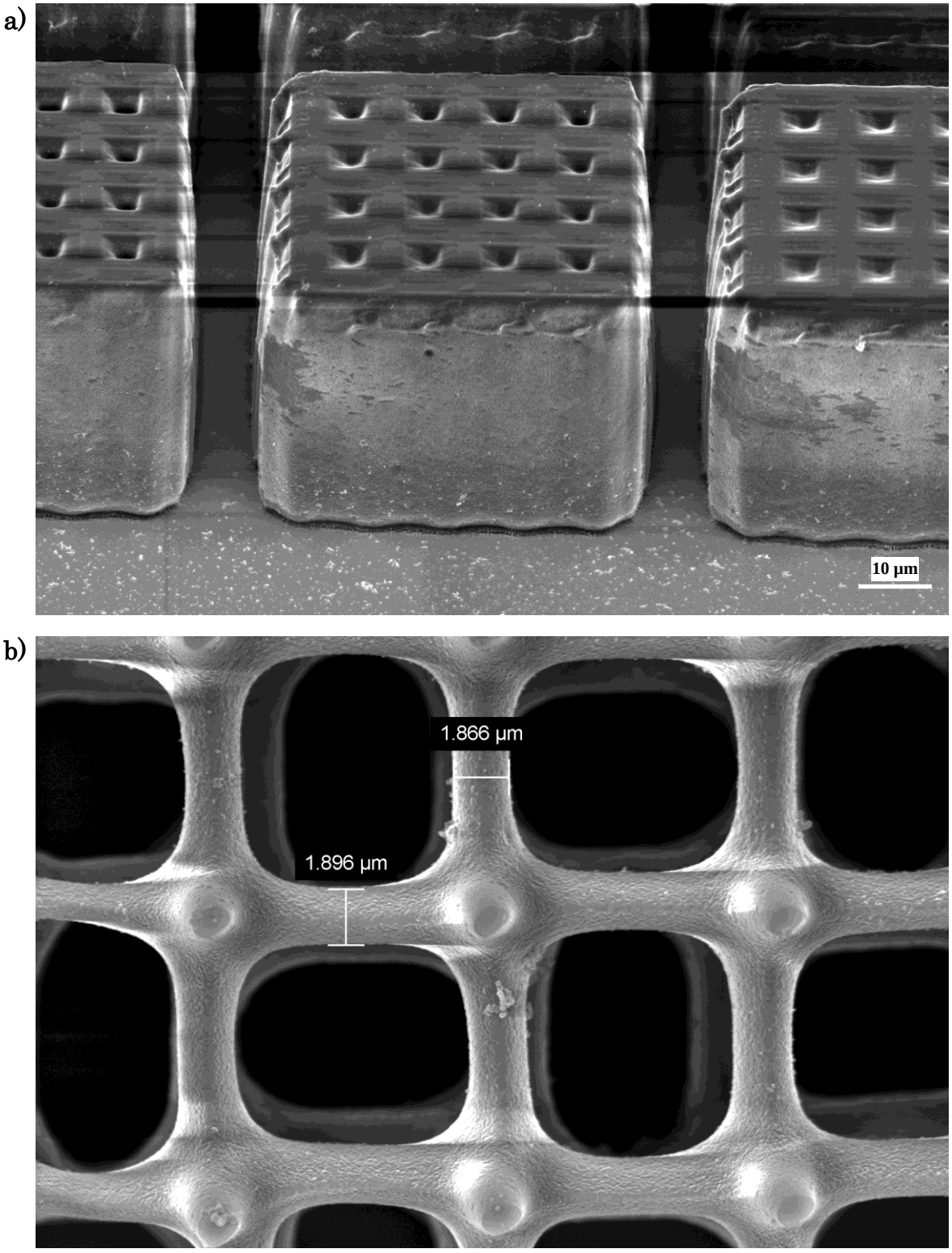

Figure C.9: a) View of an over-exposed 3D pattern object in mr-DWL 40. b) View of one polymerized 3D pattern object.

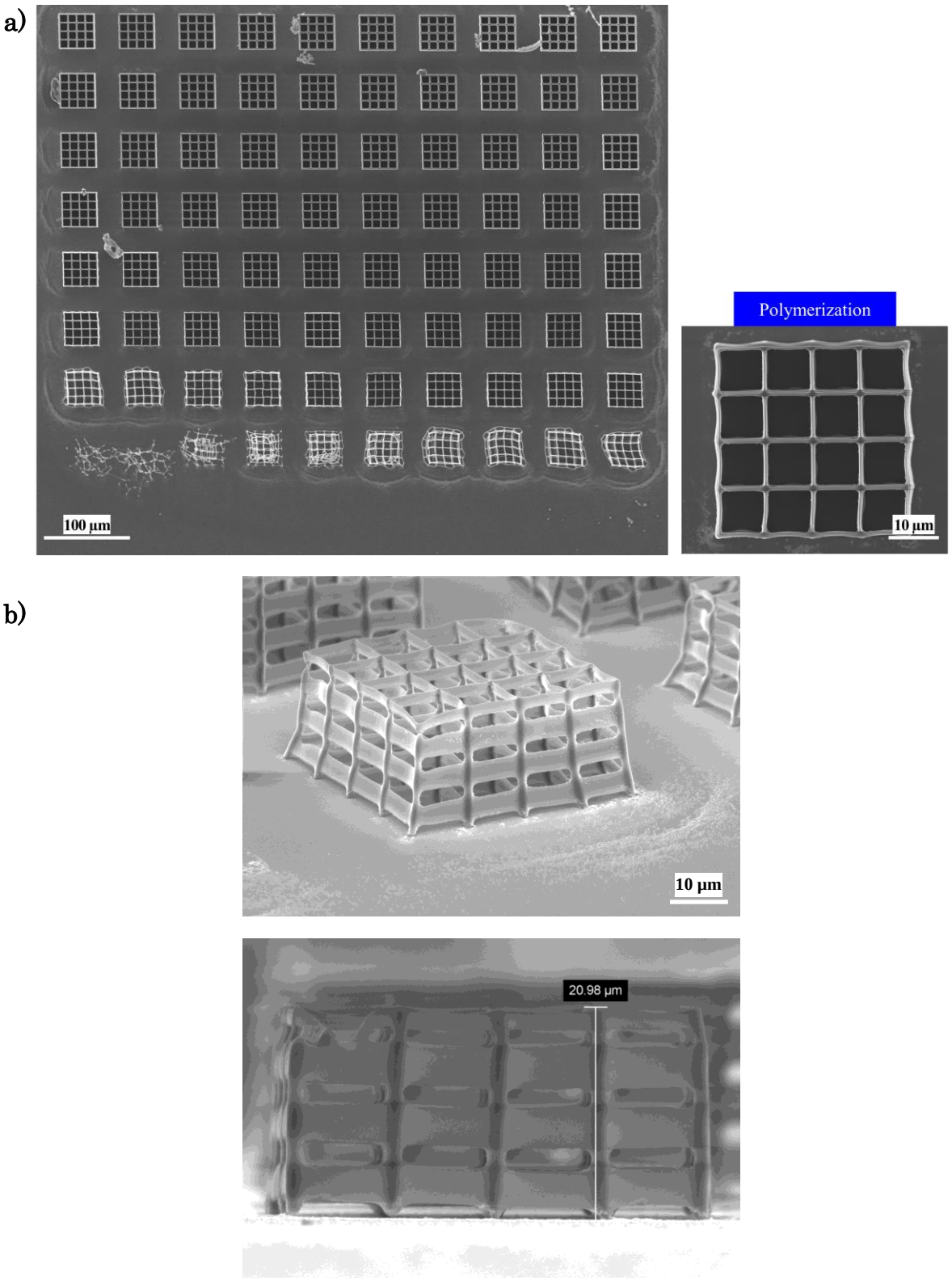

Figure C.10: a) SEM images of an entire polymerized test grid in 2PP-DLW for voxel characterization in negative-tone photoresist EpoCore 5. b) View of two 3D pattern object.

Appendix D: Voxels characterization

Characterized voxels over a wider range of scanning speeds and across the entire range of available laser power for S1800 series, SU-8, mr-DWL, and EpoCore photoresists.

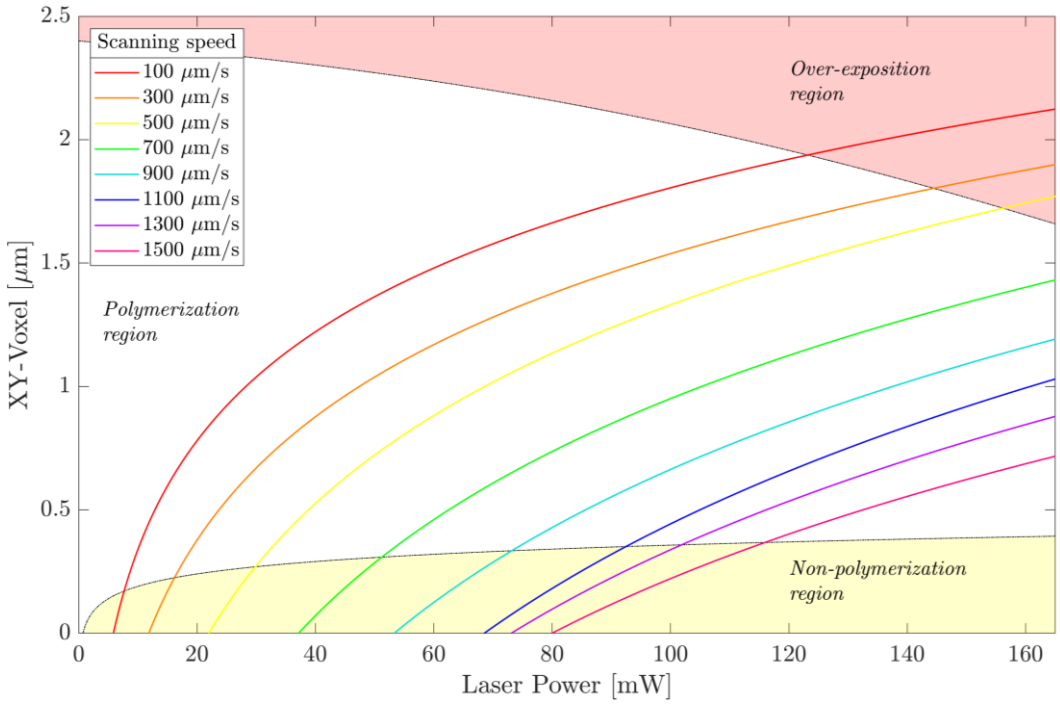

Figure D.1: Optimization of S1805 photoresist.

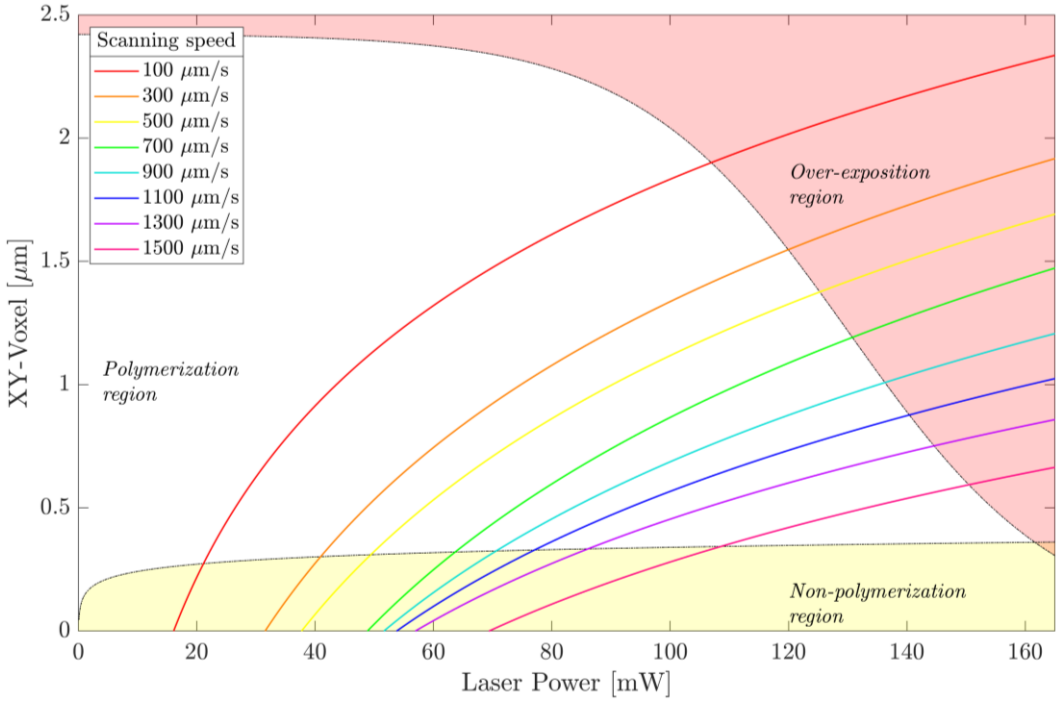

Figure D.2: Optimization of S1818 photoresist.

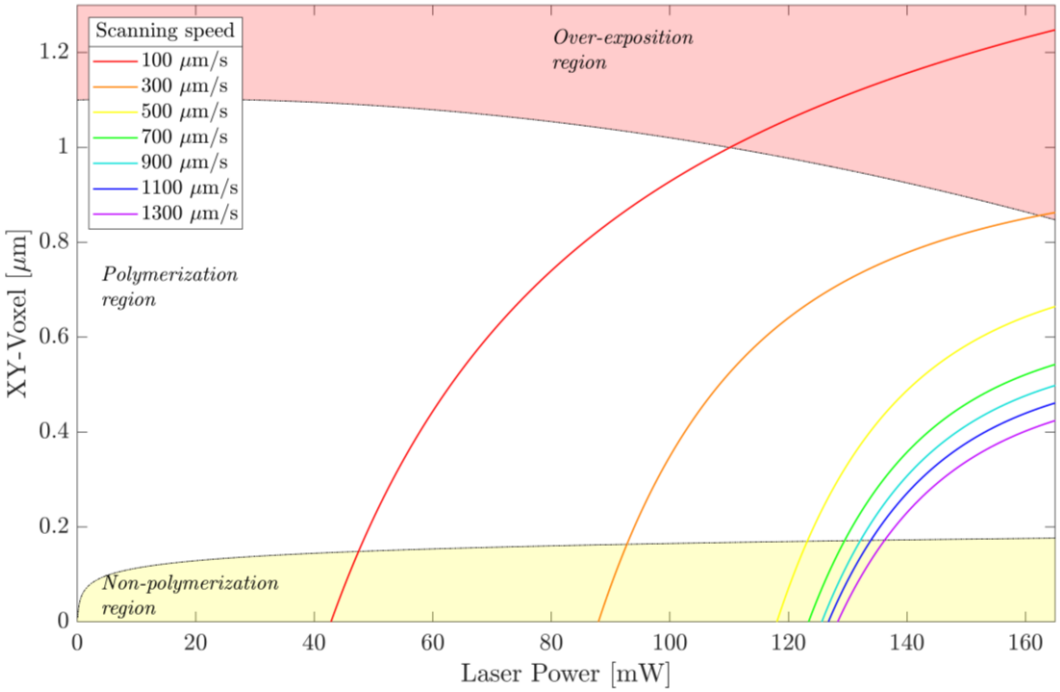

Figure D.3. Optimization of SU-8 TF 6002 photoresist.

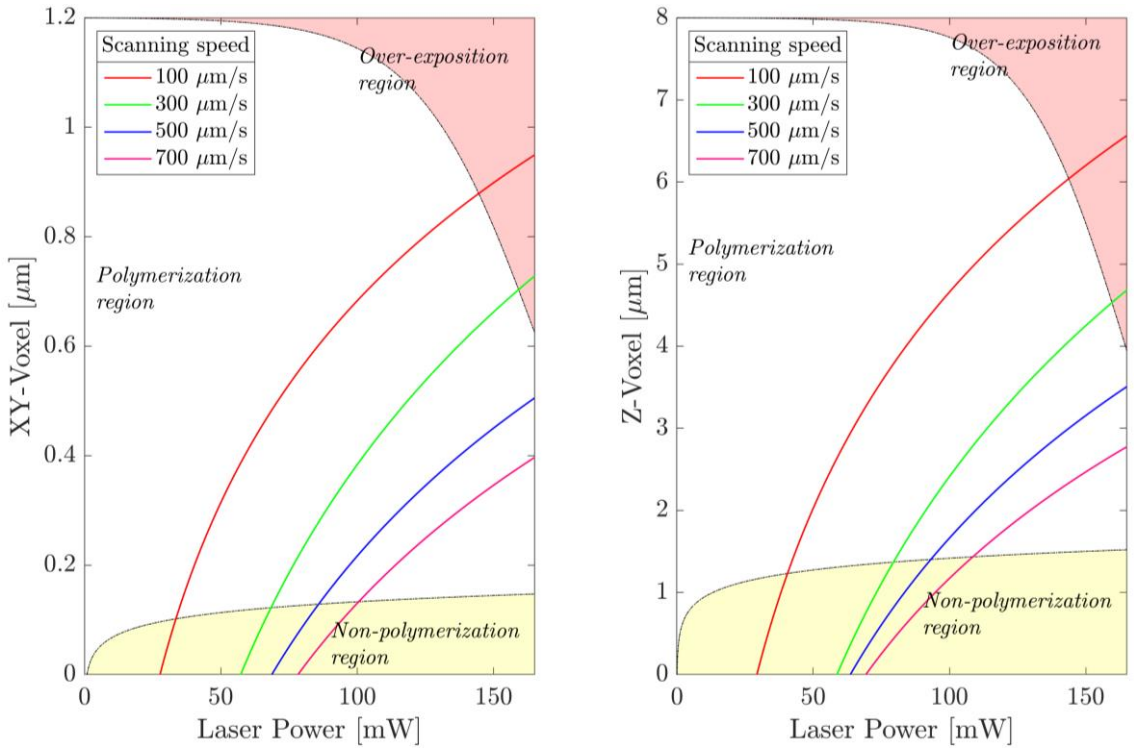

Figure D.4: Optimization of SU-8 2015 photoresist.

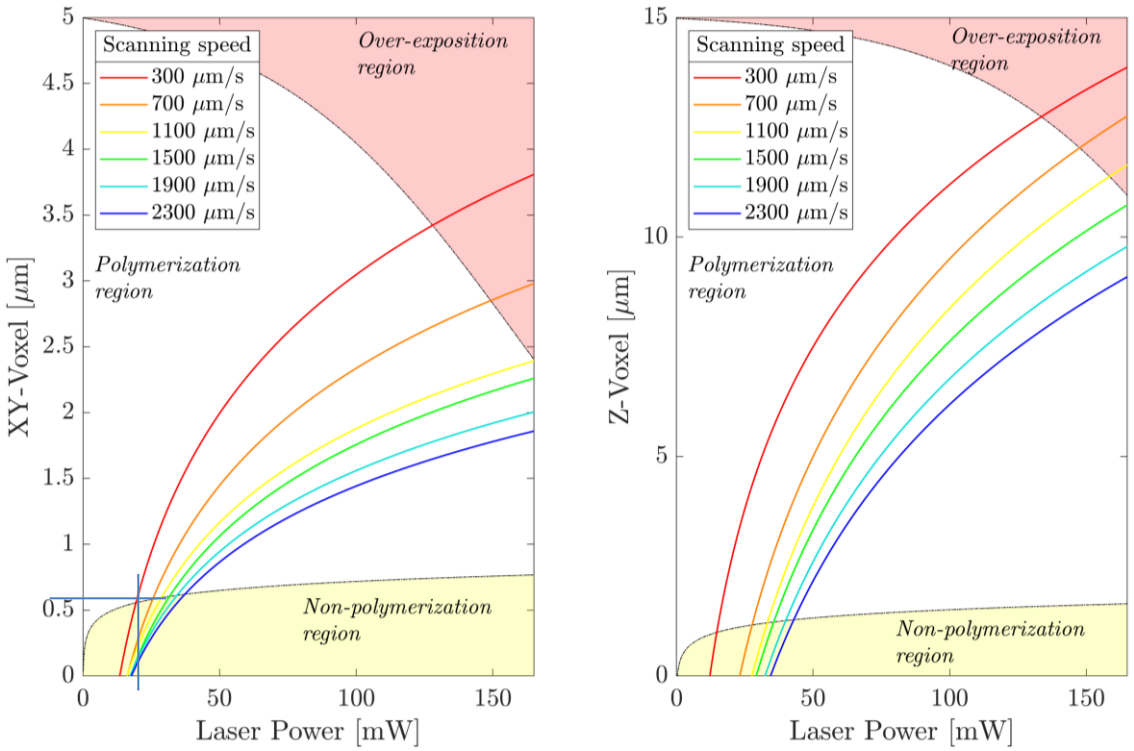

Figure D.5: Optimization of mr-DWL 40 photoresist. The maximum xy- and z-voxels were empirically defined as 5 µm and 15 µm, respectively, to compute the over-exposure limit.

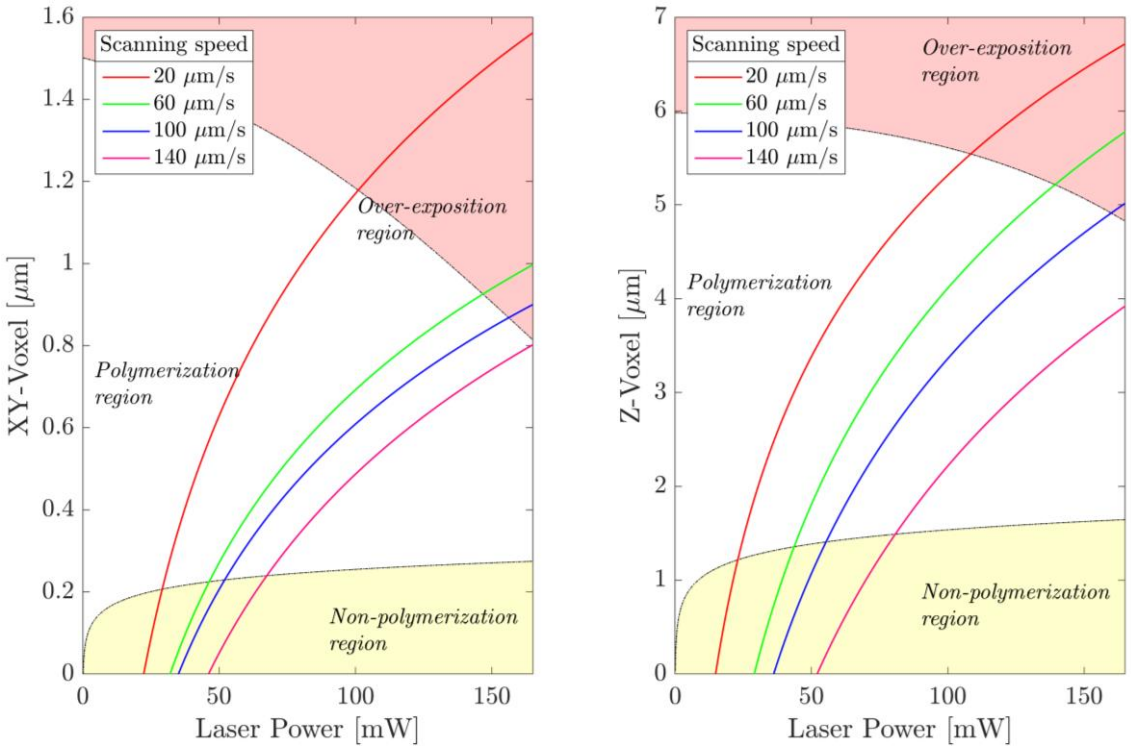

Figure D.5: Optimization of EpoCore 5 photoresist. The maximum xy- and z-voxels were empirically defined as 1.45 µm and 6 µm, respectively, to compute the over-exposure limit.

Appendix E: Results in surface alignment

Surface alignment analysis results obtained with scanning electron microscopy for both SU-8 and S1805 photoresists.

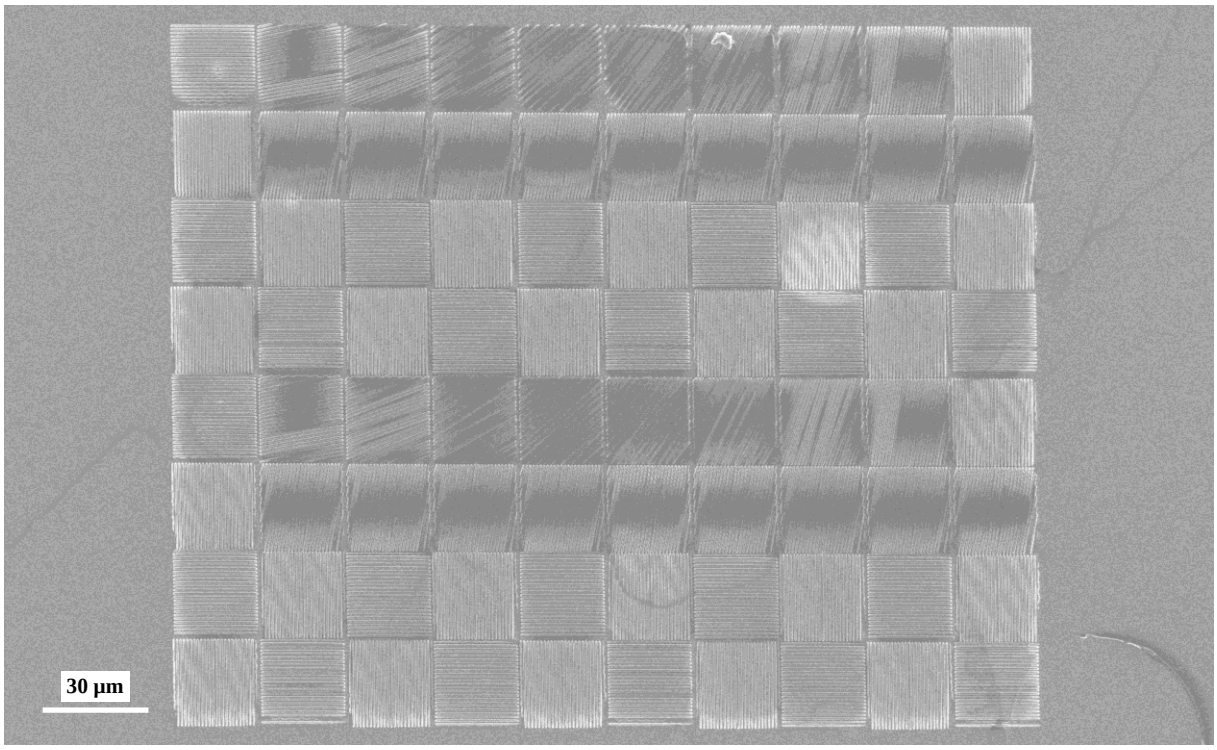

Figure D.1: Scanning electron micrographs of an entire polymerized surface in SU-8.

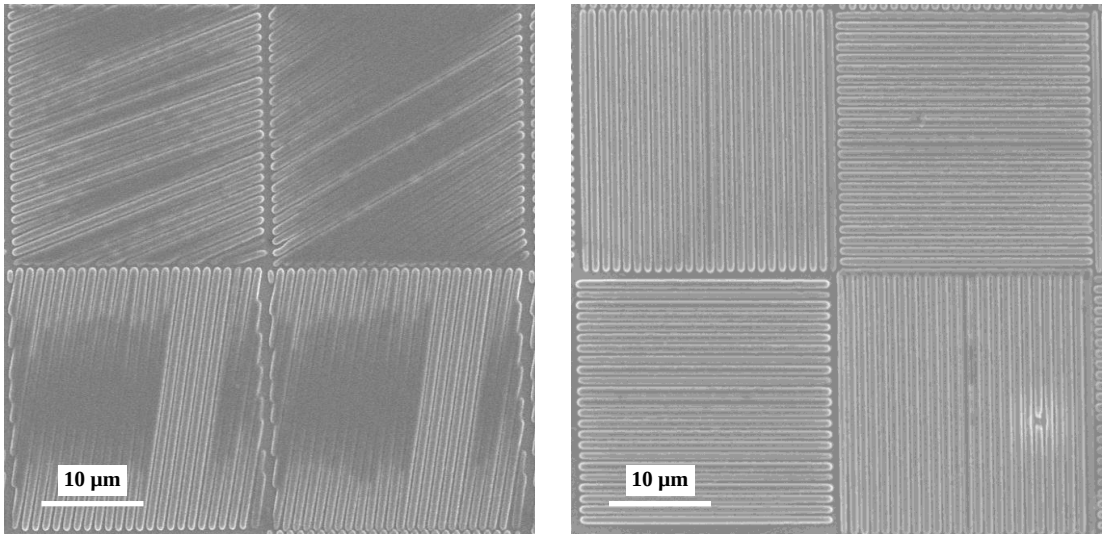

Figure D.2: Polymerized patterns at different alignment angles (φ) in SU-8.

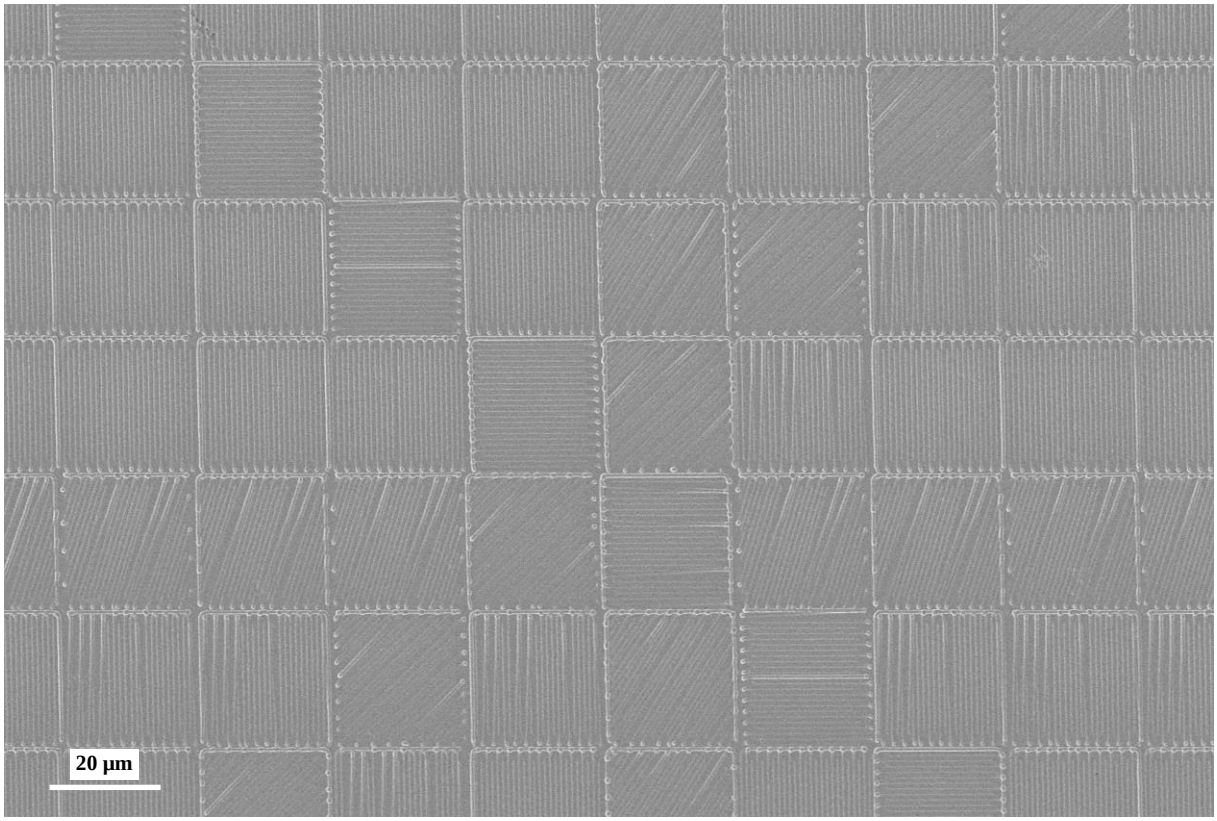

Figure D.3: Scanning electron micrographs of an entire polymerized surface in S1805.

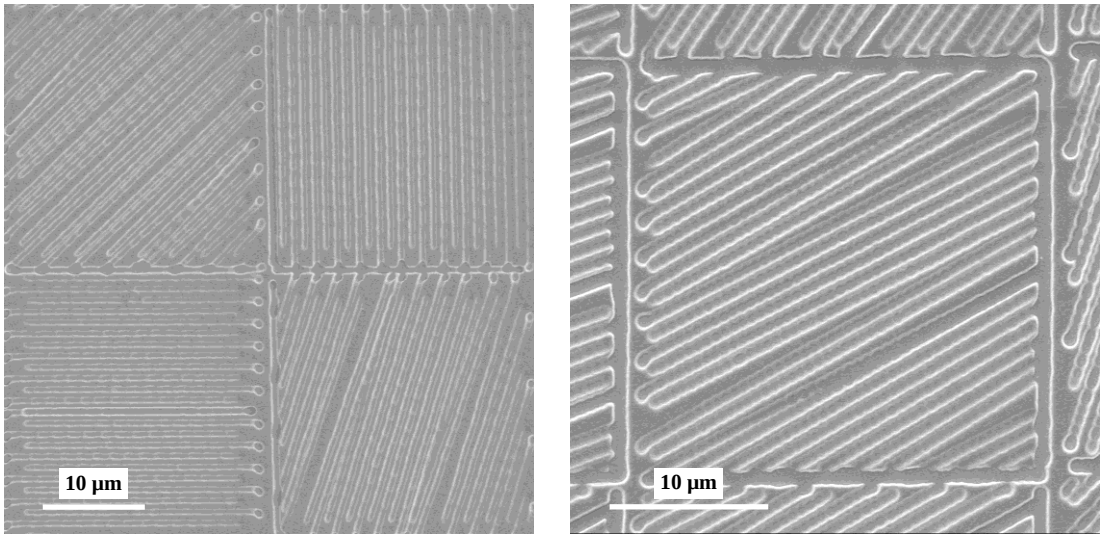

Figure D.4: Polymerized patterns at different alignment angles (φ) in S1805.

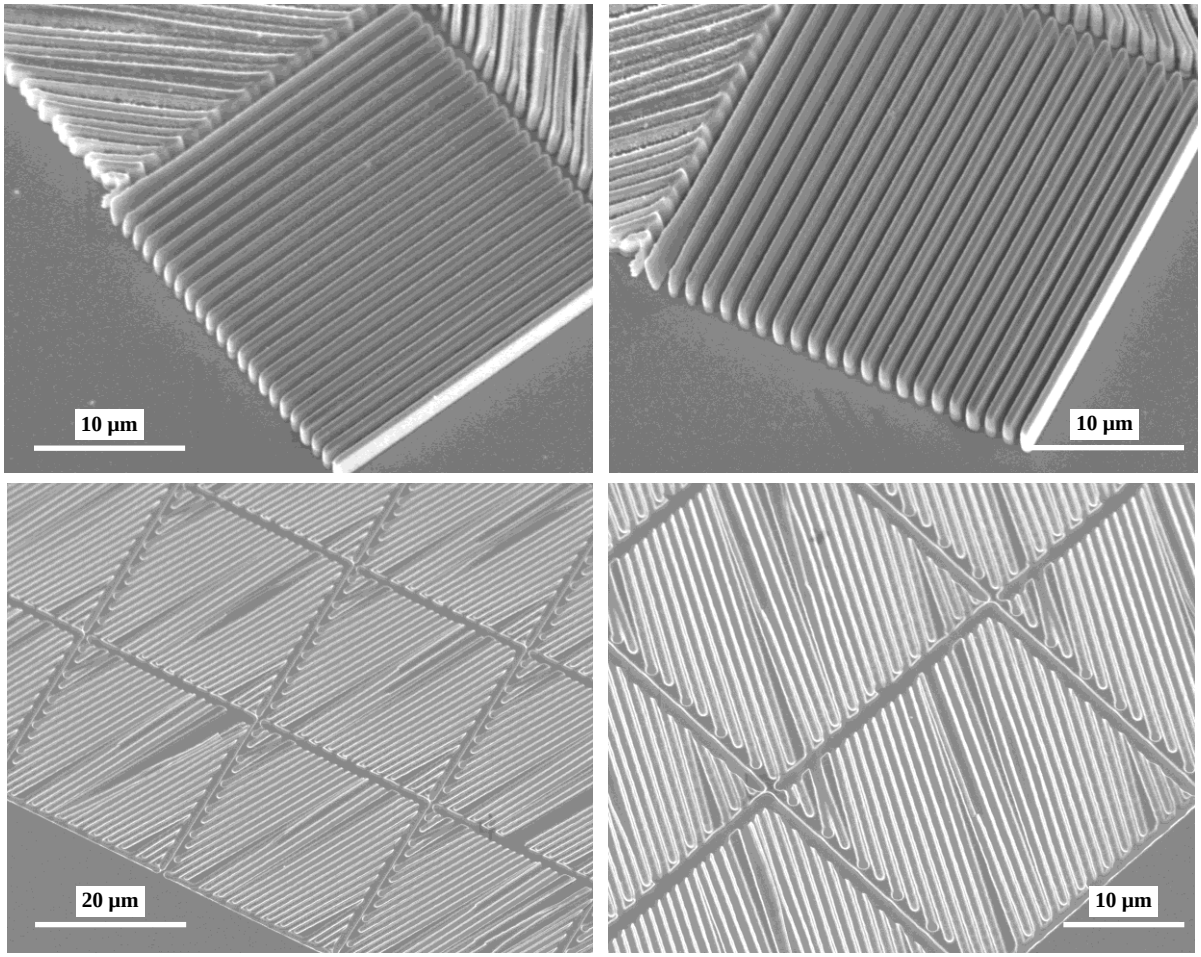

Figure D.5: 3D visualization of patterns in SU-8 (top) and S1805 (bottom).

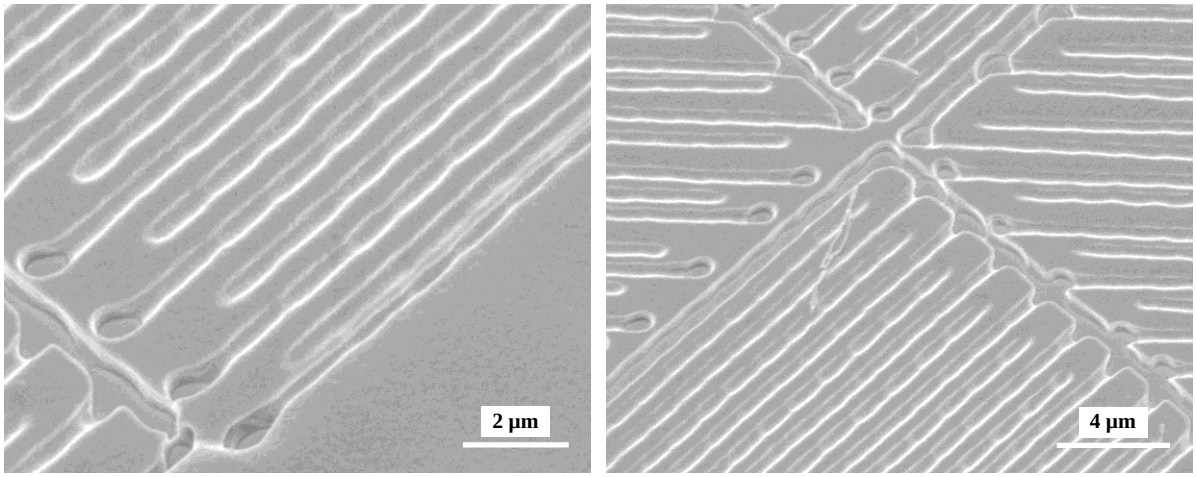

Figure D.6: Improperly polymerized surface at very high scanning speed in S1805.

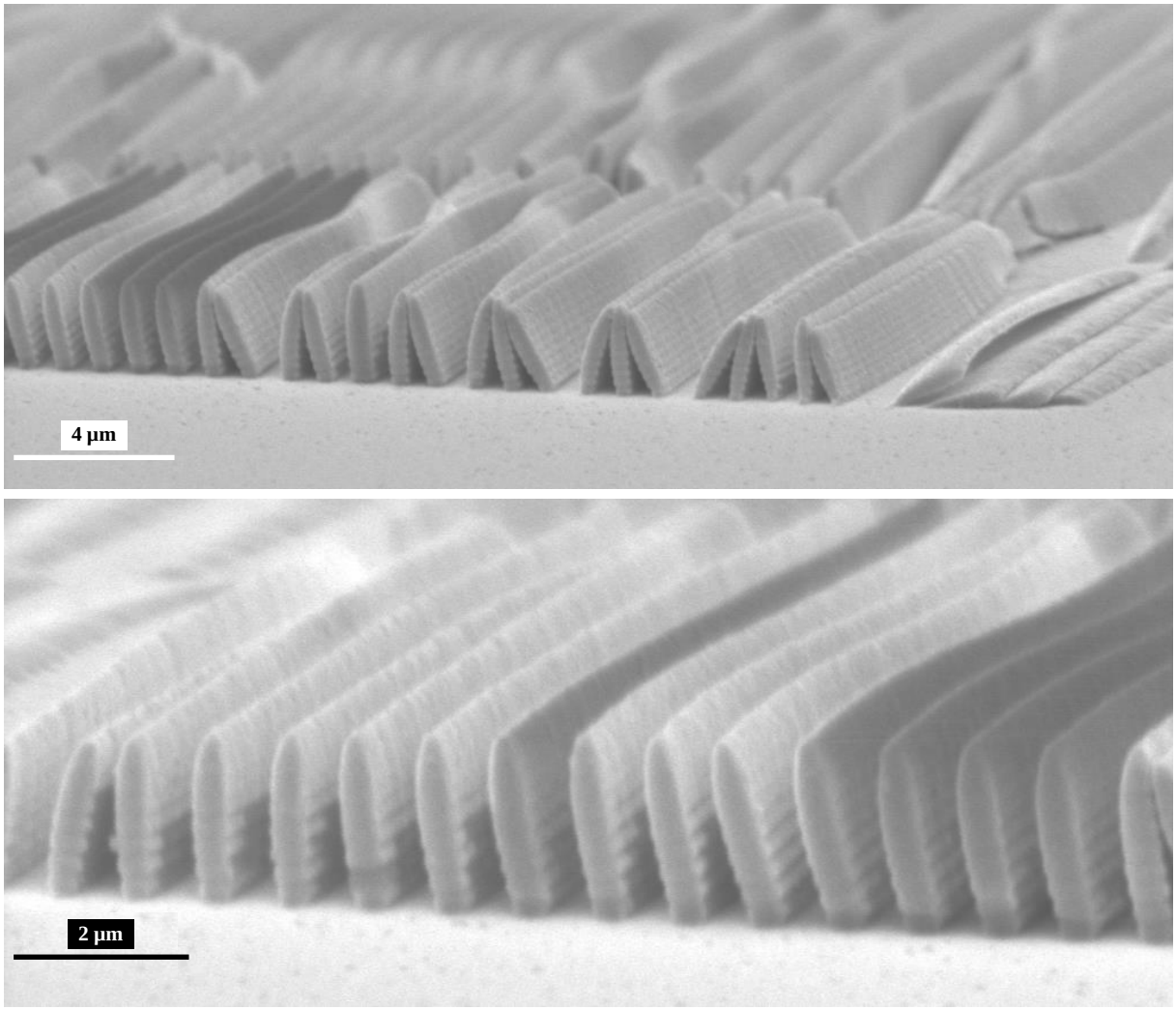

Figure D.7: Unsuitable surfaces in SU-8 thicknesses greater than 2 µm. The microlines collapse during the development process. The microgrooves are not well defined under these conditions, and consequently, LC alignment will not comply.

Appendix F: Results in 3D microstructures

SEM micrographs of 3D microstructures and their analysis conducted in these experiments.

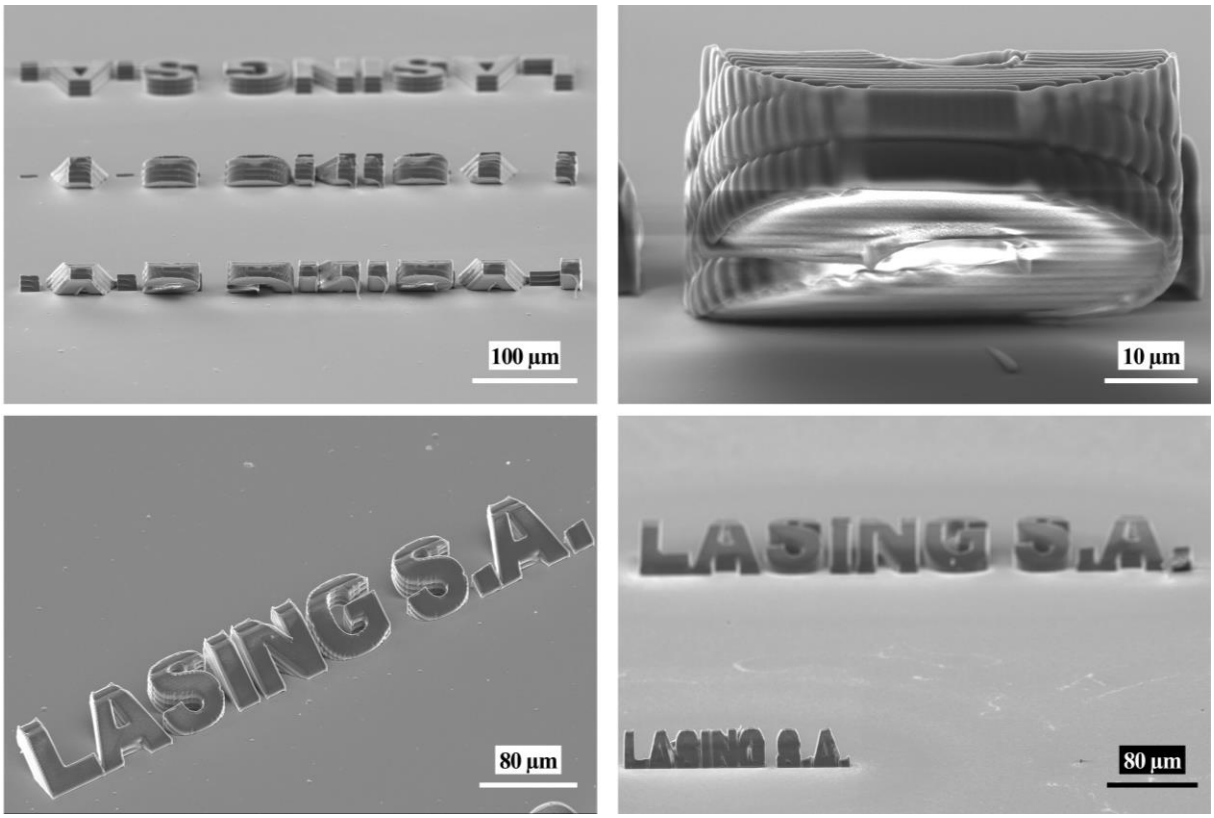

Figure F.1: SEM images of the 3D microstructure in SU-8 photoresist. The upper images were taken from behind the structure, showing the tilted layers. The cut structure shown in the upper micrograph is due to the thickness of the spin-coated photoresist being less than the height of the microstructure.

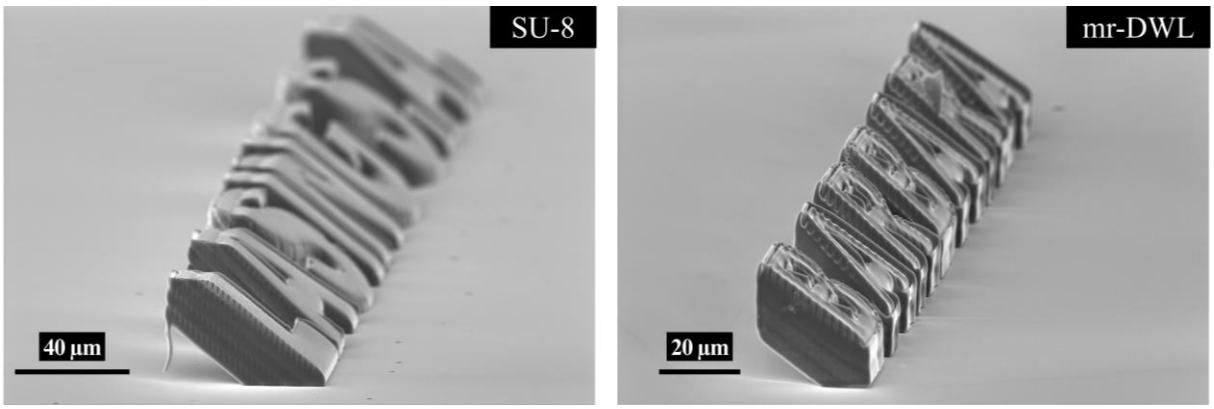

Figure F.2: 35° tilted microstructures in SU-8 and mr-DWL photoresists.

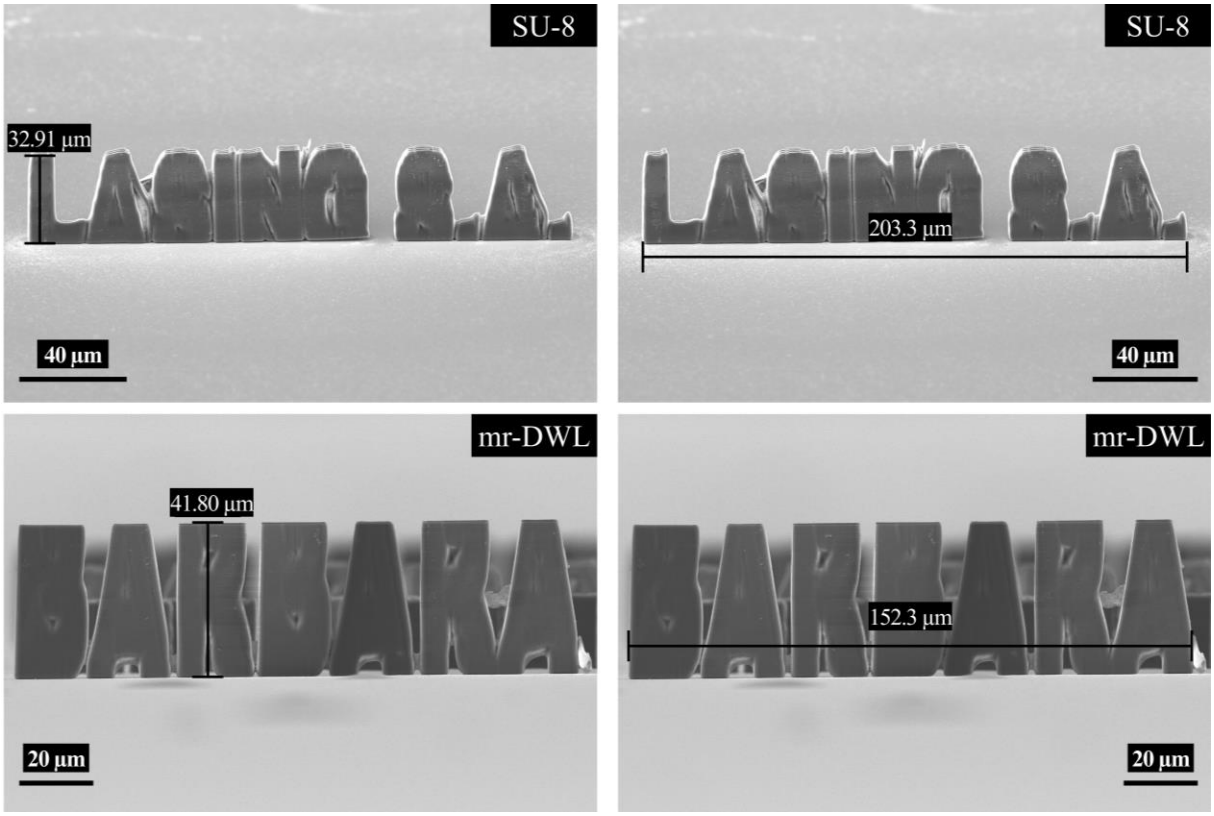

Figure F.3: 90° tilted microstructure measurements in SU-8 (upper images) and mr-DWL (bottom images) photoresists.

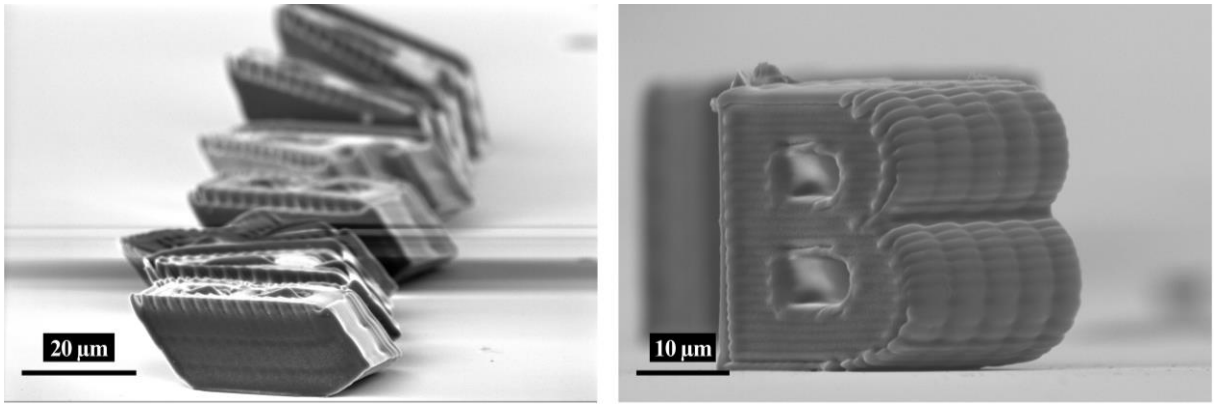

Figure F.4: Example of microstructures not adhered to the substrate. This is due to an inadequate development and substrate cleaning process, which makes the microstructures difficult to measure and hinders obtaining the desired results in the fabrication of photonic devices.

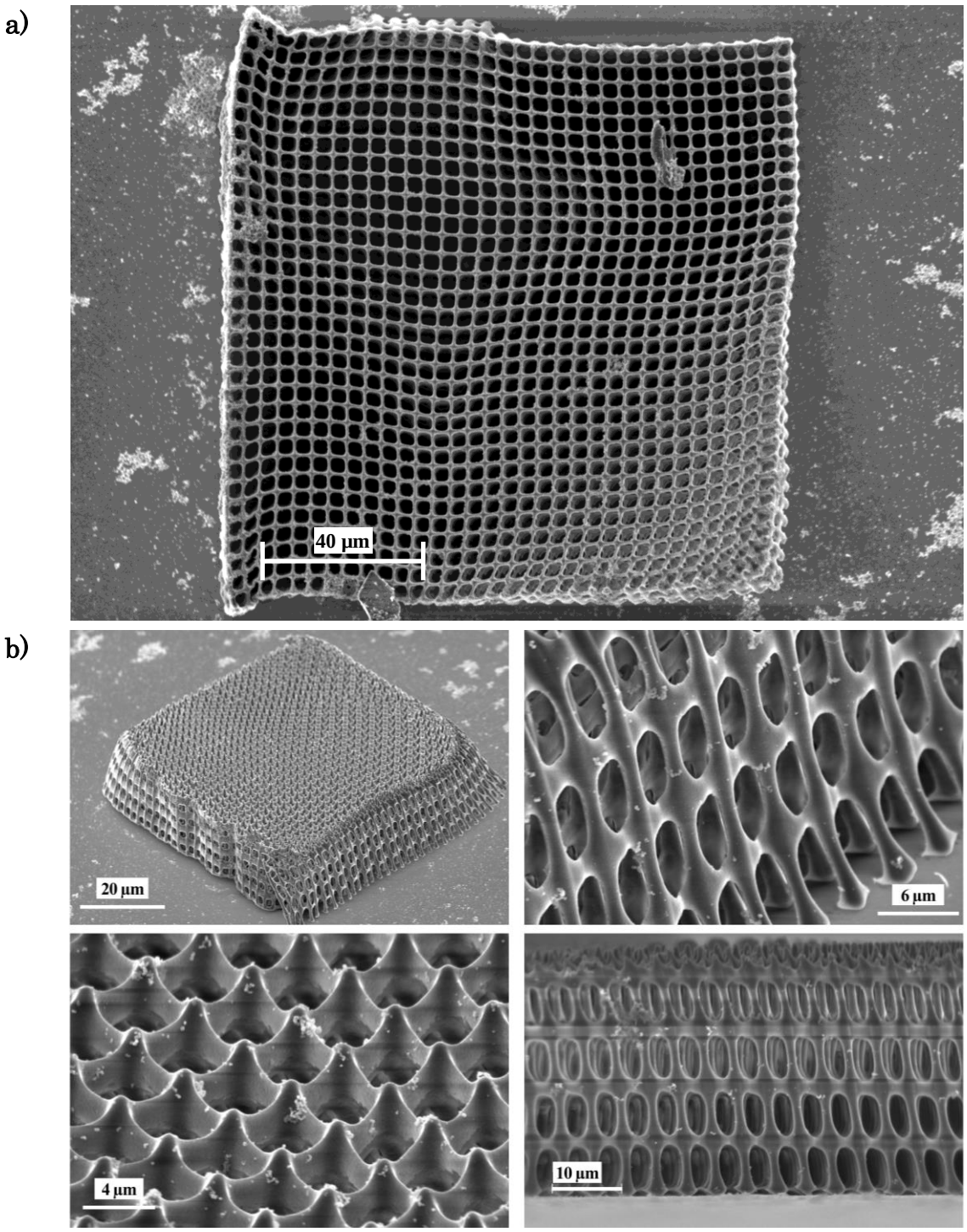

Figure F.5: Scanning electron micrographs of micro-scaffolds (micro-grids) in mr-DWL photoresist, a) top view and b) pictorial view.

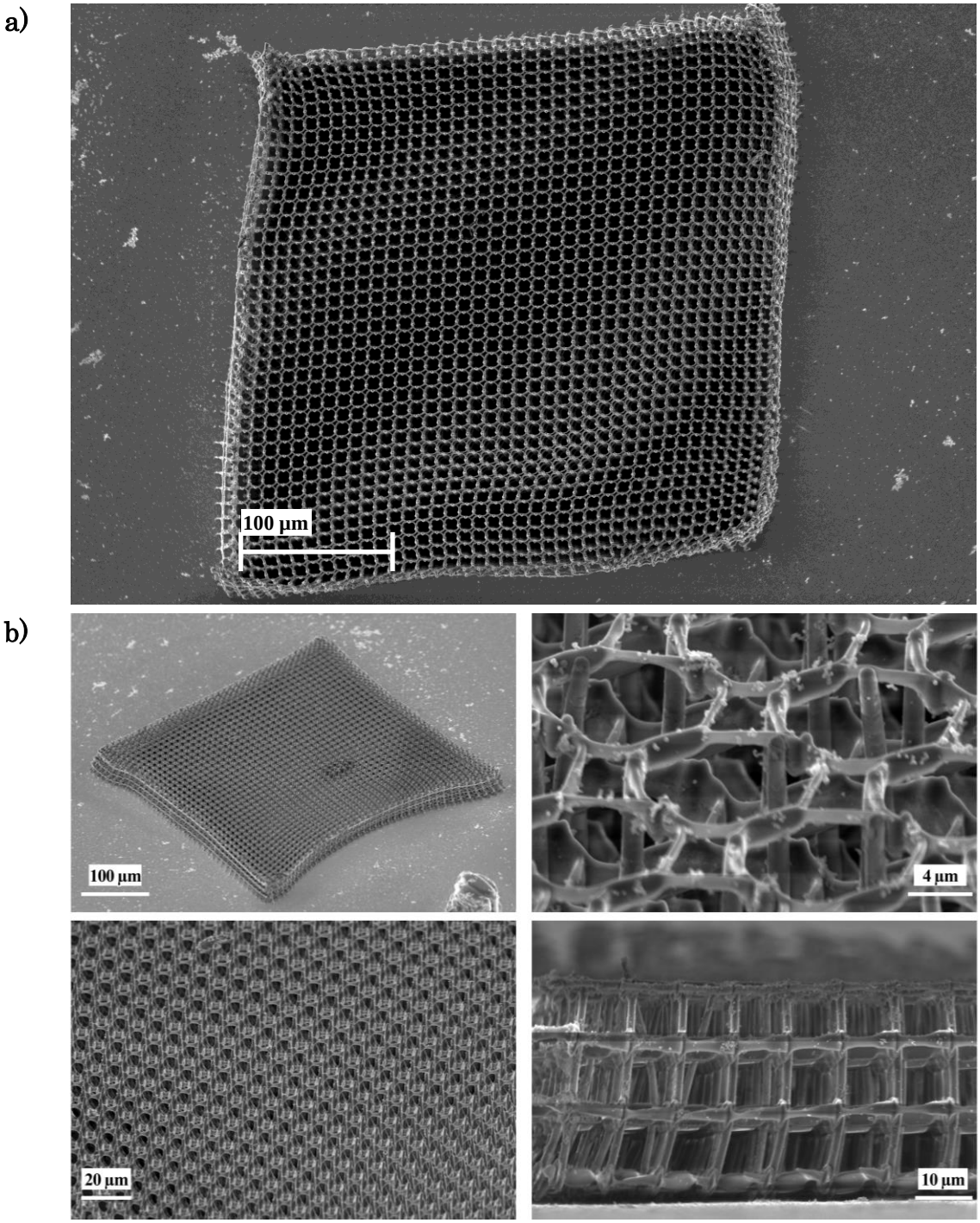

Figure F.6: Scanning electron micrographs of micro-scaffolds (micro-rings) in mr-DWL photoresist, a) top view and b) pictorial view.

Appendix G: 2PP System technical specifications

The custom 2PP system is an open-hardware prototype for microfabrication, demonstrating solid performance in this research work. However, it does not directly compete with equipment from companies specializing in 2PP lithography, such as UpNano GmbH. In this prototype version, it stands out for offering a larger build volume, enabled by long-travel linear axes (200×200×25 mm^3), and mainly for its capabilities to perform both layer-by-layer fabrication and true 3D manufacturing through vectorial voxel movements within the material. This is achieved thanks to integrated software for hardware system management and process control (CAD and code generation). Table G.1 presents the technical specifications of this first version of the 2PP system compared to its commercial counterparts.

Table G.1: Technical Specifications of the 2PP System Compared to Commercial Systems.

Equipment	**2PP System**	**NanoOne**	**Photonic Professional GT2**	**MPO 100**
Company	Lasing S.A.	UpNano	NanoScribe	Heidelberg Instruments
Average Power [mW]	250 (160 mW at focusing)	up to 1000	120	600 (≥ 200 mW at focusing)
Laser wavelength [nm]	780	780, 515	780	522
Pulse length [fs]	90	90	100	250
Light source	Femtosecond fiber laser			
Max. scanning speed [mm/s]	up to 2.3	up to 1200	up to 625	up to 10000
Manufacturing process	Layer-by-layer True 3D	Layer-by-layer		
Build volume [mm^3]	200×200×25	100×120×49	100×100×8	100×100×10
Scanner	Galvanometer scanner			
Printing configuration	Air-configuration	Oil and water immersion	Air-configuration, Oil immersion, Dip-laser lithography	
Objectives lens	50×, NA of 0.8	Reconfigurable		
Field of View [mm]	0.04	up to 5	up to 1	up to 2
Resolution [nm]	> 220	100	160	100
Roughness [nm]	> 20	≤ 10	≤ 20	≤ 10
Software	Lasing process software	Think3D	DeScribe NanoWrite	LithoSoft3D LithoStream

Equipment	2PP System	NanoOne	Photonic Professional GT2	MPO 100
Materials	Commercial photoresists	Custom 2PP photoresists and commercial ones		Commercial photoresists
Ambient conditions	Standard cleanroom conditions. Air pressure required for vibration isolation.			
Price [euros]	~200 k	0.5 – 1 M		

Appendix H: Publications and contributions

The relevant publications and contributions resulting from this work are outlined below:

1. Research journals:

    - **B. Ganazhapa**, J. Pereiro-García, X. Q. Arregui, M. A. Geday, G. Guadaño, and M. Caño-García, "Generation of arbitrarily patterned polarizers using 2-photon polymerization," Sci Rep, vol. 14, no. 1, p. 22550, Sep. 2024, doi: 10.1038/s41598-024-73946-z

    - X. Q. Arregui, J. Pereiro-García, O. Blanco-Fernandez, **B. Ganazhapa**, M. A. Geday, J. M. Otón-Sánchez, and M. Caño-García, "Recent progress in variafocal liquid crystal diffractive lens," in Liquid Crystals Optics and Photonic Devices, SPIE, Jun. 2024, p. PC130160K. doi: 10.1117/12.3022341.

2. Conference contributions:

    - **B. Ganazhapa**, X. Quintana Arregui, M. A. Geday, and M. Caño-García, "2-photon polymerization of patterned polarizers in SU-8 and S1805 photoresist alignment surface," in *Photorefractive Photonics and Beyond: Interaction of Light with Matter – RP24*, Spain, Jul. 2024.

    - **B. Ganazhapa**, J. Pereiro-García, X. Quintana, M.A. Geday, J.M. Otón and M. Caño-García, "A double UV laser system for nanostructural LC alignment," in *20th Optics of Liquid Crystals Conference – OLC 2023*, Poland, Sept. 2023.

    - J. Pereiro-García, **B. Ganazhapa**, P. de la Rosa, M. A. Geday, J. M. Otón and M. Caño-García, "Reconfigurable Liquid Crystal Beam Expander," in *16th European Conference on Liquid Crystal – ECLC2023*, Italia, Jul. 2023.

Appendix I: User Manual

User Manual of 2PP System

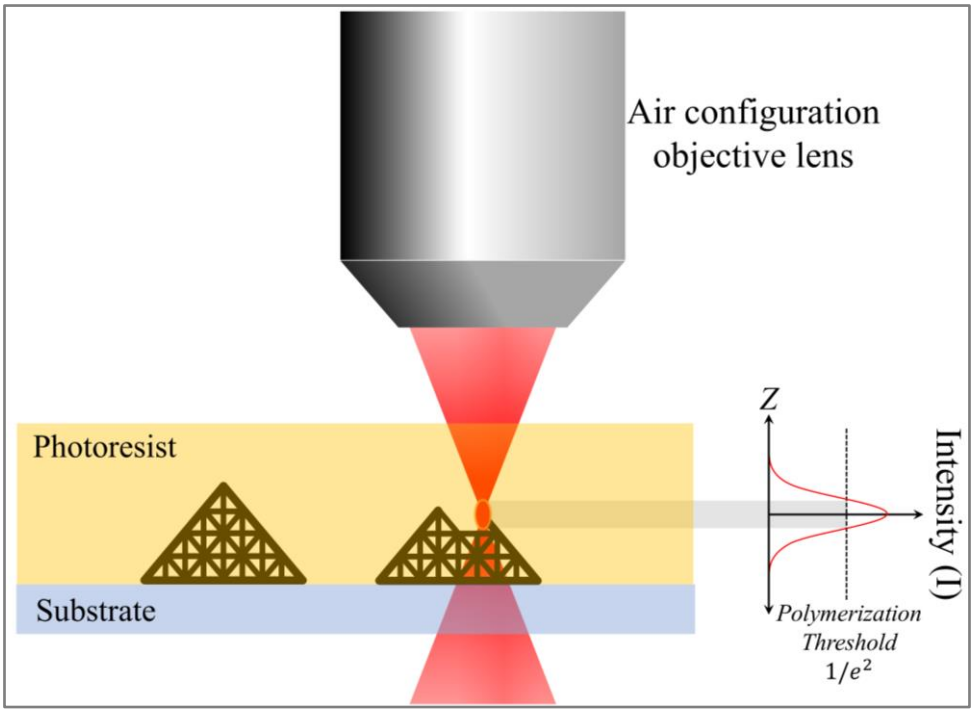

Simplified illustration of the Two-Photon Polymerization (TPP) process.

This user manual presents the hardware and software for the usage of the 2PP system for micro/nanofabrication in negative-tone and positive-tone photoresists.

Two-photon polymerization direct laser writing (2PP-DLW) is an optical lithography technology. In 2PP, the light-matter interaction occurs only within the volume of the focused laser spot, commonly known as a voxel, which can be freely traced in three dimensions within the material. This is where micro and nanostructures take shape, similar to building the pyramid brick by brick, but on a nanometric scale.

1. Hardware

This section presents the hardware and accessories of the 2PP system. Detailed explanations on the usage of each component, as well as all the procedures necessary for the proper operation of the system, are provided. The below figure shows the 2PP system completely assembled with the major viewed components.

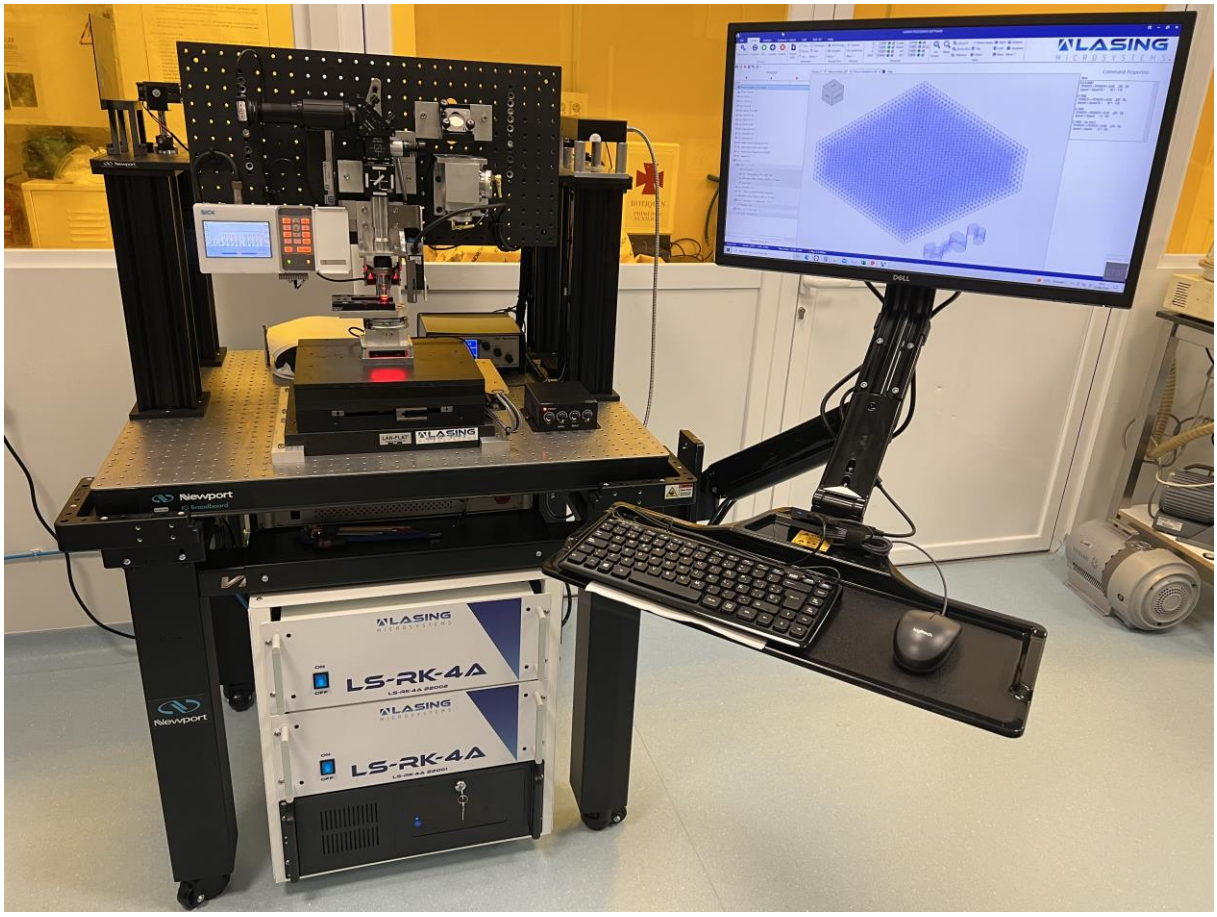

Overview of the 2PP system

1.1. Anti-vibration table

The 2PP system is mounted on an optical test table that is isolated from vibrations using pneumatic isolators. The optical table receives compressed air or nitrogen at a pressure of 5–10 psig (0.4–0.7 kg/cm²) to ensure optimal damping of vibrations and sudden movements of the 2PP system axes. The general specifications of the optical table are:

- Load Capacity (per isolator): 240 kg (60 kg).
- Dimensions: 750mm × 900mm × 58mm.

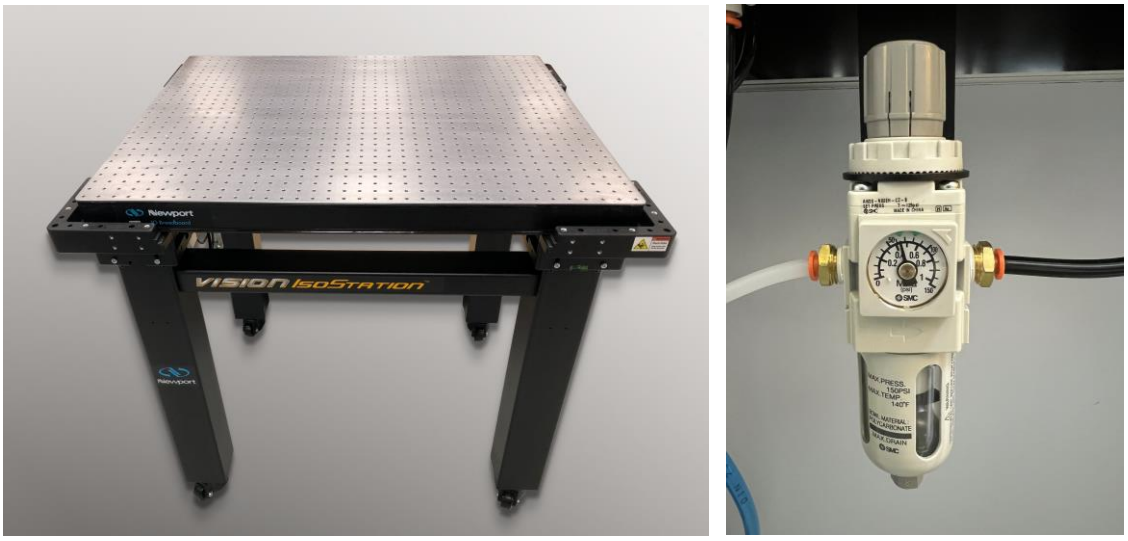

The Vision IsoStation vibration isolated workstation of the 2PP system.

1.2. Optical components table

The laser header and optics are mounted on the superior breadboard. The 2PP setup and 1PP setup are mounted in this optical table.

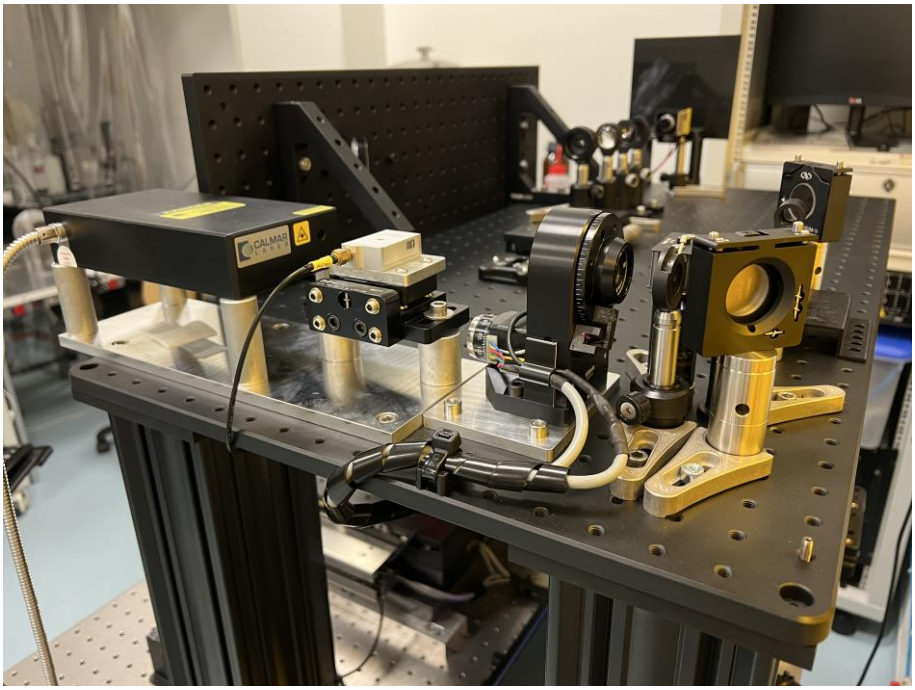

Superior breadboard.

1.3. Vision and nano-positioning stages components table

The vision components, nano-positioning stages (piezo and galvos), and optics are mounted on the vertical breadboard.

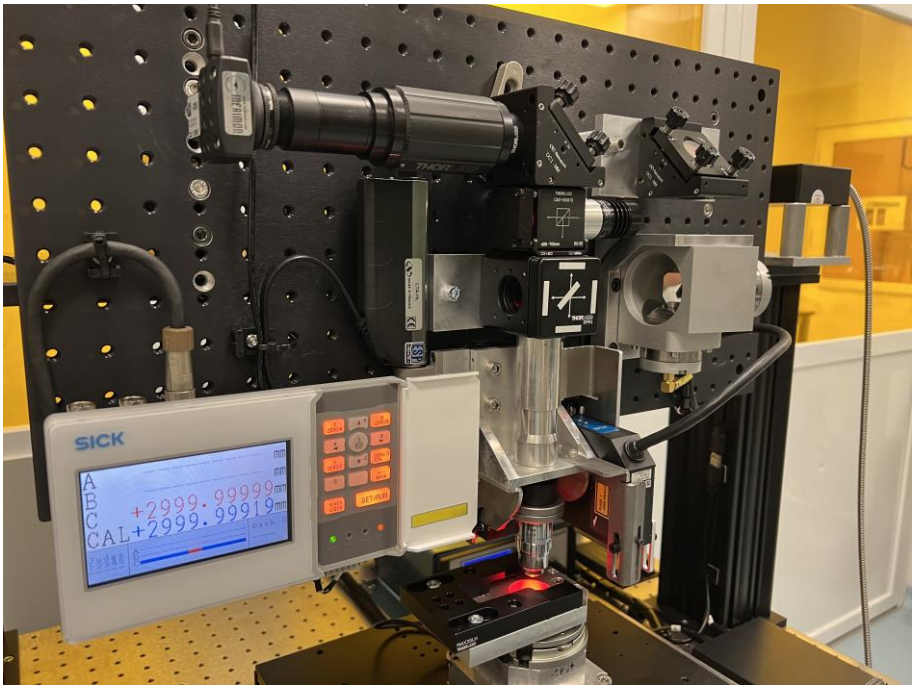

Vertical breadboard: In this illustration, the XY galvos and Z piezo stage are shown.

1.4. Focusing system

The 2PP system is composed of a 50X objective lens with a numerical aperture of 0.8 and a displacement laser to measure the distance between the objective lens and the material surface for focusing the laser beam into the photoresist and for observing the printing process.

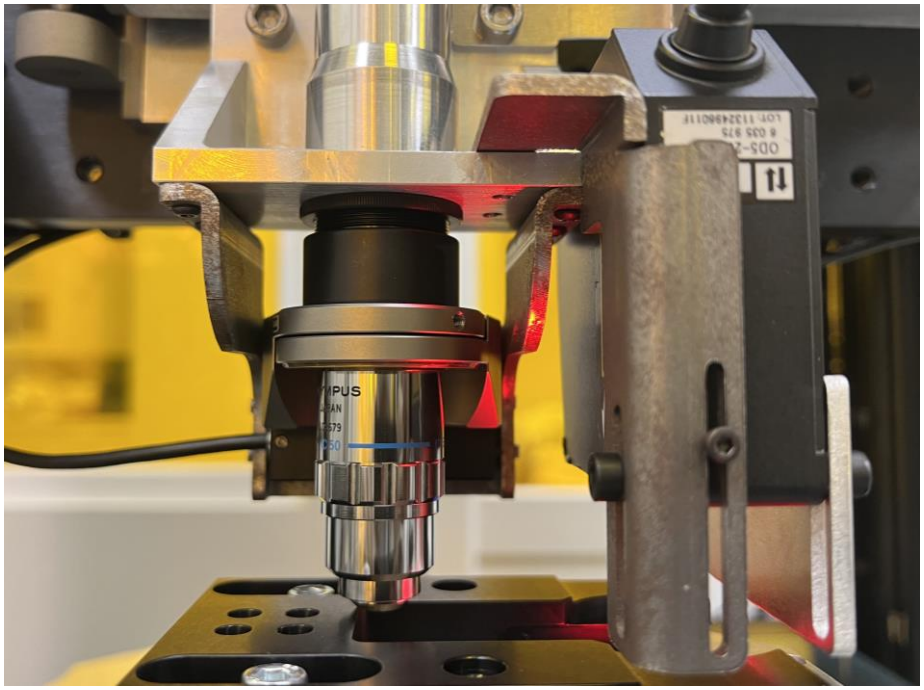

Focusing system: In this illustration, the Z piezo stage is shown.

1.5. Micro-positioning

The 2PP system is assembled with a long linear stage for coarse positioning along the X, Y, and Z axes, and a piezo stage with galvos for fine positioning along the same axes. The linear stage enables stitching processes in micro and meso-structures on a single substrate. The working area is 200 mm × 200 mm. The Z linear stage has a travel range of 25 mm.

The Z piezo stage is mounted on the vertical breadboard, and its movements are thus coordinated with the stage movements, providing a travel range of 100 µm in the Z axis. The XY galvos are mounted on the vertical breadboard in the laser beam path to move the laser beam in the XY plane across the sample. The XY galvos have a field of view of 40 µm × 40 µm (with the used objective lens) for printing on the sample.

The Z piezo stage and XY galvo work together with the X and Y linear stages for stitching and synchronize the laser movement on the sample. They are also perfectly programmed to perform the focusing for direct laser writing processes.

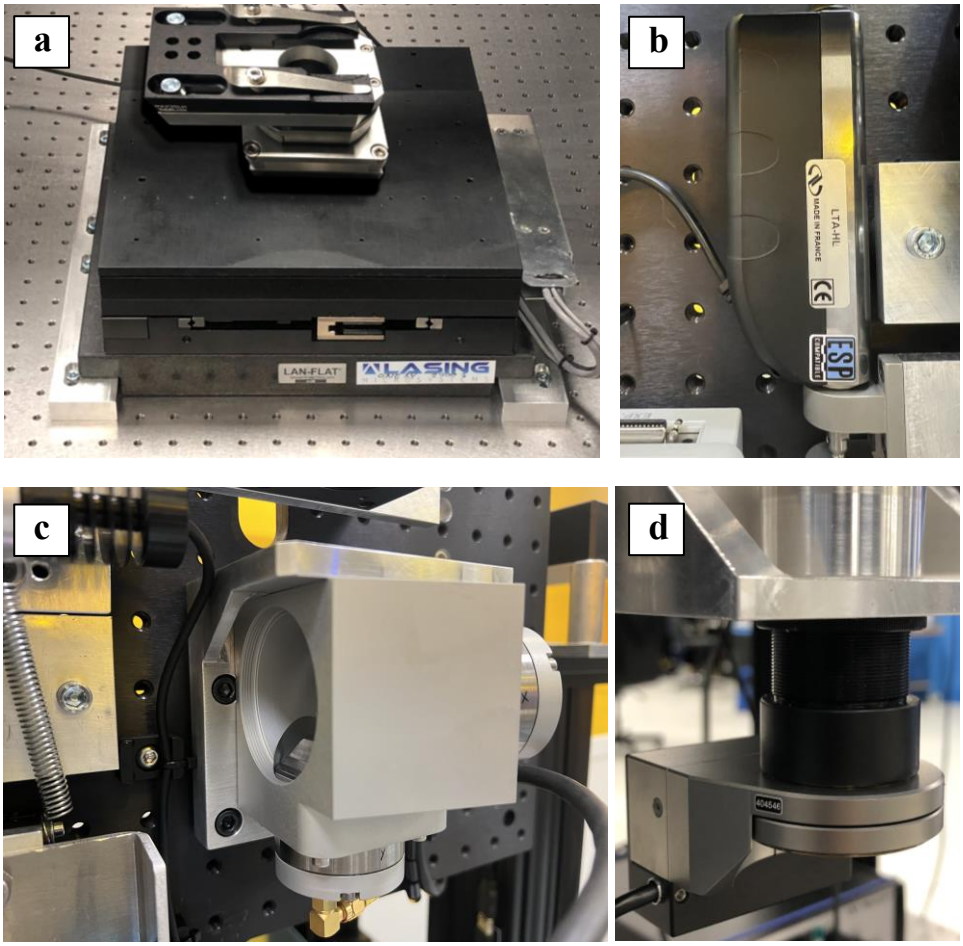

Micro-position stages: X and Y linear stage in (a), and Z linear stage in (b). Nano-position stages: XY galvos in (c), and Z piezo stage in (d).

1.6. Laser

The 2PP system is equipped with a femtosecond pulsed fiber laser source with a central wavelength of 780 nm. The laser power varies between 0 mW and 160 mW, with pulse widths of 90 fs. To adjust the laser power, the user must configure a variable in the software to control a rotating stage that rotates a half-wave plate, thereby varying the intensity of the polarized output.

The laser module is located under the anti-vibration table, while the laser header is located on the Superior breadboard.

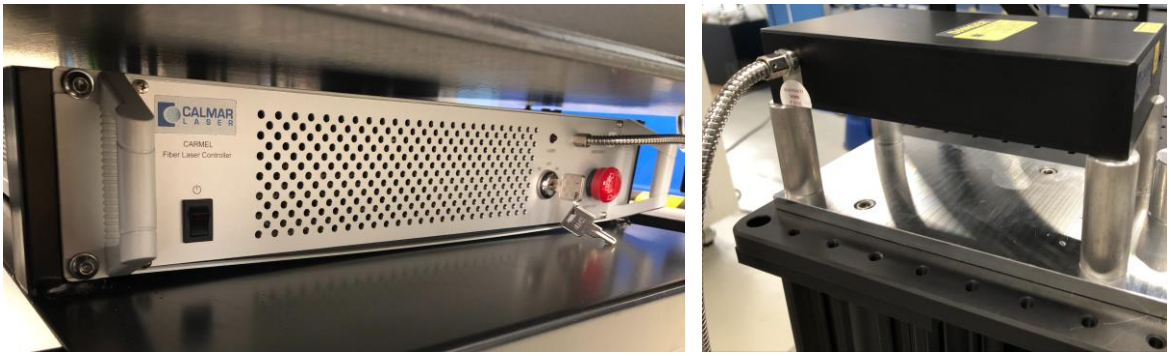

Laser module (left) and laser header (right).

1.7. Control rack

The control rack is located under the laser module and anti-vibration table. The control rack houses the power supply case, the control case, and the computer for the 2PP system, as well as the galvos controller within the control case.

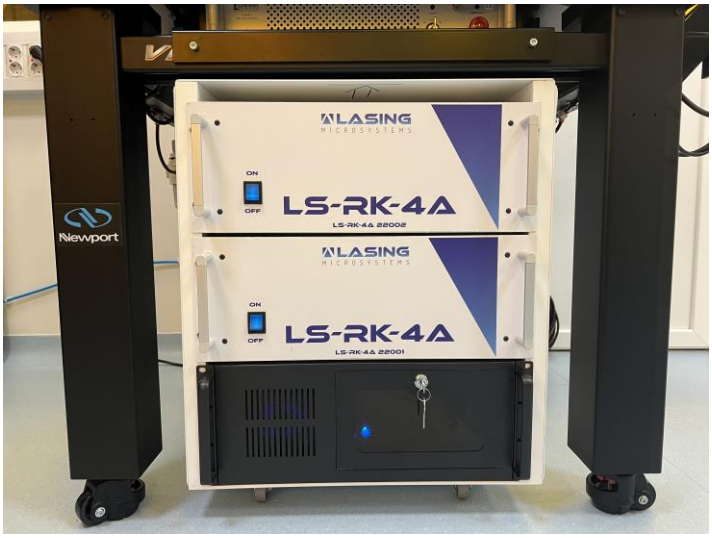

Control rack.

2. Start Up the Hardware of the 2PP System

Before using the 2PP system, the user must follow several steps to power on all electronic components and prepare the 2PP system prior to the DLW process, considering laser safety standards and ensuring proper functionality for polymerization on photoresist materials. The following steps outline the necessary procedures.

1) Turn on the **control rack**. The main switch, located at the back of the rack, distributes power to the entire 2PP system.

2) Turn on the **control case**, **power case**, and **computer case**. Each case has its own switch for added safety. The switches are located at the front of the cases.

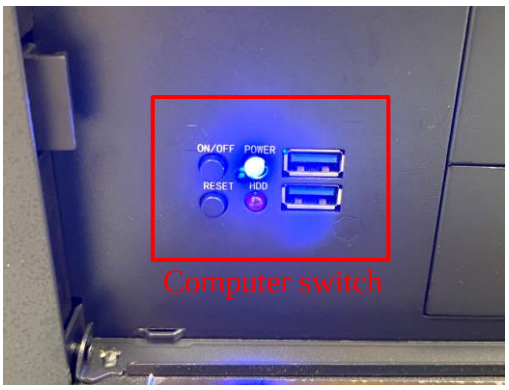

3) Turn on the **piezo controller**. The switch is located at the back of the piezo controller. Ensure that the piezo stage is correctly initialized in controller.

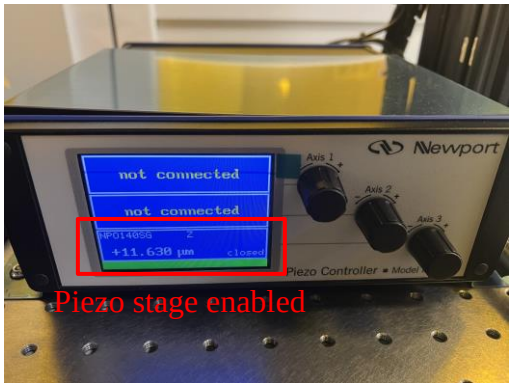

4) Turn on the **illumination controller**. Although the illumination does not affect the DLW processes, it ensures proper functionality of the vision system.

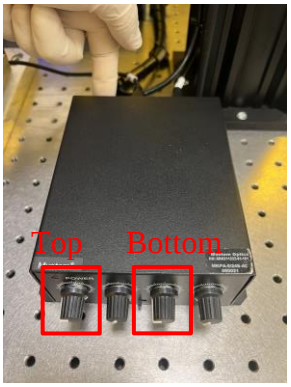

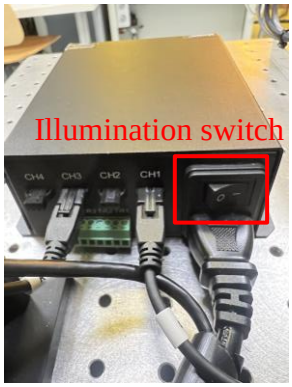

5) Finally, turn on the **laser module** without switching on the shutter. The shutter should only be enabled for DLW processes; in all other situations, it must remain off.

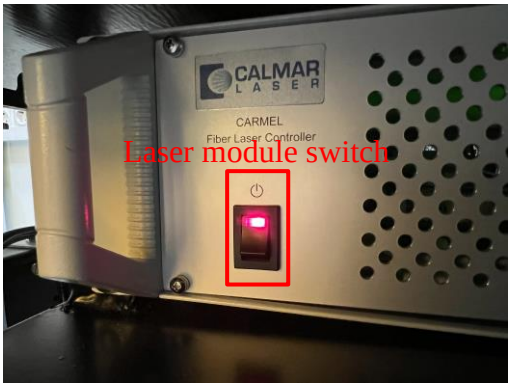

When the laser is fired, use protective glasses for the laser radiation to prevent eye damage when operating the 2PP system.

3. Software

This section introduces the Lasing Processing Software (LPS) commonly used in conjunction with the 2PP system. However, it does not provide detailed instructions for programming the LPS software, as these will be covered in the software guide. Please refer to the Help tab in the LPS software for more details and specific instructions.

LPS software is only enabled for operating systems of Microsoft Windows 10 and 11.

Icon of LPS software.

3.1. Front panel

The LPS software provides an easy-to-use graphical front panel for controlling the 2PP system. The entire system hardware is managed by software, which is correctly configured and calibrated for DLW processes.

The front panel is divided into **tools menu**, **recipe window**, **command properties window** and **preview window**.

- The **tools menu** provides all available configurations for the 2PP system.
- The **recipe window** lists sequential commands, such as variables, functions, CAD files, geometric objects, controller code files, ports, settings, etc.
- The **command properties window** shows the settings for the command selected in the recipe window, such as program variables, geometric object shapes, hatching, marking properties, etc.
- The **preview window** displays a representation of the recipe, including geometric objects and CAD files.

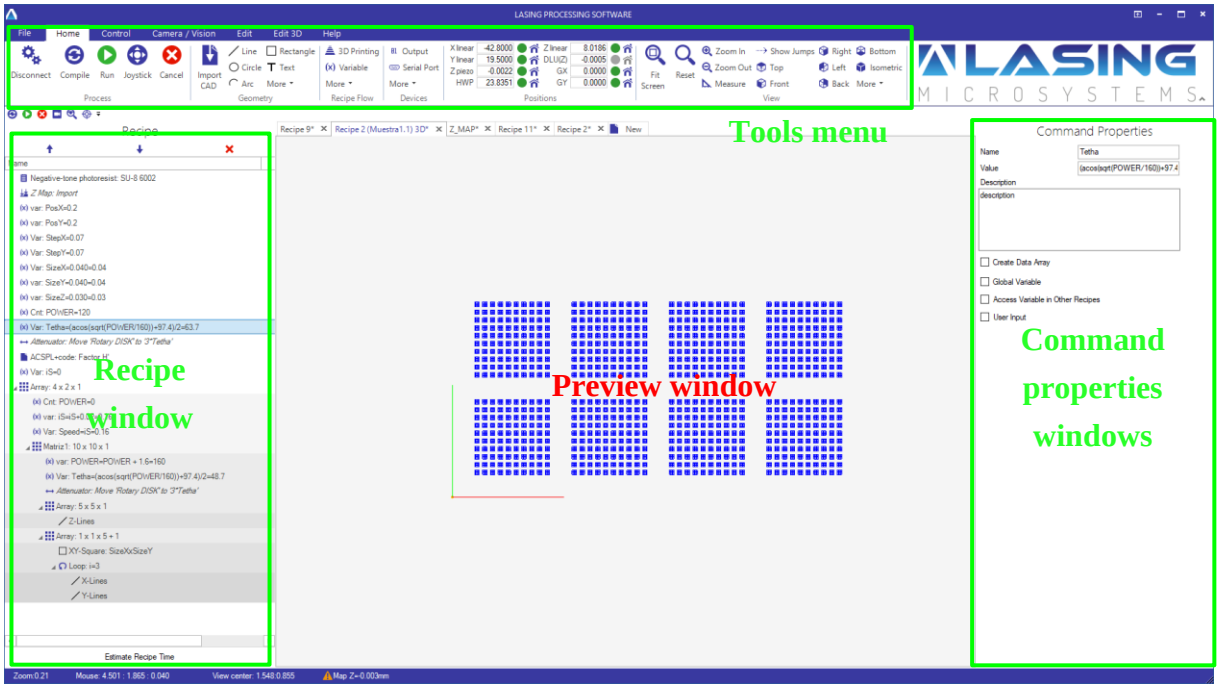

Front panel of the LPS software.

3.2. Tools menu

The Tools menu provides all available tools for processing, calibration, and management of the 2PP system, organized into the following tabs:

Tabs	Description
File	File management tools and General Settings.
Home	Main Tools used in the machining process.
Control	Tools used to control various connected devices
Camera/Vision	Tools related to cameras, their adjustment and control (visible only when Machine Vision module is installed and at least one Camera is enabled in the Settings).
Edit	Tools used in CAD Object Editing.
Edit 3D	Tools used in 3D CAD Object Editing.
Help	Support contacts, bug reporting and manual.

3.3. File tab

The File tab is a drop-down menu that allows users to create new recipes, open software files in the .rps format, save recipes (also in .rps format), and open the **Settings window**. Additionally, sample files are provided for running examples in the LPS software. Please note that only the English language is available in the LPS software.

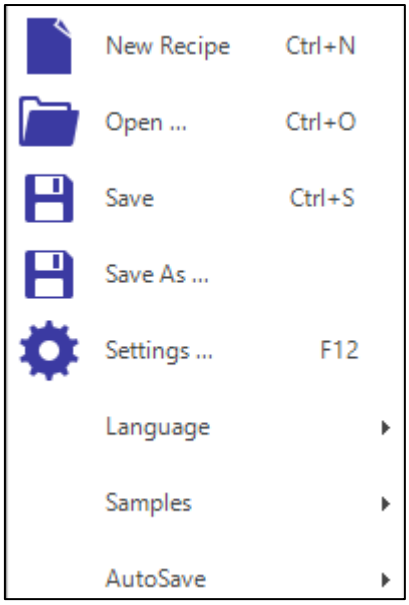

File tab functions.

3.4. Settings window

The general settings window can be accessed via the **File tab**, opening a new window with multiple pages, some of which are subdivided into tabs. This settings window contains all configurable hardware options available for the 2PP system controlled by the software, such as motion controller, stages, galvos, laser, camera, etc.

All hardware must be configured in this window for the correct use of the 2PP system.

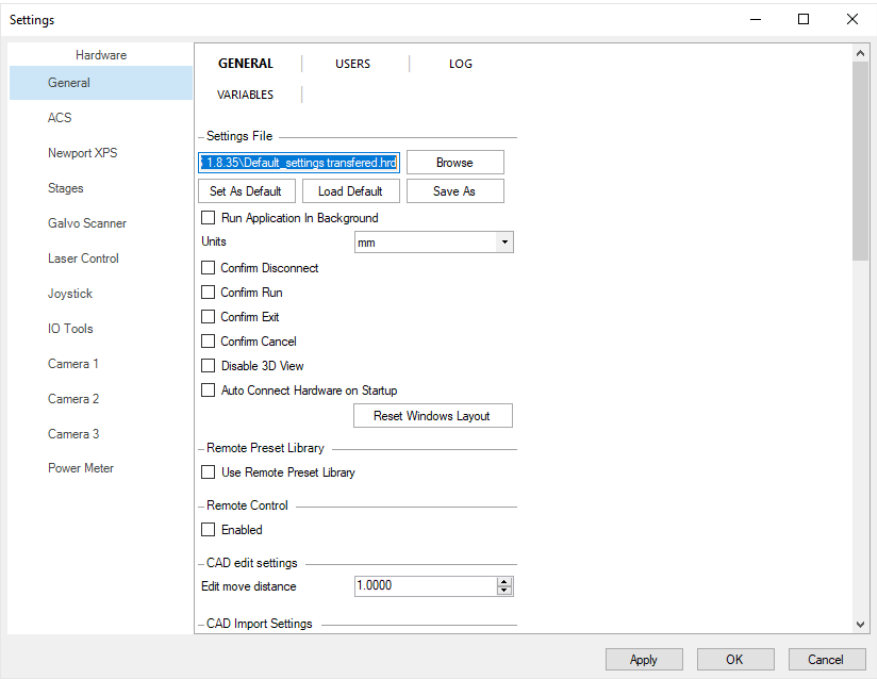

Settings window of the 2PP system hardware.

3.5. Home tab

The home tab can be divided into **process**, **geometry**, **recipe flow**, **device**, **positions** and **view**.

- **Process** provides access to the main functions in the manufacturing workflow, such as **Connect/Disconnect** System, **Compile** Recipe, **Run** Recipe, **Joystick** window, and **Cancel** Process.
- **Geometry** is used to create motion trajectory commands for positioning stages, galvo scanners, or other motion devices, such as lines, circles, rectangles, text, etc.
- **Recipe Flow** describes the use of tools and commands in the recipe window that influence the behavior of other commands during recipe execution. For example, creating sequences of geometric objects with the array command, repeating a geometric object with the for command, applying conditions with the if command, exporting/importing data, adding notes, controller codes, etc.
- **Device** describes the tools and commands in the recipe window that control hardware behavior during recipe execution.
- **Positions** show current position of the positioning axes, i.e, X, Y, Z linear stages, Z piezo stage, X and Y galvos stages, and can be shown the Displacement Laser Unit (DLU) for Z axis – DLU(Z).
- View controls the preview window.

Home tab in Tools Menu.

3.6. Joystick window

The joystick window is a tool allowing manual control of all available positioning stages in the 2PP system.

The keyboards displayed in the window for each linear stage control the position by setting a specific speed or jog distance. Homing and enabling/disabling of each stage can be done using the buttons next to the stage name.

The **Faser Fire** button triggers the laser to fire at the current power setting.

Please wear safety goggles and adhere to other system-specific safety requirements when firing the laser.

Position buttons (P1, P2, P3, P4) allow the user to store specific frequently used positions, such as loading/unloading positions. Motion to predefined positions can be executed by clicking on the P1...P4 buttons. The current position can be assigned to a button by pressing Ctrl + position number on the keyboard (1, 2, 3, 4) or set manually in the Joystick settings. In the Joystick settings, each axis must be enabled or disabled for each position. For example, if the rotary axis is disabled for P1, it will not rotate when P1 is clicked.

Finally, the **settings window** can be opened directly by clicking the **settings** button.

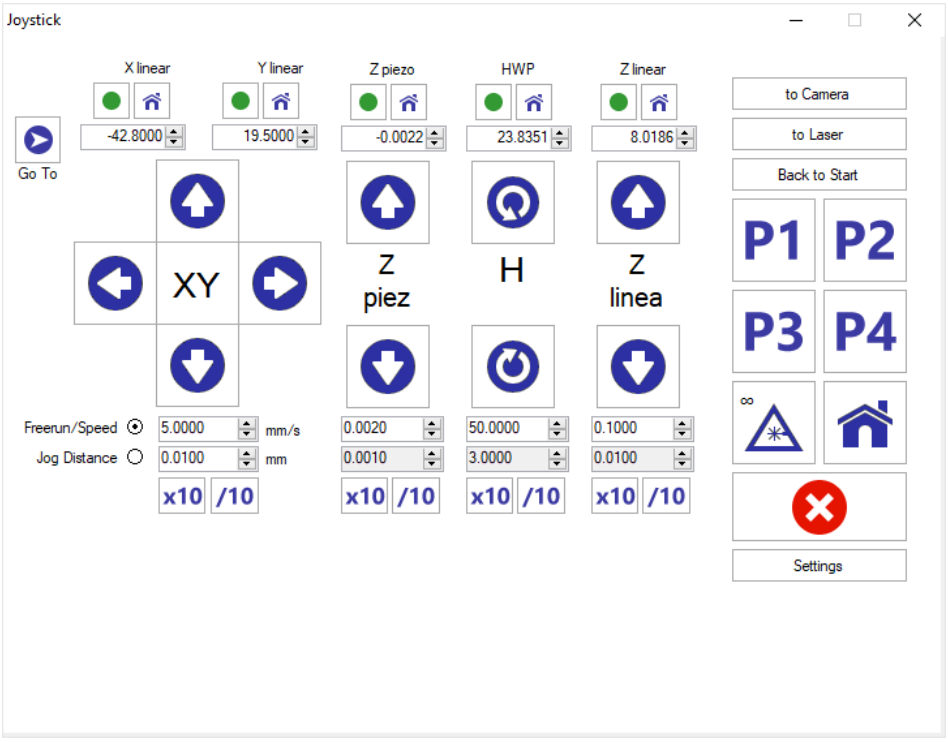

Joystick window. XY galvos buttons are not shown in this window.

3.7. Other Tools menu tabs

For detailed information on the **Control**, **Camera/Vision**, **Edit**, and **Edit 3D** tabs, refer to the **Help** tab in the LPS software directly, or press F1.

4. Start Up the Software of the 2PP System

Before starting a DLW process, the user must follow several steps to prepare the LPS software, ensuring that all hardware is correctly configured and calibrated.

1) Open the LPS software. It can be found in your computer desktop or Windows start tab.

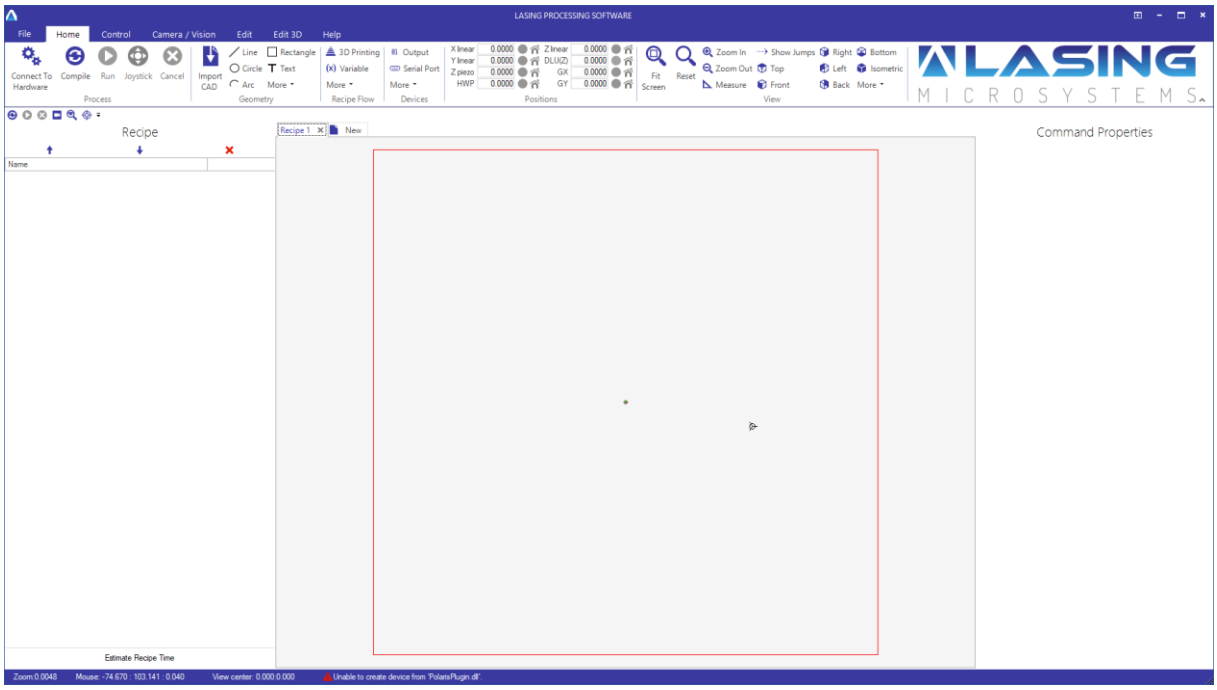

2) Press **Connect To Hardware** button. It can be found in Home tab > Process.

It identifies and checks that all hardware is correctly connected to the 2PP system; otherwise, an error may be displayed if any hardware is not connected.

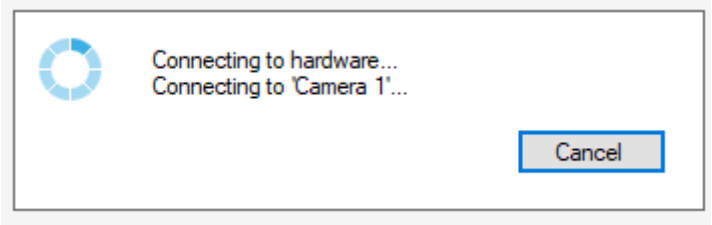

The homing processes for all positioning axes are automatically executed if no errors are present, but some warnings can be appeared in the **positions** tab.

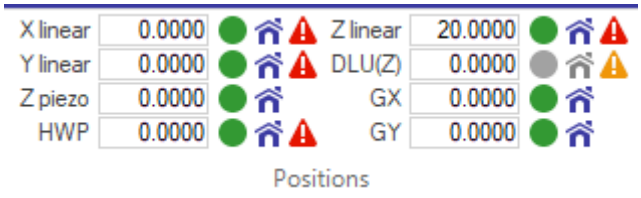

If homing is not executed correctly, press the icon for each stage to repeat it one by one.

To clear all warnings and possible errors, simply press the icon for all stages.

The warning for the Displacement Laser Unit (DLU) is triggered because the sensor is not positioned on the surface of the sample, resulting in a measurement range outside of 24 mm to 26 mm. This error does not stop or hinder your DLW processes.

3) Execute the "Find Focus" example to find the height of the objective lens relative to the surface, i.e., the working distance of the objective lens.

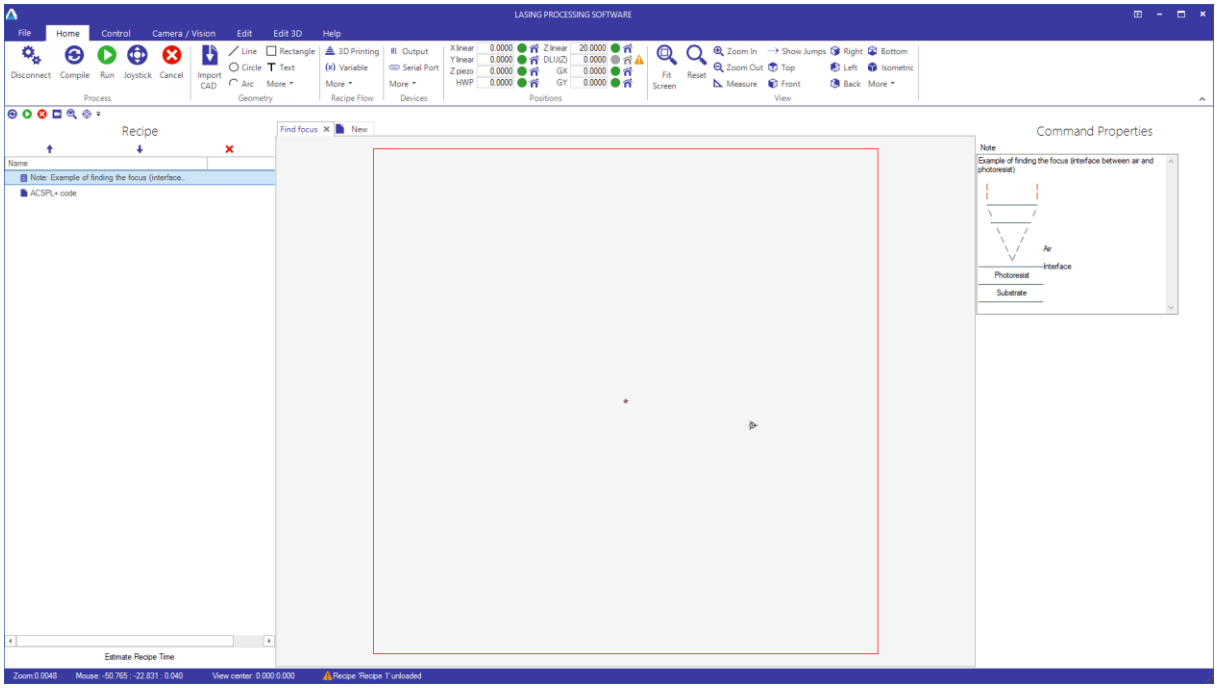

A sample e.g., glass or silicon must be placed on the sample holder to execute the example; otherwise, the objective lens may collide with the sample holder, and it may damage the objective lens.

This example is not available in the example recipes of the LPS software; therefore, it can be easily programmed by adding an ACSPL+code command, which can be found in the Home tab > Recipe Flow > More > ACSPL+code.

In the Command Window, you can enter the following code by selecting ACSPL+code command in the Recipe window:

```
START 7, FOCUS
TILL ^PST(7).1
STOP
```

Then, press the run icon to automatically find the focus. It process is known as coarse focusing.

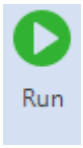

Finally, you can verify the focus by checking the position indicators of the stages, where the Z piezo is related to the measurements from the DLU (0.0028 mm in the below picture). The height of the objective lens is computed automatically and can be displayed in the Z linear stage indicator (8.0123 mm).

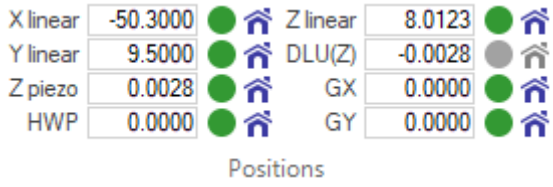

The height of the objective lens may vary if a different sample is placed in the sample holder. To find the new focus, the "Find Focus" example must be executed again.

4) Execute the "Surface mapping" example to determine the topology of the surface sample. This step allows you to find the inclination of the sample on the sample holder and the height (in the Z axis) of the measurement points.

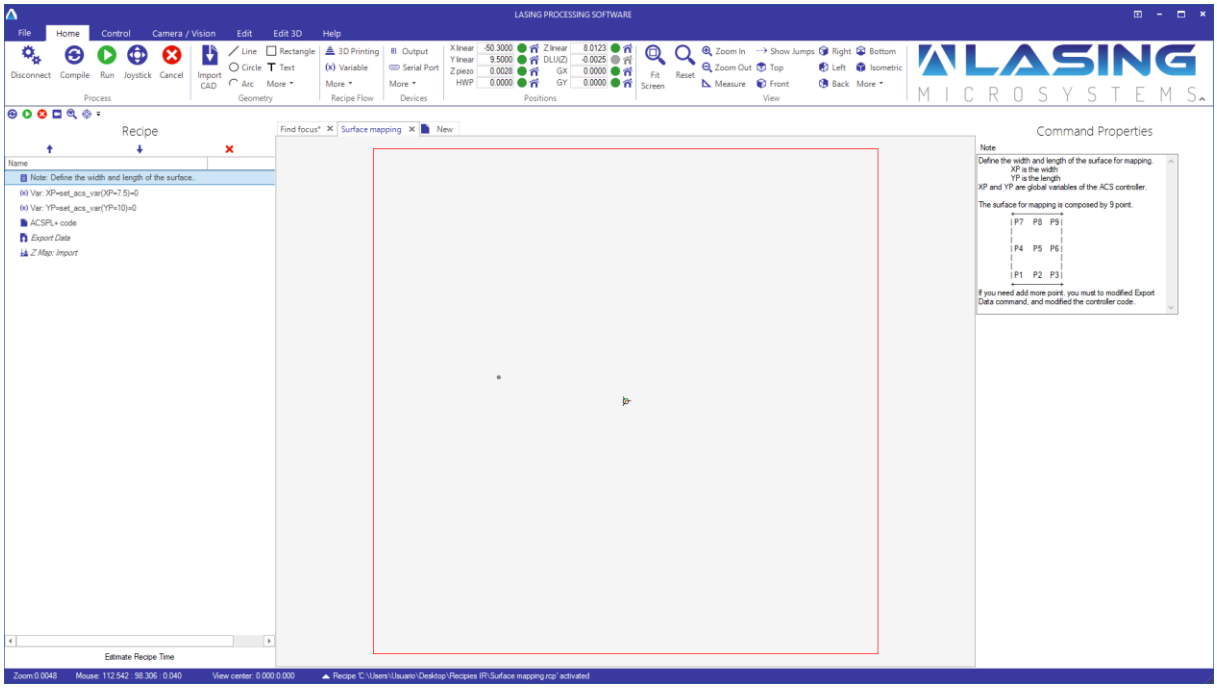

This example is not available in the example recipes of the LPS software; therefore, it can be easily programmed by adding some commands found in the Home tab > Recipe Flow > More. Below is the list of commands needed for this example.

- Variable
- ACSPL+code
- Export Data
- Z Map

Two variables are used to set the width (XP) and length (YP) of the surface to be analyzed. In the Command Window, you can enter the following code by selecting each variable command in the Recipe window:

```
set_acs_var(XP=7.5)
set_acs_var(YP=10)
```

This XP and YP can be changed according to the used needs.

In the Command Window, you can enter the following code by selecting ACSPL+code command in the Recipe window:

```
START 7, Z_MAP
TILL ^PST(7).1
STOP
```

By selecting the Export Data command in the Recipe window, you can program the list of measured points on the surface. These measurements are obtained from the global variables of the ACS controller, and the LPS software builds a table that you can save as a TXT file in any location.

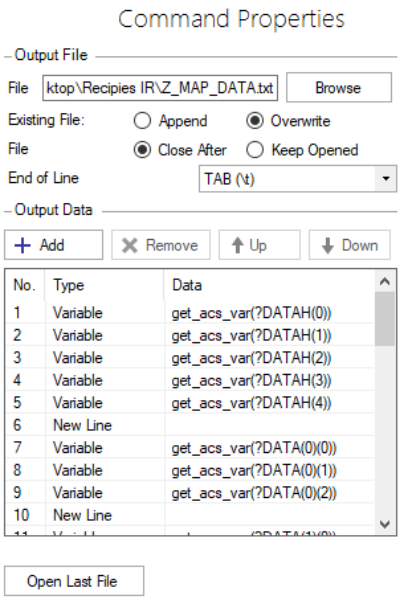

Each item must be programmed one by one, and the following table provides the details for each of them:

No.	Type	Data	No.	Type	Data
1	Variable	get_acs_var(?DATAH(0))	22	New Line	
2	Variable	get_acs_var(?DATAH(1))	23	Variable	get_acs_var(?DATA(4)(0))
3	Variable	get_acs_var(?DATAH(2))	24	Variable	get_acs_var(?DATA(4)(1))
4	Variable	get_acs_var(?DATAH(3))	25	Variable	get_acs_var(?DATA(4)(2))
5	Variable	get_acs_var(?DATAH(4))	26	New Line	
6	New Line		27	Variable	get_acs_var(?DATA(5)(0))
7	Variable	get_acs_var(?DATA(0)(0))	28	Variable	get_acs_var(?DATA(5)(1))
8	Variable	get_acs_var(?DATA(0)(1))	29	Variable	get_acs_var(?DATA(5)(2))
9	Variable	get_acs_var(?DATA(0)(2))	30	New Line	
10	New Line		31	Variable	get_acs_var(?DATA(6)(0))
11	Variable	get_acs_var(?DATA(1)(0))	32	Variable	get_acs_var(?DATA(6)(1))
12	Variable	get_acs_var(?DATA(1)(1))	33	Variable	get_acs_var(?DATA(6)(2))
13	Variable	get_acs_var(?DATA(1)(2))	34	New Line	
14	New Line		35	Variable	get_acs_var(?DATA(7)(0))
15	Variable	get_acs_var(?DATA(2)(0))	36	Variable	get_acs_var(?DATA(7)(1))
16	Variable	get_acs_var(?DATA(2)(1))	37	Variable	get_acs_var(?DATA(7)(2))
17	Variable	get_acs_var(?DATA(2)(2))	38	New Line	
18	New Line		39	Variable	get_acs_var(?DATA(8)(0))
19	Variable	get_acs_var(?DATA(3)(0))	40	Variable	get_acs_var(?DATA(8)(1))
20	Variable	get_acs_var(?DATA(3)(1))	41	Variable	get_acs_var(?DATA(8)(2))
21	Variable	get_acs_var(?DATA(3)(2))	--	--	--

The LPS software also includes the FOCUS and Z MAP commands for finding the focus of the objective lens and performing the surface mapping process, respectively. However, these commands are not reliable as they exhibit errors in stage positioning at resolutions below 5 microns.

Finally, Z MAP is only used to import files for applying surface mapping in the recipes obtained during this startup step.

Finally, the Z Map command is used to display the mapped surface by reading the previously created TXT file.

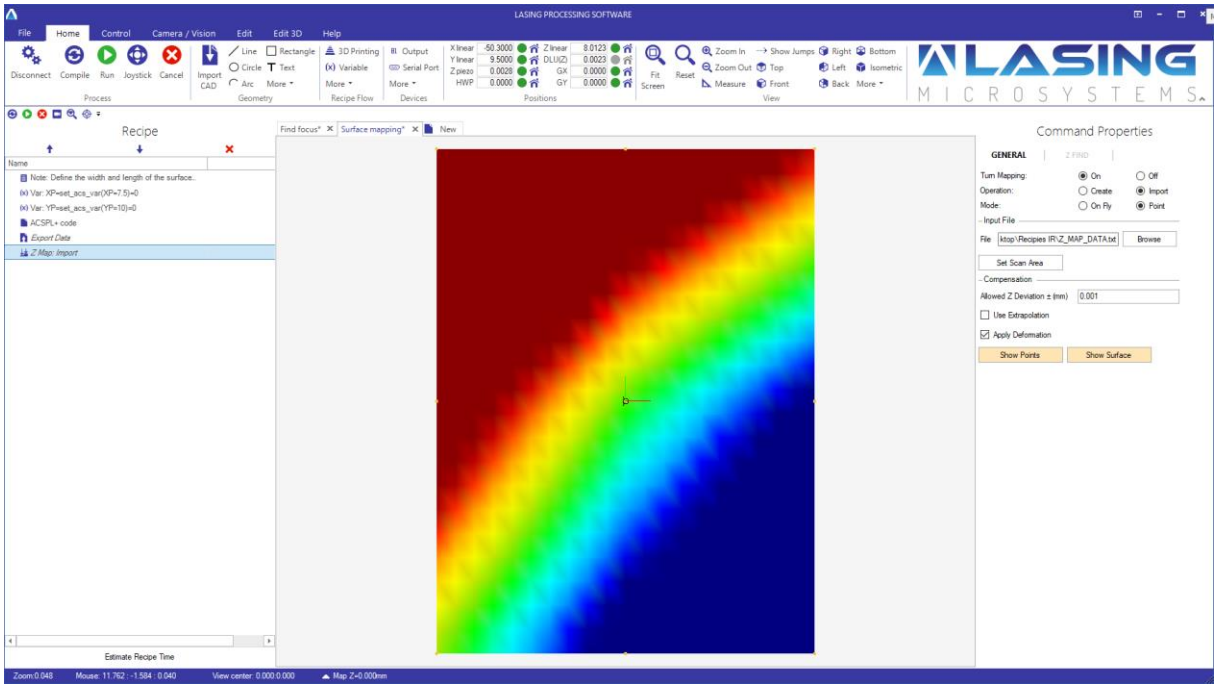

Nine default points are defined in this example. If you need to extend the measurement range with more points, you must modify Export Data command adding more variables and modified the “DATA” array from the ACS controller code, located in D-Buffer and Buffer 7.

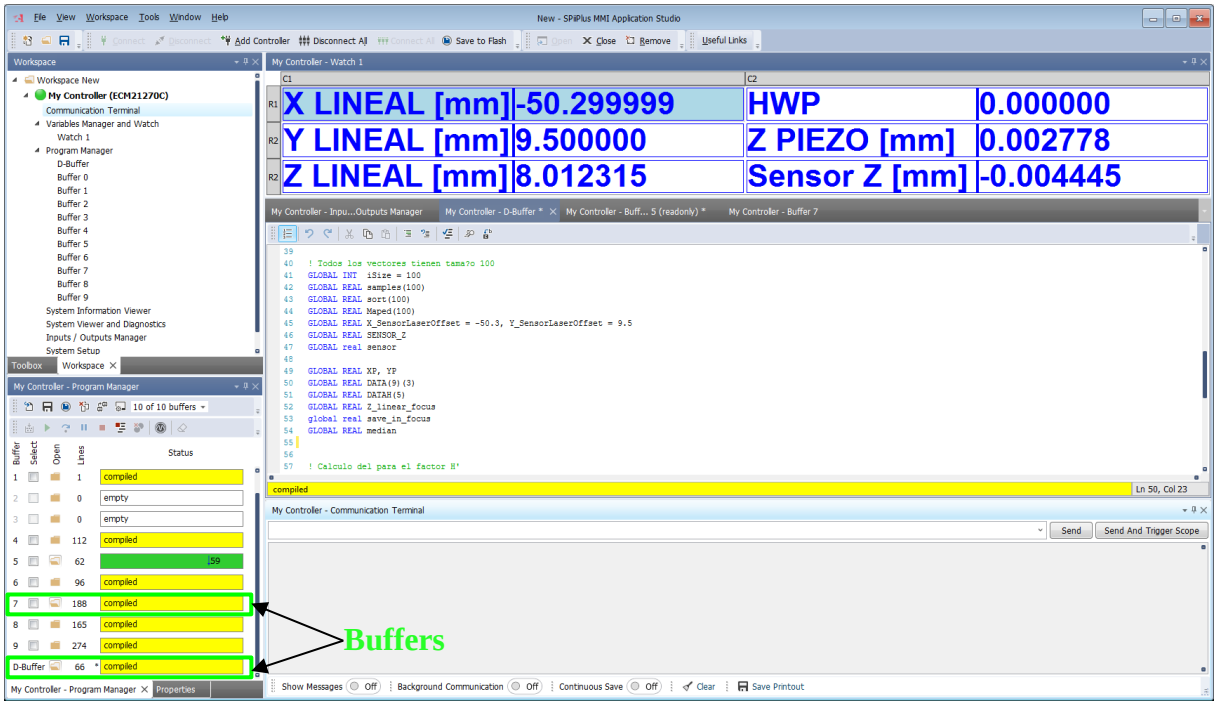

The "Find focus" and "Surface mapping" examples can be used as many times as needed for the required samples before executing the DLW processes.

5. Application examples

2D and 3D structures are commonly polymerized in the 2PP system; therefore, the following examples show how to program them in the LPS software.

The LPS software does not have a structured programming format; you must ensure that all commands used are correctly ordered according to the sequential lines in the recipe window.

5.1. Process Geometric Objects

In this example, you will program a 10×10 matrix of square objects. Each square object is configured with different laser power, increasing from 0.1 mW for the first object to 160 mW for the last object. All objects will be polymerized at the same scanning speed of 0.1 mm/s. The size of the square objects is 40×40 μm^2. Additionally, a cross object is inserted inside each square object.

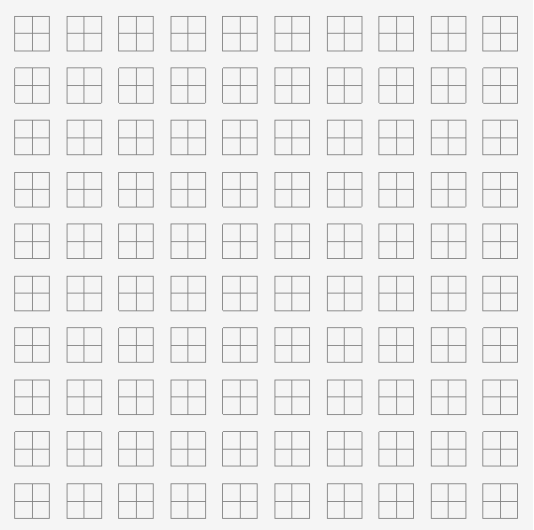

The LPS software must be prepared beforehand to program 2D structures; this means that focusing using the "Find Focus" example and mapping the topology of the photoresist with the "Surface Mapping" example must be performed on the photoresist surface where the structure will be polymerized.

"Find Focus" and "Surface Mapping" examples are explained in section 4.

1) First, insert the necessary variables to define object positions, object sizes, and initialize scanning speed or laser power. Using these variables is not mandatory but simplifies the program's flow.

   The **variable** command can be found in Home tab > Recipe Flow > Variable

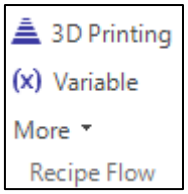

2) Next, a mandatory command is to import the mapping file of the material surface created by the previously specified "Surface Mapping" example.

   The **Z Map** command can be found in Home tab > Recipe Flow > More > Z Map.

   In the Command Window, you can configure the required parameters to import the file and display the mapped surface topology in the Preview window:

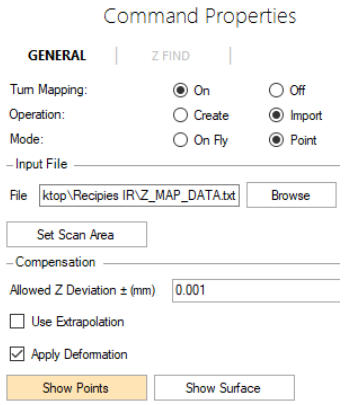

3) If the thickness of the photoresist is less than the voxel depth of the focused femtosecond laser along the optical axis, the factor *H'* cannot be applied.

$$z\text{-}voxel = \frac{2\lambda\eta}{NA^2}$$

4) Then, you insert to the recipe window an Array command, to build a matrix of squared objects with crosses. For this, **Array** command can be found in Home tab > Recipe Flow > More > Array.

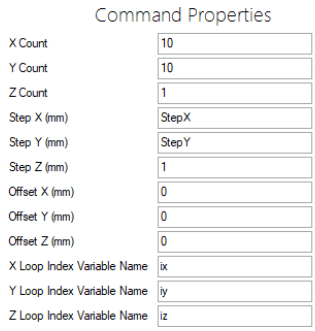

   X and Y Count parameters let set the size of the matrix, it is 10×10 objects.

   StepX and StepY are optional variables inserted in the first step of this example to define the separation between consecutive objects along the X and Y axes.

5) To increase the laser power for each object, two variables will be used to control each iteration, and will be inserted inside of the Array command.

   The One variable command is set as $Power = Power + 0.1$

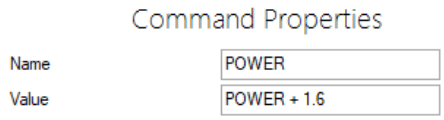

The laser power value may vary depending on the used photoresist. You should verify the data available in "Appendix D: Voxels characterization" of this PhD project.

   The laser power is defined by the next equation:

$$Power = 160\, cos^2(2\theta - 97.4°)$$

   where the power is attenuated by varying the angle θ.

   So, the second variable command is set as $\theta = \frac{1}{2}\left(\text{acos}\left(\sqrt{\frac{Power}{160}}\right) + 97.4°\right)$

6) According to the θ computed in the variable command, you need to rotate the half-wave plate (HWP) assembled inside the rotary stage. Therefore, you must use an **Axis** command to rotate the HWP based on the angle obtained from the variable command.

   The **Axis** command can be found in Home tab > Devices > More > Axis.

   In the Command Window, you can select the Rotary HWP to move the stage and set the angle θ multiplied by 3. The constant is used because the axis of rotation of the rotary stage is reduced by a factor of 3 with respect to the internal motor's rotation.

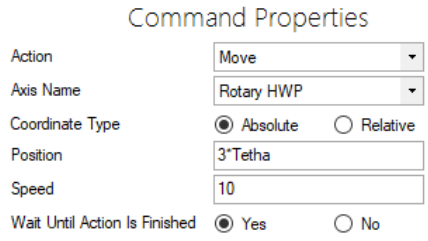

   The speed of the rotary stage can be set according to the user requirements.

7) Next, you can insert the geometric object to be polymerized in the photoresist. The squared object can be found in Home tab > Geometry > Rectangle.

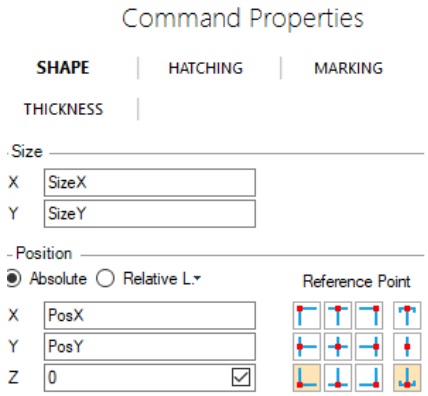

SizeX and SizeY are variables to set the object size, it is 40×40 μm².

PosX and PosY are variables to set the object position in the Preview Window.

The cross object can be created by inserting two-line command, and it can be found in Home tab > Geometry > Line.

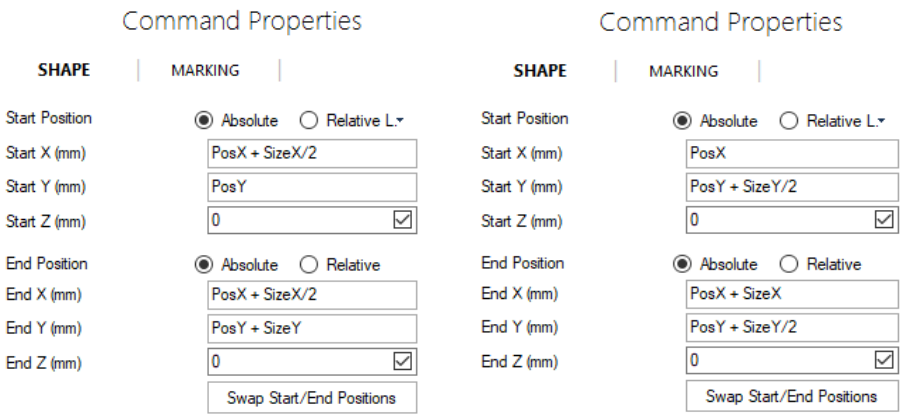

8) Finally, the objects to be polymerized on the photoresist are configured according to scanning speed parameter in marking properties.

If scanning speed parameter is not configured, the object will not be polymerized.

In the Command Window, you can configure this parameter by selecting marking tab of the geometry object.

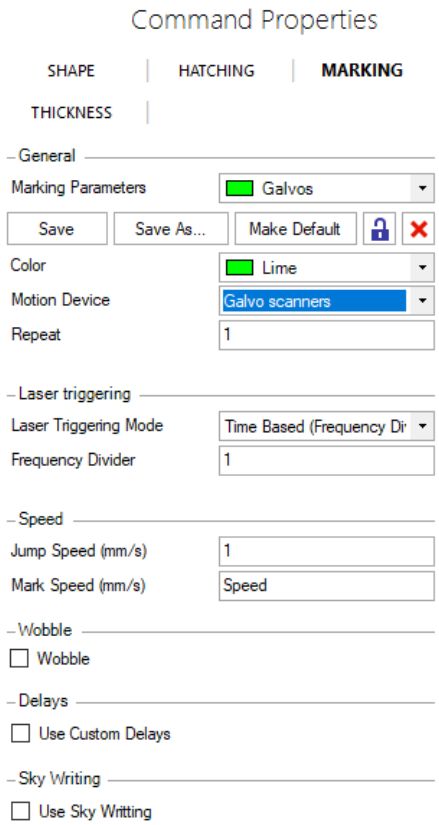

Marking parameters can be created and saved for use in other objects or recipe projects.

The Motion Device allows you to select which stages can be used to execute motion for the DLW processes.

If the size of the geometric objects is larger than the field of view of the XY galvos, the **stitching** command must be added to the recipe window; otherwise, errors may appear during compilation.

The Mark Speed (mm/s) allows you to set the scanning speed for DLW processes. The stages will be moved to the set speed. This can be used and variable command to set the speed variable for other recipes projects or objects.

9) In the next figure you can see the completed example in the LPS software with all commands displayed in the recipe window.

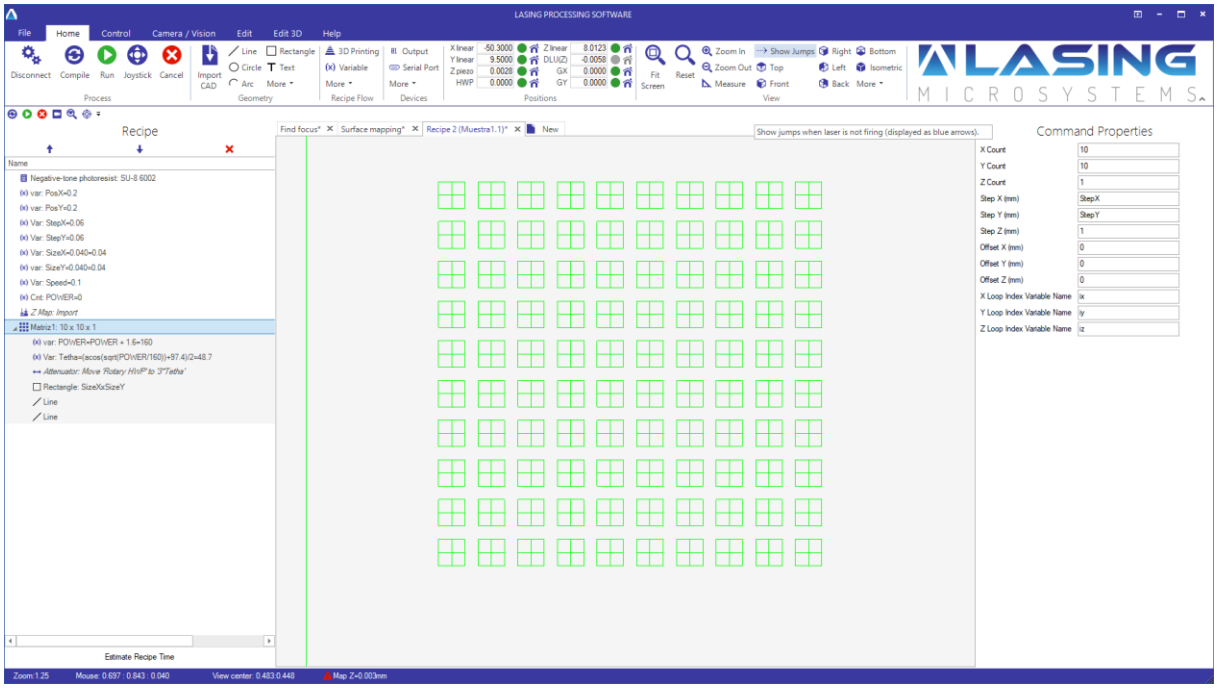

5.2. Process DXF file

In this example, you will load a DXF file to be processed in 2PP system. This file will be configured according to the processing parameters, adding hatching parameters and stitching command.

The LPS software must be prepared beforehand to program 2D structures; this means that focusing using the "Find Focus" example and mapping the topology of the photoresist with the "Surface Mapping" example must be performed on the photoresist surface where the structure will be polymerized.

"Find Focus" and "Surface Mapping" examples are explained in section 4.

1) First, insert the necessary variables to define, for example, CAD positions, CAD sizes, and initialize scanning speed or laser power. Using these variables is not mandatory but simplifies the program's run flow.

   The **variable** command can be found in Home tab > Recipe Flow > Variable

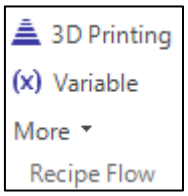

2) Next, a mandatory command is to import the mapping file of the material surface created by the previously specified "Surface Mapping" example.

   The **Z Map** command can be found in Home tab > Recipe Flow > More > Z Map.

   In the Command Window, you can configure the required parameters to import the file and display the mapped surface topology in the Preview window:

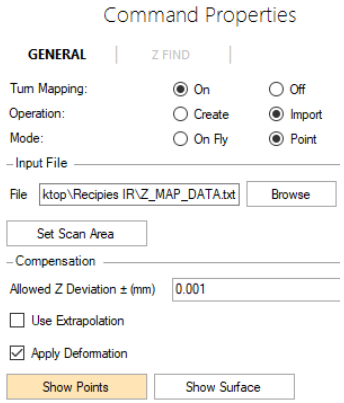

3) Then, you can insert the stitching command. This command can be found in Home tab > Devices > More > Stitching.

   In the Command Window, you can configure all parameters by selecting stitching command in recipe window.

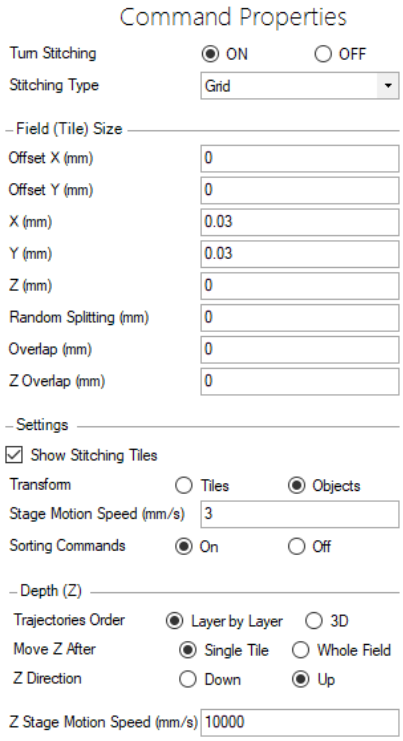

The Stitching Type allows you to choose how to divide the CAD object into n processing tiles.

The X and Y dimensions of the tiles must be configured to be less than the field of view of the galvos in X (mm) and Y (mm), here it can be set to 30 × 30 µm².

4) If the thickness of the photoresist is less than the voxel depth of the focused femtosecond laser along the optical axis, the factor *H'* cannot be applied.

$$z\text{-}voxel = \frac{2\lambda\eta}{NA^2}$$

5) The configured laser power is constant in this example. Therefore, two variable commands are used to configure it.

One variable command is set as $Power = 150$

The laser power value may vary depending on the photoresist used. You should verify the data available in "Appendix D: Voxels characterization" of this PhD project.

The laser power is defined by the next equation:

$$\text{Power } = 160\cos^2(2\theta - 97.4°)$$

where the power is attenuated by varying the angle θ.

So, the second variable command is set as $\theta = \frac{1}{2}\left(\text{acos}\left(\sqrt{\frac{Power}{160}}\right) + 97.4°\right)$

6) According to the θ computed in the variable command, you need to rotate the half-wave plate (HWP) assembled inside the rotary stage. Therefore, you must use an **Axis** command to rotate the HWP based on the angle obtained from the variable command.

   The **Axis** command can be found in Home tab > Devices > More > Axis.

   In the Command Window, you can select the Rotary HWP to move the stage and set the angle θ multiplied by 3. The constant is used because the axis of rotation of the rotary stage is reduced by a factor of 3 with respect to the internal motor's rotation.

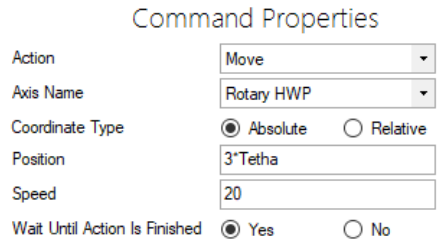

   The speed of the rotary stage can be set according to the user requirements.

7) Next, you can insert the CAD object to be polymerized in the photoresist. The DXF file can be loaded from Home tab > Geometry > Import CAD.

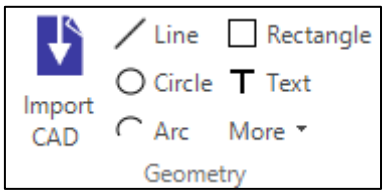

   In the Command Window, you can configure all parameters by selecting the CAD Object command in the recipe window.

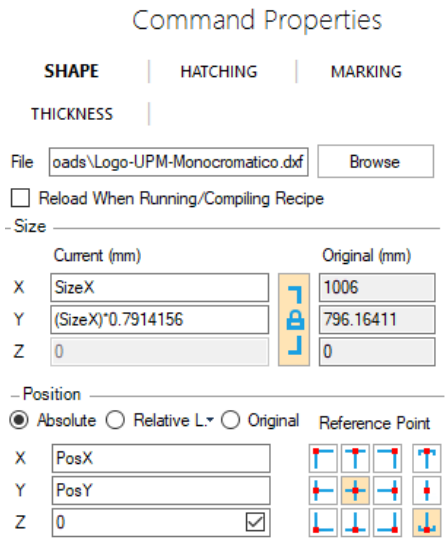

The CAD size can be set using a user variable command (SizeX).

The position of the CAD object can be set using PosX and PosY variables.

8) Then, the CAD object is configured to add hatching properties.

In the Command Window, you can configure this parameter by selecting the hatching tab of the CAD object.

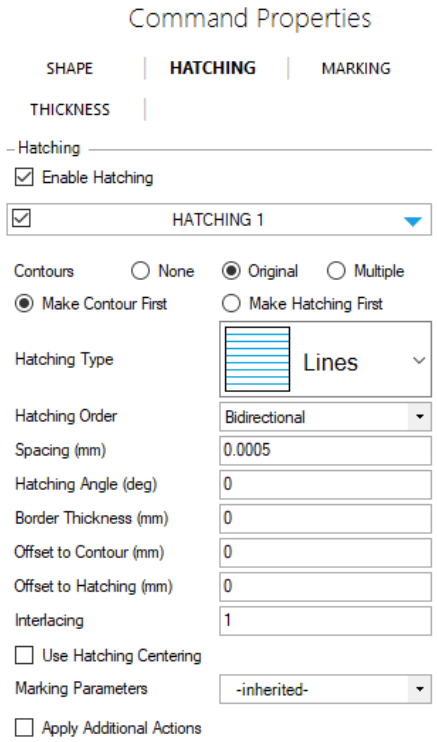

Different hatching types are available, allowing you to set the spacing, angle, order, etc.

9) Finally, the CAD object to be polymerized on the photoresist are configured according to scanning speed parameter in marking properties.

If scanning speed parameter is not configured, the object will not be polymerized.

In the Command Window, you can configure this parameter by selecting marking tab of the geometry object.

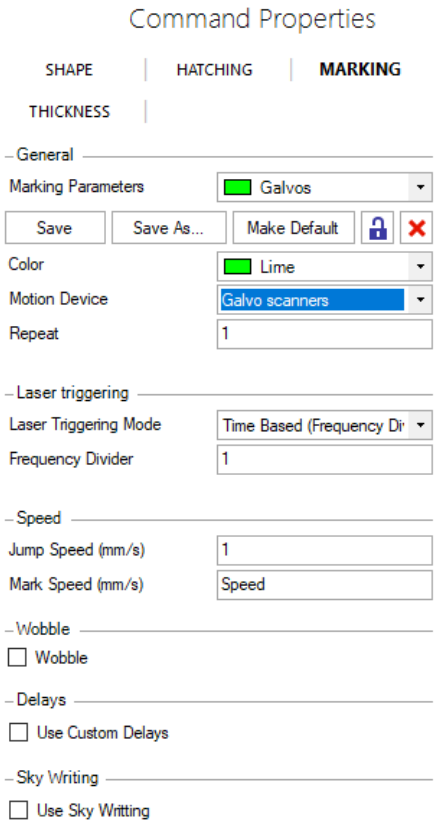

Marking parameters can be created and saved for reuse in other objects or recipe projects

The Motion Device allows you to select which stages can be used to execute motion for the DLW processes.

If XY linear stages are used for DLW processes, the stitching command does not need to be used.

The Mark Speed (mm/s) allows you to set the scanning speed for DLW processes. The stages will be moved to the set speed. This can be used and variable command to set the speed variable for other recipes projects or objects.

10) In the next figure you can see the completed example in the LPS software with all commands displayed in the recipe window.

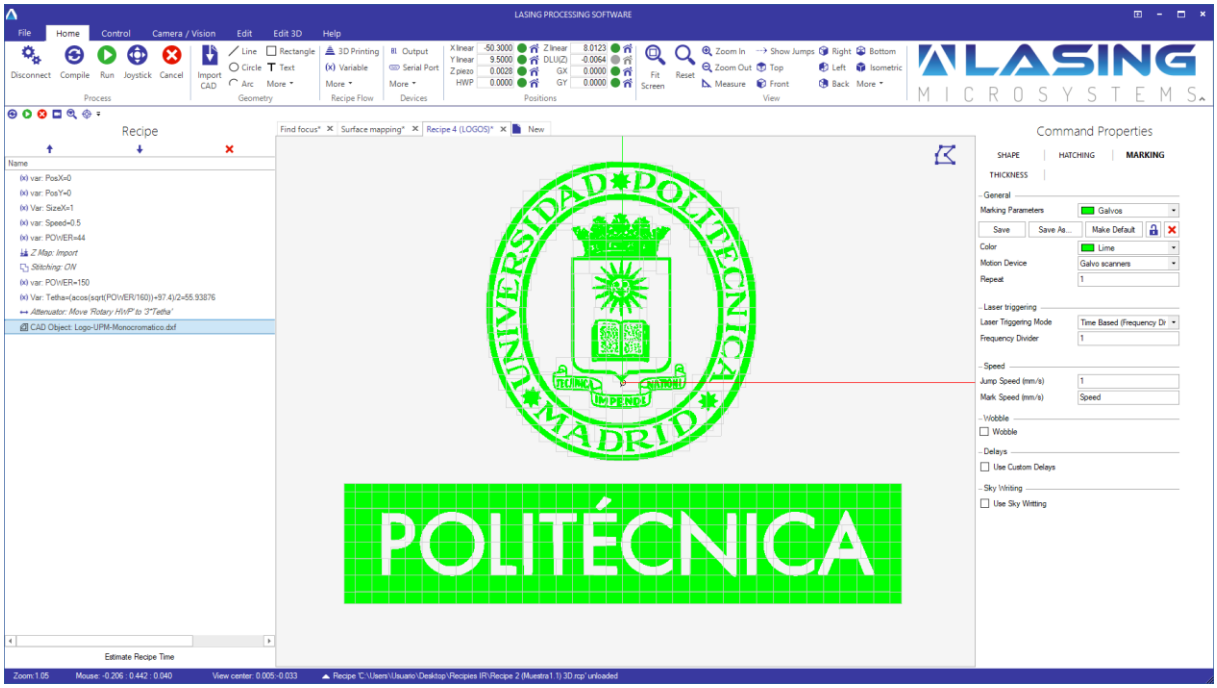

5.3. Process STL files

In this example, you will load an STL file to be processed in the 2PP system. This file will be configured according to the processing parameters, with added hatching parameters and 2.5D settings. You will program a wafer of lenses, as shown in the figure below. All lenses are configured with the same laser power and scanning speed.

The lens design can be downloaded from Newport or Thorlabs in any format and then converted to STL format. The lens size is flexible but will be resized to micron dimensions within the LPS software.

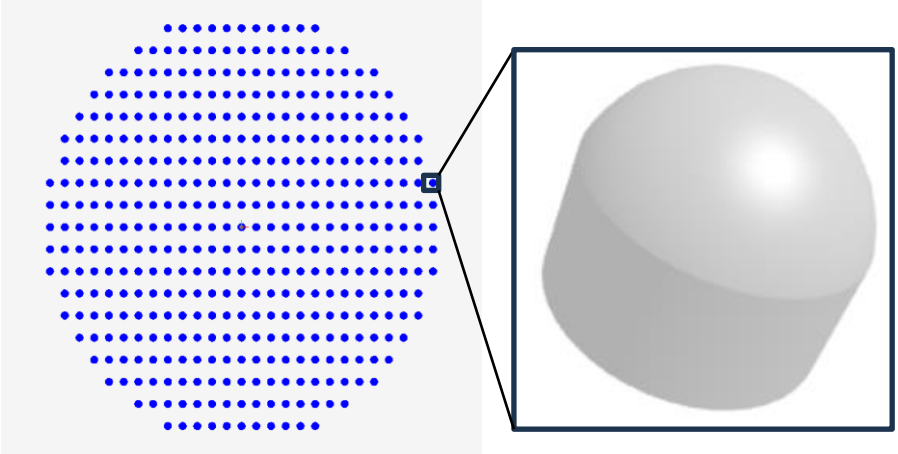

Find Focus and Surface Mapping must be previously performed on the photoresist. "Find Focus" and "Surface Mapping" examples are explained in section 4.

1) First, insert the necessary variable commands to define parameters such as lens positions, lens sizes, separation between lenses, scanning speed, and laser power, etc.

   The **variable** command can be found in the Home tab > Recipe Flow > Variable.

   Next, the inserted variables for this example are shown in the recipe window in the figure below.

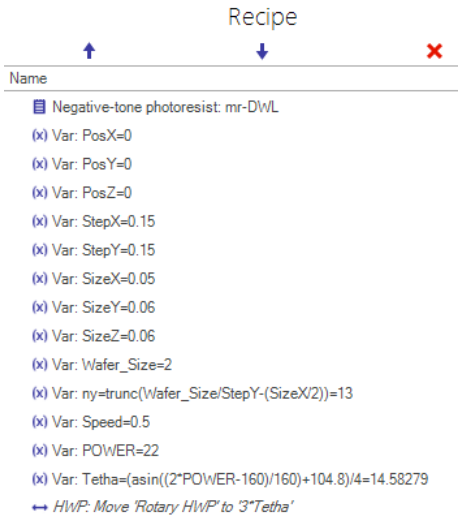

   The wafer size can be bigger or less than 2 mm. If it is bigger, the LPS software can take more time to compile the example.

   The photoresist used in this example is mr-DLW 40. Therefore, the height of the lenses must be less than the thickness of the spin-coated photoresist.

   The laser power is defined as a constant value in this example, and all lenses will be processed with the same intensity as a function of θ.

   To define the angle θ at the given laser power, you will set the following equation in a variable command:

$$\theta = \frac{1}{2}\left(\operatorname{acos}\left(\sqrt{\frac{Power}{160}}\right) + 97.4°\right)$$

   According to the θ computed in the variable command, you need to rotate the half-wave plate (HWP) assembled inside the rotary stage. Therefore, you must use an **Axis** command to rotate the HWP based on the angle obtained from the variable command.

   The **Axis** command can be found in Home tab > Devices > More > Axis.

   In the Command Window, you can select the Rotary HWP to move the stage and set the angle θ multiplied by 3.

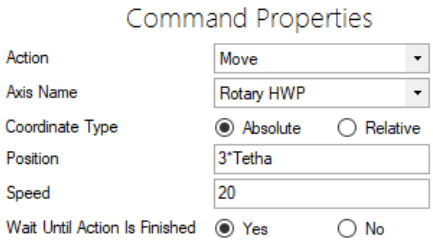

2) Next, import the mapping file of the photoresist surface created by "Surface Mapping" example.

   The **Z Map** command can be used to import the TXT file, and it can be found in Home tab > Recipe Flow > More > Z Map.

   In the Command Window, you can configure the required parameters to import the file and display the mapped surface topology in the Preview window:

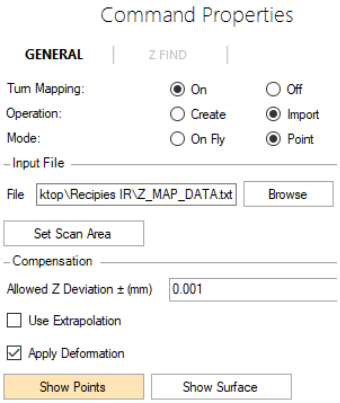

3) Next, insert an ACSPL+ code command to compute the factor *H'* for the mr-DLW 40 photoresist. This will move the Z linear stage downward until the laser spot is aligned with the photoresist-substrate interface.

   The **ACSPL+code** command can be found in the Home tab > Recipe Flow > More > ACSPL+code.

   In the Command Window, you can enter the following code by selecting ACSPL+code command in the Recipe window:

```
!Set the thickness of the spin-coated photoresist in mm.
THK=0.060

START 7, mr_DLW
TILL ^PST(7).1
STOP
```

   To apply the factor *H'*, you must know the thickness of the spin-coated photoresist. In this example the thickness is 60 µm. The photoresist datasheet must be checked to obtain the desired thickness.

   The following table lists the photoresist codes available in the ACS controller database.

Photoresist	Code in ACSPL+code command
S1800 G2 serie	S1800
SU-8 2000 serie	SU8_2000
SU-8 6000 serie	SU8_6000
mr-DLW serie	mr_DLW
EpoCore serie	EpoCore

4) Next, insert Loop commands to construct the wafer. This is achieved by using two nested Loops to calculate the arrangement and quantity of lenses that will form the wafer.

   The **Loop** command can be found in the Home tab > Recipe Flow > More > Loop.

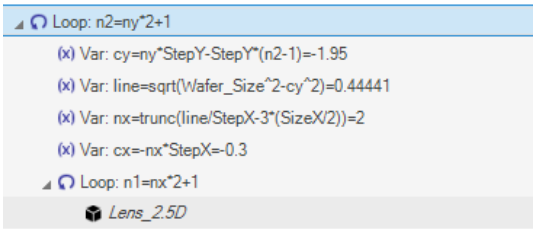

   Each loop is assigned by n2 for iteration in y-axis, and n1 for iteration in x-axis.

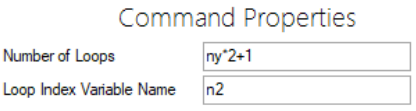

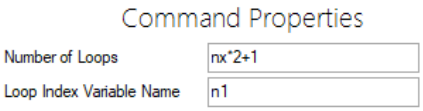

5) Next, you can insert the STL object to be polymerized in the photoresist. The STL file can be loaded from Home tab > Geometry > Import CAD. And it is nested in the second Loop command.

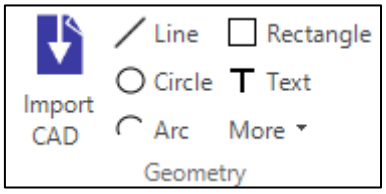

   In the Command Window, you can configure all parameters by selecting the CAD Object command in the recipe window.

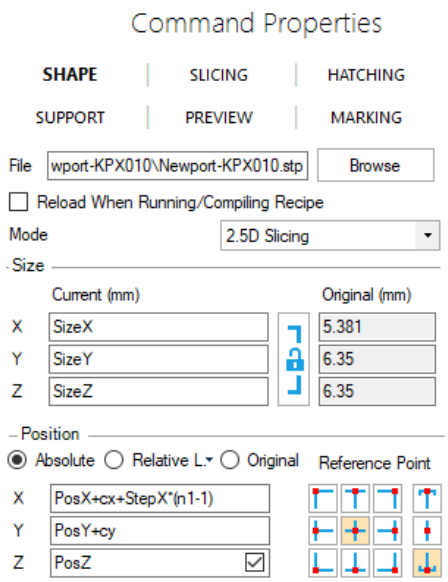

The lenses size can be set using a user variable command (SizeX, SizeY and SizeY).

The positions of the lenses can be defined using the expressions shown in the figure above. These define the distribution of the lenses on the wafer.

The mode used in this example is 2.5D Slicing. This means that the lenses will be polymerized by layers.

A 3D mode for STL files is also available in the LPS software.

6) Then, the Lenses are configured to define the separation between layers.

In the Command Window, you can configure it by selecting the Slicing tab of the STL object.

The distance between layers is determined by the voxel height for the given photoresist.

7) Then, the Lenses are configured to add hatching properties.

   In the Command Window, you can configure it by selecting the hatching tab of the STL object.

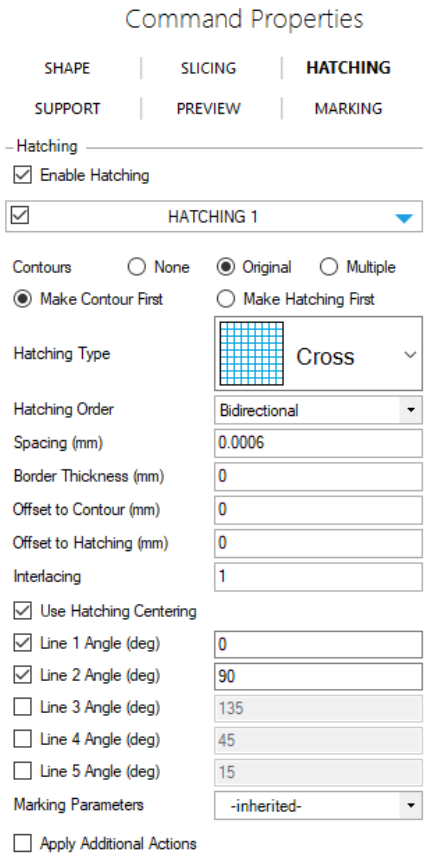

   Different hatching types are available, allowing you to set the spacing, angle, order, etc.

The hatching parameter is defined by the lateral voxel size in the XY plane for the given photoresist.

8) Finally, the scanning speed parameter in the marking properties will be configured for the STL objects. Linear stages are used instead of galvos.

   In the Command Window, you can configure it by selecting the marking tab of the geometry object.

If scanning speed parameter is not configured, the object will not be polymerized.

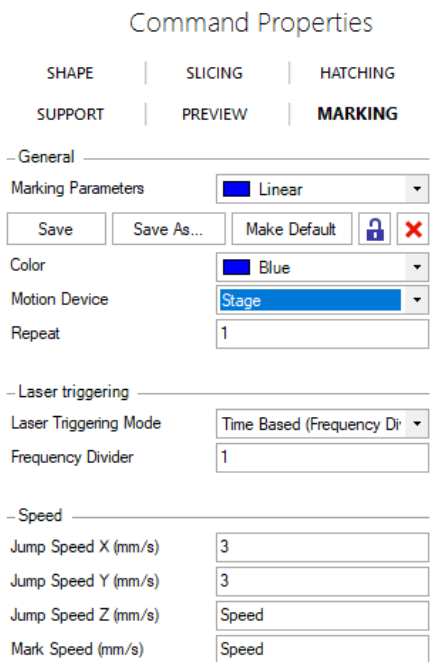

Marking parameters can be created and saved for reuse in other objects or recipe projects.

The Motion Device allows you to select which stages can be used to execute motion for the DLW processes.

If XY linear stages are used for DLW processes, the stitching command does not need to be used.

The Mark Speed (mm/s) allows you to define the scanning speed for DLW processes, adjusting stage movement to the specified speed. This setting can be used with a variable command to set the speed as a variable for other recipe projects or objects.

9) In the next figure you can see the completed example in the LPS software with all commands displayed in the recipe window.

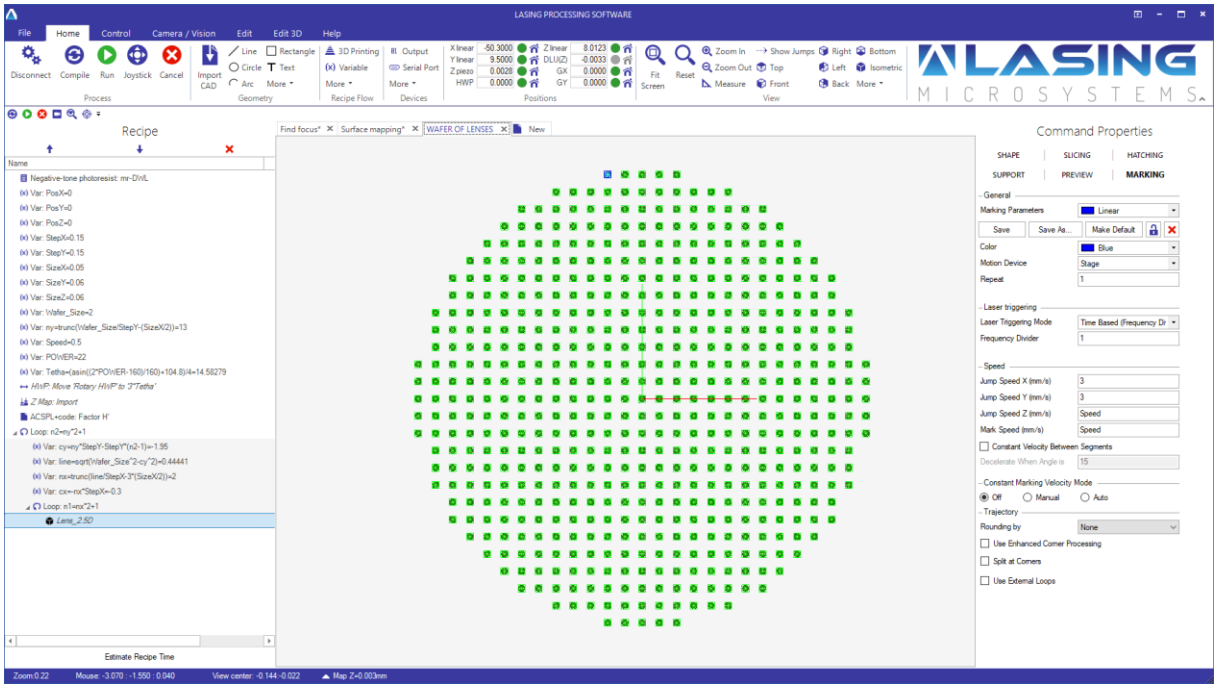

Additionally, you can see the layers of the Lenses in Preview tab.